

In-situ Real-time Monitoring of Waterborne Low Energy Betas



Nile Edward James Dixon

**This thesis is submitted for the degree of
Doctor of Philosophy**

January 2025

School of Engineering

Declaration

I, Nile E J Dixon certify that this thesis has not been submitted in support of an application for another degree at this or any other university and is the result of my own work and does not include anything that is the outcome of work done in collaboration except where specifically indicated.

Parts of chapter 3 within this thesis have been published in MDPI Sensors:

- Nile E. J. Dixon; Stephen D. Monk; James Graham; David Cheneler Compact Back-End Electronics with Temperature Compensation and Efficient Data Management for In Situ SiPM-Based Radiation Detection. *Sensors* 2023, 23, 4053. <https://doi.org/10.3390/s23084053>

Parts of chapters 4 and 1.1 within this thesis have been published in MDPI Radiation:

- Nile E. J. Dixon; Stephen D. Monk; James Graham; David Cheneler Laminated Flow-Cell Detector with Granulated Scintillator for the Detection of Tritiated Water. *Radiation* 2023, 3, 211-225. <https://doi.org/10.3390/radiation3040017>

This work has also been presented at the following events:

- NDA PhD Bursary Seminar, January 2023, Manchester – Poster and Presentation
- NDA PhD Bursary Seminar, 25th January 2022, Manchester – Poster and Presentation
- TRANSCEND and NDA Conference, December 2020, Virtual - Presentation
- Science Week: PGR Speed Talks, March 2023, Lancaster University – Poster and Winning Presentation

Abstract

Nuclear Licenced sites like Sellafield, Dounreay, and Dungeness B handle hazardous radioactive material which is stored before it can be reprocessed for permanent storage. To ensure the safety of these sites, groundwater sampling is performed from an array of onsite boreholes. Boreholes containing low energy betas are of additional interest due to the difficulty in their detection, requiring advanced measurement techniques which are not yet suited to an in-situ setting.

This research has implemented granulated scintillators within a manufactured novel flow cell detector aimed at detecting low energy betas. The detector is to be placed within the borehole itself to take direct measurements of the groundwater, removing the delay of sampling and transporting the samples offsite. Methods have been tested for granulating and separating solid scintillators, with finer particulates achieving higher detection efficiencies for tritium. Silicon Photomultipliers (SiPMs) in contact with the flow cell have been used to detect radiation interacting with the scintillator.

A Field Programmable Gate Array (FPGA) has been implemented to shape pulses from a SiPM into spectra that are accumulated and stored within a database hosted within the detector. This system has been validated experimentally using four sealed gamma sources by identifying and fitting photopeaks within the captured spectra to known gamma energies. LED blink testing has been conducted to study how the pulse shaper delay coefficients affect recorded spectrums.

The electrical system and flow cell have then been combined into a benchtop system and tested with multiple concentrations of tritiated water, results show a correlation between detected count rate and the activity concentration within the flow cell. Experiments with strontium-90 tracers show an increase in count rate as the tracer entered the flow cell, and two borehole groundwater samples taken from the Sellafield site have been passed through the detector obtaining two spectra. Finally, the benchtop system has been compacted to fit within the limited confines of standard 50 mm boreholes.

Acknowledgements

I would like to thank and acknowledge my supervisors Dr David Cheneler, Dr Stephen Monk and Dr James Graham for their help and guidance across the whole project, and for allowing access to samples taken from Sellafield. I would also like to thank Dr Jackie Pates who allowed us access to their lab to perform all open-source experiments, Dr Ashley Jones for providing feedback and approval of key risk assessments, Dr Dave Hughes for access to sources and equipment and finally Dr Vassil Karloukovski for his knowledge and help using auto sieve equipment.

Finally, I would like to give an enormous thank you to the NDA bursary scheme for their financial support which without this research could not have been done, as well as the added insight into the nuclear decommissioning industry through the NDA bursary seminars.

Contents

1 INTRODUCTION	1
1.1 Radioactivity	2
1.2 Low Energy Beta Decay of Tritium	3
1.3 The Creation of Tritium	4
1.4 Uses of Low Energy Beta Emitters	4
1.5 Importance of Environmental Tritium Monitoring	5
1.6 Borehole In-situ Detection	6
1.7 Overview of Scintillator Detectors and Sample Preparation	9
1.8 Difficulties in Low Energy Beta Detection and Characterisation	11
1.9 Objectives and Thesis Structure	14
2 LITERATURE REVIEW	16
2.1 Introduction	16
2.2 Sellafield Groundwater Monitoring	16
2.3 Detection of Soft Betas using Geiger Muller Tubes	18
2.4 Detection of Beta Radiation using Image Sensors	18
2.5 Tritium Enrichment and Separation Methods	19
2.5.1 <i>Electrolytic Enrichment</i>	19
2.5.2 <i>Membrane Diffusion</i>	22
2.5.3 <i>Hydrogen Separators</i>	23
2.5.4 <i>Polyphosphazene Membrane</i>	24
2.5.5 <i>Chemical Reduction</i>	25
2.6 Tritium Detection and Well Monitoring Reviews	25
2.7 Existing Detection Systems	28
2.7.1 <i>Layered Scintillator with Coincidence Counting</i>	28
2.7.2 <i>CosmicWatch</i>	31
2.7.3 <i>In-situ Underwater Beta Monitoring System</i>	32
2.7.4 <i>Well-Logging Probe Capable of Measuring Tritium</i>	33
2.7.5 <i>Real-Time Tritium Monitor System for Water Quality Surveillance</i>	34
2.7.6 <i>Development of a Real-Time Tritium-in-Water Monitor</i>	35

2.7.7 Flow Cell Detectors Fabricated using CaF ₂ Solid Scintillator	36
2.7.8 Tritiated Water Online Detector System based on Plastic Scintillators....	37
2.7.9 Efficiency Enhanced Electrolysis-based Tritium Continuous Monitor.....	39
2.7.10 Heavy Water Detection for Pressurised Heavy Water Reactors	40
2.7.11 Tritium Detection by Electrochemical Assisted Radiometrics.....	40
2.7.12 Scintillator Fiber Flow Cell Radioactivity Detector for Liquid Chromatography.....	42
2.7.13 Flow Cell Patent.....	43
2.7.14 Alternative Approach to Tritium-in-Water Monitoring.....	44
2.7.15 In-Situ Monitoring of Groundwater Radionuclides with Emphasis on Tritium Detection	45
2.7.16 β Ionix 3™: Portable Tritium Monitor	48
2.7.17 Tritium Monitor using Plastic Scintillator (Sheets and Pellets)	49
2.7.18 Advanced Blind-Tube Monitoring Instrument.....	50
2.8 Scintillator Comparison and Selection	51
2.9 Silicon Photomultiplier Devices	52
2.10 Silicon Photomultiplier Temperature Compensation Methods	53
2.11 Conclusions.....	55
3 BACKEND ELECTRONICS.....	58
3.1 Introduction	58
3.2 System Outline	58
3.3 Early Electrical Design.....	60
3.4 Field Programmable Gate Array Selection and Compaction.....	62
3.5 Silicon Photomultiplier Amplification Design	63
3.5.1 Electrical Noise Reduction Methods	64
3.5.2 Alternative Amplifier Designs.....	67
3.6 Analogue to Digital Converter Board Design	68
3.7 Pulse Data Processing	69
3.7.1 Spectrum Accumulation.....	71
3.7.2 Spectrum Memory Serial Data Transfer	72
3.7.3 Database Design and Implementation	74

3.7.4	<i>Pulse Visualisation with Bokeh</i>	75
3.7.5	<i>Spectrum Visualisation with FastSpec and Database Files</i>	77
3.8	Detector Resolution Determination Using Light Emitting Diode Pulse Testing	78
3.8.1	<i>Light Emitting Diode Blinking Experiment Results</i>	81
3.9	Zener Diode Temperature Compensation.....	85
3.9.1	<i>Temperature Compensation System Simulation</i>	87
3.9.2	<i>Zener Diode Selection</i>	89
3.9.3	<i>Temperature Compensation Experiment Results</i>	93
3.10	Coincidence Counting Implementation	95
3.11	System Validation with Sealed Sources.....	96
3.12	Conclusions.....	104
4	FLOW CELL DEVELOPMENT	106
4.1	Introduction	106
4.2	Methods for Creating a Granulated Scintillator	108
4.2.1	<i>Grinding Stone Method</i>	108
4.2.2	<i>Ball Mill Method</i>	109
4.2.3	<i>Blade Grinder Method</i>	109
4.2.4	<i>Mortar and Pestle Method</i>	112
4.3	Potassium Chloride Liquid Packs	113
4.4	Auto Sieve Separation	116
4.5	Liquid Scintillation Counting Granulated CaF ₂ (Eu).....	118
4.6	Liquid Scintillation Counting Granulated BC408	121
4.7	Scintillator Moulding.....	122
4.8	Conclusions	124
4.9	3D Printed Flow Cell.....	125
4.9.1	<i>Testing 3D Printed Flow Cell with Potassium Chloride</i>	127
4.10	Layered Flow Cell.....	129
4.11	Laminated Flow Cell.....	131
4.11.1	<i>Flow Cell Filter Alternative</i>	136
4.11.2	<i>Sensor Head Design and Development</i>	137

4.11.3 Bench Top Detector System	138
4.11.4 Bench Top Cooling System	140
4.11.5 Temperature Effects on Background Count Rate.....	142
4.12 Improvements to Existing Detectors.....	144
4.13 Conclusions.....	145
5 DETECTOR VALIDATION	147
5.1 Introduction	147
5.2 Tritium Experiments	147
5.2.1 Issues with Filters	148
5.2.2 Tritium Detection Results.....	150
5.3 Strontium-90 Experiments	157
5.3.1 Count Rate Analysis	157
5.3.2 Spectrum Analysis	160
5.4 Sellafield Groundwater Experiments.....	162
5.4.1 9782 Experiment.....	164
5.4.2 10202 Experiment.....	166
5.5 Conclusions	168
6 IN-SITU DETECTOR OUTER CASING DESIGN AND DEVELOPMENT	170
6.1 Introduction	170
6.2 Battery Pack Design	171
6.3 Supply Regulation and Protection.....	173
6.4 Flat Flex Cable Interconnect Adapters	175
6.5 Compacted Cooling System.....	177
6.6 Activated Carbon Filtration	179
6.7 Conclusions	180
7 CONCLUSIONS.....	182
7.1 Effectiveness of Granulated Scintillators.....	182
7.2 Ease of Maintenance	183
7.3 Detection of Low Energy Betas.....	183
7.4 Backend System Compaction	185

7.5 Temperature Stabilisation	185
7.6 Pulse to Spectrum Conversion.....	186
7.7 Future Work.....	187
8 REFERENCES.....	189
9 APPENDIX.....	214

List of Tables

Table 1: Measured detection efficiency of CCD based detector, tested with two weak plane sources [40].....	19
Table 2: Tolerances for voltage drop and temperature coefficients [90], [120], [121].....	92
Table 3: Calibration table of peak channels detected for the photopeaks of the tested sealed sources, ^{60}Co [171], ^{137}Cs [172], ^{22}Na [123], [173] and ^{241}Am [125].....	101
Table 4: Detection efficiency of each gamma peak, with all peak channels adjusted to a zoom of 1.....	103
Table 5: Size distribution of ground BC408 obtained using Mastersizer 2000 (values have been averaged from multiple measurements of identical sample).....	110
Table 6: Contents of both laminated sample packs.....	114
Table 7: Masses within sample vials containing tritiated water, for powder testing with the LSC. Weights of scintillator added to each vial are to within ± 0.0001 g. All measurements were repeated three times for four hours each and statistics calculated. Background counts have been removed from listed counts.....	119
Table 8: Activity of non-active control samples denoting background activity. All measurements were repeated three times for four hours each and statistics calculated.....	119
Table 9: Weights and LSC count results from vials containing tritium and granulated BC408 or $\text{CaF}_2(\text{Eu})$ scintillator created using blade grinder.....	121

Table 10: Count data recorded from experiment with tritiated water resulting in the loss of scintillator from the flow cell cavity. Measurement time recorded to within one sample (± 0.006 hours). Scales calibrated to ± 0.003 g.....148

Table 11: Measurement time, mass of water, and mass of dilute tritiated water present in each round of the experiment. Scales calibrated to ± 0.003 g. Measurement time recorded to within one sample (± 0.006 hours).....150

Table 12: Detected CPM recorded by the flow cell detector for each round, along with the calculated full loop tritium activity concentration based upon the added mass of tritiated water. Detection efficiency has been calculated using equation (5.1) and (5.2).....151

Table 13: Deionised water added and removed over two flush cycles measured by the detector. Measurement time recorded to within one sample (± 0.006 hours). Scales calibrated to ± 0.003 g.....156

Table 14: Detected CPM recorded by the flow cell detector for flush cycles. Detection efficiency has been calculated using equation (5.1) and (5.2).....156

Table 15: Results from spectra measurement of diluted tritiated water. Measurement time recorded to within one sample (± 0.006 hours). Scales calibrated to ± 0.003 g.....160

Table 16: Results from spectra measurement of diluted strontium-90 tracer. Measurement time recorded to within one sample (± 0.006 hours). Scales calibrated to ± 0.003 g.....160

Table 17: Measured activity of radioisotopes contained in sample from borehole number 9782 [161]. Total beta activity for day of testing has been adjusted using strontium-90 half-life.163

Table 18: Measured activity of radioisotopes contained in sample from borehole number 10202 [161]. Total beta activity for day of testing has been adjusted using strontium-90 half-life.163

Table 19: Count data and measurement times for borehole 9782 groundwater experiment. Measurement time recorded to within one sample (± 0.006 hours). Scales calibrated to ± 0.003 g. Measurement ended on 17/05/2024.165

Table 20: Count data and measurement times for borehole 10202 groundwater experiment. Measurement time recorded to within one sample (± 0.006 hours). Scales calibrated to ± 0.003 g. Measurement ended on 05/06/2024.167

List of Figures

Figure 1.1: Beta decay spectrum of tritium from Radiological ToolBox [5].	3
Figure 1.2: Diagram of sampling system used for retrieving samples from Sellafield's on-site boreholes. Based on description by Dr James Graham [25].	8
Figure 1.3: Diagram of ideal solid scintillator setup.	12
Figure 2.1: Activity of key beta emitters tritium, carbon-14, and strontium-90 within borehole number 10202, sampled over multiple years. Provided by Sellafield [36].	17
Figure 2.2: Diagram of the electrolytic cell for the enrichment of tritium in water, current is passed through anode and cathode to break water into hydrogen and oxygen. SPE film carries hydrogen ions between electrodes [42].	20
Figure 2.3: Front view diagram of 1 cell within 10 cell unit, labelled with its key parts [43].	21
Figure 2.4: Pervaporation system for the recovery of tritiated water [44].	22
Figure 2.5: Diagram of a reverse osmosis system.	23
Figure 2.6: Diagram showing cross section of the gaseous hydrogen separator offered by Power+Energy [47].	24
Figure 2.7: Conceptual design for detector, consisting of two PMTs and multiple scintillating layers, re-created from article [57].	29
Figure 2.8: Graph plotting the effect on scintillator thickness (0.5 mm, 1.0 mm, 1.5 mm and 2.0 mm) and number of channels on the counting rate of the detector [58].	30
Figure 2.9: Extract from CosmicWatch schematic showing amplifier and peak detector stages [60], re-created in Falstad [61].	31

Figure 2.10: Diagram of system setup for beta monitoring showing how converting water into a hydrogen gas increases the penetration of emitted betas, re-created from paper [63].	32
Figure 2.11: Diagram of the probe's main components [65].	33
Figure 2.12: Diagram of TRITIUM-0 showing internal scintillating fibres, based on system description [66].	34
Figure 2.13: Diagram of Averio-0 detectors internal scintillator compared to Tritium-0/1 designs [70].	35
Figure 2.14: Diagram of detector setup consisting of two coincidence PMTs facing into a cartridge that holds one or multiple Teflon tube detection cavities [71].	37
Figure 2.15: Diagram showing the internal layout of the tritium detector, re-created from paper [72].	38
Figure 2.16: Image of detector setup within light tight case showing dual PMTs, based on detector photograph [73].	39
Figure 2.17: Diagram of heavy water quick detection system, re-created from graphical abstract [74].	40
Figure 2.18: Diagram of experimental setup including electrochemical cell and scintillation detector, re-created from report [75].	41
Figure 2.19: Cross-sectional diagram of flow cell detector showing scintillating fibres held within the glass tubing, re-created from publication [76].	42
Figure 2.20: Illustration of flow cell invention [77].	43
Figure 2.21: Diagram of proof of principle experiment setup, re-created from paper [78].	44

Figure 2.22: Graph from paper [78] showing the resulting increase in chamber current as tritium is introduced to the detector setup..... 45

Figure 2.23: Image of setup used in thesis: CaF₂(Eu) scintillator attached to SiPM and preamplifier board, taken from thesis [33]..... 46

Figure 2.24: Schematic of circuit used to bias SiPM and amplify output pulses [33], re-created in Falstad [61]..... 46

Figure 2.25: Diagram of designed flow cell chamber showing internal disks covered with heterogeneous scintillator, created from photograph of detector [33]. 47

Figure 2.26: Data from conducted transient flow experiment (plotted as total counts per window of time, 15 minutes, 30 minutes or 60 minutes), taken from thesis [33]..... 48

Figure 2.27: Image of β Ionix 3™ detector [80]..... 49

Figure 2.28: Diagram of sheet/pellet detector, re-created from paper [82]. 50

Figure 2.29: Simplified schematics of three existing SiPM temperature stabilisation methods. Left shows serially connected PN junctions in forward bias, top right shows analogue thermistor control [91] and bottom right shows digital thermistor control [92]..... 54

Figure 3.1: Block diagram of the whole backend system including the digital processing and database access method. An encapsulated NaI(Tl) Scintillator has been included for testing with sealed sources (see section 3.11)..... 60

Figure 3.2: Schematic of early SiPM amplifier created in Falstad [61], peak holder, and pulse height comparator for detection with Arduino Uno. 61

Figure 3.3: Image of FPGA before (left) and after (right) hardware alterations... 62

Figure 3.4: Two stage EL5171 op-amp based amplifier. The first stage is a transimpedance amplifier with differential output, and the second phase is an inverting amplifier..... 63

Figure 3.5: Simulated LTSpice schematics used to study the effectiveness of adding input filtering: (A) With common mode filter on negative bias supply, (B) without common mode filter on negative bias supply. 66

Figure 3.6: Simulation of schematics in Figure 3.6. Green trace is from the output of circuit (A) with common mode filter. Blue trace is from the output of circuit (B) without common mode filter. 66

Figure 3.7: Image of early SiPM board design incorporating both sensor head and amplification into a single board..... 67

Figure 3.8: Image of unused prototype SiPM amplification board, using easily accessible gain adjustment switches. These switches were used again for the final amplifier design. Two connectors connect to the ADC board and SiPM sensor head..... 68

Figure 3.9: Image of a manufactured ADC board, populated with two AD9244 ADCs and supporting circuitry, sitting on top of the Cyclone II minimal development board. A one pound coin is shown for scale..... 69

Figure 3.10: Block diagram of trapezoidal shaper algorithm. Showing the implementation of the three sample delays [103]..... 70

Figure 3.11: Finite state machine of the pulse peak storage system implemented on Cyclone II FPGA. Each transition occurs every clock cycle. The variable SUM_4 is the output of the shaper algorithm. 72

Figure 3.12: Timing diagram showing order in which channel data is sent from the FPGA to the single board computer (Raspberry Pi). 73

Figure 3.13: Example interactive Bokeh plot of pulse data captured of background, cluster highlighted shows electrical noise. One sample is equal to 20 ns..... 75

Figure 3.14: Graph depicting how the pulse is stored within the Lookback and Sample FIFO. 76

Figure 3.15: Schematic of LED pulse circuit used in LED blinking experiment. It includes a 555-timer for blinking followed by an edge detector to produce short pulses for LED..... 79

Figure 3.16: Images of detector head circuit as each SiPM was added..... 80

Figure 3.17: Visual representation of the effect of the delay values on the shape of the window, i.e., for the far-left example delay one and three are 30 samples, and delay two is 140 samples..... 80

Figure 3.18: Combined raw unfiltered spectra of 8 LED blink tests with a single SiPM. The legend indicates the duration of delays one, two, and three..... 82

Figure 3.19: Combined raw unfiltered spectra of 8 LED blink tests with two SiPM. The legend indicates the duration of delays one, two, and three..... 82

Figure 3.20: Combined raw unfiltered spectra of 8 LED blink tests with three SiPM. The legend indicates the duration of delays one, two, and three..... 82

Figure 3.21: Channel FWHM from each detected peak across all LED testing experiments, with three-sigma error bars. Three lines of best fit consisting of coloured dotted lines have been added on each set of results for one, two, and three SiPMs..... 84

Figure 3.22: Channel resolution from each detected peak across all LED testing experiments, with three-sigma error bars. Three lines of best fit consisting of coloured dotted lines have been added on each set of resolution values for one, two, and three SiPMs..... 84

Figure 3.23: Simplified schematic of simulated temperature compensation circuit. 86

- Figure 3.24: LTspice simulation of an amplified pulse from the two systems over the temperature range of -20°C to 50°C with a step of 5°C . Traces of blue correspond to the non-compensated system and red traces correspond to the Zener compensated system..... 88
- Figure 3.25: LTspice simulation plotting the peak to peak magnitude of each simulated pulse against temperature $^{\circ}\text{C}$. Blue points correspond to the non-compensated system and red points correspond to the Zener compensated system, both fitted with a linear dotted line. Three sigma error bars have been added based on the results of 10 simulations..... 89
- Figure 3.26: Measured voltage drop of the combined Zener diodes over the temperature range of 30°C to 140°C . A negative supply voltage of 32.61 V and a $10\text{ k}\Omega$ biasing resistor were used. A linear line of best fit (dotted blue line) has been added to estimate the temperature dependence and voltage drop of the combined Zener diodes at 0°C . Voltages were measured to $\pm 0.01\text{ V}$ accuracy, and temperature was measured to $\pm 1^{\circ}\text{C}$ accuracy. 90
- Figure 3.27: Combined plot of the extrapolated voltage drop caused by the measured Zener diodes compared with a set DC bias, ideal voltage drop region for biasing the SiPM, and the region of tolerance given to the Zener diode's voltage drop by the manufacturer. 91
- Figure 3.28: Detector setup used for testing the Zener diodes temperature compensation system..... 93
- Figure 3.29: A log graph (a) plotting cumulative spectra taken over the full heating experiment. A log graph (b) of individual spectra taken at 30°C and 65°C , for both compensated (blue trace) and non-compensated (red trace) systems. Only channels 1600 to 2600 have been displayed for purposes of clarity... 94
- Figure 3.30: Diagram depicting data pipeline and coincidence checking: Upper example is of pulses being accepted, lower an example of random pulses being rejected..... 96

Figure 3.31: Image of ^{60}Co source placed upon the NaI(Tl) crystal. The SiPM sensor head has been placed below the circular window of the encapsulated crystal. After placement of the source, the lid was closed and locked to ensure that no ambient light could enter..... 97

Figure 3.32: The spectrum of the ^{60}Co sealed source with background counts removed, taken at zoom level 1. Blue trace is raw channel data, solid red trace is 20 sample moving average, dashed red trace is Gaussian fit around peaks. 98

Figure 3.33: Spectrum of ^{22}Na sealed source with background counts removed, taken at zoom level 1. Blue trace is raw channel data, red trace is 20 sample moving average, dashed red trace is Gaussian fit around peaks..... 98

Figure 3.34: Spectrum of ^{241}Am sealed source with background counts removed, at zoom level 0.5. Blue trace is raw channel data, solid red trace is 20 sample moving average, dashed red trace is Gaussian fit around peaks..... 99

Figure 3.35: Spectrum of ^{137}Cs sealed source with background counts removed, taken at zoom level 0.5. Blue trace is raw channel data, solid red trace is 20 sample moving average, dashed red trace is Gaussian fit around peaks. 99

Figure 3.36: Spectra of ^{137}Cs and ^{60}Co sealed sources with background counts removed, at zoom level 1. Blue trace is raw channel data, solid red trace is 20 sample moving average, dashed red trace is Gaussian fit around peaks.100

Figure 3.37: Calibration fit for the detector with three-sigma error bars based upon the collected peak channel data in Table 3. A line of best fit (dotted blue line) has been fitted on the data to relate each channel to a detection energy. The fit has a gradient and intercept standard error of 0.65 ± 0.02 and -56.08 ± 35.39 , respectively (a 95% confidence interval).102

Figure 3.38: Energy resolution of the detector with three-sigma error bars. A power trend line has been added to the data alongside a value for the fit..102

Figure 3.39: Plot of the calculated detection efficiency for each peak in the recorded spectra with three-sigma error bars. A power trend line has been added to the data alongside the value for the fit.....104

Figure 4.1: Diagram of a granulated scintillator in contact with a tritiated liquid sample.....107

Figure 4.2: Two sections of BC408 scintillator both before (left) and after (right) being placed in the ball mill overnight.....109

Figure 4.3: Result of granulating BC408 within the blade grinder.....110

Figure 4.4: Plot of granulated BC408 size distribution against grinding time, data taken from Table 5.....111

Figure 4.5: Ageing effect of vial containing dilute tritiated water with blade ground $\text{CaF}_2(\text{Eu})$ scintillator (left vial) alongside a vial containing granulated $\text{CaF}_2(\text{Eu})$ produced using a mortar and pestle (right vial, discussed in section 4.2.4).....112

Figure 4.6: Image of $\text{CaF}_2(\text{Eu})$ crushed using the mortar and pestle method.....113

Figure 4.7: Image of both KCl packs. After the addition of granulated scintillator, KCl, and deionised water, all four sides were sealed using a manual hand sealer. The packs allowed the detector to be tested with a liquid source without risking damage to the detector electronics.....114

Figure 4.8: Captured raw spectrum data of background pack (red) and KCl pack (blue). Note spectrum counts have been plotted with log scale.....116

Figure 4.9: Final step of sieve separation, powder at and below 90 μm is added to a 50 μm sieve.....117

Figure 4.10: Graph of the resulting data from the counted vials containing mixtures of dilute tritium and $\text{CaF}_2(\text{Eu})$ scintillator. A power trendline (dotted blue

line) has been added to the plot along with its R2 value and trendline equation.....	120
Figure 4.11: Result of droplets placed onto BC408 moulding patches.....	123
Figure 4.12: Images of the BC408 covered packet being manufactured.....	124
Figure 4.13: Diagram of first flow cell design labelled with key parts.....	126
Figure 4.14: Top of 3D printed flow cell filled with granulated BC408 scintillator, before the addition of the window.....	126
Figure 4.15: CAD rendering of 3D printed flow cell showing internal cavity, window and filters.....	126
Figure 4.16: Recorded Spectrum containing raw count rate data (CPM) from KCl experiment with 3D Printed flow cell. Background counts have been removed.	129
Figure 4.17: Cross-sectional diagram of layered acrylic flow cell design.....	130
Figure 4.18: Image of inside of layered acrylic flow cell cavity.	130
Figure 4.19: Layout of all parts of the laser cut flow cell, from left to right: Pump assembly, sample outlet, outlet filter (filter paper folded over acrylic spacer), cavity top rubber seal, cavity with SiPM holder, cavity bottom rubber seal, inlet filter (filter paper folded over acrylic spacer), inlet seal and faceplate.	131
Figure 4.20: Cross-sectional diagram of laminated flow cell with outer casing, within the cavity three beta decays have been added showing paths photons take to reach both SiPMs.....	132
Figure 4.21: Side and front view of 3D printed end adapter labelled with key design features.....	133

Figure 4.22: Images showing a flow cell being manufactured, (from top to bottom) sheets are cut and laminated, filled and end adapters attached.....134

Figure 4.23: Image of flow cell and casing parts both before and after assembly of the outer casing around the laminated flow cell. Two flat flex cable (FFC) connectors allow rapid connection and disconnection of each SiPM array from the electrical system.....136

Figure 4.24: Image of manufactured flow cell with cut foam filter (left) and image of multiple foam filters being cut from solid block of 45 PPI aquatic foam.137

Figure 4.25: Image of electrical system used in the flow cell detector. Two channels perform coincidence counting with the SiPM sensor heads placed across the centre of the flow cell. Temperature stabilising Zener diodes have been placed in close proximity to the SiPMs to ensure good temperature matching.....138

Figure 4.26: Diagram of detector setup, key parts include the light tight enclosure, silicon tubing, electronics enclosure, flow cell, flow cell casing, peristaltic pump and sample beaker. The cooling bath and cooling pump were placed directly next to the enclosure.....139

Figure 4.27: Image of detector system before the addition of the cooling and power supply unit, labelled with key parts.....140

Figure 4.28: Image of SiPM sensors with masked front faces while adding the waterproofing anti corrosion coating142

Figure 4.29: Graph plotting the total background CPM recorded (using gamma settings, see section 3.5) over the cooling period. An exponential fit (dotted red line) has been added to the data points.....143

Figure 4.30: Graph plotting raw background total counts recorded (using tritium settings, see appendix D) with no temperature stabilisation (Blue trace), and with temperature stabilisation (Orange trace).143

Figure 4.31: Cross sectional diagram of two coincidence counting systems, one using PMTs with cooling coils and a second with SiPM arrays and Peltier coolers.144

Figure 4.32: Concept SiPM array replacement for coincidence counting PMTs. The new design allows the placement of the inlet or outlet hose to pass directly through the centre of the detector face.145

Figure 5.1: Raw spectra data from failed tritium experiment, red trace in both graphs plots the background measurements and blue traces plot the spectrums measured after the first (a) and second (b) addition of tritiated water.149

Figure 5.2: Image of flow cell after round 2 testing, due to insufficient filtering the scintillator has migrated away from the cavity centre.149

Figure 5.3: Spectrum of background taken by the flow cell detector while filled with deionised water. The blue trace plots the raw channel data, and red trace plots a 20-sample moving average.152

Figure 5.4: Spectrum taken by detector after each addition of tritium, background removed. A 50-sample moving average has been applied to each trace. Trace colours red, blue, green, orange and purple represent the spectra taken in rounds 1, 2, 3, 4 and 5 respectively.153

Figure 5.5: Tritium activity concentration within flow cell plotted against measured CPM, where concentrations ranged from 0 Bq g⁻¹ to 416.18 Bq g⁻¹. A linear line of best fit (dotted blue line) has been added to predict the detectors overall response to the activity of tritium.154

Figure 5.6: Plot of raw count rate data recorded by detector after the addition of 534.96 Bq of strontium-90 tracer. Blue, orange, vertical red and horizontal red line represent the raw count rate, 20 sample moving average, start of count rate average, and average count rate respectively.158

Figure 5.7: Plot of raw count rate data recorded by detector after the addition of 31.93 Bq of strontium-90 tracer. Blue, orange, vertical red and horizontal red lines represent the raw count rate, 20 sample moving average, start/end of count rate average and average count rate respectively.....159

Figure 5.8: Spectrum taken of ³H overlaid with spectrum taken of ⁹⁰Sr. Spectrums have been filtered using a 50 sample moving average and normalised each to 1,000 CPM to compare spectrum shape. Only channels from 0 to 1,500 have been shown for clarity.....161

Figure 5.9: Spectrum taken by detector while flow cell is filled with groundwater from borehole 9782, background removed. Blue trace: Raw count data. Red trace: 10 point moving average.164

Figure 5.10: Spectrum taken by detector while flow cell is filled with groundwater from borehole 10202, background removed. Blue trace is raw count data. Red trace is 10 point moving average.....167

Figure 6.1: Images showing the attachment of two battery holders using a white 3D printed battery clip.....172

Figure 6.2: Image of waterproof casing adapter which holds together sections of the detectors outer casing. Brass inlet can be seen on right, inserted screw can be seen on left.....173

Figure 6.3: Image of supply regulation boards prior to assembly and fitting into the outer casing, labelled with key design features.....173

Figure 6.4: Image of supply boards fully assembled, cutouts in end (right) PCB allow ribbon cables to connect to Raspberry Pi shield.....174

Figure 6.5: FFC interconnects for final detector electrical system. Includes an adapter for the ADC board, Raspberry Pi Zero shield and debugging breakout board.....176

Figure 6.6: ADC Adapter board, this PCB was used to convert the original 2.54 mm pin header of the ADC board into FFC ribbon cables allowing for the system to fit within the cylindrical housing.176

Figure 6.7: Diagram showing how the Peltier coolers move thermal energy away from the laminated flow cell and into the coolant.....177

Figure 6.8: Image of separate cooling parts before being combined to create the cooling system.178

Figure 6.9: Image of compacted cooling system placed within the detector housing. The image is labelled with its key components.....178

Figure 6.10: Graph of recorded temperatures from compacted cooler experiment. Blue trace is the reservoir, red plot is the inner casing attached to the first cooling block, and orange plot is the inner casing attached to the second cooling block.179

Figure 6.11: Image of concept active carbon filter made with the same method as the laminated flow cell but with active carbon instead of powdered scintillator.180

Figure 6.12: Image of final detector, compacted to fit within the confines of Sellafield’s boreholes. A clear outer acrylic casing has been used to show the internal systems. Technology developed throughout this thesis have been integrated, labels have been added to link each part to their section within the thesis.180

Figure 7.1: Suggested detector setup for testing in fume cupboard.187

List of Appendices

Appendix A.	Liquid Scintillation Counter Calibration.....	215
Appendix B.	Minimum Detecting Time.....	220
Appendix C.	Printed Circuit Board Design Drawings and Schematics	226
Appendix D.	Detector Switch Settings.....	232
Appendix E.	Field Programmable Gate Array Pulse Shaper Code	233
Appendix F.	Advatech Scintillator Comparison	238

List of Abbreviations and Acronyms

ADC	Analogue to Digital Converter
APT	Accelerator Production of Tritium
AS	Active Serial
BLOB	Binary Large Object
CaF ₂ (Eu)	Calcium Fluoride doped with Europium
CCD	Charge-Coupled Device
CMOS	Complementary Metal-Oxide-Semiconductor
COTS	Commercial Off-The-Shelf
CPLD	Complex Programmable Logic Device
CPM	Counts Per Minute
CPS	Counts Per Second
CSV	Comma Separated Values
DAC	Digital to Analogue Converter
DAQ	Data Acquisition Board
DC	Direct Current
DPM	Disintegrations Per Minute
EVA	Ethylene-Vinyl Acetate
FFC	Flat Flex Cable
FIFO	First In First Out
FPGA	Field Programmable Gate Array
FSM	Finite State Machine
FWHM	Full Width Half Maximum
HPLC	High-Performance Liquid Chromatography
HTML	Hypertext Markup Language
I/O	Input or Output
IC	Integrated Circuit
IFIC	Institute for Corpuscular Physics
IP	Internet Protocol
JTAG	Joint Test Action Group

KCl	Potassium chloride
LED	Light Emitting Diode
LSC	Liquid Scintillation Counter
MDA	Minimum Detectable Activity
MDT	Minimum Detecting Time
Msp/s	Mega-Samples Per Second
NTC	Negative Temperature Coefficient
OLED	Organic Light-Emitting Diode
Op-amp	Operational amplifier
PC	Polycarbonate
PCB	Printed Circuit Board
PDE	Photon Detection Efficiency
PDMS	Polydimethylsiloxane
PEEK	Polyetheretherketone
PEM	Proton Exchange Membrane
PET	Polyethylene Terephthalate
PHWR	Pressurised Heavy Water Reactor
PMT	Photomultiplier Tube
PPI	Pores Per Inch
PS	Polystyrene
PTC	Positive Temperature Coefficient
PTFE	Polytetrafluoroethylene
RAM	Random Access Memory
RBE	Relative Biological Effectiveness
RFI	Radio Frequency Interference
SAPO	Silicoaluminophosphate
SD	Secure Digital
SEPIC	Single Ended Primary Inductor Converter
SiPM	Silicon Photomultiplier
SLA	Stereolithography
SMD	Surface-Mounted Device
SNR	Signal-to-Noise Ratio

SPE	Solid Polymer Electrolytic
SPI	Serial Peripheral Interface
SSH	Secure Shell
TAC	Time-to-Amplitude Converter
tSIE	transformed Spectral Index of External standard
VHDL	VHSIC Hardware Description Language
VHSIC	Very High-Speed Integrated Circuit
Wi-Fi	Wireless Fidelity

1 Introduction

This thesis covers the topic of in-situ low energy beta detection, that is radiation detectors that can be fitted into boreholes for the continuous measurement of radiologically contaminated groundwater, ensuring the safety of the surrounding environment. This contamination is the result of nuclear reprocessing and waste storage in buildings that have slowly degraded overtime. Radionuclides that emit low energy betas are of additional interest due to their difficulty in detection, requiring state-of-the-art equipment typically liquid scintillation counters (LSCs). Currently LSCs are not well suited to confined in-situ environments leading to the development of other detection methods like scintillator flow cells.

An overview of radioactive decay and the difficulties involved in its detection will be discussed before moving on to the importance of monitoring tritium, a low energy beta emitter highly mobile in the environment. Current techniques for sample collection and scintillator-based detectors will also be covered, leading to the development and experimental verification of a new flow cell detector in further chapters.

At the close of this chapter, the objectives of this work will be defined based on the current needs of nuclear-licenced sites for an in-situ borehole detector. A breakdown of each chapter within this thesis is also provided.

1.1 Radioactivity

All atoms within the universe wish to become stable. One form of instability is caused by an atom containing too many neutrons within its nucleus, hence, to lose this extra neutron, the atom has a chance to undergo beta minus decay. Additionally, atoms can decay through beta plus, alpha and gamma decay, the phenomenon we call radioactivity [1].

A beta particle (β) is an electron created when the extra neutron within an unstable atom (A) decays into a proton converting the atom into another element (B). The electron is expelled from the nucleus with kinetic energy which is simply referred to as the beta energy. Unlike gamma decay in which a discrete energy is given to the emitted photon, a range of beta energies are emitted and can be affected by interactions with matter. Equation (1.1) for beta minus decay is as follows [2]:



One particle yet to be discussed is the anti-neutrino ($\bar{\nu}$), this chargeless particle is created in addition to the beta particle. It shares a proportion of the total energy released with the beta particle in a ratio that varies from decay to decay and cannot be predicted. However, the maximum energy of the beta and anti-neutrino combined is a known constant for a particular isotope.

When a beta particle collides with another atom it can 'bounce' off the positively charged nucleus losing some of its kinetic energy in the process (elastic collision). Alternatively, the beta particle could be absorbed by the atom causing it to be excited/ionized (inelastic collision). In practice, a beta particle can undergo many elastic collisions before causing ionization with each prior collision taking a portion of the beta's original energy. This gives the beta an effective travel distance, where the maximum distance a beta particle can travel into a material corresponds to its starting energy and the density of the material, this is referred to as the 'stopping power'. The greater the initial energy of the beta particle the

further it can travel away from its origin and the greater amount of energy that can be transferred through ionization.

The maximum energy of the beta and anti-neutrino combined varies from isotope to isotope, with some radionuclides possessing a relatively low max energy. While the point at which energy is classed as 'low' or 'soft' is not defined precisely, it is generally agreed that carbon-14 and tritium (approximately 0.02 MeV to 0.2 MeV max beta energy) are lower-energy 'soft' beta emitters, and radionuclides like ^{90}Sr and ^{90}Y (approximately 0.5 MeV to 2.3 MeV max beta energy) are high-energy beta emitters. The terms 'soft' and 'low' energy will be used interchangeably throughout this thesis.

1.2 Low Energy Beta Decay of Tritium

Tritium is a radioactive isotope of hydrogen possessing two extra neutrons, its half-life is $4,000 \text{ days} \pm 8 \text{ days}$ [3] or approximately 12.33 years. Tritium only decays through beta minus decay to produce a beta particle up to a maximum energy of $18.591 \text{ keV} \pm 0.059 \text{ keV}$ [4]. Once the nucleus decays, it becomes a stable form of helium, the beta decay spectrum is shown below (Figure 1.1).

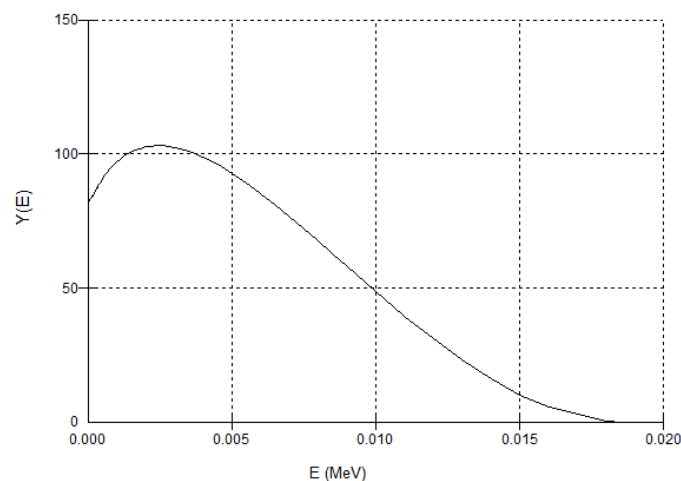


Figure 1.1: Beta decay spectrum of tritium from Radiological Toolbox [5].

The decay of tritium into helium can be represented with the following chemical equation (1.2) [6]:



In terms of low energy beta detection, tritium is of great interest as it is one of the hardest isotopes to detect. Consequently, tritium is a good benchmark to compare liquid low energy beta detectors as, like other isotopes of hydrogen, tritium can form bonds with oxygen to create tritiated water. This water behaves almost identically to hydrogen-based water in every way except for its radioactivity and mass.

1.3 The Creation of Tritium

Since the advent of nuclear technology, more significant quantities of tritium have been produced through the operation of nuclear fission reactors, subsequent waste operations and reprocessing, nuclear weapons testing [7], and particle accelerators like the accelerator production of tritium (APT) plant in the USA which was required to produce 2 kg to 3 kg of tritium per year [8].

As an example, CANDU reactors use heavy water (deuterium) as a moderator and coolant. As the heavy water is bombarded by neutrons from the fuel rods, the deuterium can be irradiated into tritium which slowly builds up within the reactor. Theoretically, this produces 130 g of tritium per year [9]. A Wolsong tritium removal facility (WTRF) has been built on-site at the Wolsong nuclear power plant which runs four CANDU reactors. WTRF has reportedly extracted 370 PBq (~1 kg) of pure tritium from reactor #1 since it commenced operation in 1983 [10].

1.4 Uses of Low Energy Beta Emitters

Tritium is an important radionuclide being used as a fuel in fusion reactors [11]. Multiple fuel types have been implemented for fusion, including D-³He, D-D, and p-B. Nevertheless, D-T (deuterium and tritium) still has the best energy release rate with the fusion beginning at lower temperatures compared to other fuel types [12].

Other uses involve tritium as a radioisotope tracer which is injected into boreholes for the investigation of seepage from dams, reservoirs, and canals. This allows details like flow direction, velocity, and travel time to be studied [13], [14].

1.5 Importance of Environmental Tritium Monitoring

Like any other material that produces ionising radiation, tritium (if consumed or inhaled) has the potential to damage DNA leading to cancers and other life-threatening conditions. Its low energy beta decay allows it to easily move within the environment undetected by conventional detection techniques (handheld Gieger counters), as its emitted beta particles are easily attenuated by water, soil, rock, and air, and hence cannot reach the detector for detection.

There have been multiple releases of tritium, both controlled and uncontrolled, into the environment. A recent example is that of the Fukushima disaster, which was reported in 2020 to be producing 55,000 m³ to 80,000 m³ of tritiated water a year at an average activity of 1,000 Bq cm⁻³ [15]. Sellafield itself releases multiple low energy radioactive materials into its local vicinity, including 403 TBq of tritium and 1.67 TBq of carbon-14 through airborne discharges, in addition to 5,210 TBq of tritium and 15.3 TBq of carbon-14 discharged into the Irish Sea over 5 years (2016 to 2020) [16].

A review of risks from tritium [17] focuses on workers at nuclear sites, the relative biological effectiveness (RBE) of tritium is about twice that of gamma radiation, implying that for an equivalent dose, tritium is more damaging. Tritiated nucleic acid can also be incorporated into DNA, but this is stated as low risk as few workers use such compounds and modern safety procedures ensure low exposure. Experiments with mice showed a 50% survival rate within 30 days when given a total tritium oxide dose of 30 GBq kg⁻¹ [18]. Another study fed mice 3 µCi mL⁻¹ of HTO finding a 4.7% increase in liver abnormal cell frequency after 90 days, 9.0% increase after 330 days, and 6.8% increase after 530 days ± 30 days [19].

Due to the presence of tritium in the environment and the risks it possesses to biological life, detection limits within drinking water have been put in place by the

World Health Organization at a guidance level of 10,000 Bq L⁻¹ [20] and by the European Commission at 100 Bq L⁻¹ under the Drinking Water Directive [21].

1.6 Borehole In-situ Detection

The Sellafield site was home to the first commercial-sized nuclear power station opened in 1956. Over its lifetime the site has reprocessed Magnox fuel from the array of gas-cooled reactors around England, along with nuclear material from other countries, including Japan. Reprocessing has now ceased at Sellafield and the site has now entered a phase of decommissioning of legacy facilities along with continued waste and material storage. This decommissioning phase is projected to require another 100 years of work [22]. Today the site can be split into two main areas consisting of legacy and modern operational buildings, the former storing large quantities of hazardous material that over time is slowly being processed into a form suitable for long-term storage and disposal. Leaks from these legacy structures have resulted in contamination of the ground below the site and a number of associated migrating groundwater plumes. Along with contamination of the subsurface, two rivers (Calder and Ehen) are located in the direct vicinity of the site with connection to the groundwater aquifer. For environmental reassurance purposes, Sellafield undergoes an extensive groundwater monitoring programme [23] where groundwater samples are taken from around the site and sent to an external laboratory for analysis. Site boreholes, with a standard diameter of 50 mm, allow easy access and manual sampling groundwater up to several tens of meters below the site. This data allows the agency to monitor the movement of these radioactive plumes and study their behaviour as radionuclides travel at differing velocities through the soil and rock below the site. Two of the most mobile radionuclides are tritium and technetium-99 as reported by Sellafield [24].

Manual groundwater sampling and laboratory testing is the industry standard approach to groundwater monitoring; however, the technique does have a number of negative aspects. Firstly, samples must be transported offsite to be analysed which involves a number of clearance and despatch steps. Once at the laboratory

a sequence of sample preparation steps may be required (depending on the analyte) before the measurement can be taken and the result ultimately being reported back to site. This may result in a lag of up to several weeks between the sample being collected and the results being available. This is therefore not ideal for applications where timeliness is paramount. Manual sampling also has health and safety considerations as while the activity and dose of the sample can be anticipated from previous results, only after removing the sample from the borehole can the radiological hazard be determined. As a result, diligence is required in some areas during sampling including attendance of health physics specialists. Overall the manual and procedural nature of groundwater sampling and the associated health and safety considerations results in it being a costly annual exercise and given the 100 year remaining duration before site decommissioning is complete, this cost is likely to continue unless alternative approaches are developed.

In terms of the actual removal of the samples at Sellafield, a low-flow micro purge system is implemented. Within each borehole, a bladder has been placed with a pipe running from the bladder to the surface. As this bladder is inflated, the water surrounding it is displaced and forced upwards, and one-way valves fitted along the depth of the borehole stop water from flowing back down. As pressure is reduced, the bladder deflates as groundwater enters through the well lining and the process repeats.

For regulation of the bladder, a pump controller is used. This monitors and varies the pressure and pulse rate of the bladder depending on the depth of the borehole. An air compressor powered by a lead acid battery provide pressure to inflate the bladder and a power supply respectively.

Once water is pumped to the top of the borehole it is fed into a Teflon tube. The operator has two options; feed water into a flow cell or feed directly into a container through an inline filter which ensures little sediment is collected. Afterwards, the sample container is sealed and sent off-site for further measurements.

Passing water through the flow cell allows its conductivity, pH and oxygen level to be measured once the flow cell reaches an equilibrium. These data provide metrics to determine when the purging process is complete as well as being useful indicators of water quality for characterisation purposes. After leaving the flow cell the sample is collected in a waste container that will be added to a larger reservoir for monitoring and disposal. The flow cell is reused and so is operated separately from the sample collection to avoid cross-contamination. A simplified diagram of this sampling equipment is depicted in Figure 1.2 [25].

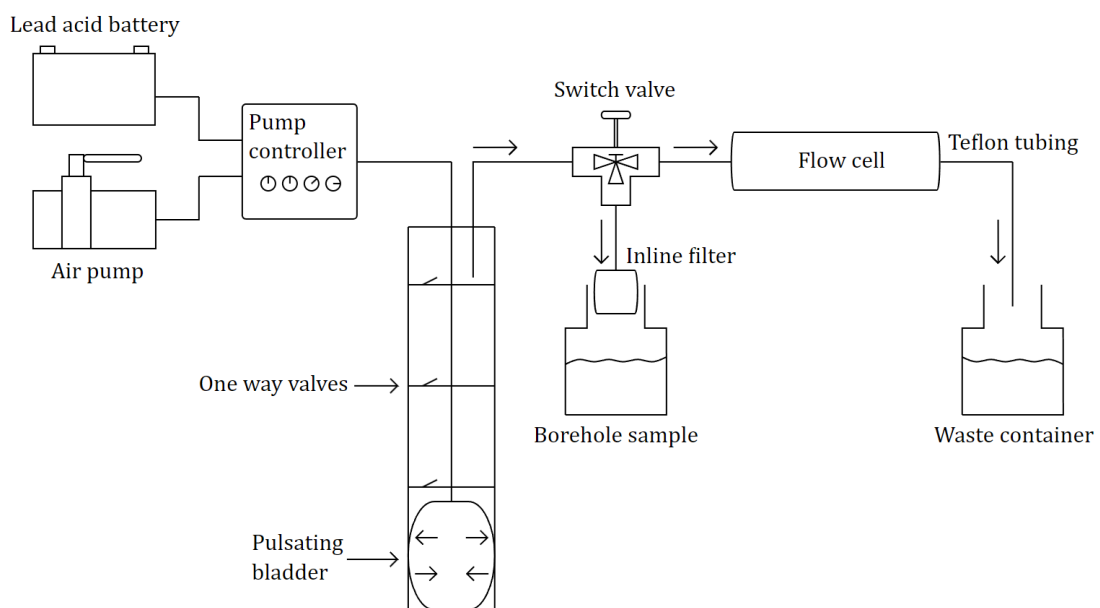


Figure 1.2: Diagram of sampling system used for retrieving samples from Sellafield's on-site boreholes. Based on description by Dr James Graham [25].

Sellafield's groundwater monitoring programme is the largest on a nuclear site in the UK; however similar but smaller programmes occur on all the main nuclear sites. For instance Dounreay, a fast reactor research and development site located in the north of Scotland, is currently in the process of decommissioning, it also hosts a water quality monitoring network consisting of 198 boreholes in addition to 36 surface water locations, the data from which allows Dounreay to understand the impact of the site on the environment [26].

Dungeness B, located on the southern coastline of England, also utilises 160 onsite boreholes for groundwater monitoring. In December 2012, EDF Energy which owns and operates the site found elevated levels of tritium in several boreholes

during routine monitoring, as a result, the frequency of borehole monitoring was increased [27].

Given the stated technical, health and safety and cost issues associated with routine groundwater monitoring, this thesis serves to develop a method of detecting low energy betas in-situ by designing and building a compact borehole detector capable of measuring beta energies while also being compatible with the limited size restraints of pre-existing boreholes located on the Sellafield site.

1.7 Overview of Scintillator Detectors and Sample

Preparation

There are many ways to detect radiation; the ionisation of a gas within a sealed canister (Geiger counter), visible traces within cloud chambers and most importantly the detection of light from scintillators. Scintillators are a preferred option as they have a higher density than gas and so are more likely to interact with incoming radiation. Additionally, scintillators can quantify energy based on the intensity of the produced photons, while for a Geiger counter there is no such relationship [28].

A scintillator is a material that can undergo the process of scintillation with radiation. That is when ionising radiation enters the material there is a chance for it to be absorbed exciting a molecule. The molecule de-excites through phosphorescence or fluorescence [29], by emitting one or more photons proportional to the energy that the incident radiation has processed. Scintillators can be either liquid or solid with each having its advantages and disadvantages depending on the use case. The two groups can be further divided depending on their chemical make-up, for example, organic and non-organic scintillators, and types of mixing agents added into liquid scintillators.

What makes a detector useful is its ability to record and measure the number of radiation ionisation events per unit of time. To do this a light detector is required to sense the photons produced and emitted by the scintillator, converting them

into electrical pulses that can increment a counter or collected into spectra which can be used to differentiate between different radioisotopes.

Two common light detectors used are the photomultiplier tube (PMT) and silicon photomultiplier (SiPM). A PMT first converts a photon into a photoelectron which is then multiplied into a pulse signal at the anode using multiple dynodes, these devices require high voltages to accelerate the electronics. SiPMs on the other hand use an array of avalanche diodes, when a photon strikes a diode, it conducts current for a small period, resulting in a pulse of current across the device.

Often these devices need to be actively cooled to reduce the noise floor on their output signal. One cooling method for PMTs is the use of a cooling coil where a liquid coolant (such as liquid nitrogen) is passed around a copper tube wrapped around the outer surface of the PMT [30]. Another cooling method is to use a Peltier cooler to move heat away from the PMT or SiPM device. A Peltier cooler is a thermoelectric device consisting of n-type and p-type semiconductors connected with metallic pads. When an electric current is passed through the device heat is moved or pumped from one side to the other, this results in a temperature gradient where one side becomes cold and the other becomes hot providing a refrigeration capability [31].

When counting a radiological sample, the PMT or SiPM will output current pulses, the maximum current and total charge are of interest to understand the energy of the incoming radiation. Commonly analogue to digital converters (ADCs) are used to digitise pulses so that they can be counted or stored. As ADCs measure voltage, the current pulse from the PMT or SiPM must be converted into a voltage pulse, to do this a transimpedance amplifier is used and is formed of an operational amplifier (op-amp). Following this a second op-amp can be used to apply gain to the signal to maximise the dynamic range of the ADC, as so to use the full range in which the ADC can measure a voltage.

For applications where a continuous measurement of a fed liquid sample is required, the scintillator can be encased in a flow cell which allows a sample to flow continuously through, the scintillator itself can take many forms including

sheets, pellets, granules and coatings depending on the application and energy range of interest. Chapter 2 will discuss many of these flow cells that are published. Scintillator detectors often quote a minimum detectable activity (MDA) which is the minimum activity that that be detected for a specified confidence interval (commonly 95%). MDA depends on factors such as the background count rate, detection efficiency and counting times for both the sample and background.

If a radiological sample is below a detector MDA, one solution to allow the sample to be measured is to enrich the sample beforehand. The change in activity concentration before and after enrichment is represented by the enrichment factor. Methods for enrichment include electrolysis, membrane diffusion and chemical reduction (see section 2.5 for further discussion). Additional techniques can be used to improve the enrichment factor such as controlling the pH level of the initial sample by adding chemicals and repeating the enrichment process in multiple stages which feed into each other sequentially.

Often with the implementation of enrichment the complexity and size of the detector must increase, this is undesirable if the detector needs to fit in a confined in-situ location and if the detector must run for days on end.

1.8 Difficulties in Low Energy Beta Detection and Characterisation

Tritium is a low energy beta emitter and as a result, these beta particles are easily attenuated by their surrounding environment, in the case of groundwater monitoring, by the water itself. Previous work by T. L. Alton et al [32] found through simulations that beta particles emitted by tritium could only travel a distance of approximately 7 μm within water, and only 2 μm within calcium fluoride doped with europium ($\text{CaF}_2(\text{Eu})$) which is a common scintillator used for the detection of low energy betas. This reduces further when looking at the displacement, which is approximately 3 μm in water and 1 μm in $\text{CaF}_2(\text{Eu})$ [33]. As a result, the surface area between the sample and scintillator plays a significant part in maximising the detection rate of low energy betas.

To get an understanding of the best case scenario for detecting dilute tritiated water with a solid scintillator, imagine a basic ideal detector (Figure 1.3), its electrical system, optical coupling and scintillator are fully efficient in that all beta particles that enter the scintillator will undergo scintillation and all these interactions will be counted. The circular flat 50 mm face of the scintillator is in contact with dilute tritiated water with a concentration of 100 Bq L^{-1} .

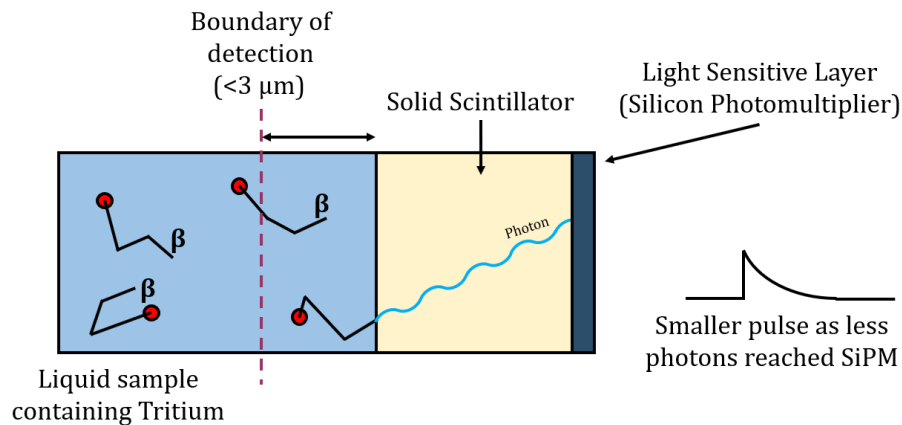


Figure 1.3: Diagram of ideal solid scintillator setup.

For this defined setup (Figure 1.3), the number of beta particles that can reach the scintillator can be approximated. From previous research, beta particles from tritium can travel a displacement of $3 \mu\text{m}$ in water. Therefore, only tritium atoms within $3 \mu\text{m}$ of the scintillator face can be detected, placed further, any beta particle resulting from decay will be self-attenuated before reaching the scintillator and hence not detected.

The area of the scintillator face in contact with the sample can be calculated simply from the area of a circle with a diameter of 50 mm, the volume of the sample within which decaying betas can reach the scintillator face can then be found as $5.890 \times 10^{-6} \text{ L}$ by multiplying the scintillator area by the displacement. Now knowing the volume of sample that can be detected, the tritium activity within this volume can be found by multiplying the concentration of tritium by the sample volume, this results in the decay rate of $5.890 \times 10^{-4} \text{ Bq}$.

As the direction the beta particle leaves the decaying atom is uniform, it is estimated that approximately half of the beta particles do not travel towards the

scintillator and hence are uncountable. As a result in an ideal case, the decay rate of betas that enter the scintillator would be 2.945×10^{-4} Bq. If 100% of these betas interact with the scintillator producing light that is counted by the photomultiplier, the detector would measure a count rate of 2.945×10^{-4} counts per second (CPS) or 1.060 counts per hour in this best-case scenario. As this is an ideal system, if implemented, the detection efficiency would be far less than 50% and so counts below 1.060 counts per hour should be expected.

If the detector is given an hour to count the sample, the standard deviation of the measured gross count rate can be obtained using equation (1.3) [34].

$$S_{N_g} = \sqrt{\frac{n_g}{t_g}} \quad (1.3)$$

Where S_{N_g} is the standard deviation of the measured gross count rate, n_g is sample count rate (CPS) and t_g is the counting period (seconds).

$$S_{N_g} = \sqrt{\frac{n_g}{t_g}} = \sqrt{\frac{2.945 \times 10^{-4}}{60 \times 60}} = 2.86 \times 10^{-4} \text{ CPS} \approx 0.02 \text{ CPM} \quad (1.4)$$

This idealised system is not possible for numerous reasons including the fact that some photons emitted by the scintillator will never reach the photodetector due to the optical attenuation within the scintillator and reflection away from the detector window due to the difference in refractive index between materials. Also, thermal noise introduces false counts that need to be removed, in doing so counts from very weak radiation interactions will also be ignored lowering the overall detection efficiency.

The ability to an accurate reading of a low energy beta emitter relies on four key factors: Detection efficiency, detector volume, sample activity and time. For borehole detectors where space is limited and the sample activity is defined by the environment, a much larger focus is required to maximise the detectors detection efficiency and working life to allow for longer measurement times.

1.9 Objectives and Thesis Structure

The following points detail the objectives of the research:

- Investigate the effectiveness of granulated scintillators on the detection of low energy beta radiation and how particle size helps or hinders detection efficiency.
- Include design features to make the system as easy to maintain and disassemble as possible given the confines of its in-situ environment.
- Design and manufacture a system capable of the detection of low energy-betas and obtain values of detection efficiency and MDA through experimental means.
- Integrate the necessary backend systems to allow the functionality of the detector independently without the need for external support systems: mains power, wired communication and supervision. Compact such a system into a standard 50 mm diameter borehole.
- Produce a temperature stabilisation system within the detector to minimise the influence of temperature on background measurements.
- Implement and demonstrate a high-speed algorithm capable of converting pulses into spectra using multiple experimental methods, as well as electronics to amplify and capture said pulses.

The thesis will be structured in the following manner:

- **Chapter 2** analyses and compares existing beta detection literature as it relates to the defined objectives, and whether there is a viable method to enrich low beta radioisotopes in-situ. Also, the chapter concatenates many current detector systems to inform the design of the new detector.
- **Chapter 3** covers the development of the backend electrical system from the photodetectors to the software capturing and processing spectra. Results from light emitting diode (LED) blink tests, experiments with sealed radioactive sources, and temperature testing have been included to demonstrate the validity of the system.

- **Chapter 4** begins investigating granulated scintillators, including methods for their creation, particle size filtering and characterisation using an LSC to find a relationship between particle size and detection efficiency. This chapter will then move onto the design and justification of the flow cell, showing a step-by-step guide to making a flow cell and older design ideas that were each innovated upon to result in our final design.
- **Chapter 5** demonstrates the detector tested with multiple concentrations of tritiated water and strontium-90 tracer as well as samples taken from boreholes located on the Sellafield site.
- **Chapter 6** discusses the manufacture and implementation of the final detector casing, cooling systems, electrical wiring, and battery pack design. Which together compact the system below a diameter of 50 mm.
- **Chapter 7** is the thesis conclusion and will discuss the outcomes of the thesis and how they compare to the defined objectives. Examples of future work are also given.

2 Literature Review

2.1 Introduction

With the objectives defined, this chapter will identify and discuss existing literature with the ultimate goal of outlining common design features of a low energy beta detector for the application of borehole groundwater monitoring. The resulting design features will be used to guide the detector development in the chapters to follow.

The following will be covered in this chapter:

- Current state of Sellafield borehole monitoring systems
- Viability of enriching beta-emitting isotopes within a borehole
- Analysis of existing literature on low energy beta detectors
- Scintillator and silicon photomultiplier (SiPM) selections
- Existing SiPM temperature compensation systems

2.2 Sellafield Groundwater Monitoring

Over the years Sellafield has released reports [23], [35] detailing the monitoring and discharges from the site. These documents provide a great insight into the methods used to detect low energy betas, the breakdown and abundance of radiological waste and finally the steps in place to ensure the safety of the site and its surrounding environment.

Historical sampling data (Figure 2.1) provided by Sellafield [36] shows the breakdown of beta emitters within borehole 10202 into three key isotopes: tritium, carbon-14 and strontium-90. In summary, an upward trend can be seen

for each, with a sudden spike in tritium content after April 2020. Sampling frequency for tritium within this borehole ranges from approximately 1.75 samples per month from 2012 to 2014 and 0.67 samples per month from 2014 to 2018. For an in-situ detector this would allow a maximum count time of 489 hours to 1278 hours to measure and report activity readings.

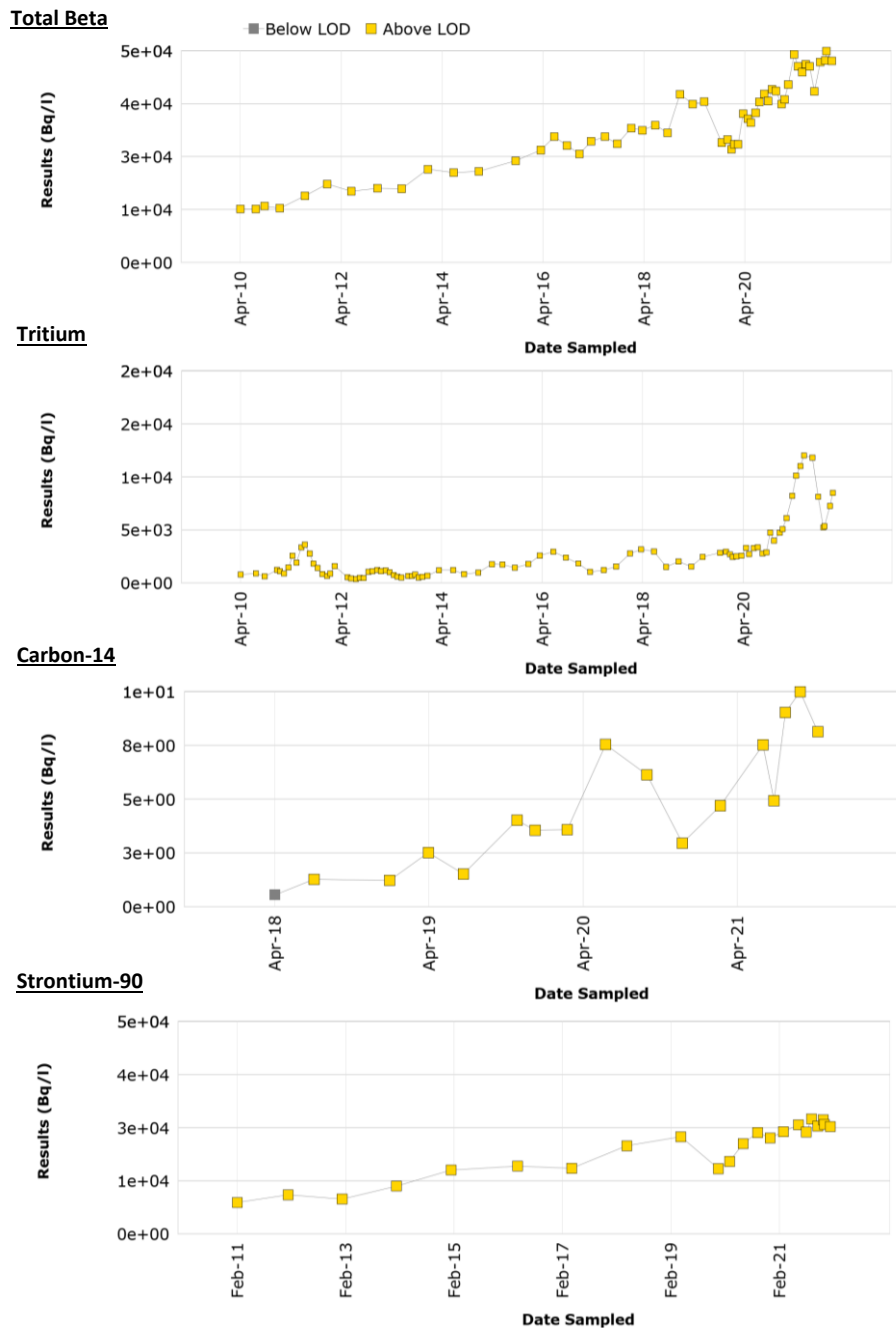


Figure 2.1: Activity of key beta emitters tritium, carbon-14, and strontium-90 within borehole number 10202, sampled over multiple years. Provided by Sellafield [36].

2.3 Detection of Soft Betas using Geiger Muller Tubes

A Geiger Muller tube commonly consists of an enclosed tube with a centre wire in which a large voltage potential is placed across. The tube is filled with an inert gas (commonly helium or argon) which is ionized as radiation enters the tube. The liberated electron or electrons cause an avalanche where the electric field formed from the voltage potential accelerates electrons causing collisions with atoms within the gas to produce more liberated electronics. This results in a sudden current flow across the tube which can allow gains in the order of 10^9 [37]. The higher the activity the greater the number of pulses counted per sampling period.

In the context of soft betas, most to all are absorbed by the end window of the tube, which is used to keep the surrounding ambient air from entering and displacing the filled gas. Therefore, while detecting soft betas using Geiger Muller Tubes is possible [38] given micrometre thick polycarbonate films (50% of tritium penetration with a 20 μm thick window), the resulting devices use incredibly fragile windows that must be placed in almost direct contact with the radioactive substance.

Another report discussing Pancake detectors [39] explicitly mentions that tritium cannot penetrate the mica window of a pancake detector and therefore the detection efficiency for tritium is always zero regardless of the quantity of tritium.

2.4 Detection of Beta Radiation using Image Sensors

A charge coupled device (CCD) and a complementary metal-oxide-semiconductor (CMOS) are two similar electrical components that can convert incident light into a charge which is then collected and measured. The measured charge can then be digitised and used to re-create an image where image pixels relate to the physical individual pixels of the device itself.

The difference between CCD and CMOS devices is that the latter incorporates an amplifier per pixel within the semiconductor die itself, while the former relies on a single amplifier in which pixels are measured sequentially.

A study [40] discussing the use of these devices with multiple forms of radiation tested a web camera CCD image sensor (surface area of $1.37 \times 10^{-2} \text{ cm}^2$) with two planar sources of beta radiation (flat area coated with radioactive material), recorded data shown in Table 1.

Table 1: Measured detection efficiency of CCD based detector, tested with two weak plane sources [40].

Source Type	Maximum Decay Energy (MeV)	Radioactive Activity (Bq/cm^2)	Detections (per 100s)	Detection Efficiency (%)
^{14}C	0.156	37.97	6.5 ± 1.5	12.5 ± 2.9
$^{90}\text{Sr}/^{90}\text{Y}$	2280	22.67	3 ± 1	9.6 ± 3.2

Another CCD performance study [41] discusses types of noise that are introduced including noise from the pixels themselves (~ 10 electrons) and dark current from thermally excited electrons. Due to the latter, the CCD was cooled to a temperature of 121K for its performance testing. Carbon-14 again was used with an activity of $3.74 \text{ kBq} \pm 5\%$ resulting in an absolute detection efficiency of 8.4%.

This shows that CCD and CMOS image sensors could be used as an alternative to photomultiplier tubes (PMTs) for a scintillator-based detector but would require a complex electrical system to access and read the voltage at each pixel. Therefore, SiPMs are still the most advantageous as they come in a small form factor and require fewer supporting electronics (discussed further in section 2.9).

2.5 Tritium Enrichment and Separation Methods

Many existing systems come in a range of sizes and shapes, it is important to compare each of these existing designs in the interest of finding the more advantageous and feasible features that can be combined into a new detector.

2.5.1 Electrolytic Enrichment

The paper by Muranaka and Shim [42], details the design and testing of a solid polymer electrolytic (SPE) film electrolytic apparatus in which porous electrodes

sandwich a porous SPE film. This allows hydrogen ions to move between the electrodes without the need to add an alkaline electrolyte, removing the extra step of neutralising the sample afterwards. Figure 2.2 shows the electrolyser and its placement in the cell.

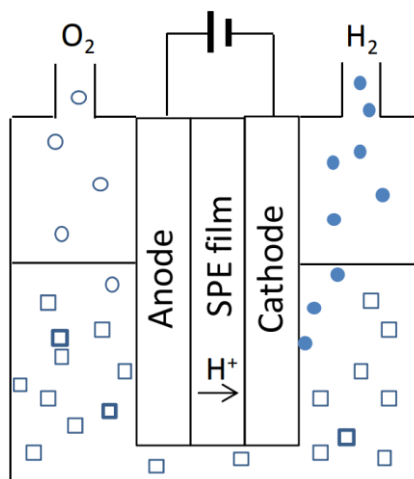


Figure 2.2: Diagram of the electrolytic cell for the enrichment of tritium in water, current is passed through anode and cathode to break water into hydrogen and oxygen. SPE film carries hydrogen ions between electrodes [42].

The method increases the concentration of between tritium and deuterium in a water sample using electrolysis. As experimentally confirmed, light hydrogen is more easily electrolysed compared to tritium and deuterium, and so over time, the leftover water will be enriched with tritium and deuterium [42].

A test of the electrolyser was conducted with a current of 3 A and a 300 g sample containing tritium of concentration 8 Bq L^{-1} . As a result, the sample decreased in weight from 300 g to 60 g with the average enrichment ratios calculated as 3.36 ± 0.21 for tritium and 3.10 ± 0.07 for deuterium.

Leading on from this a two-stage electrolysis is described to give a total volume reduction factor of 15, by combining a commercially available apparatus and the electrolyser from the previous testing. It is mentioned that for testing coastal seawater using the two-stage enrichment process, the water was distilled to remove contained salts. Therefore, to install such a system in-situ would require a high-capacity battery to distil the incoming sea water as well as to perform the electrolysis, limiting the amount of time the detector can run continuously before

requiring a recharge. For the detection of tritium, only the liquid scintillation counting (LSC) method is discussed implying that for sea water monitoring LSC is still the standard.

Another paper [43] details a multi-electrolytic cell automatic tritium enrichment unit (one of ten cells shown in Figure 2.3). The system can enrich a distilled water sample up to 2 L, having an enrichment factor greater than 100 times. The unit is aimed towards measuring low tritium levels (<0.36 DPM per 1 kg of water) in combination with traditional methods like liquid scintillation counting.

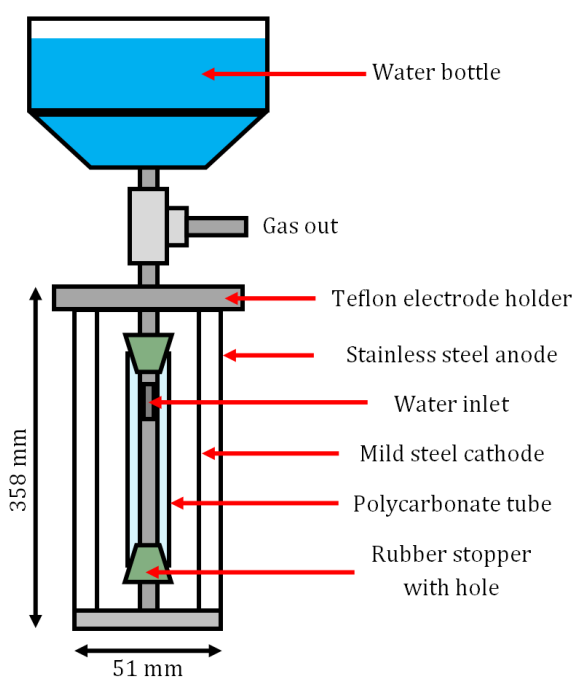


Figure 2.3: Front view diagram of 1 cell within 10 cell unit, labelled with its key parts [43].

The conventional enrichment process outlined is that a volume of 250 g to 500 g of distilled water is added to a cell and mixed with an electrolyte (Na_2O_2), a current of 3 A to 10 A is passed through the cell and after completion, the solution is neutralised by adding PbCl_2 . This results in enrichment factors in the order of 25 to 30.

The new system describes an automatic filling process where a reservoir (2 L) feeds into a cell (250 mL), as the volume reduces the system automatically keeps the cell fed. The bubbling of CO_2 gas into the cell neutralises the alkalinity of the

enriched samples. Once the process has finished cryogenic distillation (at -20°C) is used to retrieve the sample.

Linking back to the project at hand, to implement any electrolytic enrichment would require distillation, filtering and control of pH level, adding great complexity and also increasing the total power consumption of the system. The benefit of using this enrichment process before detection is that low energy isotopes like tritium can be concentrated increasing the effective minimum detectable activity of the system as a whole.

2.5.2 Membrane Diffusion

A report by Bhave, Jubin, and Spencer [44] discusses the separation of tritium using the difference in diffusion rates through a zeolite molecular sieve membrane (see Figure 2.4). The membrane consisted of silicoaluminophosphate (SAPO-34) crystals layered onto an alumina support structure, with the crystal layer in contact with a feed containing tritiated water and the alumina support connected to a vacuum pump via a liquid nitrogen-cooled cold trap to collect the concentrated solution.

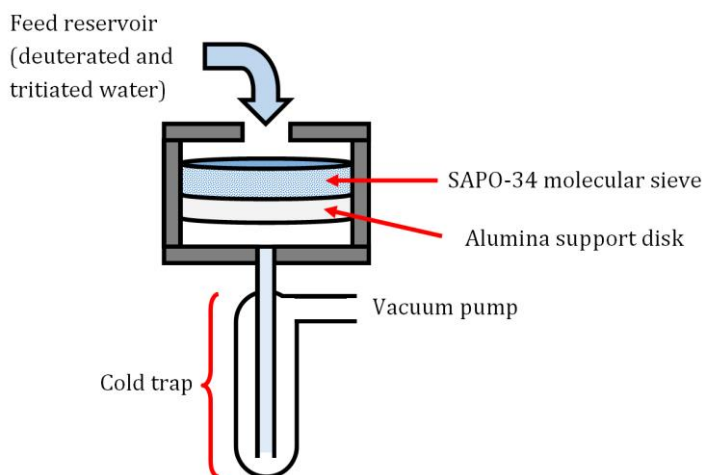


Figure 2.4: Pervaporation system for the recovery of tritiated water [44].

Multiple experiments were performed on the setup testing the concentrations of HTO and HDO in the resulting permeate. Sadly, the separation factor for tritiated water (HTO) did not reach 1 implying that a lower concentration of HTO was present in the permeate, but for heavy water (HDO) the separation factor ranged

from 10.5 to 19.0. For the purposes of this project, this shows that the current setup is unsuitable for concentrating tritium but shows that these membranes can separate heavy water molecules which could be used to filter HDO from the sample before passing into a detector.

Another publication by Li et al. [45] showed that reverse osmosis membranes can be used to treat environmental water samples containing low tritium concentrations. This method could reduce pretreatment time by over 77% compared with atmospheric distillation. Reverse osmosis is a process for removing impurities including particulate matter, microorganisms and dissolved contaminants from water using a diffusion-controlled separation process [46]. A simplified diagram showing a reverse osmosis system is shown in Figure 2.5.

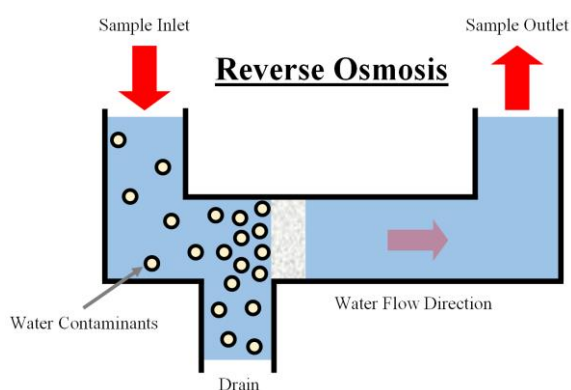


Figure 2.5: Diagram of a reverse osmosis system.

2.5.3 Hydrogen Separators

The company Power+Energy manufactures a product for use in nuclear plants for separating hydrogen and its isotopes from a mixed stream of gases, it quotes a purity level of over 99.9% [47]. In relation to this project, this separator could be used in combination with an electrolyser to break down groundwater into oxygen and hydrogen and then purify the hydrogen in preparation for passing through a gas-proportional counter. This has the downside of only working for tritium detection as other beta emitters like ^{90}Sr and ^{14}C will be removed. A cross-sectional diagram of the system can be seen in Figure 2.6.

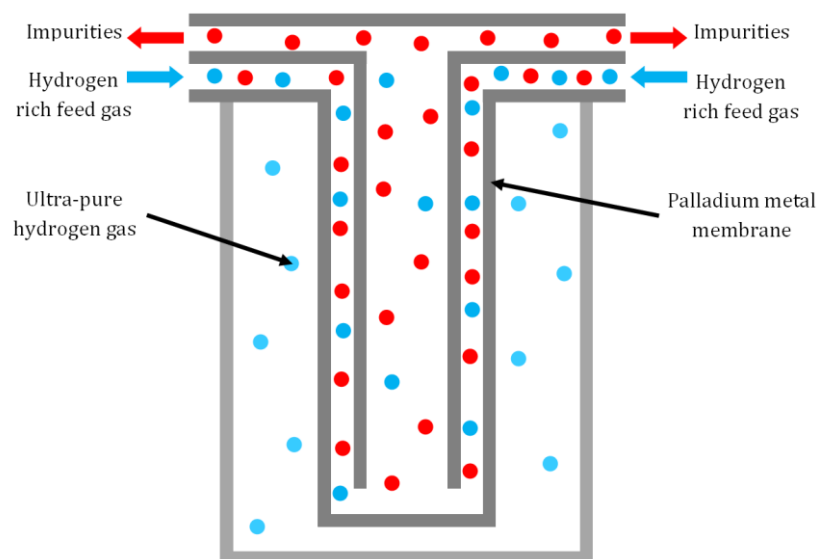


Figure 2.6: Diagram showing cross section of the gaseous hydrogen separator offered by Power+Energy [47].

The working principle of the separator relies on a patented palladium alloy [48] in which hydrogen can dissociate into, diffuse, and recombine on a low-pressure side. Absorption of tritium onto a metallic layer shares similarities with an existing system which will be discussed in section 2.7.11.

2.5.4 Polyphosphazene Membrane

In a report by Woods [49], a polyphosphazene membrane was used for the separation of tritium from water using a counter-current cascade process with an optimum operating temperature of 4°C. The membrane has a working life of 2 years and a separation factor of 2.33.

Also, another system examining polyphosphazene membranes found that adding salts (CaCl_2 , Na_2SO_4 and CaSO_4) to the HTO solution did not contribute to the overall separation factor, but for a feed with a concentration of 399.6 BqL^{-1} (HTO) under basic conditions saw an increase in average depletion from 19.0% to 33.6% for 9.7 pH and 10.7 pH levels respectively. For a HTO concentration of 111 kBqL^{-1} average depletion reached a maximum of 22.1% at a pH level of 10.7 [50].

For the application of tritium detectors, a polyphosphazene membrane can be placed before a scintillation flow cell help separate HTO while blocking other

contaminants and organics. Although to optimise the membrane a cooling system would have to keep the membrane at 4°C, and a basic solution would have to be added and mixed to lower the pH of the incoming solution adding complexity.

2.5.5 Chemical Reduction

Like electrosynthesis, a chemical method can be used to reduce tritiated water into tritium gas that can be passed through a detector. A paper by Stanga [51] explains that adding magnesium breaks the water into hydrogen gas and magnesium oxide. A clear benefit of reduction over electrosynthesis is that no oxygen gas is produced and therefore reduces the risk of hydrogen produced in the reaction combusting.

A magnesium bed could be added before a scintillator flow cell to convert a dilute tritiated water sample into hydrogen gas, as hydrogen gas is of a lower density than water the beta particles from the decay of tritium can travel further before being self-attenuated, increasing the chance they interact with the scintillator, improving detection efficiency.

2.6 Tritium Detection and Well Monitoring Reviews

A review by Atomic Energy of Canada Limited [52] discusses the need for tritium in-water monitoring as an early indication of heavy water leaks from nuclear reactors, desiring a lower limit of detection down to tens of Bq mL⁻¹. The status of monitors at the time includes taking grab samples (take a water sample and test its tritium concentration using liquid scintillation) with the disadvantage of requiring manpower and lower sampling rates. An automated batch sampling system is discussed, using a liquid scintillator with a batch sample rate of 10 per hour. The continuous operation length was limited by the failure of the tubing within the peristaltic pump used to measure the volume of the sample and liquid scintillator mixed together. Another major problem for these systems is ensuring the water and liquid scintillator are mixed correctly, some solutions are combined through agitation by air, magnetic stirring, or sonication where sound waves are applied to agitate the solution [52]. This draws similarities with Sellafield which also monitors tritium in-water using grab samples, issues with liquid scintillator

mixing could be mitigated by implementing a solid or granulated scintillator and allowing the sample to flow in contact.

The report further discusses various types of solid scintillator flow cells, with some notables being thin scintillator sheets and scintillator beads. Thin scintillators are preferred to thicker counterparts due to the very short range of tritium betas and therefore there is no advantage of implementing thick scintillators. Thick scintillators also increase the detection of interfering radiation, but many interactions still occur within the sample water itself and cannot be differentiated from betas produced from tritium decay. Detection methods utilising flow cells often fail in the field due to the sample being dirty or containing luminescent materials like chlorine. Therefore, filtration down to between 10 μm and 5 μm is required along with charcoal filters to remove chlorine, the disadvantage being they would require frequent replacement. If there is a lack of filtration, the sample will foul the surface of the scintillator decreasing the amount of light seen by the photon detectors reducing sensitivity. Ultraviolet sterilisers can be used to help kill unwanted microbes that could latch onto the cell and start growing [52].

A discussion by Bruyere and Cadwallader [53] focuses mainly on the repair and downtime of currently existing in-situ detectors. The difficulty of preparing unclean water samples is discussed for a solid scintillator detector created by Savannah River National Laboratory (SRNL) with a sensitivity of 56 Bq mL^{-1} (1514 pCi mL^{-1}). The SRNL detector uses mesh, charcoal, anion, cation and mixed bed ion filters for removing particulates down to 0.5 μm . An ultraviolet steriliser was used to sterilise the sample. The estimated operating hours for this detector were 8,700 hours per year with a 60 hours per year (~ 1 hours per week) downtime for maintenance including cleaning, replacing parts and calibration. Most of the failures reported are caused by the pump or filter system, including leaking filters and hose ruptures due to lack of sample flow and clogs from algae build-up. Twelve of the failures occurred in the first year and a further five failures occurred in the second, for a unit lifetime of five years to six years [53].

The report [53] provides a table of maintenance information for the SRNL unit, the preventive tasks involved checking the monitor, analysis cell and valves of the

system as well as replacing rubber hosing. Most of the reactive maintenance (taking 22 minutes to 24 minutes) involves replacing filters and pumps, as well as checking for water leaks leading to further replacements. A short discussion is included on the benefit of flash distilling as an alternative to filtering, where a dirty water sample is evaporated and then condensed to remove contaminants before measurement [53]. But to implement such a system in-situ would require a substantial power source to constantly boil and condense water, especially if there is no access to the main power grid.

Next, a review by Kang et al [54] compares current research into low energy beta detectors with existing machines on offer commercially. Also, scintillator materials are discussed including BC408 which has a high light output and is efficient for X-ray, alpha, and beta measurements below 100 keV. Calcium fluoride doped with europium ($\text{CaF}_2(\text{Eu})$) is also mentioned as being used to detect gammas and beta radiation up to hundreds of keV. A portable LSC by the SRNL group, created to supplement the shortcomings of current in-situ solid scintillator detectors, is noted as using a spectroscopy grade amplifier, lead shielding, radio frequency interference (RFI) guards and shielded cables to reduce background noise. Details are also given on a range of alpha and beta detectors by Ortec, using gas-flow proportional counters or dual phosphors, the performance of said detectors ranged from 45% to 63% detection efficiency for strontium-90 and yttrium-90 [54]. In reflection, BC408 and $\text{CaF}_2(\text{Eu})$ have been noted to be suitable for beta detection up to hundreds of keV, which encapsulates the range of low energy beta emitters.

Bala et al [55] note that for the oil and gas industry, the application of gas and scintillator-filled radiation detectors within wells allows the surrounding rock type and density to be studied using the naturally decaying radioisotopes within the rock and the Compton-scattering caused by photons emitted from a gamma source built into the detector itself [55]. Therefore, a new detector could include a solid scintillator working alongside a granulated flow cell to detect not only contaminants in the groundwater, but also contaminants in the surrounding soil.

Parker et al [56] focused on tritium detection within a liquid form noting that LSC is a staple measurement system used due to its high sensitivity for low energy betas as the sample and scintillant are brought into direct contact greatly increasing the probability that a disintegration will reach the scintillant. Current systems have reported efficiencies of up to 44% for HTO and have taken HTO measurements down to 20 Bq L^{-1} . Proportional gas counters have been able to achieve even lower detection levels of $\sim 10 \text{ Bq L}^{-1}$. Apart from the work by T. L. Alton [33], no other systems implementing a SiPM for the detection of tritium are mentioned [56]. In summary using an LSC for monitoring tritium is the current standard but would bring many downsides when in-situ (insufficient scintillator mixing, failure of pump for measuring sample and liquid scintillator). SiPMs also seem to be currently underutilised for the detection of tritium, and so the further development of SiPM based detectors is of interest for this work.

2.7 Existing Detection Systems

This section will discuss and compare literature, reports, and patents on existing low-beta detection systems, with a focus on tritium detection. As a result of this evaluation, key areas, design decisions and technologies can be identified which will then be adapted for the design of a new detector.

The in-situ conditions and size limits of standard 50 mm diameter boreholes will also be considered when discussing the relevance and feasibility of current detection techniques.

2.7.1 Layered Scintillator with Coincidence Counting

An article by Chiles [57] tests the feasibility of using a $\text{CaF}_2(\text{Eu})$ scintillator for detecting low-level betas from tritium. The system uses two PMTs coupled to both sides of the scintillator made from sheets so that both can detect light pulses created by the incident betas, also known as coincidence counting. This system allows the removal of random noise pulses which can be of similar magnitude to low-level beta counts.

The design in Figure 2.7 shows how the PMTs connect with the scintillator sheets. Interestingly solid $\text{CaF}_2(\text{Eu})$ sheets have not been used in favour of evaporating $\text{CaF}_2(\text{Eu})$ onto both sides of a flat 2 mm thick Pyrex glass plate. A thin layer is desirable to detect the maximum energy betas from tritium while not generating detectable pulses for background gammas, this optimal thickness is stated for their detector as approximately $920 \mu\text{g cm}^{-2}$ [57].

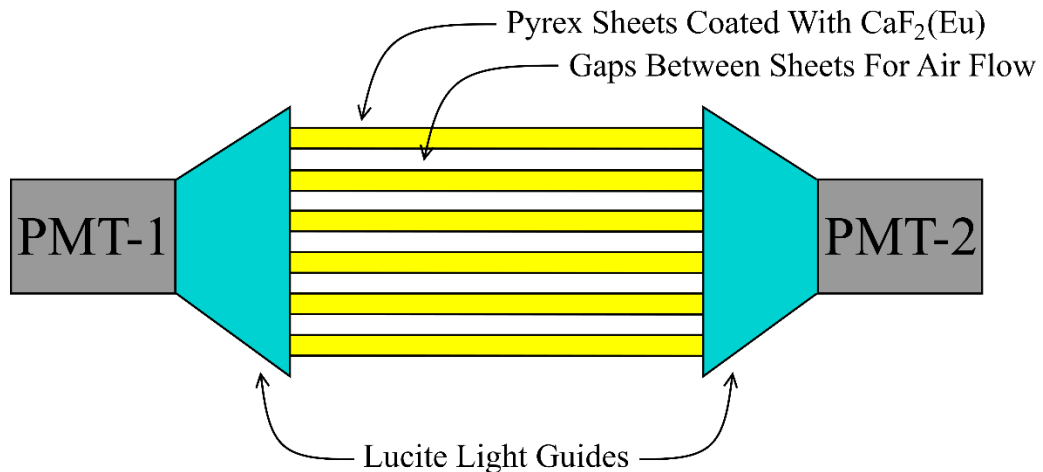


Figure 2.7: Conceptual design for detector, consisting of two PMTs and multiple scintillating layers, re-created from article [57].

The article concludes the feasibility of such a system but mentions that to detect low activities of $1 \times 10^{-13} \text{ Ci mL}^{-1}$ in the air (with 10% accuracy within 2 minutes) would require a very large detection area of 2 m^2 .

Leading from this, a paper [58] simulated a flow cell containing multiple layers of scintillator sheets for the detection of tritium in air. They found that the rate of detection initially increases logarithmically with the number of channels (air gaps between the scintillating layers) before reaching a maximum that thereafter decays. As the total height and width of the flow cell in the simulation was fixed, as the number and thickness of the scintillating layers increases, the individual channels become thinner lowering the overall volume of active sample within the flow cell. This trade-off between scintillator surface area and sample volume has led to a plateau for each thickness of scintillator showing an ideal number of channels to maximise count rate. The simulated count rate against number of channel for four thicknesses of scintillator is shown in Figure 2.8.

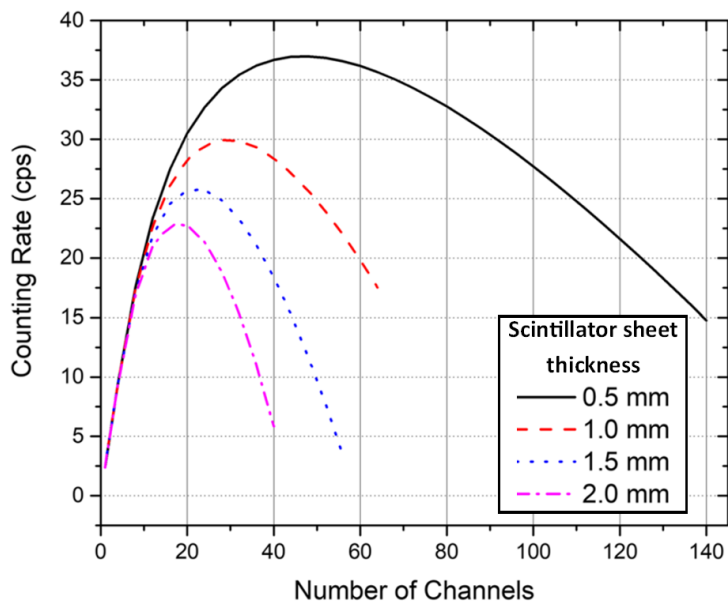


Figure 2.8: Graph plotting the effect on scintillator thickness (0.5 mm, 1.0 mm, 1.5 mm and 2.0 mm) and number of channels on the counting rate of the detector [58].

Following the simulations a physical detection chamber using coincidence counting PMTs was fabricated. It was noted that the plastic scintillator sheets used for the layered cavity were sourced from Epic-Crystal [59] had a refractive number of 1.58 and a critical angle of 39.2° . This low critical angle would help guide photons through total internal refraction towards the PMTs at either end of the detector cavity.

In summary simulations of a single-channel and 12-channel cavity predicted a detection efficiency of 3.36% and 36.56% respectively for the detection of tritium gas. This was then compared with the experimental detector setup which obtained a detection efficiency of $1.78\% \pm 0.04\%$ and $27.91\% \pm 0.49\%$ for single and 12 channels respectively. The tritium gas used for the experiment was produced through the electrolysis of tritiated water, the resulting gaseous sample had an activity concentration of $0.832 \text{ Bq mL}^{-1} \pm 0.012 \text{ Bq mL}^{-1}$.

2.7.2 CosmicWatch

This website [60] contains a complete tutorial for building a scintillator-based detector using an Arduino Nano and a Micro-FC 60035 SiPM. The detector uses a plastic solid scintillator for detecting cosmic rays, but this scintillator could easily be swapped for another better formulated for detecting betas. Two versions of the Arduino code are provided by CosmicWatch, one which prints text to a secure digital (SD) card when a pulse is detected, and another which prints to an organic light-emitting diode (OLED) screen when a pulse is detected.

Comparing the circuit produced by CosmicWatch (Figure 2.9) with the circuit from T. L. Alton's thesis (Figure 2.24) shows the addition of a second-stage peak detector which holds the peak of the amplified pulse for a short time. This allows a slower analogue to digital converter (like the one found integrated with the Arduino Nano) to get an accurate measurement of the peak without creating and processing the vast amount of data produced when using a high sampling rate.

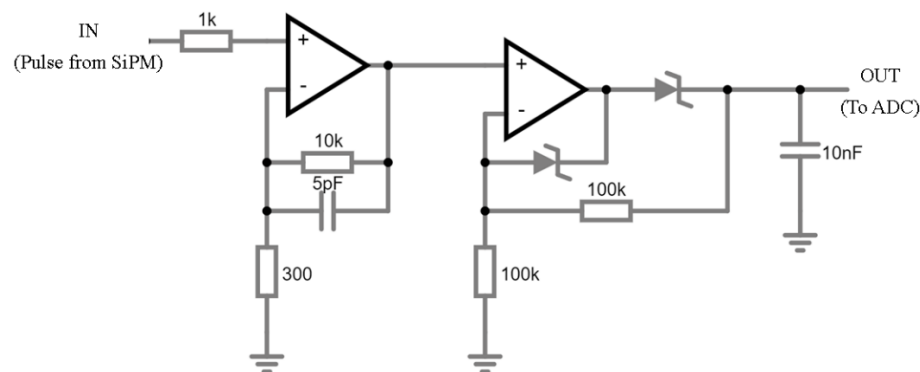


Figure 2.9: Extract from CosmicWatch schematic showing amplifier and peak detector stages [60], re-created in Falstad [61].

A downside to collecting only the peak of a detection pulse is that this is unsuitable for an organic scintillator, as the digitised height of the pulse is not proportional to the number of scintillated photons being detected, which indicates the original energy of the incident neutron particle. Therefore, a waveform digitiser is required to find the integral of detected pulses [62].

2.7.3 In-situ Underwater Beta Monitoring System

A paper coordinated by Choi et al [63] discusses a test setup for a water beta monitoring system, shown in Figure 2.10 below.

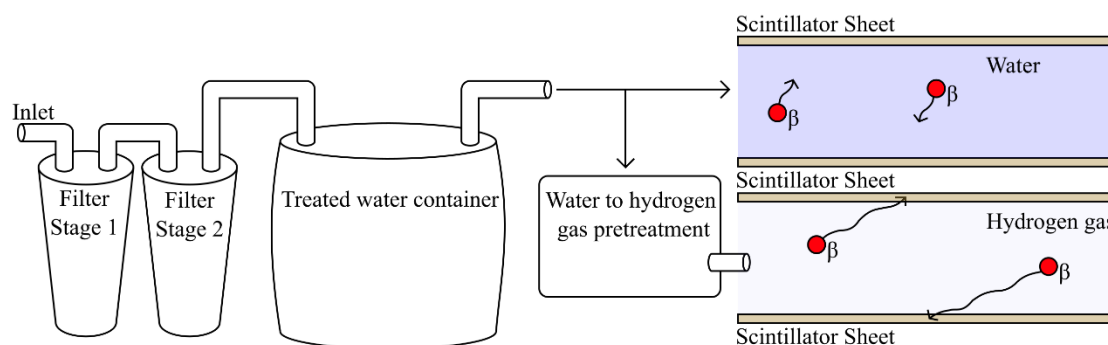


Figure 2.10: Diagram of system setup for beta monitoring showing how converting water into a hydrogen gas increases the penetration of emitted betas, re-created from paper [63].

Two design decisions can be taken away, firstly dual scintillator sheets are placed on both sides of the sample stream (see scintillator sheets in Figure 2.10) to increase the number of interactions over time, this draws parallels with Marion M. Chiles article [57] where multi-layer scintillators were investigated.

The second improvement is converting sample water into hydrogen gas, which would break down tritiated water resulting in molecules of tritium that will enter the detection cavity. As the tritium gas has a lower density than tritiated water, the geometric path length of its emitted betas will be longer allowing for more beta particles to reach the scintillator for detection.

The paper does not give details on how this conversion is made, but as previously discussed in section 2.5.1 a common method used is electrolysis. The measurement time required to reach a minimum detectable activity (MDA) of 10 Bq g^{-1} for tritium was predicted to take two years and an MDA of 0.1 Bq g^{-1} for strontium-90 would take five minutes.

2.7.4 Well-Logging Probe Capable of Measuring Tritium

This method [64], [65] describes a detector design to be placed in a well or borehole, which can detect tritium levels down to background (probes components shown in Figure 2.11). It takes samples from the air and uses a catalyst to convert the tritium in the air into tritium oxide, this is then collected in a cold trap cooled thermoelectrically. The sample is converted to a hydrogen gas using a magnesium bed held at an operating temperature of 590°C [65].

This hydrogen gas is then passed through a proportional counter. The setup has two identical detectors, one for the processed sample and one for background, the readings are then taken away from each other to find the elevation in activity.

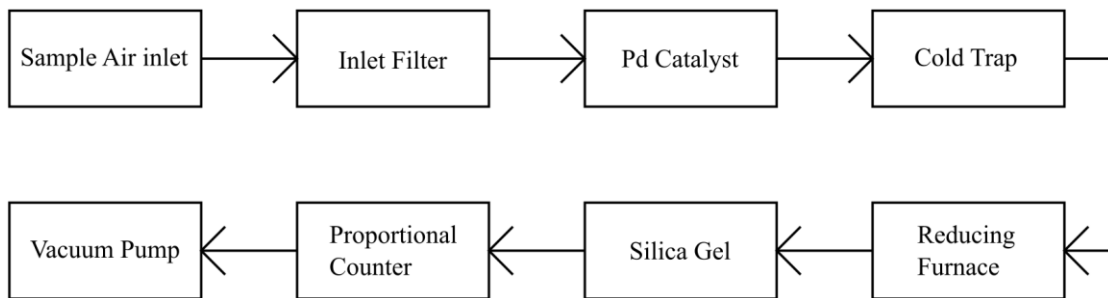


Figure 2.11: Diagram of the probe's main components [65].

Even though this probe is meant to be placed in a water well, it does not sample water directly, instead choosing to inlet air which will contain water vapour. This is likely done as air samples are also much cleaner as they will not contain heavy sediment. The outer diameter of the proportional counter is 60.3 mm, too large for standard 50 mm diameter boreholes.

A performance test of the instrument introduced tritiated water directly into the cold trap finding a detection sensitivity of approximately 1.85 Bq mL^{-1} , and a linear measurement range from 1.85 Bq to 29,600 Bq. It should be noted that the detection sensitivity does not include the efficiency of capturing and converting tritium within water vapor which could significantly decrease overall sensitivity. Additionally, this system is only suitable for tritium detection and cannot be used for measuring other low energy beta emitters within the well waters.

2.7.5 Real-Time Tritium Monitor System for Water Quality Surveillance

This detector system [66] has been developed with environmental monitoring in mind aimed for installation around rivers and nuclear power plants. Scintillating fibres have been packed into a polytetrafluoroethylene (PTFE) tube where samples of hyper-pure water and hyper-pure tritiated water are passed.

TRITIUM-0 (depicted in Figure 2.12) was manufactured with 35 scintillating optical fibres each with a diameter of 1 mm. Two additional versions were created, TRITIUM-1 at the institute for corpuscular physics (IFIC) with 64 fibres and Aveiro-0 at the University of Aveiro with 400 tightly packed fibres. For all designs, two covers hold the ends of the fibres in contact with two photomultiplier tubes (PMTs) running in coincidence mode.

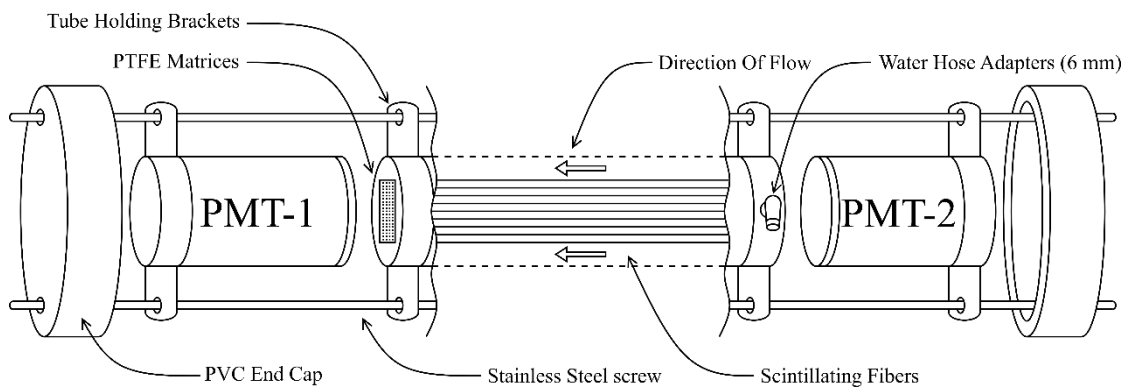


Figure 2.12: Diagram of TRITIUM-0 showing internal scintillating fibres, based on system description [66].

Geant4 simulations were used to study the interactions of the fibres with tritium finding that 99.7% of events that reach the fibre originate from a distance less than 5 μm from its surface. Secondly, simulations showed that deposited energy by cosmic muons decreased with 1 mm diameter fibres when compared to 2 mm fibres, hence 1 mm diameter fibres were used in the built detectors to minimise background counts.

To summarise the electrical system, the 400-fibre system used Hamamatsu R2154-02 PMTs which have a physical diameter of 51 mm with a minimum of 46 mm being sensitive to incident photons [67]. The PMTs had a coincidence

window of 500 ns. A CAEN V1724 digitiser with approximate dimensions of 483 mm by 356 mm by 480 mm [68] allows eight channels to be sampled at a maximum of 100 mega-samples per second (Msps) [69].

Results from the TRITIUM-0 detector and its predecessors; TRITIUM-1 IFIC and Aveiro-0 show a clear increase in activity over background when tritium is introduced. Precise values for count rate and activity are not provided in the report. Placing this detector in the context of in-situ borehole measurement, the electronics utilised are too large for installation within a 50 mm diameter, including the PMTs and data acquisition board (DAQ). Thus, alternatives would have to be identified.

2.7.6 Development of a Real-Time Tritium-in-Water Monitor

Again, the team responsible for TRITIUM-0 and TRITIUM-1 reported an updated design named Aveiro-0 also implementing fibres [70]. Two 2 inch diameter PMTs face inward each connected to either end of a scintillating fibre bundle held within a Teflon cell, the scintillators used are Saint-Gobain BCF-10. Figure 2.13 shows the organisation of the fibre bundles for both old and new systems.

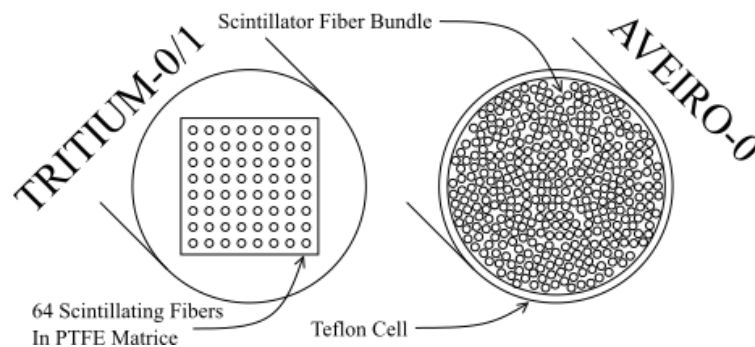


Figure 2.13: Diagram of Aveiro-0 detectors internal scintillator compared to Tritium-0/1 designs [70].

The system was first tested with a Fe-55 sealed source placed towards one end of the fibre cavity, it showed that pulses emitted by the PMT close to the source were of a greater amplitude compared to the PMT further away. This was explained as the result of the difference in photon attenuation between the source and PMTs as the closer the sealed source is to the PMT the lower the attenuation of the

scintillation photons. The next experiment saw the detector placed horizontally and filled with pure water for a background measurement resulting in a recorded value of 540 ± 23 CPM. Following this, tritiated water was slowly introduced into the cavity until the count rate reached 656 CPM, a value needed to ensure a false-negative rate no larger than 5%, the activity within the water sample was then measured finding an MDA of 29.8 ± 3.6 Bq mL⁻¹ for a one hour measurement period.

Finally, a simulation was performed to see how using multiple modules (detectors) in tandem would impact MDA, results showed that more modules would improve MDA but not significantly, with five modules having an MDA of approximately 1.6 Bq mL⁻¹.

2.7.7 Flow Cell Detectors Fabricated using CaF₂ Solid Scintillator

A granulated CaF₂ scintillator for detecting tritiated water was the focus in this publication [71]. The apparatus consisted of two inward facing PMTs, between which was placed a flow cell consisting of a Teflon tube filled with a scintillating powder. A flow pump forced a constant flow of a liquid sample through the tube. A total of three powders were tested: 50 µm, 100 µm and 300 µm diameters, with three concentrations of tritium with activity: 10 Bq mL⁻¹, 50 Bq mL⁻¹ and 100 Bq mL⁻¹. A diagram of the system showing how the flow cell slides in between the PMTs is shown in Figure 2.14.

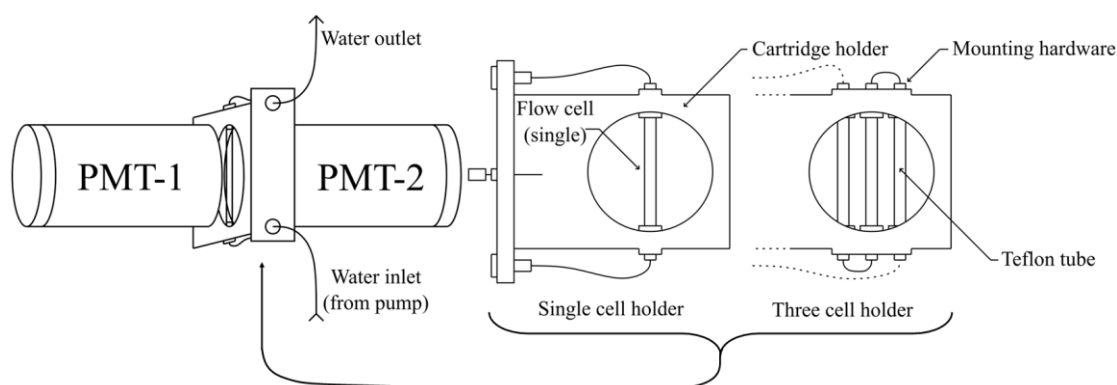


Figure 2.14: Diagram of detector setup consisting of two coincidence PMTs facing into a cartridge that holds one or multiple Teflon tube detection cavities [71].

Results from these experiments showed a definite linear relationship between tritium concentration and count rate validating that a granulated scintillator is suitable for soft beta detection. It was also shown that using finer granulated scintillators resulted in a lower detection limit with a minimum detection limit of 6.95 Bq mL^{-1} ($6,950 \text{ Bq L}^{-1}$) obtained. But this is still far above the EU Drinking Water Directive limit of 100 Bq L^{-1} for tritium concentration [21].

CaF_2 was selected as the granulated scintillator as it was best suited to the application due to its very good chemical stability, supply, and cost. No details are given about how the powder is kept within the flow cell or the manufacturer of the granulated material.

2.7.8 Tritiated Water Online Detector System based on Plastic Scintillators

A study by Dong et al [72] designed and tested an online detector system that used plastic scintillators to monitor tritium in liquid waste from nuclear power plants. The built detector (diagram in Figure 2.15) consists of drilled scintillating rods in which the sample could pass, increasing the contact area. Two PMTs were attached to both ends of the polycarbonate (PC) tube containing the fibres to perform coincidence counting. A SPARTAN 6 field programmable gate array (FPGA) was used to process pulse data digitised using a 12-bit ADC.

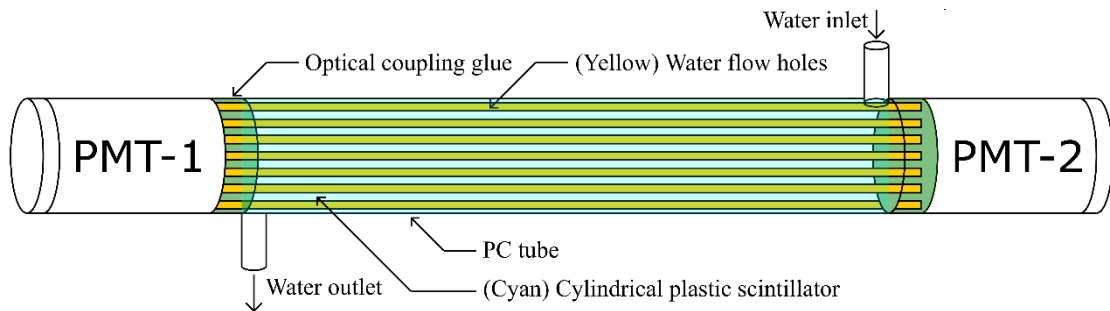


Figure 2.15: Diagram showing the internal layout of the tritium detector, re-created from paper [72].

Geant4 Simulations were performed on the fibre scintillator design finding that the distance travelled by beta particles from tritium would line between $4\ \mu\text{m}$ and $5\ \mu\text{m}$ in water. For tritium decay within a plastic scintillator, the range of beta particles was also less than $5\ \mu\text{m}$.

Another simulation kept the diameter and number of fibres static while varying the length of the flow cell, it was reported that the detection efficiency increased from 3.74% to 4.19% as the flow cell's length was decreased from 60 cm to 2 cm. Hence implying that there is a trade-off between the extra surface area from longer fibres and the increased optical attenuation of generated photons traveling further to reach each PMT.

Due to limitations in procurement, the built detector was not tested with tritium but with potassium-40 (^{40}K). Due to the much greater beta energy emitted by ^{40}K compared to ^3H (up to 1.31 MeV vs 18.6 keV), the degree of pulse amplification required could be reduced. Thirteen activities of ^{40}K were passed through the detector from $10\ \text{Bq L}^{-1}$ to $4,500\ \text{Bq L}^{-1}$, the PMT high voltage supply was also varied from 1,000 V to 1,350 V for each activity to ascertain an ideal supply voltage for maximum measurement linearity. Results showed that 1,300 V provided the best linear fit and demonstrated a clear positive increase in the detected count rate as the activity concentration was increased. No detection efficiency results were directly reported for the experiment.

2.7.9 Efficiency Enhanced Electrolysis-based Tritium Continuous Monitor

This configuration of a tritium detector uses a 10-stack proton exchange membrane (PEM) electrolysis cell to break down a water sample into hydrogen and oxygen [73], the hydrogen is then separated and passed through a detection chamber (Figure 2.16). This chamber consists of an acrylic structure and two plastic scintillators each paired to their constituent PMT, a time-to-amplitude converter (TAC) was connected to the PMTs to perform coincidence counting.

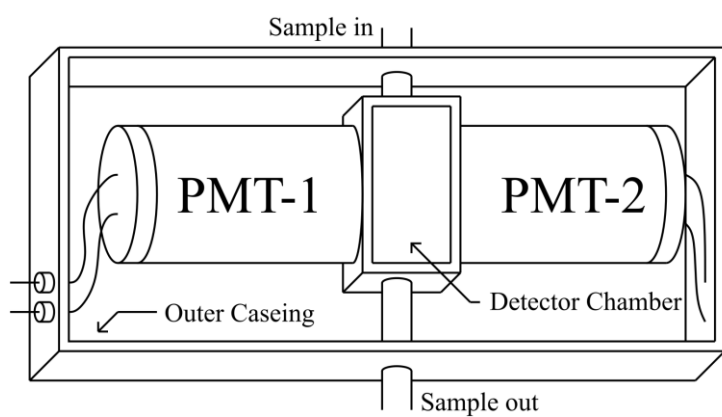


Figure 2.16: Image of detector setup within light tight case showing dual PMTs, based on detector photograph [73].

The electrolysis cell was tested using six samples containing different tritium concentrations from 156 Bq mL^{-1} to $2,173 \text{ Bq mL}^{-1}$, after collecting the produced hydrogen gas it was then passed into a commercial tritium detector for measurement, and results showed a clear positive relationship between the activity of tritium within the produced hydrogen gas and the activity of tritiated water passed into the cell.

Another experiment was completed using tritiated water with an activity of $7,500 \text{ Bq mL}^{-1}$, it was passed continuously through the complete setup (electrolysis cell and dual PMT detector chamber) for measurement, values for detection efficiency were obtained at 4.25% and minimal detectable energy was reported as 655 Bq mL^{-1} and 133 Bq mL^{-1} for a measurement time of 60 minutes and 24 hours respectively [73].

2.7.10 Heavy Water Detection for Pressurised Heavy Water Reactors

Within a pressurised heavy water reactor (PHWR) heavy water is used as a primary coolant, due to neutron activation this water can be converted into tritium among other side products. Consequently, a detector (Figure 2.17) was designed to monitor the presence of tritium within the coolant as it is pumped to and from a PHWR.

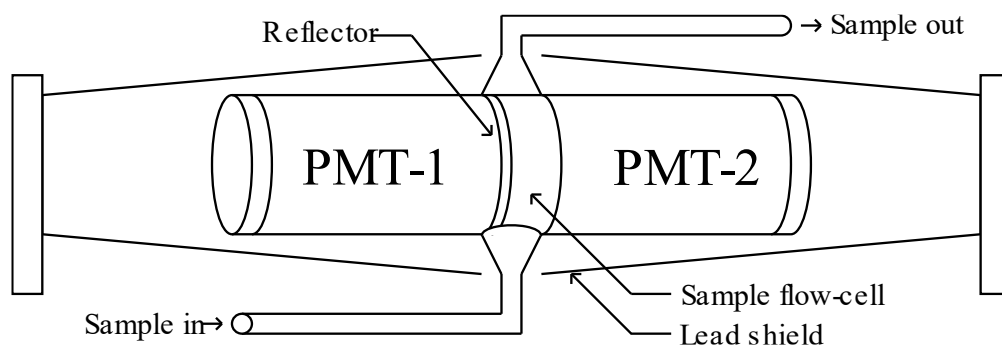


Figure 2.17: Diagram of heavy water quick detection system, re-created from graphical abstract [74].

Contained within this system are two PMTs surrounded by a 30 mm thick lead shield to reduce background counts, a polythene plastic flow cell (20 mL) allows a liquid sample (water) to flow through the cavity between the photomultipliers. The water sample itself acts as the scintillator with counts detected from photons created by Cherenkov radiation. Testing with ^{90}Sr with ^{90}Y showed a detection efficiency of $22.2\% \pm 1.1\%$ [74]. A system using water as the scintillator itself could benefit from an increased flow cell sample capacity as a solid or liquid scintillator would not have to be added which would displace any liquid samples. Again, as seen in other detection systems coincidence counting PMTs have been used.

2.7.11 Tritium Detection by Electrochemical Assisted Radiometrics

This work by Berhane et al [75] demonstrates the use of a Pd porous layer which has an affiliation to capture and hold hydrogen. This behaviour can be exploited to incorporate tritium within the Pd matrix. By placing this layer in contact with a solid scintillator and photomultiplier tube (Hamamatsu H7828-01), the decay from the 'trapped' tritium can be detected. The build-up of tritium on the face of the scintillator will increase counts over time allowing the detection of low

concentrations that would otherwise be undistinguished from background. An electrochemical cell allows the held harvested tritium to be ejected from the Pd layer, thus allowing the layer to be reused. Figure 2.18 shows the system setup.

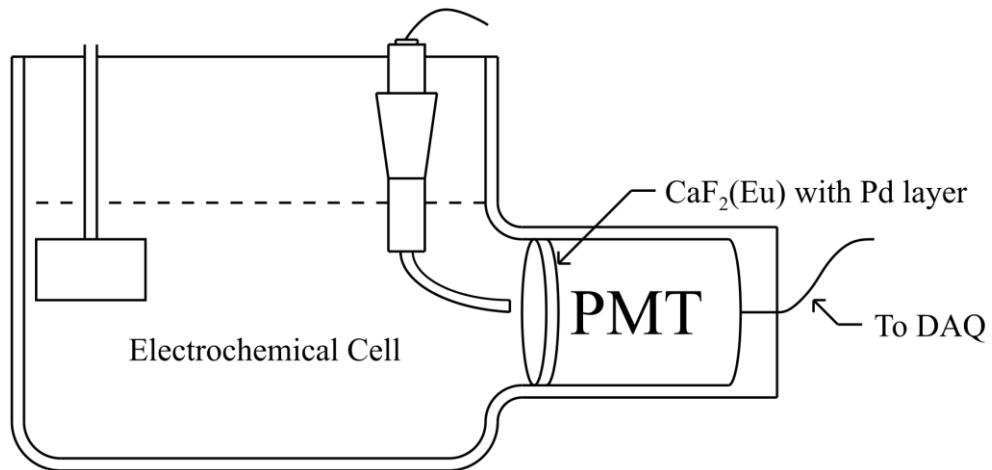


Figure 2.18: Diagram of experimental setup including electrochemical cell and scintillation detector, re-created from report [75].

The report states CASINO Simulations were created to find the most effective Pd layer thickness, with example simulations using a 60 nm thick layer given. Results from testing the setup with 10 kBq g^{-1} of tritiated water were given showing an increased count rate once the HTO solution was introduced. The non-porous layer achieved 0.21 CPS before pre-concentration and 1.63 CPS post-concentration (both with non-porous Pd layers). A maximum of 3.91 CPS was then achieved when a nanoporous Pd layer was used post-concentration.

A noticeable downside of this configuration is that only one PMT is used, therefore dark counts cannot be removed using coincidence counting. Also, the Hamamatsu counting head is not temperature stabilised and therefore dark counts may vary with temperature.

2.7.12 Scintillator Fiber Flow Cell Radioactivity Detector for Liquid Chromatography

This flow cell [76] (Figure 2.19) consisted of a bundle of scintillator fibres that have been axially aligned and placed inside a glass tube. Two PMTs in coincidence have then been placed over the outside of the glass tube to detect the scintillated photons. The sample is passed into one end of the glass tubes, around the fibres and out.

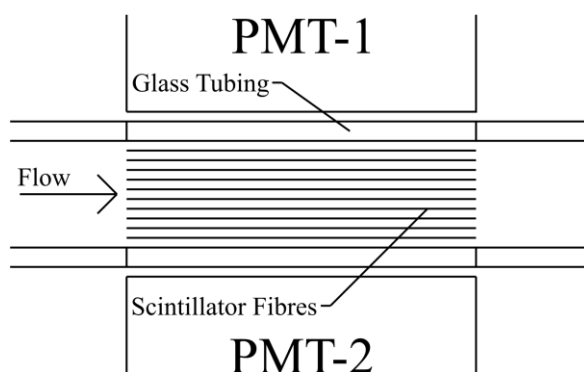


Figure 2.19: Cross-sectional diagram of flow cell detector showing scintillating fibres held within the glass tubing, re-created from publication [76].

Computer simulations with 0.1 mm diameter fibres predicted a 61% detection efficiency for carbon-14 with square-packed fibres and 80% for hexagonal packing. Measured results with carbon-14 show an improvement in detection efficiency from 33% to 55% when comparing 0.28 mm and 0.1 mm diameter fibres respectively.

The paper also discusses a packed powder scintillator cell using a Y_2SiO_5 scintillator with less than 25 μm diameter particles. A detection efficiency of 65% was measured for carbon-14 using the powder. But required 50 times more backpressure compared to the fibre cell. It was also noted that the fibre cell could be more closely packed with around three times less interstitial volume compared with a powder cavity.

2.7.13 Flow Cell Patent

This patent [77] describes a flow cell for use in high-performance liquid chromatography (HPLC). A diagram of the flow cell can be seen in Figure 2.20.

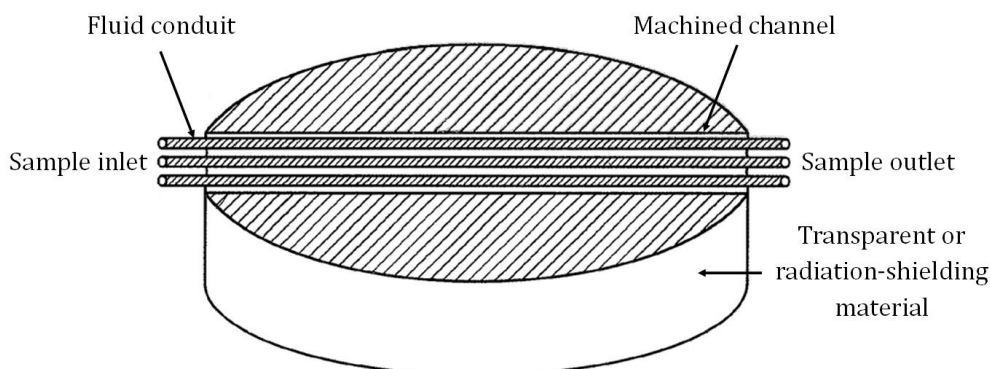


Figure 2.20: Illustration of flow cell invention [77].

The flow cell [77] is to be placed after a HPLC system and uses PMTs to detect light resulting from the radioactive solutions, this allows a plot of counts against retention time to be recorded. The data can then be used to study the purity of radiological tracers such as fluorine-18, which are in turn used to image cancer cells within the body.

The invention consists of an etched plexiglass block in which three polyetheretherketone (PEEK) tubes are placed. The plexiglass block is then mounted over a radiation-detecting crystal (scintillator) which is connected to a PMT. Radiation emitted by the sample passes into the scintillator and is converted into light which is then detected by the PMT.

In terms of low energy beta detection, some issues would arise. Mainly most particles would not be able to pass through the tubing and plexiglass block due to attenuation and so would not interact with the scintillator. But some design solutions are still applicable:

- The sample is passed co-planer to the face of the PMT.
- The radioactive sample is contained in multiple plastic tubes running parallel to each other.

2.7.14 Alternative Approach to Tritium-in-Water Monitoring

The paper by Kherani [78] demonstrates a detector (Figure 2.21) that converts tritium within water to steam via evaporation caused by heating from a hot place. Having tritium in a gaseous form allows low energy betas from tritium to have a range over multiple millimetres as opposed to micrometres within liquid water. Also, a benefit mentioned is that monitoring steam as opposed to liquid simplifies water filtration requirements as dirt and biological elements would be left within the boiler. After the steam has been monitored it can be condensed and collected.

The monitor itself consists of a heated ionisation chamber in which a -100 V DC bias is applied and monitored using a Keithley 617 electrometer. Figure 2.22 shows the measured current across the ionisation chamber, the first three injections are of tritiated water containing approximately 0.4 Bq mL^{-1} to 4 Bq mL^{-1} , with the following two injections containing approximately 0.4 Bq mL^{-1} to 4 MBq mL^{-1} worth of activity.

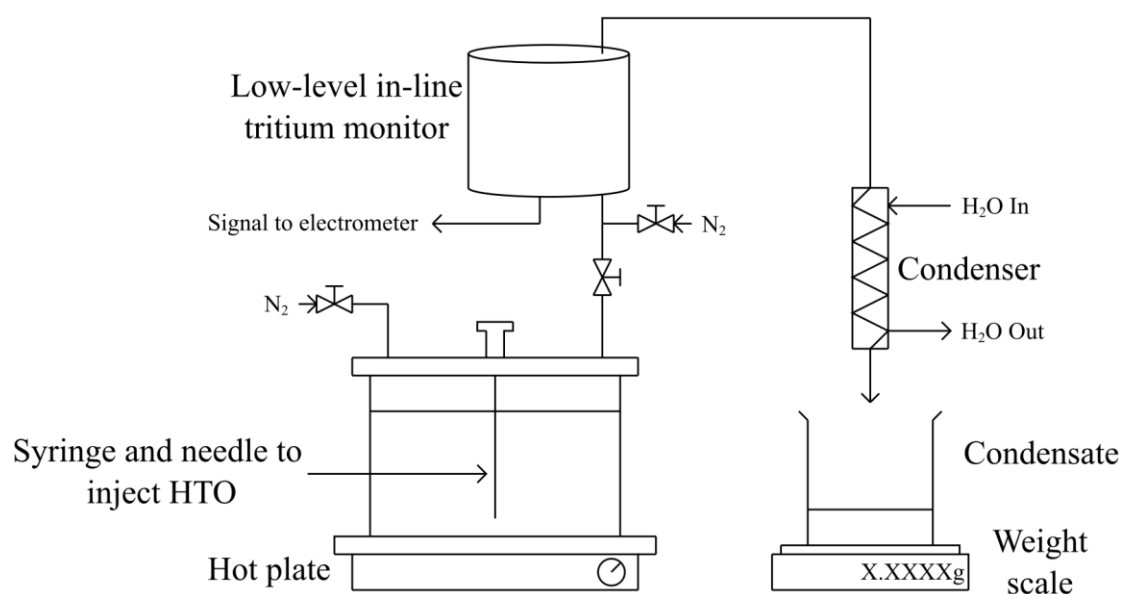


Figure 2.21: Diagram of proof of principle experiment setup, re-created from paper [78].

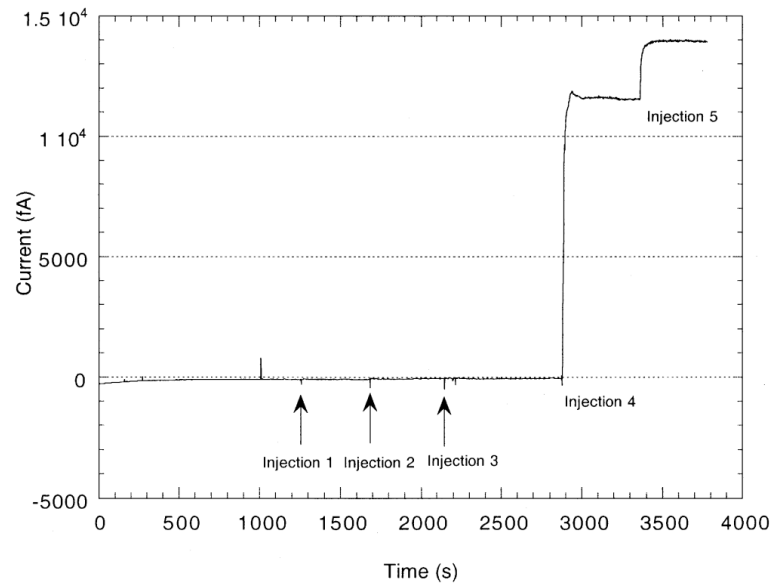


Figure 2.22: Graph from paper [78] showing the resulting increase in chamber current as tritium is introduced to the detector setup.

The last two injections resulted in a clear increase in current, attributed to ionisation caused by the increased presence of tritium within the steam. In the conclusion of the work, it is stated that this method allows the detection of tritiated water to concentrations as low as 20 mCi L^{-1} (approximately 7.4 Bq mL^{-1}). A similar dual cavity background and airborne tritium ionisation chamber has also been implemented in a portable handheld device [79] back in 1980.

2.7.15 In-Situ Monitoring of Groundwater Radionuclides with Emphasis on Tritium Detection

A thesis by T. L. Alton [33] discusses a scintillator that has been crushed using a mortar and pestle and then bonded to a substrate disk using polydimethylsiloxane (PDMS), multiple layers were then placed into the cavity for testing. Before the creation of the flow cell a pulmonary test was performed to compare the heterogeneous scintillator to a single crystal scintillator, results show an increase in detected counts when using the created heterogeneous scintillator over the single crystal. An image of the pulmonary test setup is shown in Figure 2.23 and the SiPM circuit used is shown in Figure 2.24.

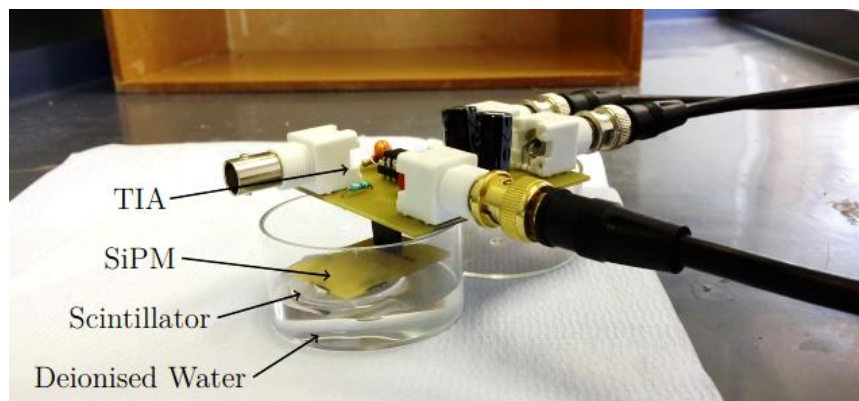


Figure 2.23: Image of setup used in thesis: $\text{CaF}_2(\text{Eu})$ scintillator attached to SiPM and preamplifier board, taken from thesis [33].

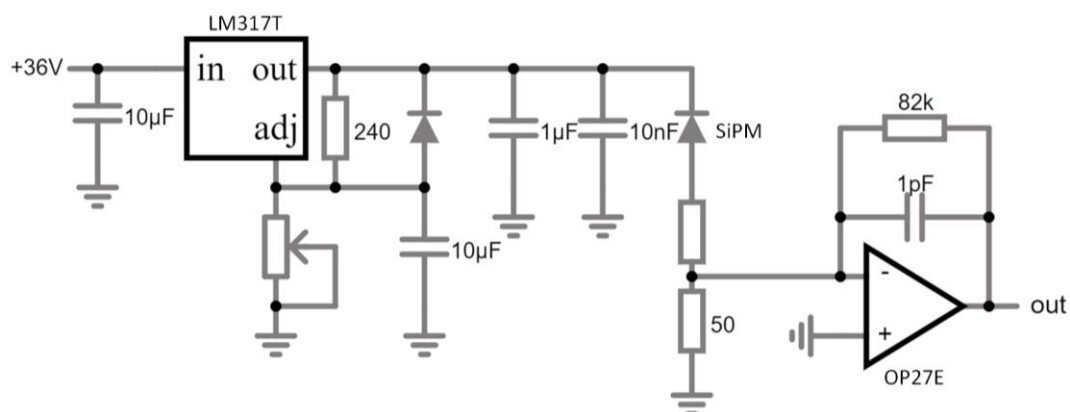


Figure 2.24: Schematic of circuit used to bias SiPM and amplify output pulses [33], re-created in Falstad [61].

The flow cell system in Figure 2.25 was designed for the detection of tritiated water, it consists of a cylindrical aluminium cavity topped with a transparent Perspex lid, a ridge around the top of the cylinder allows a rubber ring to be added to act as a seal. A singular SiPM was placed in contact with the centre of the lid surrounded with a reflective material. A peristaltic pump was then used to feed a sample from a reservoir in which tritiated water was added.

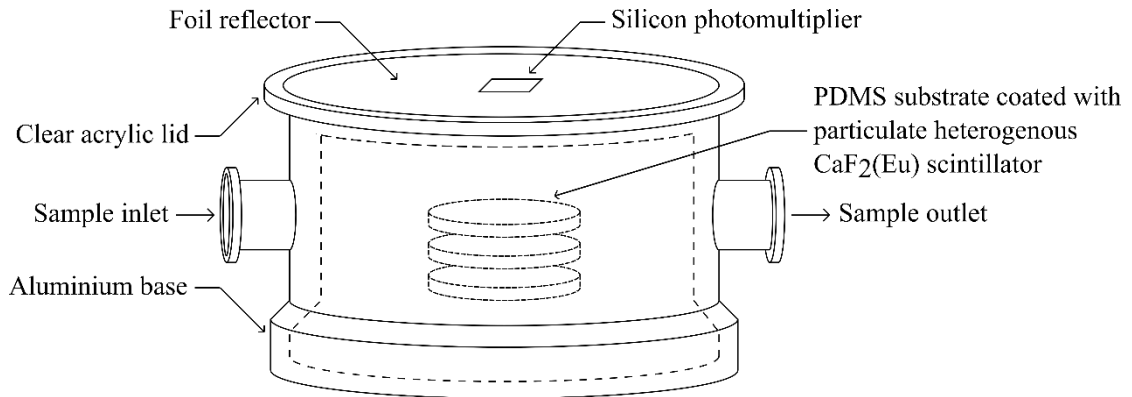


Figure 2.25: Diagram of designed flow cell chamber showing internal disks covered with heterogeneous scintillator, created from photograph of detector [33].

Recorded counts for 15 minute, 30 minute and 60 minute windows can be seen in Figure 2.26, as tritiated water was passed into the flow cell. In relation to this data the thesis does note some issues; 1.5 hours into the experiment a sudden peak can be seen approximately 30 minutes after the addition of the tritium into the sample reservoir, this 1.5 hour peak is not attributed to the presence of tritium within the flow cell chamber as it was estimated it would take 50 minutes for the tritium to start entering the flow cell followed by another 40 minutes to fill the cell.

It is instead stated that the impact of tritium can be seen in the main peak starting at the four hour point, but further into the explanation it is mentioned that the SiPM gradually failed and therefore the peak rising after four hours could have been caused by the failure of the SiPM. The time at which the SiPM failed within the experiment is not stated and the experiment was not repeated.

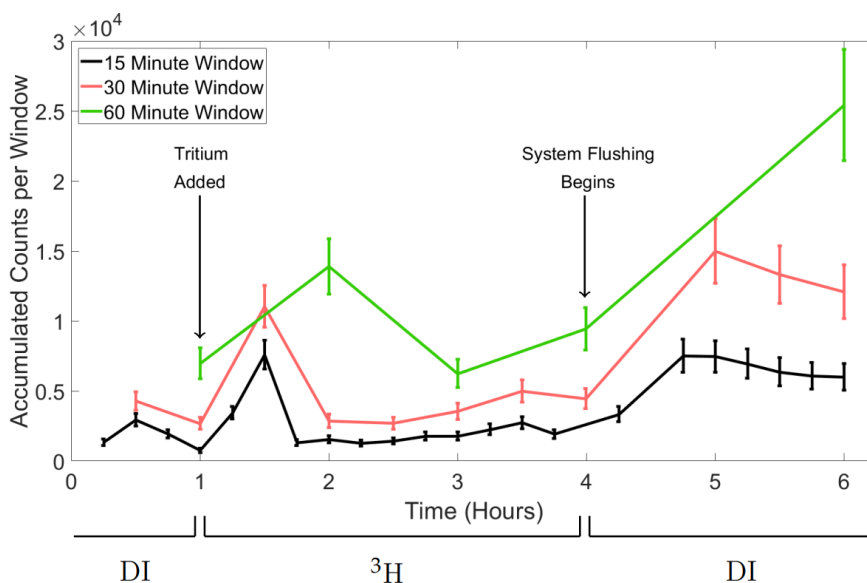


Figure 2.26: Data from conducted transient flow experiment (plotted as total counts per window of time, 15 minutes, 30 minutes or 60 minutes), taken from thesis [33].

Another set of experimental results compare using three to twelve layers of scintillator disks. Background counts have been subtracted but their values are not given, thus the minimal detectable energy cannot be calculated. Interestingly an increased scintillator surface area of four times resulted in 43 times the measured total counts, not matching a logarithmic relationship as previously described when increasing scintillator layers [58].

2.7.16 β Ionix 3™: Portable Tritium Monitor

This commercial product offered by Mirion Technologies is a portable low energy beta detector with a focus on tritium monitoring for usage in applications relating to decommissioning and environmental surveys [80]. The bench top system (Figure 2.27) can perform continuous measurement with a tritium detection limit of $0.0125 \text{ Bq mL}^{-1}$, the unit dimensions measure approximately $235 \text{ mm} \times 210 \text{ mm} \times 111 \text{ mm}$ (length \times width \times height) and lasts six hours on battery power.



Figure 2.27: Image of β Ionix 3™ detector [80].

The unit detects radionuclides in air via a gas inlet and outlet, this feed is passed through an ionisation chamber in which a 160 V direct current (DC) ionisation voltage is placed. Mirion Technologies also offers other related products including a tritium bubbler used to concentrate samples containing tritium before measurement [81].

Evaluating the product for the objectives of this application, the system is not capable of fitting into a 50 mm diameter borehole, nor is it capable of measuring low energy betas within water directly. The limited battery life would also pose issues for long-term continuous measurements as access to mains power is not guaranteed.

2.7.17 Tritium Monitor using Plastic Scintillator (Sheets and Pellets)

The study by Sanada et al [82] created a monitor for the detection of tritium. Again, as seen in similar scintillator-based setups, two PMTs in coincidence have been implemented (see Figure 2.28). The detector used a plastic scintillator which has a polymer base of polystyrene (PS).

Two physical forms of PS scintillator (sheet and pellet) were tested in the device with four concentrations of tritiated water ranging from 4 Bq mL⁻¹ to 300 Bq mL⁻¹. This resulted in a detection efficiency of 3.64×10^{-5} CPS Bq⁻¹ and 3.11×10^{-4} CPS Bq⁻¹ for sheets and pellets respectively.

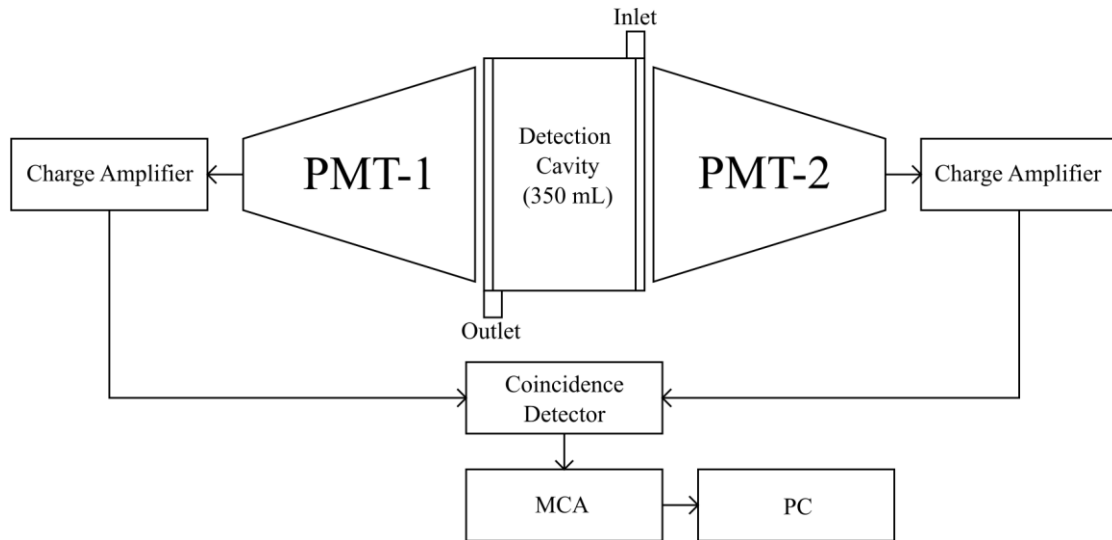


Figure 2.28: Diagram of sheet/pellet detector, re-created from paper [82].

Temperature control is also discussed in the paper. Peltier coolers have been implemented to keep the photomultipliers at 5°C to 10°C, although it is not discussed how this Peltier cooler has been implemented. It is speculated that the metal case of the detector is being used as a heat sink.

2.7.18 Advanced Blind-Tube Monitoring Instrument

Research by Elísio et al. [83] investigated and implemented a CeBr_3 scintillator detector placed into a 75 mm diameter blind-tube test bed to detect subsurface radioactive plumes. Experiments involved the use of two sealed gamma sources, caesium-137 and europium-152, showing that the detector can indeed detect the characteristic photopeaks. Additionally, the angle of the source in relation to the face of the detector had a measurable impact on the detected count rate with a maximum count rate measured at zero degrees (head-on).

The detection of bremsstrahlung radiation from a strontium-90 source was demonstrated while the detector was within a carbon steel tube. The strontium-90 source was fixed to the outer tube wall while the detector was placed within the tube [83].

2.8 Scintillator Comparison and Selection

There are many scintillators on the market aimed at detecting beta decay, with a smaller proportion suitable for low energy beta detection. Ideally:

- A material resistant to moisture is required for a waterborne beta source to be placed in direct contact.
- Non-intrinsically radioactive scintillator is preferred. As any additional energetic decay can easily overshadow low energy beta decay, and greatly increase background.
- The peak wavelength of the scintillator should be as close as possible to the peak sensitivity of the SiPM.
- The density of the scintillator should remain low to reduce interactions with cosmic rays.
- Light yield should be maximised to increase the probability of photons reaching SiPM.

Based on a comparison of scintillators from Advatech [84] (see Appendix F) $\text{CaF}_2(\text{Eu})$ and plastic scintillators possess the properties most ideal for waterborne low-beta detection and therefore will be a focus for this work. While there are many plastic scintillators, BC408 has been shown to be capable of detecting beta decay from tritiated water [85] and so will be tested alongside $\text{CaF}_2(\text{Eu})$. Of note is the fact that the luminescence efficiency of $\text{CaF}_2(\text{Eu})$ has a negative temperature dependence [86] which has also been shown for a range of plastic scintillators [87]. As a result, keeping the scintillator at a constant temperature will be of interest to ensure counts from background and low energy betas remain constant from measurement to measurement.

2.9 Silicon Photomultiplier Devices

The detection of beta particles and gamma rays using scintillating materials has become a standard technique. Classically, photomultiplier tubes (PMTs) have been integrated with the scintillators for photon detection, but more recently SiPMs have been a popular alternative despite the effects of temperature-induced drift in the gain given a constant bias voltage [88].

SiPMs are light-sensitive devices containing many individual light-sensitive microcells which each contain an avalanche diode and quenching resistor. When a photon strikes the diode, it conducts for a short period before being reset. These devices consist of thousands of microcells where multiple microcells can be activated simultaneously, resulting in a current spike proportional to the active number of microcells. SiPMs are preferred over PMTs in some applications, as they are not sensitive to magnetic fields and are compact. In addition, SiPMs require lower bias voltages to operate and therefore are more suitable for handheld counting and in-situ isotope detection where power infrastructure is limited.

This section will give a summary of existing SiPM devices to identify a suitable device for use in the detector design. But firstly, the technical aspects need to be outlined for a fair comparison to be made:

- Fill factor, given as a percentage, quantifies how much area of the SiPM's face is sensitive to incident photons, this is because each pixel has its own quench resistor and other supporting infrastructure (bonding wires) which are not sensitive to light. The greater the fill factor, the higher the probability an incident photon is detected.
- Package type, not all package types are as easy to handle and solder as others and different soldering techniques are required based upon this type.
- Photon detection efficiency (PDE), given as a percentage, is a measure of the probability a photon incident with the SiPM will be detected. PDE varies depending on the wavelength of the incident photon and so is normally defined for a given wavelength and bias voltage.

Broadcom is a world leader in semiconductor design and supply. They offer a range of SiPMs including the AFBR-S4N44P163 and AFBR-S4N66C013. The former is created from an array of smaller SiPMs that have been soldered onto a backing medium to provide a larger area of sensitivity. The latter consists of a single part with a size of 6 mm by 6 mm, a fill factor of 77% and a typical PDE of 44% at 420 nm [89]. The single part has a ball grid array package type that can be difficult to solder.

Onsemi is another world-leading semiconductor manufacturer offering two main lines of SiPMs. The first are C-series which are offered in both 3 mm by 3 mm and 6 mm by 6 mm package footprints, they have a fill factor of 64% and a PDE of 41% at 420 nm [90]. This part was selected as it has four square pads that can be soldered using a soldering iron or hot plate, it has also been previously integrated into scintillator detector systems [33], [60] which have been discussed in this work.

2.10 Silicon Photomultiplier Temperature Compensation

Methods

Dark noise hereby referred to as dark pulses is the main source of noise that affects SiPMs, dark pulses occur randomly at a rate dependent on the overvoltage of the SiPM, which itself is affected by temperature. Therefore, to keep this noise at a constant rate (i.e. to have a consistent background count rate) the overvoltage must be adjusted as temperature varies, for further details on the mathematics of temperature compensation see section 3.9.

To date, multiple methods for the temperature compensation of a SiPM have been investigated and implemented, this thesis will focus on three types taken from two publications. The schematics of each have been combined and are shown in Figure 2.29.

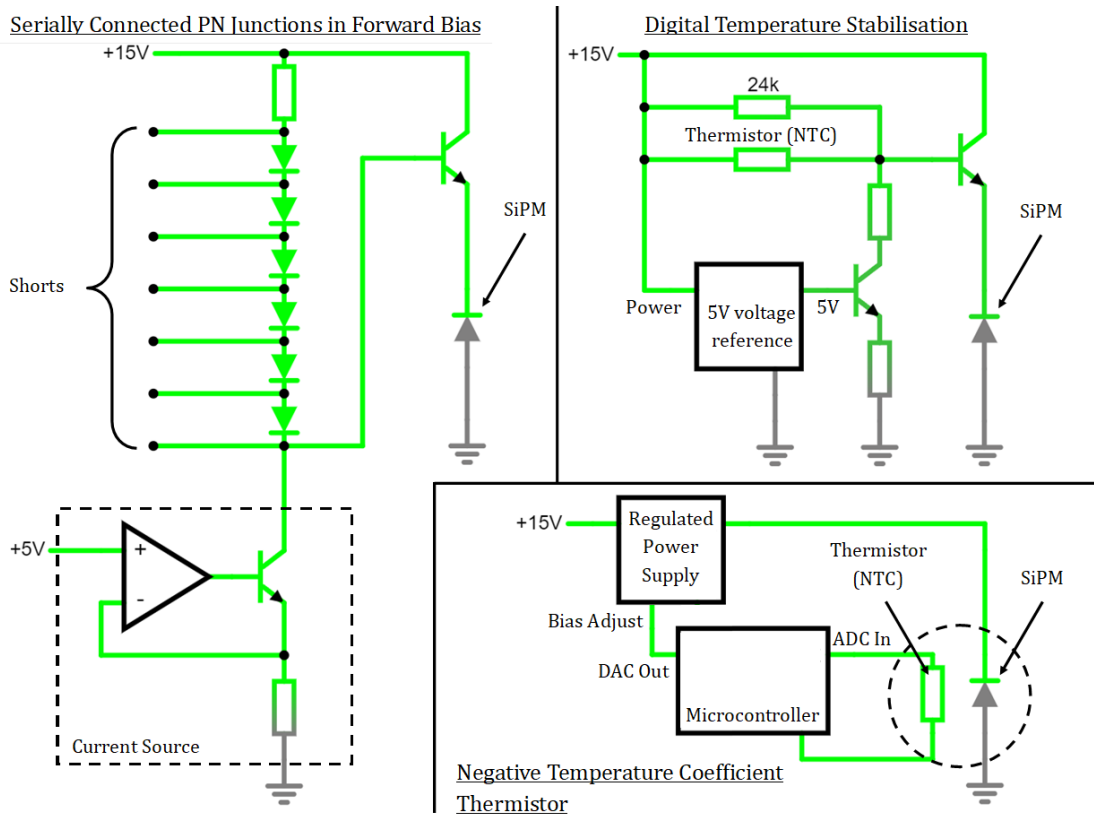


Figure 2.29: Simplified schematics of three existing SiPM temperature stabilisation methods. Left shows serially connected PN junctions in forward bias, top right shows analogue thermistor control [91] and bottom right shows digital thermistor control [92].

Starting with serially connected PN junctions, this design [91] is developed towards integration on the silicon itself along with the SiPM, allowing the temperature sensing component (the PN junctions) to be in close proximity to the SiPM substrate itself, a downside of such a design is the difficulty of getting custom silicon manufactured and means that existing well-characterised SiPMs like the C-series or J-series could not be used.

Implementing a digital control system as proposed by Ivanovs et al. [92] would involve the addition of a microcontroller to take current readings of a thermistor which is then digitised and used to adjust the output of a DC/DC converter integrated circuit (IC). Compared to the other fully analogue methods adding a microcontroller would add further complexity with the further possibility of software faults and switching noise. Another similar implementation [93] uses an ADT7310 digital temperature sensor connected to an Arduino microcontroller to again adjust the bias voltage placed across the SiPM.

Implementation of a negative temperature coefficient (NTC) thermistor using a purely analogue-only system has also been previously discussed [91]. Instead of digitising the thermistor current, the resistance is used directly to vary current through a bipolar transistor which then regulates the voltage placed across the SiPM.

2.11 Conclusions

In reflection of the existing low energy beta detectors discussed, an overwhelming majority use scintillators coupled to PMTs where sample flows in direct contact with the scintillating material. Furthermore, all but one PMT systems use coincidence counting to reduce noise and improve the identification of low energy betas. Some systems have been shown to improve detection rates by heating and boiling samples into steam which is then passed through a proportional counter. But looking at the feasibility of evaporation for in-situ implementation, such systems would be unsuitable due to the limited battery life being unable to supply the high power necessary to continuously boil water, and the fowling that would occur as impurities in the sample are left behind on the heating element. Furthermore, there is a greater risk of contamination and exposure working with a radioactive gas as opposed to a liquid sample.

For scintillator-based detectors, $\text{CaF}_2(\text{Eu})$ is the most implemented due to it having no intrinsic radioactivity and being non-hygroscopic. It has also been shown that this glass-like material can be easily crushed into a powder allowing its properties as a powdered scintillator to be easily studied. This aligns with a comparison of scintillators from Advatech which finds $\text{CaF}_2(\text{Eu})$ to be ideal but also suggests that a plastic scintillator could be a viable alternative. The plastic scintillator BC408 has been selected for further discussion and testing based on its prior implementation within a beta detector.

All but three discussed scintillator-based systems implemented PMTs to detect photons, with the others implementing a single SiPM showing that replacing PMTs with SiPM could be viable. A downside is that multiple SiPMs would have to be

implemented to match the area of sensitivity offered by existing PMTs. SiPMs come in a vastly smaller package size compared to PMTs which offers an advantage for implementation in such limited space as found within the boreholes typically found on nuclear licenced sites.

Overall, there is a lack of discussion on the inclusion of temperature compensation systems, as even though PMTs are more resistant to temperature changes compared to SiPMs, the scintillators alone will still be affected by temperature. As a result, changes in the measured count rate caused from a change in ambient temperature could be mistakenly correlated with the addition and detection of radioactivity, therefore the design of the new detector will include a temperature compensation system to help mitigate this problem. Existing temperature compensation techniques discussed show that a fully analogue system is possible with all systems adjusting the voltage across the SiPM based on the feedback from a temperature sensing device.

Based upon the findings of the literature review the following design decisions for the final detection system have been outlined, influenced additionally by the restrictions of the borehole in-situ environment and the objectives of the research:

- A continuous sampling system using a flow cell to allow liquid samples to flow in and through the detector without needing to pause or prepare multiple sample batches.
- Use of a scintillator placed in direct contact with the sample. All existing systems using scintillators placed them in direct contact due to the low path length of low energy betas.
- Implementation of SiPMs as a replacement for PMTs. This will greatly reduce the overall size of the detection cavity, allowing its integration into the limited borehole diameter.
- Use of a coincidence counting system to reduce thermal and shot noise. Almost all systems detecting in the low energy range incorporate such a system commonly with PMTs.

- Addition of a temperature compensation system to actively counter the changes in the gain of the SiPM(s) caused by the varying temperature of the environment.
- Flexibility to add filters and sterilisation systems in line with the detector to remove particulates like soil and grit before entering the detector to reduce the rate of fouling.
- On-board memory to store large volumes of recorded data without the need for a constant connection to an end-user.

3 Backend Electronics

3.1 Introduction

After reviewing existing low energy beta detectors and selecting a scintillator-based detector as the ideal choice, development can be done on a backend system which will interact and link all parts together. Along the way, decisions have been made on selected electrical components, field programmable gate array (FPGA), data processing algorithms and temperature compensation. Multiple experiments will also be performed with light emitting diode (LED) blinking and sealed gamma sources to validate and characterise the developed system.

3.2 System Outline

The block diagram depicted in Figure 3.1 shows the structure of the developed backend system, from the scintillator-based detector through to the method of retrieving data using a wireless fidelity (Wi-Fi) network. Each square represents a discrete part of the system with the following functionality of key areas:

- The Zener Diode Temperature Compensation system has been developed to counter the drift in the gain in the silicon photomultipliers (SiPMs) due to temperature changes.
- A Bias Supply Low-pass Filter is used to remove high-frequency noise from the supply of the SiPM.
- A SiPM Array Board is a circuit board developed to hold a maximum of 17 SiPMs in an array in contact with the scintillator.
- The Two stage SiPM Amplifier converts current pulses from the SiPM into pulses of voltage that can be digitised for further analysis.

- The Re-Biasing Circuit removes dark voltage and adds a set bias to maximise the analogue to digital converter (ADC) range.
- Channel 1 & 2 ADCs are integrated into a circuit board with the FPGA to digitise pulses from the SiPM.
- The Trapezoidal Shaper is a digital algorithm implemented in a very high-speed integrated circuit (VHSIC) hardware description language (VHDL) to process pulses from SiPM into a suitable spectrum.
- Spectrum Memory is internal FPGA memory that holds the channel data, recording the number of interactions detected and their corresponding energy levels.
- Python Script: Spectrum Receive and Store listens for spectrum data collected by the FPGA, formatting it into a MySQL database, while a second script running on a remote PC queries the database to obtain the stored spectrum data.
- The MySQL Database: Spectrum Table database holds every spectrum taken at a set rate (every 1.34 seconds or 21.48 seconds), allowing a record to be kept and accessed wirelessly at a later point.
- With an End User Computer, an end user can access the database and retrieve the spectra data via a private network and then visualise it using a developed Python script.

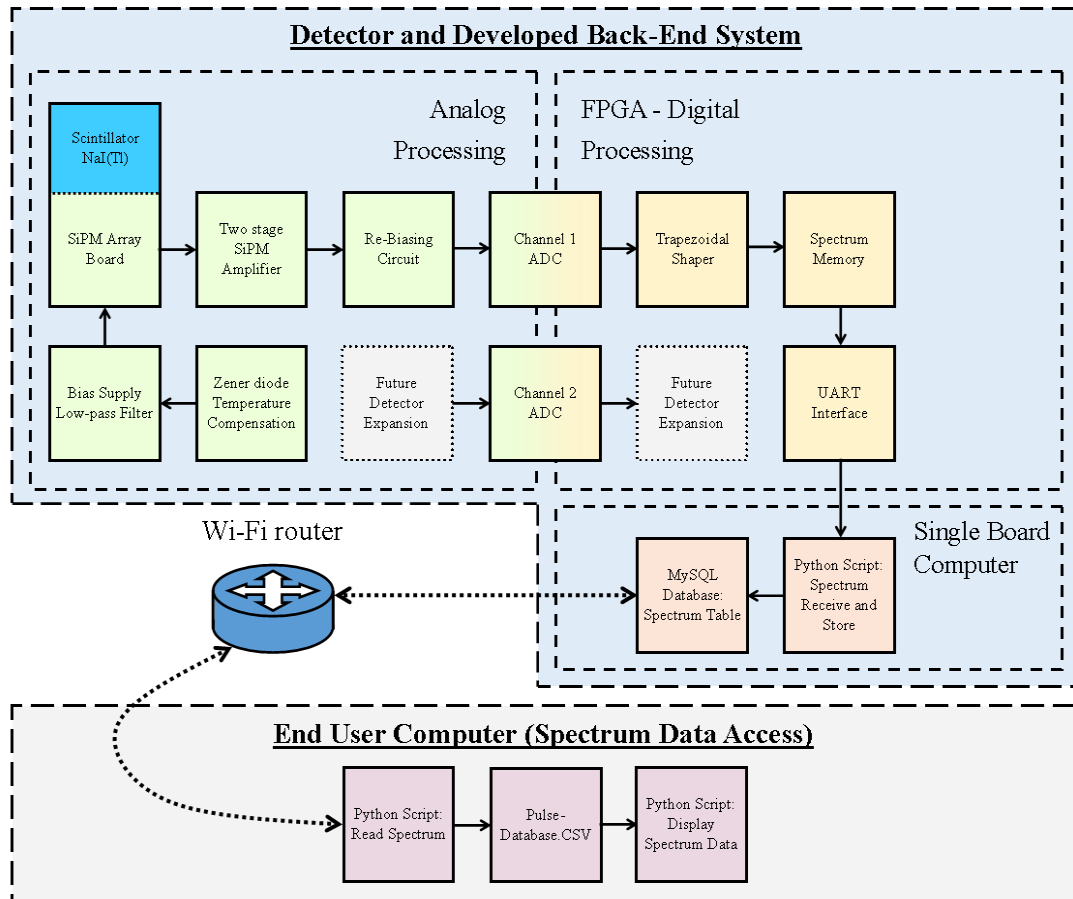


Figure 3.1: Block diagram of the whole backend system including the digital processing and database access method. An encapsulated NaI(Tl) Scintillator has been included for testing with sealed sources (see section 3.11).

3.3 Early Electrical Design

The early attempt at a radiation detector used an Arduino Uno microcontroller [94] attached with circuitry (see Figure 3.2) to detect pulses emitted from a C-Series SiPM. This design was used in the potassium chloride (KCl) testing with the 3D printed flow cell discussed in section 4.9. Key parts of the design include:

- SiPM Bias filter: A second order RC low-pass filter used to remove noise from the SiPM supply.
- Transimpedance amplifier: Converts the spike in current flow from the SiPM into a voltage pulse.
- Comparator: Compares the voltage of the pulse to a threshold voltage set by a potentiometer. If the pulse voltage is greater than the threshold the

output of the comparator will set to ground (used as an interrupt for the microcontroller).

- Peak holder: Holds the peak voltage of the pulse while the microcontroller reacts to the interrupt.
- Output buffer: Used to isolate the peak holder from interference and provide a gain to the signal to maximise the voltage range of the ADC.

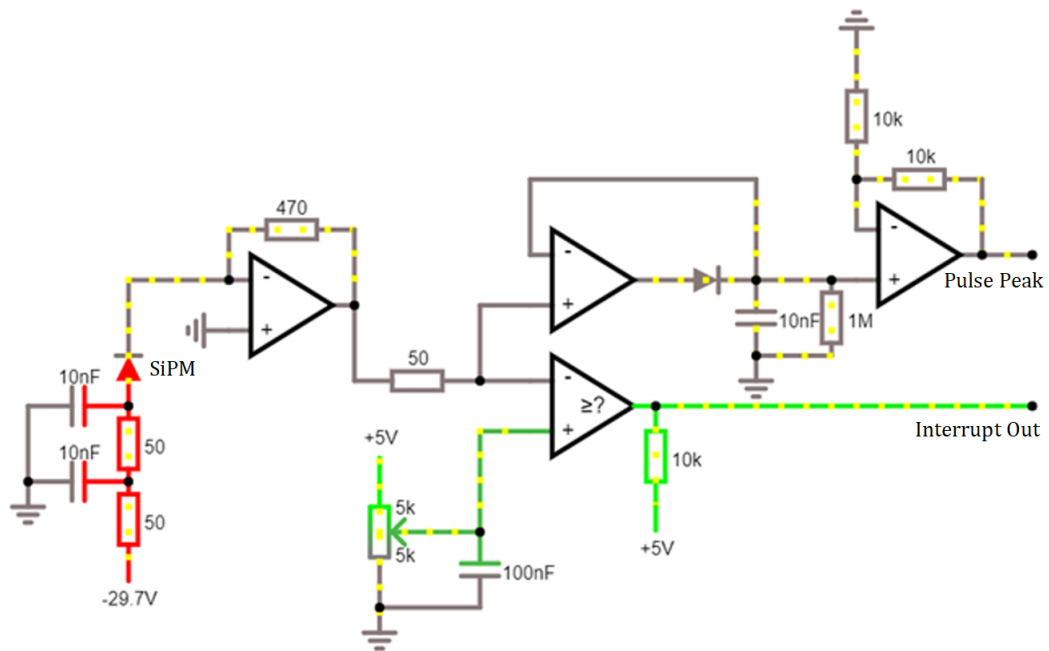


Figure 3.2: Schematic of early SiPM amplifier created in Falstad [61], peak holder, and pulse height comparator for detection with Arduino Uno.

The design of this initial detector circuitry is partly based on a single channel of three-layer neutron detector designed and built by Hamrashdi et al [95] and the CosmicWatch project [60].

The comparator output of the circuit was fed into an interrupt pin of an Arduino Uno, another analogue input pin was connected to the output buffer of the peak holder. When a pulse meeting the threshold set by the potentiometer occurs, an interrupt is sent to the microcontroller causing it to react by taking a voltage reading of the peak holder, this reading was then sent via serial to a laptop where it could be collected and displayed as a spectrum.

3.4 Field Programmable Gate Array Selection and Compaction

Field programmable gate arrays (FPGAs) are well suited to completing repetitive tasks quickly, whether that is calculating results to equations, running algorithms, or requesting data from peripherals, FPGAs also offer much higher flexibility compared to complex programmable logic devices (CPLDs). Therefore, the implementation of a FPGA a natural choice for the processing of ADC data. Linking back to this application, the major limitation when selecting a FPGA is its physical size as the board must fit within approximately 42 mm and an input or output (I/O) pin count greater than 28 would be needed to implement at least a dual 14-bit parallel output ADC as each voltage measurement taken by the ADC would require 14 pins in order to transmit the reading per clock cycle, and so for two ADCs running simultaneously, 28 pins are required to receive both readings per clock cycle. These limitations in combination lead to a cyclone II FPGA being used with one stipulation, the board would have to be modified. The modifications (shown in Figure 3.3) involved removing two rows of headers along with the joint test action group (JTAG) and active serial (AS) programming header and main voltage regulator. As a result, the board was reduced from a width of 73 mm to a width of 38 mm, a size that would fit within the detector casing.

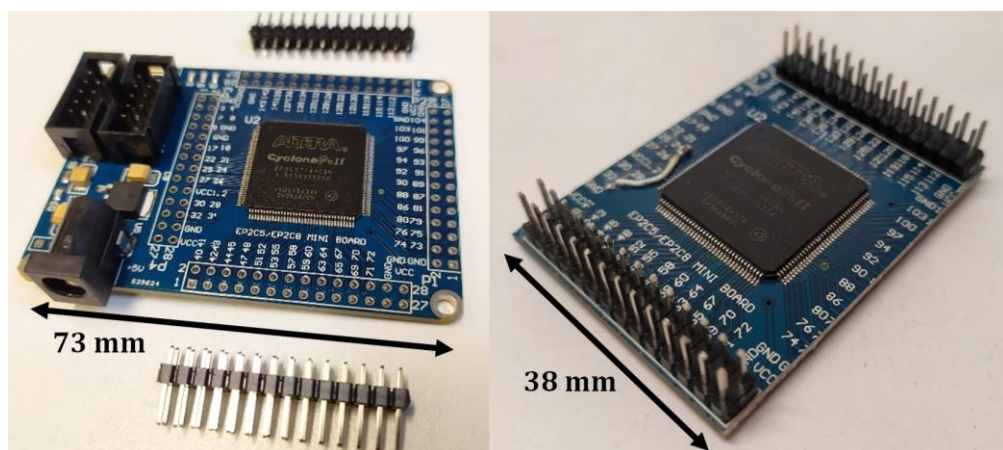


Figure 3.3: Image of FPGA before (left) and after (right) hardware alterations.

As the AS header was removed, to update the FPGA code the serial configuration IC (EPCS4SI8) had to be desoldered, reprogrammed in an unmodified board, and then resoldered using a hot air gun. The modified board has a total of 46 I/O pins that can be programmed meaning that these pins can be electrically connected to the parallel data output of both ADCs with additional pins that can be used for configuration of the ADCs and serial communication for transmitting recorded spectra (see Figure 3.12).

3.5 Silicon Photomultiplier Amplification Design

Here, SiPMs (C-series by Onsemi) [90] have been utilised, which possess a high readout gain of 3×10^6 . To amplify the SiPM output, a transimpedance amplifier is used to convert the produced pulse of current into a measurable voltage pulse that can then be digitised by an ADC for further processing. The amplification board schematic is shown in Figure 3.4, where the EL5171 op-amp [96] has been implemented, as it can be configured as a single input/dual output transimpedance amplifier.

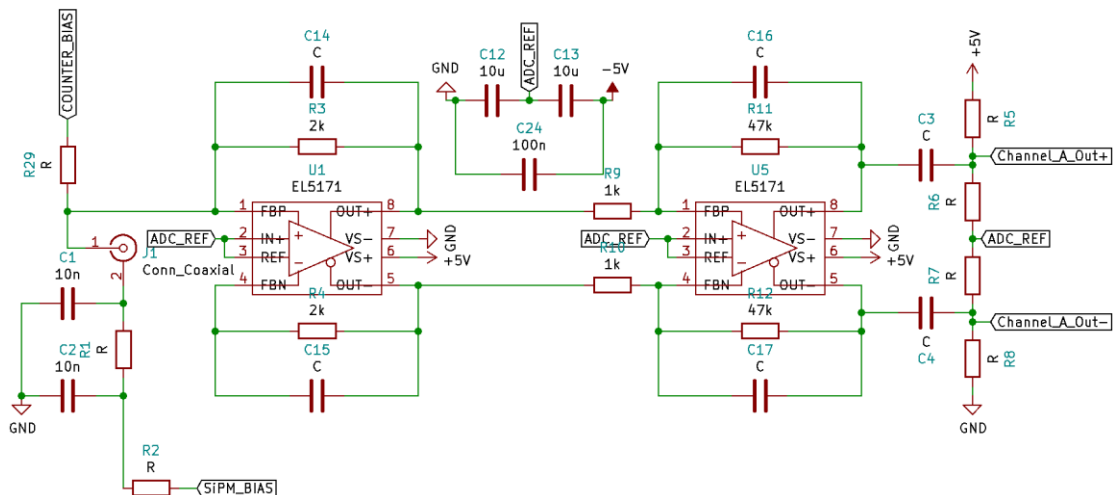


Figure 3.4: Two stage EL5171 op-amp based amplifier. The first stage is a transimpedance amplifier with differential output, and the second phase is an inverting amplifier.

The two 50 Ω resistors (R1 and R2 in Figure 3.4) and 10 nF capacitors (C1 and C2 in Figure 3.4) form a second order low-pass filter to reduce noise on the bias supply, which could be further introduced into the amplifier pulse signal. Resistors

setting the gain of the first and second stage inverting amplifiers were selected through experimental calibration to maximise the ADC range but not result in the clipping of the detected pulses. Capacitors have been added into the feedback of the amplifiers to act as low-pass filters with a frequency cut-off at 723 kHz and 1.54 MHz; as a result, this stretches the pulse, allowing more samples to be taken of its shape by the ADC board, as well as blocking high frequency noise.

Between the second stage of amplification and the ADC, a re-biasing circuit has been added, this blocks the SiPM's dark current, which has been amplified into a voltage. This addition also adds a set DC bias difference of -0.893 V, which allows a greater range of the ADC's input to be used, which has a peak-to-peak range of 2 V. It should be noted that the ADC reference voltage has been configured to be 1.5 V on the ADC board. The manufactured SiPM amplifier can be seen in Appendix C (see Figure C.9).

3.5.1 Electrical Noise Reduction Methods

When designing electrical systems for detecting low energy betas, reducing electromagnetic interference introduced into the pulse signal is of even greater importance, as only a few photons will reach the SiPM resulting in little current flow through the device. Therefore, this detector design has implemented twisted pairs to transfer pulse signals from the amplifier to the ADC.

Twisted pairs offer much greater resistance to electromagnetic noise as opposed to single ended signals, as two separate wires carry the pulse signal and its inversion. By taking the difference at the ADC, any noise that has been introduced to both wires is cancelled out, leaving only the original pulse signal.

Another benefit of using differential outputs is speed. Operational amplifiers (op-amps) have a maximum voltage slew rate which is a measure of how fast the output can respond in a given time (usually defined as $V \mu s^{-1}$). By splitting the signal in twine, only half the amplitude is required for each wire, and hence a lower slew rate can be used without degradation of the signal.

For the negative bias supply, a common mode filter was added directly after the variable voltage supply to remove high frequency noise. This inductor pair was created using a 1:1 transformer with each coil having an inductance of 300 mH. To quantify the benefit of such an addition, an LTspice simulation was created and used to plot a noise rejection amplitude plot. A sine wave with a frequency varying from 10 kHz to 100 kHz was injected into the SiPM bias supply to see how much signal would be attenuated and its dependence on frequency.

Figure 3.5 shows the circuits simulated, only the SiPM power supply and temperature control system (discussed in section 3.9) have been included. Figure 3.6 shows the resulting plot of the noise magnitude seen at the SiPM anode against input frequency. The voltage at “Vbias” has been taken as the output for the system without a common mode filter. And the voltage at “Vbias2” has been taken as the output with the addition of a common mode filter. These outputs come after the second order SiPM bias filter which connects directly to the SiPM anode.

Interpreting Figure 3.6, there is a clear reduction in high frequency noise passing through the SiPM supply with the addition of a common choke. At a frequency of approximately 410 Hz there is a resonance peak of -43.7 dB caused by the choke in combination with the decoupling capacitors, resulting in less noise rejection, but this quickly drops below having no choke at approximately 636 Hz.

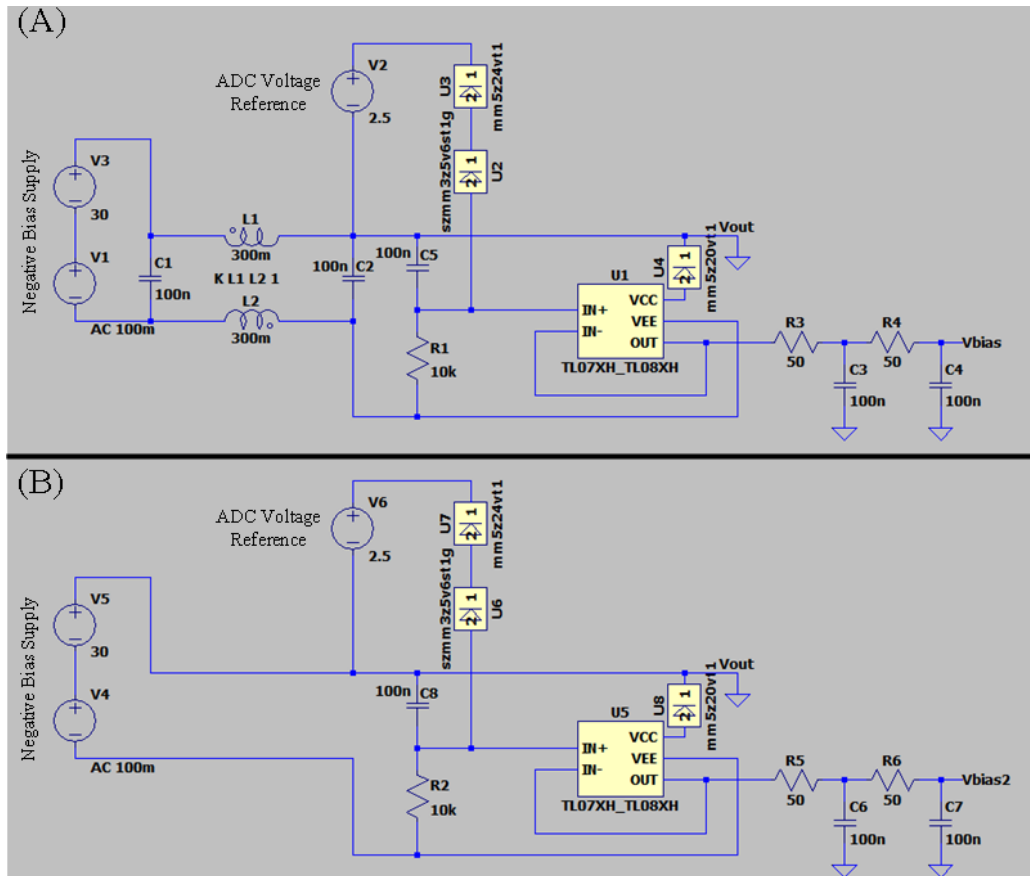


Figure 3.5: Simulated LTSpice schematics used to study the effectiveness of adding input filtering: (A) With common mode filter on negative bias supply, (B) without common mode filter on negative bias supply.

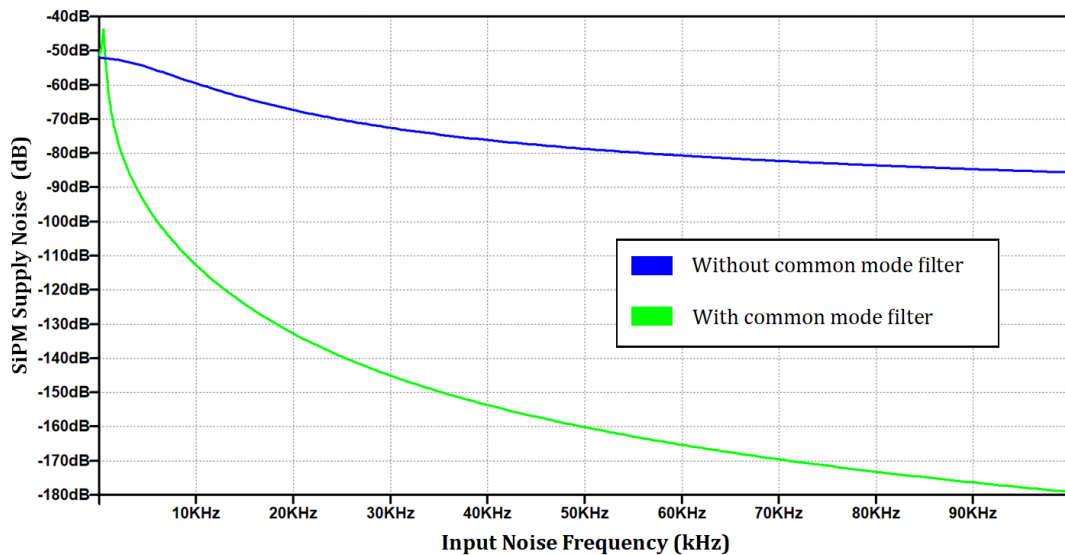


Figure 3.6: Simulation of schematics in Figure 3.6. Green trace is from the output of circuit (A) with common mode filter. Blue trace is from the output of circuit (B) without common mode filter.

3.5.2 Alternative Amplifier Designs

Over the development period multiple circuits were designed and tested, this section discusses some of the designs that were investigated but were unsuitable for the detection system or replaced by the final modular design. The prototype and final amplifier boards all use two gain stages, where the first stage is a transimpedance amplifier and the second is an inverting amplifier.

Figure 3.7 shows a prototype that combines both the sensor head and amplifier together onto a single printed circuit board (PCB). Three separate amplifier channels allow three SiPMs to be amplified independently, lowering the overall capacitance compared to if the three SiPMs are placed in parallel, this would be beneficial for pulse shape discrimination as the fast rise time and shape of the scintillator pulse would be preserved [97]. A difference between this and the final amplifier is the use of a single ended first stage (pulse signal is carried over one wire) which feeds, along with the other channels, into the differential output second stage (pulse signal and its inverse is carried by two wires). This three channel design did not incorporate any switches to quickly vary gain and filter settings and so was not used in the final detector.

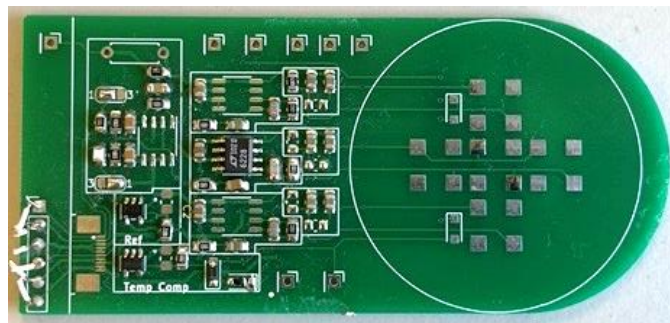


Figure 3.7: Image of early SiPM board design incorporating both sensor head and amplification into a single board.

Another unused design, Figure 3.8, was to be connected with three SiPMs placed directly in parallel. Surface mount flat flex cable (FFC) connectors were added to allow integration with the laminated flow cell sensor heads discussed in section 4.11 and rotary switches to allow quick configuration of the gain and filters. Both alternative designs suffered from instability issues caused when

converting the pulses into a differential signal, this could be due to poor selection of components or too low of a feedback capacitance which increases stability.

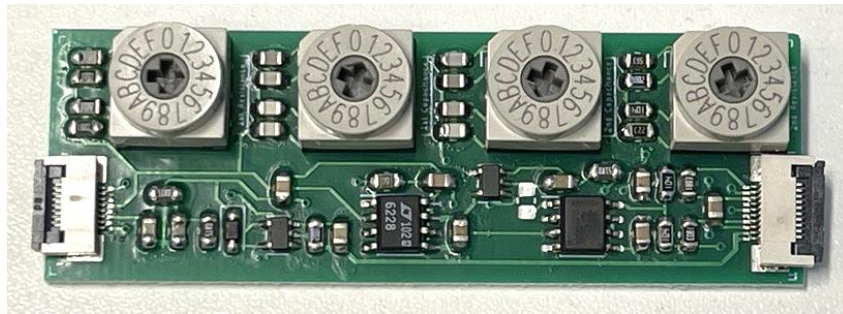


Figure 3.8: Image of unused prototype SiPM amplification board, using easily accessible gain adjustment switches. These switches were used again for the final amplifier design. Two connectors connect to the ADC board and SiPM sensor head.

3.6 Analogue to Digital Converter Board Design

To digitise the pulses from the SiPM amplification board, a digitiser board utilising 14-bit analogue to digital converters (AD9244 [98]) was used, the use of this IC has included applications such as monitoring in high-intensity heavy-ion accelerators [99] and within a calibration system for Muon experiments [100]. The ADC interconnection board was designed, manufactured, and integrated into the detector to run at a sample rate of 50 mega-samples per second (MSPS). Two ADCs were included, allowing for the possibility of two separate channels operating simultaneously, providing an improvement over systems such as the Topaz-SiPM [101], which only has one input channel without an option to add an additional channel. Compared with another similar FPGA-based wireless gamma spectrometer [102], the system developed here has a higher resolution ADC, whilst also having a greater sample rate.

An EP2C5T144 Altera Cyclone II FPGA soldered onto a minimal development board was used for running the ADC communication, serial communication, and pulse shaping algorithms. The ADC board fits atop the FPGA minimal development board to be as compact as possible and has added connections for +5 V, +3.3 V, ground, input pairs for each ADC, a voltage reference output, and a UART interface for sending data to the single board computer, a Raspberry Pi Zero 2 W. A

photograph of the dual ADC board attached to the FPGA board can be seen below in Figure 3.9.



Figure 3.9: Image of a manufactured ADC board, populated with two AD9244 ADCs and supporting circuitry, sitting on top of the Cyclone II minimal development board. A one pound coin is shown for scale.

While powered, the FPGA and two ADCs pull approximately 220 mA, with a further 260 mA used by the single board computer, and less than 1 μA used by the SiPM negative bias. For communication between the FPGA and ADCs, two headers provide two 14-bit parallel data buses and connections for the clock stabiliser, out-of-range indicator, and data format pins for configurability.

3.7 Pulse Data Processing

There are multiple methods of detecting and measuring the characteristics of pulses emitted by an amplified SiPM. Past research has investigated the use of trapezoidal and triangular pulse shaper algorithms that take the digitised samples of exponentially decaying pulses and convert them into another form that can be more easily analysed [103].

FPGA-based digital pulse processing systems have been implemented previously at The Chengdu University of Technology [104] using commercial off-the-shelf (COTS) data acquisition boards with footprints of 193 mm by 122 mm and wired USB connections to upload data to a host's computer. Multiple shapers were implemented with different "fast" and "slow" shaping constants so that multiple

pulses that overlap (double counts) can be identified and removed. As this detector is expected to work with very low activities, double count removal will not be included at this prototyping stage.

Researchers from Chung-Ang University used a commercial FPGA evaluation board integrated with an ADC board within a PC case [105]. This work had an inherent deadtime where pulses were ignored while the convolution process was unfolding, limiting count rates to approximately 1,500 pulses per second. A further example used a Digitiser XtremeData board containing both FPGA and ADCs [106]. A paper by Marques et al published in 2021 [107], compiled commercially available lightweight spectrometers; of the devices discussed in the paper, only the Raspix by Crytur has Wi-Fi built in, but this device is unsuitable for use within a 50 mm cylindrical diameter, limiting its possible applications. The listed costs are also far higher than the costs to produce the device detailed here.

Here, a trapezoidal shaping algorithm has been implemented [103] in VHDL within the Cyclone II FPGA and AD9244 ADC to create and store energy spectra formed from the pulses emitted by the SiPM. The key variables that affect the output of the shaper are three sequential sample delays that will be referred to as simply delay one, delay two, and delay three. The implementation of these delays within the algorithm can be seen in the block diagram of the trapezoidal shaper (Figure 3.10).

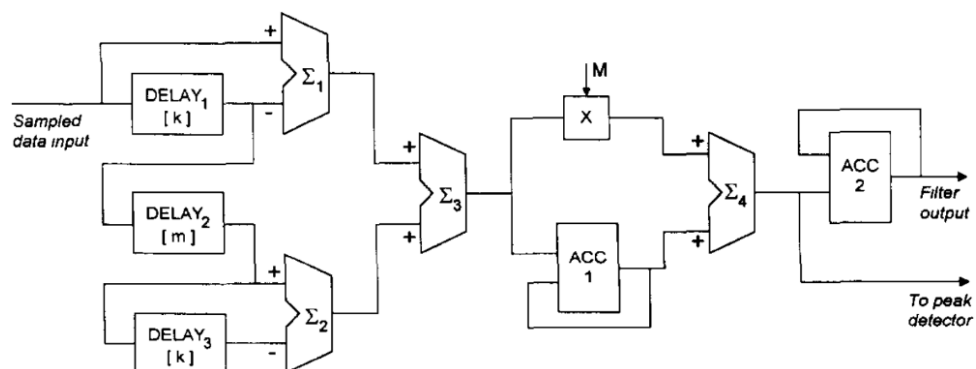


Figure 3.10: Block diagram of trapezoidal shaper algorithm. Showing the implementation of the three sample delays [103].

Also present is a threshold value that dictates when a pulse is present above a background of noise, and finally an M coefficient that is used for zero pole

cancellation, which depends on the exponential decay time of the SiPM pulses (τ) and the sample period of the ADC (T_{clk}) [108], the formula for this calculation is shown as equation (3.1).

$$M = \frac{1}{e^{\frac{T_{clk}}{\tau}} - 1} \quad (3.1)$$

From viewing output pulses from the SiPM amplifiers, the decay coefficient was obtained to be approximately 4.32 μ s. Given that the ADC samples at a constant frequency of 50 MHz, the M coefficient for the system can be calculated, shown by equation (3.2).

$$M = \frac{1}{e^{\frac{20 \text{ ns}}{4.32 \mu\text{s}}} - 1} = 216 \quad (3.2)$$

3.7.1 Spectrum Accumulation

In this mode of operation, a two port random access memory (RAM) module is implemented on the FPGA, which allows for both the writing and reading of 16-bit values simultaneously at two different clock frequencies. When a pulse is emitted by the SiPM, it is amplified, digitised, and shaped; the peak value of the shaped pulse is then used as the address for recording that interaction. Proceeding a set delay after the pulse threshold trigger, the current count stored in the address of the peak value is read. On the next clock cycle, the read count value is incremented by one and then written at the same memory address, thereby representing a recorded interaction at that energy.

Figure 3.11 shows a finite state machine (FSM) of this memory writing process. While the output of the shaper is below the threshold the FSM continues to wait and repeatably checks the output value (SUM_4) against a threshold. When the threshold is met a pulse has been detected and so the state changes to “Run”, in this state each value is being compared to find the height value (peak of shaped pulse) which is then used as the memory location (channel) for accessing RAM. This RAM access preformed when moving from the “Run” state to the “Update RAM” state, and incrementing the count for that channel is preformed when

moving from “Update RAM” state to the “Peak reset” state. Finally, the state returns to “Wait for pulse”, to wait for the next incoming pulse.

The output from the shaper algorithm produces a 32-bit integer which is divided down to 16-bits for the detected peaks to fit within the limited spectrum memory on the FPGA. This also allows the energy range to be adjusted to suit the energies of the different radiation sources the detector will be tested with, as the detector energy channels scale proportionally to the division factor. From here onwards, the division factor of 2^{18} will be referred to as zoom level 1 and 2^{17} referred to as zoom level 0.5. This VHDL code was simulated using Modelsim-Altera [109] before running on the detector hardware.

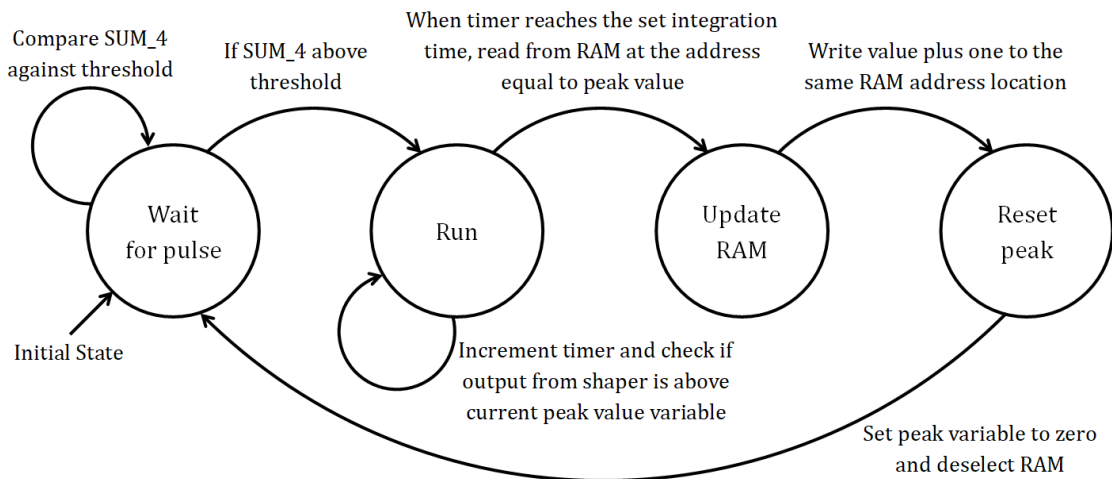


Figure 3.11: Finite state machine of the pulse peak storage system implemented on Cyclone II FPGA. Each transition occurs every clock cycle. The variable SUM_4 is the output of the shaper algorithm.

3.7.2 Spectrum Memory Serial Data Transfer

A second routine was implemented to process the saved interactions and convert them into a serial data transfer. This routine accesses the second port of the RAM module allowing it to read and write independently from the spectrum accumulation.

As the serial communication standard used, serial peripheral interface (SPI), can only send 8-bits in a packet at a time, a total of two packets were required to send each channel. The 16-bit value of each channel is separated into a lower and upper

packet for the first 8-bits and the last 8-bits respectively. Before any channel data is sent, a sync byte of 10000000 (base-2) is sent so that the receiving script and FPGA are sending and receiving bytes in the correct order. Figure 3.12 depicts the order of the bytes being sent from the FPGA.

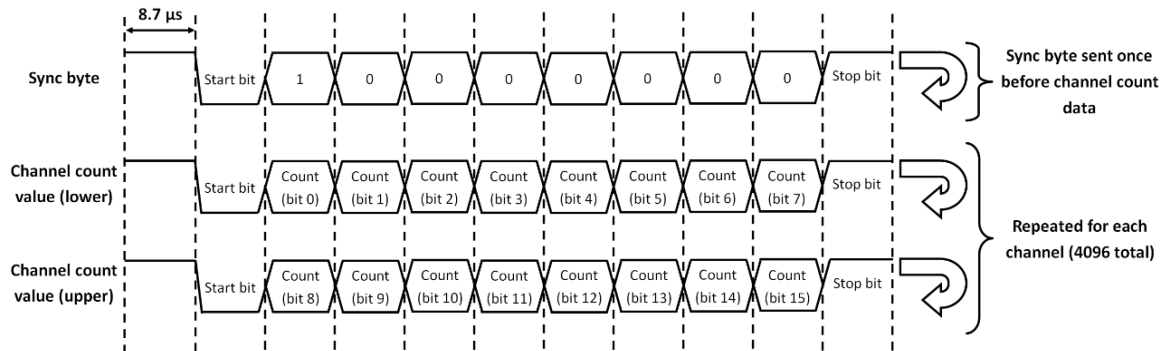


Figure 3.12: Timing diagram showing order in which channel data is sent from the FPGA to the single board computer (Raspberry Pi).

On the clock cycle the upper byte of a channel is sent, the channel count is simultaneously set to zero, signifying the start of the next exposure. Exposure in this context is used to mean that the channel is actively recording count data and hence is being ‘exposed to radiation’.

After all channels are sent, the routine enters a delay period called the exposure delay, this is to allow time for counts to be detected and accumulated, reducing the number of individual spectrums having to be stored in the database. The total active time a channel is counting for is the exposure delay plus the time taken to transmit all channels over SPI, see equation (3.3):

$$\begin{aligned}
 \text{Counting Period} &= \text{Clock Period} \\
 &\times (\text{Exposure Delay} \\
 &+ \text{Channel Count} \times 2 \times \text{SPI Transmit Cycles})
 \end{aligned}
 \tag{3.3}$$

$$\text{Counting Period} = 21.48 \text{ seconds}$$

Therefore, each spectrum transmitted from the FPGA SPI represents 21.48 seconds worth of measured counts. It should be noted that for early experiments (LED blink testing and sealed source gamma testing), a smaller

exposure of 1.34 seconds was used, this was increased in the later stages of experimental testing to reduce the volume of data having to be processed. All other detector experiments used an exposure time of 21.48 seconds.

3.7.3 Database Design and Implementation

As this detector is primarily designed for portability and in-situ use with minimal infrastructure, there is a need to provide a method of onboard data storage, as the end user may not always be available to retrieve data captured by the detector in real-time. A MySQL database was implemented in the detector to store the spectra data as it is streamed from the FPGA. MySQL is a well-suited Internet of Things solution, as multiple copies of this detector can be connected to a single network, each with a unique internet protocol (IP) address allowing access through a secure shell (SSH) connection.

The FPGA talks to the single board computer hosting the database using UART at a baud rate of 115,200 symbols per second. A preliminary exposure of 1.34 seconds was used for collecting each spectrum before the FPGA delivers the contents of the channel memory, and while doing so it resets every channel to zero, preparing for the next exposure. A Python script listens for this data, where it is then formatted and inserted as a new entry into the database as a binary large object (BLOB). When the user wishes to receive data wirelessly from the detector, the destination computer is connected to the same private network as the detector, and a second Python script on the destination computer queries each entry of the database, removing it afterwards. This queried data is then written into a comma separated value file (.csv) in a cumulative order.

The developed database has been tested up to a maximum table size of 161,717 rows of spectra data stored internally on the detector. The total count time for this data can be calculated using equation (3.4).

$$\text{Count Time} = \text{Database Rows} \times \text{Exposure Delay} \quad (3.4)$$

$$\text{Total Count Time} = 161,717 \times 1.34 \text{ seconds} = 216,700 \text{ seconds} = 2.51 \text{ days}$$

3.7.4 Pulse Visualisation with Bokeh

While manufacturing and testing the detector, noise reduction was a consistent priority and identifying noise from radiation pulses was of utmost importance. Therefore, a visualisation tool was created using Bokeh [110] a library for python [111] which can generate interactive plots and build powerful data applications. Bokeh produces hypertext markup language (HTML) files which allow processed data to be opened without Bokeh being installed and allows plots to be embedded in web pages. Bokeh visualisation can not only display captured whole pulses, but also sort pulses based on their fall time and peak. This allowed high frequency noise to be easily identified by measuring their fall time, Figure 3.13 shows a plot of background data containing noise, each point represents a captured pulse, where the y-axis is the measured fall time, and the x-axis is the pulse peak. By clicking on a point, the raw analogue samples for that pulse are displayed. Four points of high frequency noise have been highlighted in the figure.

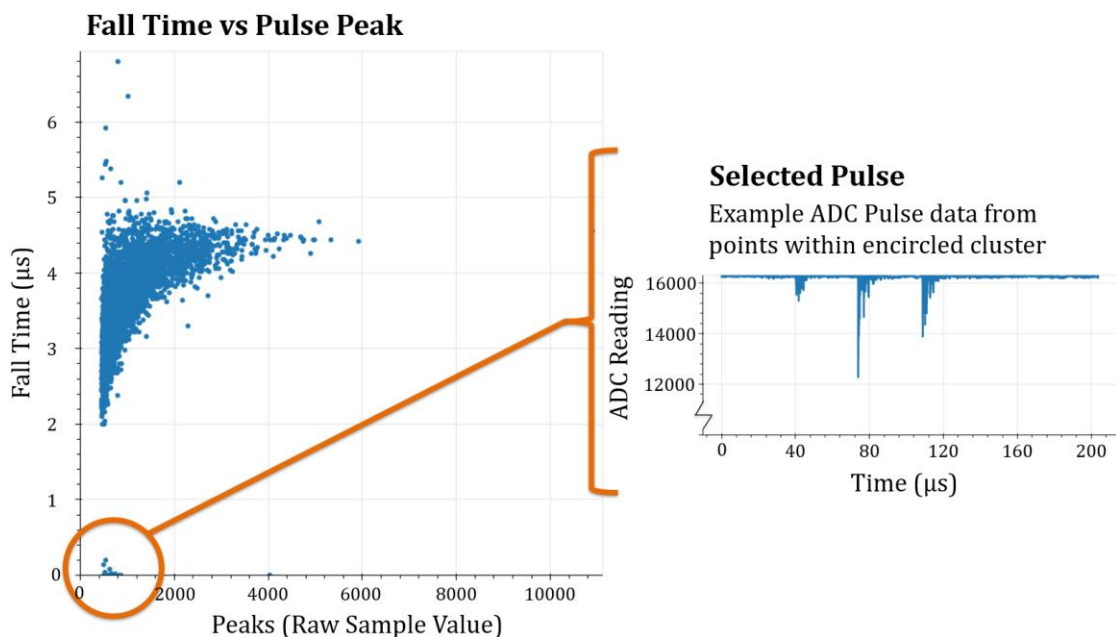


Figure 3.13: Example interactive Bokeh plot of pulse data captured of background, cluster highlighted shows electrical noise. One sample is equal to 20 ns.

Sources for this high frequency noise could be caused by radio interference. Periodically, while performing experiments with the detector bursts of noise would be seen after switching on fluorescent lights, therefore care was taken to run experiments at off-peak times (overnight).

To facilitate the storing of raw pulse data a new VHDL program was written for the Cyclone II FPGA. The heart of the program is two first in first out (FIFO) delays named 'lookback' and 'sample' which work together. The ADC is constantly sampling the input signal of the SiPM, even if no pulses are present. Before samples are discarded, they pass through the "Sample FIFO" and then are fed into the "Lookback FIFO". The sample that is being passed from the "Sample FIFO" to the "Lookback FIFO" is compared with a set threshold value. If the sample is above the threshold, the contents of both FIFOs are dumped into the UART serial interface. Any DC drift (caused from fluctuations in dark current of the SiPM) could not affect the pulse threshold as each differential input of the Analogue to Digital Converter (ADC) fed through a high pass filter (see Figure 3.4) which blocks DC.

This system not only allows samples after the threshold to be saved but also samples before the threshold is triggered allowing a full view of the pulse rise time and fall time. Figure 3.14 depicts how a saved pulse is assembled from the contents of both FIFOs.

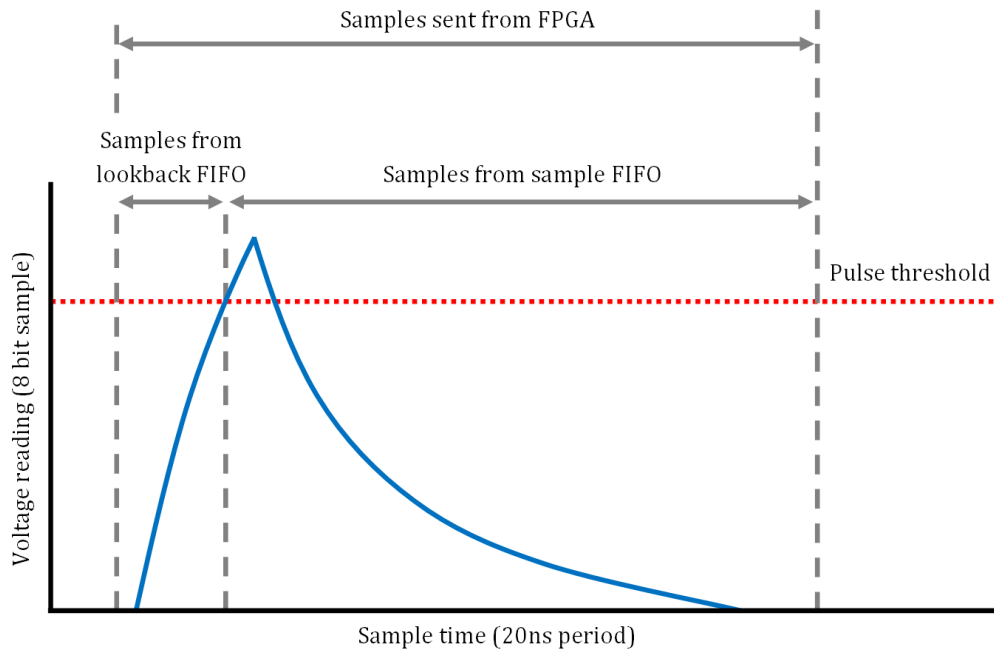


Figure 3.14: Graph depicting how the pulse is stored within the Lookback and Sample FIFO.

3.7.5 Spectrum Visualisation with FastSpec and Database Files

FastSpec is a visualisation software written purposely for this project in Python 3.9.6 [111] for the plotting of spectra data, error calculations and count data as recorded and stored by the detector, the program requires the data to be within a comma separated value (CSV) format. For plotting a spectrum data the python library matplotlib is used, matplotlib is a comprehensive library for creating many types of plots and can also add interactivity [112] similarly to Bokeh.

When the code is executed, it first opens and reads the contents of an input database (.CSV) followed by the contents of a background database (also .CSV). The counts in each background channel are then removed from the corresponding input channels hence removing background counts from the plotted spectrum. As the database files save counts cumulatively, to plot the spectrum requires only the last row to be read from each file as opposed to calculating the sum of all individual spectra recorded over the left of the experiment, reducing the overall processing time.

To convert the captured MySQL database data into a CSV file, another Python script is used. This script utilises the MySQL connector provided by Oracle [113] which allows search queries to be made to the database stored on the Raspberry Pi Zero while both computers are connected to the same network. From this each row within the database can be transferred cumulatively to a row within the CSV file, adding cumulatively allows FastSpec to plot a full spectrum without having to read every row of the CSV file. Each column represents a detector channel from 0 to 4,095.

3.8 Detector Resolution Determination Using Light Emitting Diode Pulse Testing

With the electrical system manufactured, spectrums could be recorded and collected for viewing. Here, the resolution of the captured spectra was benchmarked using light emitting diode (LED) pulse testing, similar systems have been implemented in previous studies characterising full width half maximum (FWHM) [114] and photon detection efficiency (PDE) [115]. This involves placing an LED in a set position above the SiPM, where it is fed voltage pulses to modulate the LED and thus test the efficacy of the SiPM detecting the bursts of light.

The blinker circuit was created on a breadboard and powered from a benchtop supply. The frequency of the blinking and the LED brightness were kept constant for all testing, to study only the effects on the recorded spectra caused by adding SiPMs and changing the delay constants of the pulse shaper. The LED was kept at a constant distance of approximately 5 cm from the SiPM within a light tight enclosure for the three experiments.

The light tight box had a hinge to open and close the container with an inset O-ring within the ridge to ensure no light could enter through the opening once closed. The blinker circuit consists of multiple NAND gates, hex Schmitt-Trigger Inverters and a 555-timer implemented with the schematic shown in Figure 3.15. The pulse duty cycle is set by the propagation delay of the two Schmitt inverters and the single NAND gate (140 ns and 24 ns respectively) thus the LED is powered on for a period of approximately 304 ns. The frequency of the blinking is set by the potentiometer R_POT and the brightness is set by R.

The LED blinking experiment was repeated a total of three times with one, two and three SiPMs to study the impact of varying numbers of SiPMs. Figure 3.16 shows the addition of each SiPM throughout the three sets of testing.

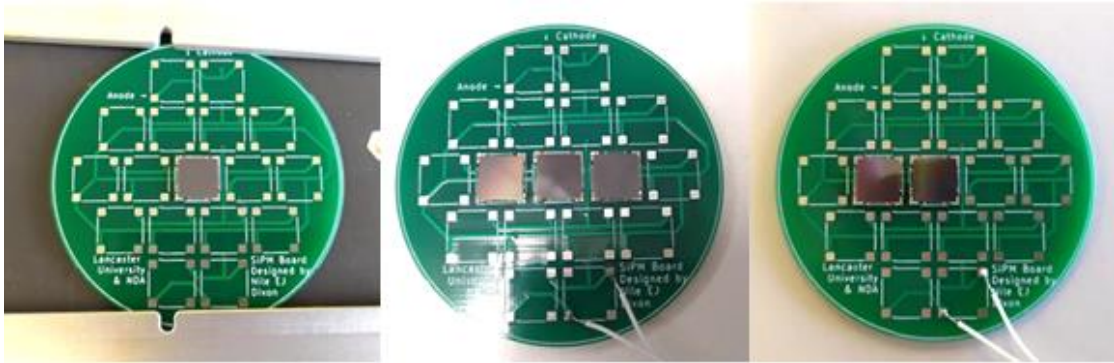


Figure 3.16: Images of detector head circuit as each SiPM was added.

The delays of the implemented shaper have been selected to transition from a trapezoidal to a triangular shaped window to see the effect on the calculated FWHM and resolution. Figure 3.17 shows three examples of the transition from a trapezoidal to a triangular shaper. For the experiment, seven different windows were used in the transition, and the sum of the three delays was kept constant at 200 samples.

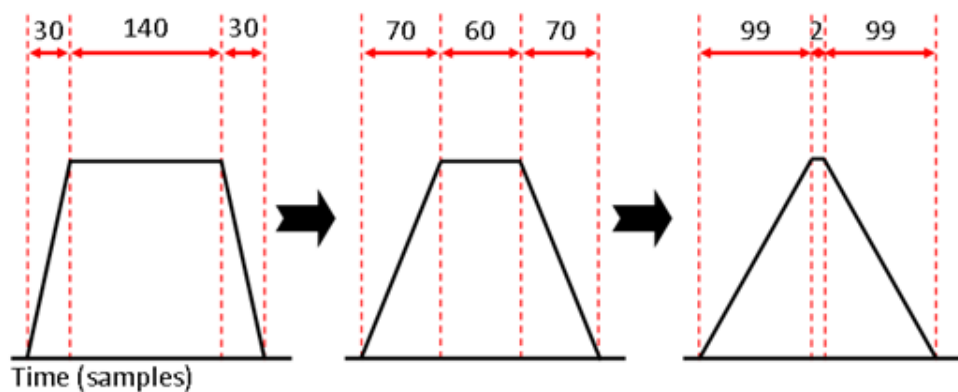


Figure 3.17: Visual representation of the effect of the delay values on the shape of the window, i.e., for the far-left example delay one and three are 30 samples, and delay two is 140 samples.

3.8.1 Light Emitting Diode Blinking Experiment Results

The recorded spectrum for each window with 1, 2 and 3 SiPMs was taken over 13.4 minutes made from a cumulative total of 600 individual spectra taken every 1.34 seconds. The FWHM and resolution were obtained from the recorded spectrum by placing a Gaussian fit over the peak. The recorded set of spectra have been plotted in Figure 3.18, Figure 3.19 and Figure 3.20 for one, two and three SiPMs respectively. The graph legend has been formatted with the values selected for delay one, delay two, and delay three. The detector resolution has also been calculated using equation (3.5), as it is an indicator of how capable the detector is in terms of distinguishing energy.

$$\text{Resolution} = \frac{\text{FWHM}}{\text{Peak Channel}} \times 100\% \quad (3.5)$$

Note that each figure consists of seven individual spectrums measured in seven rounds of testing, where each peak corresponds to a particular set of delay coefficients. Each round the delay values are set within the VHDL program, uploaded to the FPGA and then a measurement of 600 spectra was recorded. The raw spectra data from each of the seven rounds was then plotted with separate traces.

The ratios between peaks as the number of SiPMs increases are important in gauging the benefit of having multiple within the detector. In an ideal case, doubling the sensitive area of the detector would result in a peak ratio of two, as the pulse would be twice the magnitude, as the two spikes of current from each SiPM would sum together.

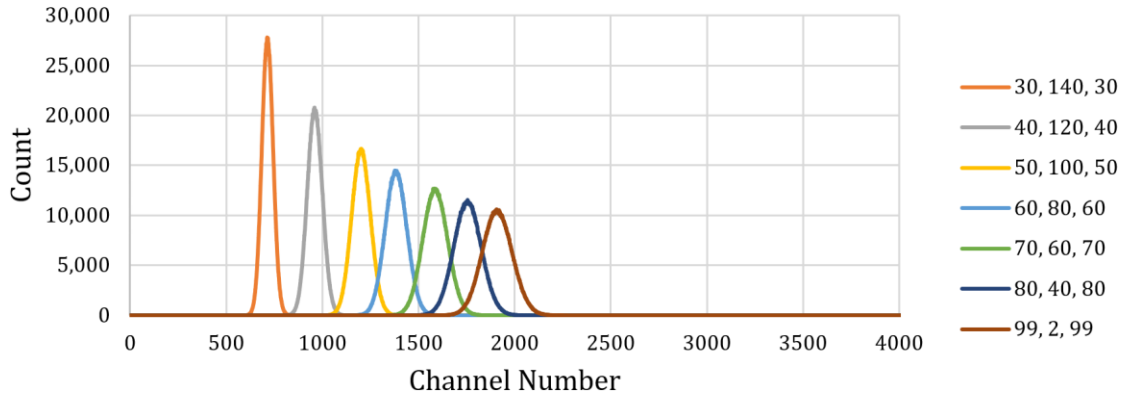


Figure 3.18: Combined raw unfiltered spectra of 8 LED blink tests with a single SiPM. The legend indicates the duration of delays one, two, and three.

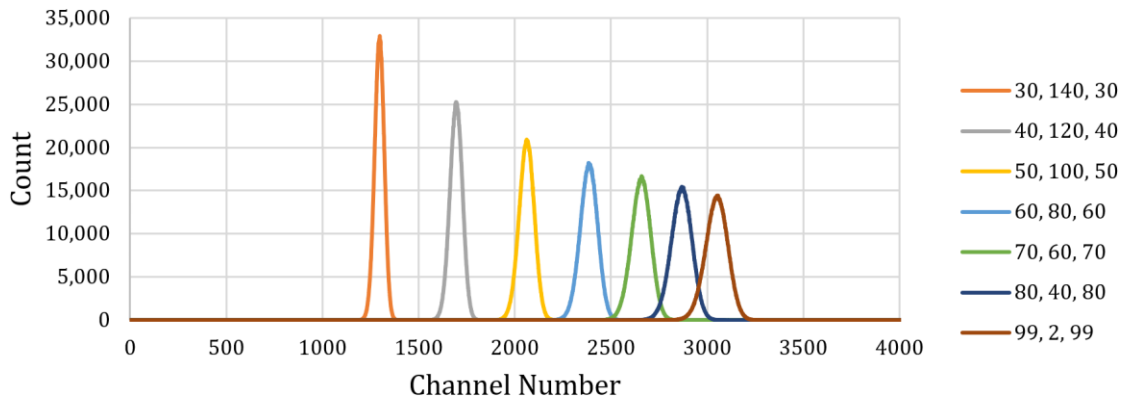


Figure 3.19: Combined raw unfiltered spectra of 8 LED blink tests with two SiPM. The legend indicates the duration of delays one, two, and three.

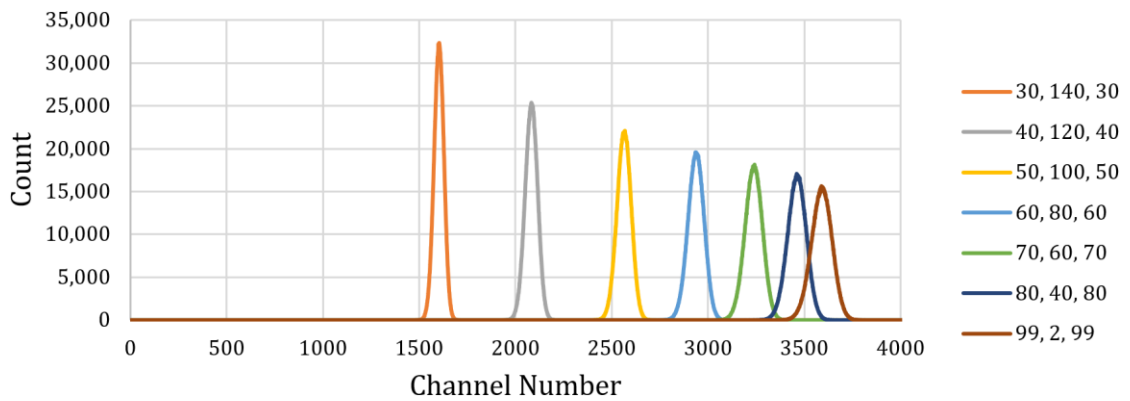


Figure 3.20: Combined raw unfiltered spectra of 8 LED blink tests with three SiPM. The legend indicates the duration of delays one, two, and three.

As expected, a single peak is captured individually for each test run with a different shaping window. The peaks are at increasingly higher channels when produced by windows with decreasing delay two values, i.e., as the window becomes more triangular. This trend continued when using one, two or three SiPMs. Comparing the number of SiPMs used, a positive shift in the detected peak was seen with each additional SiPM, as increasing the detectors' sensitive area has increased the voltage magnitude of the output pulses, as it can collect more light from the LED.

By taking the ratio between the peak channels for one and two SiPMs (Delays: 99, 2, 99), the gain is found to be 1.60, and between one and three SiPMs (Delays: 99, 2, 99) was found to be 1.88. One contribution to this gain inefficiency is the combined capacitance between the anode and cathode of each SiPM affecting the rise time of the pulse. This can be improved using active summation [97], although at an added cost and complexity.

The channel FWHM has been plotted in Figure 3.21 and the resolution has been plotted in Figure 3.22 for all LED experiments, with a linear fit added for each SiPM count. Black dotted lines have also been added to link the results using the same shaper delays. Interpreting Figure 3.21, the FWHM and peak channel tend to increase as the shaper becomes more triangular. While an increased FWHM is not advantageous, when combined with the apparent gain increase, the resolution (Figure 3.22) tends to stay relatively constant for all tested shaper delays. The change of one to two SiPMs improves the resolution by an average factor of 2.16, and the change from one to three SiPMs improves by an average factor of 2.79. As a result, the use for three SiPMs over one or two results in the best detection resolution.

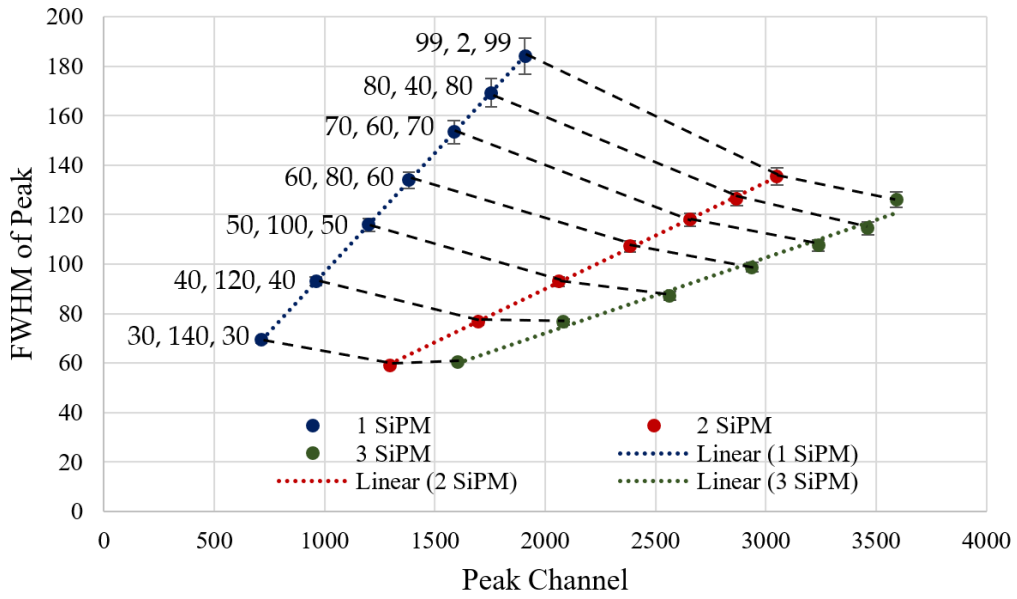


Figure 3.21: Channel FWHM from each detected peak across all LED testing experiments, with three-sigma error bars. Three lines of best fit consisting of coloured dotted lines have been added on each set of results for one, two, and three SiPMs.

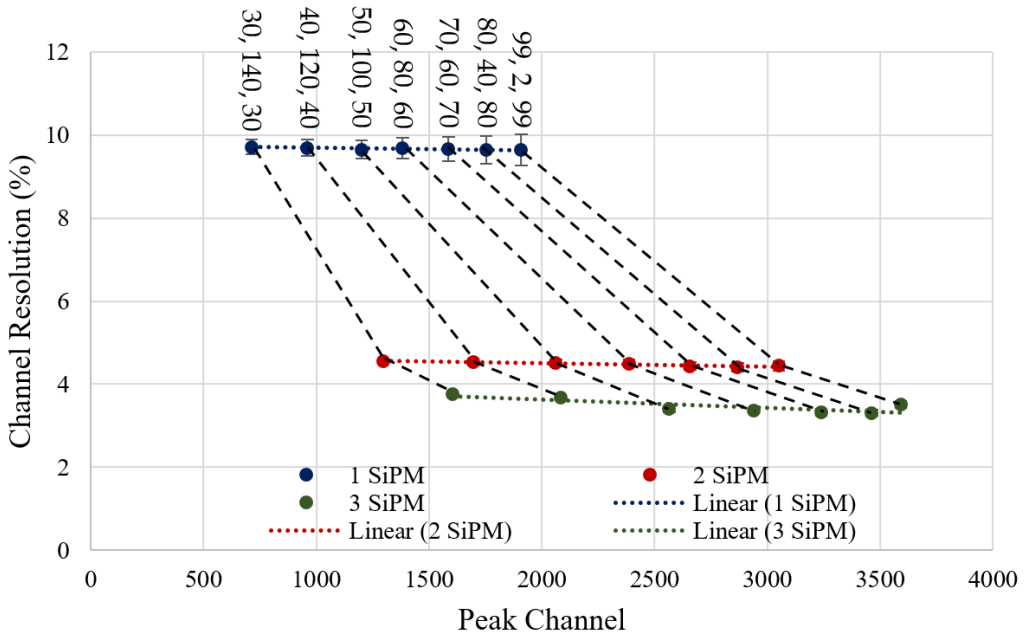


Figure 3.22: Channel resolution from each detected peak across all LED testing experiments, with three-sigma error bars. Three lines of best fit consisting of coloured dotted lines have been added on each set of resolution values for one, two, and three SiPMs.

3.9 Zener Diode Temperature Compensation

As discussed in section 2.10, to have a constant dark count rate there is a need to include temperature compensation to keep the gain of the SiPM constant. Where this work diverges from previous implementations is in the use of Zener diodes as the means of continuously sensing the temperature of the SiPM.

These diodes feature a Zener voltage, which is the voltage at which a Zener diode will conduct in reverse bias. However, this is not constant and instead varies as a function of temperature according to its temperature coefficient, which itself changes from diode to diode due to manufacturing tolerances. The C-series SiPMs possess a breakdown voltage from 24.2 V to 24.7 V at 21°C, a recommended overvoltage range from 1.0 V to 5.0 V, and a breakdown voltage temperature dependence of 21.5 mV/°C [90]. This allows the breakdown voltage of a general SiPM to be represented by equation (3.6) and for the C-series SiPM as equation (3.7).

$$V_{SiPM\ Breakdown} = V_{SiPM-br} + K_{SiPM}(T_{SiPM} - 21^\circ\text{C}) \quad (3.6)$$

$$V_{SiPM\ Breakdown} = 24.2 + 0.0215 \times (T_{SiPM} - 21^\circ\text{C}) \quad (3.7)$$

where $V_{SiPM\ Breakdown}$ is the breakdown voltage at a temperature of T_{SiPM} °C, $V_{SiPM-br}$ is the given breakdown voltage at 21°C, and K_{SiPM} is the temperature dependence of $V_{SiPM\ Breakdown}$. As the SiPM overvoltage is simply the difference between the breakdown voltage and the bias voltage, equation (3.8) can be used to formulate the overvoltage, $V_{SiPM\ Overvoltage}$.

$$V_{SiPM\ Overvoltage} = V_{SiPM\ Bias} - V_{SiPM-br} - K_{SiPM}(T_{SiPM} - 21^\circ\text{C}) \quad (3.8)$$

To keep a constant gain, this overvoltage must be kept at a constant value close to the upper end of the overvoltage range (5.0 V) to maximise the SiPM gain. The breakdown voltage of the Zener diode (Zener Voltage) can also be formulated in a similar manner, see equation (3.9).

$$V_{Zener\ Breakdown} = V_{Zener-br} + K_{Zener}(T_{Zener} - 21^{\circ}\text{C}) \quad (3.9)$$

where $V_{Zener\ Breakdown}$ is the Zener breakdown voltage at a temperature of T_{Zener} °C, $V_{Zener-br}$ is the given breakdown voltage at 21°C, and K_{Zener} is the temperature dependence of $V_{Zener-br}$. As the voltage drop across the diode is equal to the bias voltage placed over the SiPM (see Figure 3.23), represented by equation (3.10), the SiPM overvoltage can be derived in equation (3.11).

$$V_{SiPM\ Bias} = V_{Zener\ Breakdown} \quad (3.10)$$

$$\begin{aligned} V_{SiPM\ Overvoltage} &= V_{Zener-br} + K_{Zener}(T_{Zener} - 21^{\circ}\text{C}) - V_{SiPM-br} \\ &\quad - K_{SiPM}(T_{SiPM} - 21^{\circ}\text{C}) \end{aligned} \quad (3.11)$$

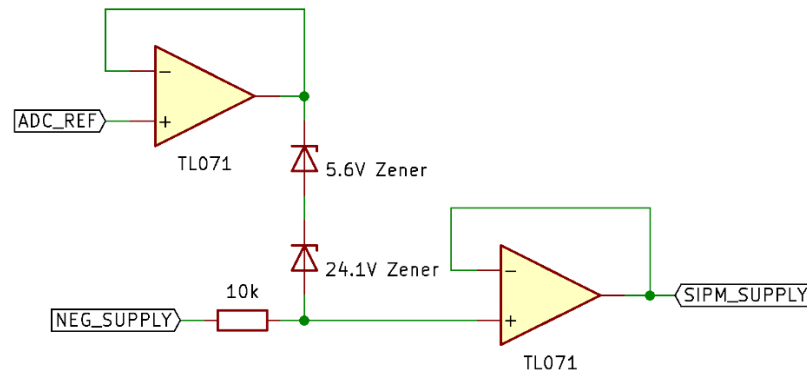


Figure 3.23: Simplified schematic of simulated temperature compensation circuit.

Therefore, given that the SiPM and Zener diode are held at the same temperature, for the overvoltage to stay constant (perfect temperature matching), equations (3.12) and (3.13) must be true.

$$V_{Zener-br} = V_{SiPM-br} + V_{SiPM\ Overvoltage} \quad (3.12)$$

and:

$$K_{Zener} = K_{SiPM} \quad (3.13)$$

If a suitable Zener diode with the exact required characteristics cannot be located, multiple Zener diodes connected in series can be used instead, as their individual voltage drops (equation 3.14), and temperature coefficients (equation 3.15) would be combined.

$$V_{Zener-1-br} + V_{Zener-2-br} + \dots = V_{SiPM-br} + V_{SiPM\ Overvoltage} \quad (3.14)$$

$$K_{Zener-1} + K_{Zener-2} + \dots = K_{SiPM} \quad (3.15)$$

3.9.1 Temperature Compensation System Simulation

LTspice (version XVII, Linear Technologies [116]), a SPICE-based analogue electronic circuit simulator, was selected to produce the simulations, as it can utilise models directly from Onsemi, the manufacturer of the Zener diodes, resulting in a more accurate simulation.

To simulate the electrical behaviour of SiPMs, a simplified Single Photon Avalanche Diode model (SPAD model) was used. Similar models have been used when focusing on SiPM modelling for front-end electronics [117] and SPICE electrical models [118]. This allows the breakdown voltage, terminal capacitance, quench resistance, and diode switching characteristics to also be modelled. For the C-series SiPM, limited model data is provided by the manufacturer, therefore only the terminal capacitance and breakdown voltage were modelled for the SiPM in this work.

The SiPM has been implemented in the simulation using three components: a voltage source, which varies using equation (3.7), a digital switch with a short closed duration which represents a single photon striking the SiPM, and a 3,400 pF capacitor representing the total capacitance across the anode and cathode of the SiPM.

Figure 3.23 shows the temperature compensation system using a combination of two Zener diodes in series. These diodes have Zener voltages of 5.6 V and 24.1 V, making the total series voltage drop 29.7 V. This circuit has been simulated in LTspice [116] alongside a non-temperature controlled ‘static’ system using a set

bias voltage created from a voltage divider. The bias voltage of both the temperature-compensated and non-temperature-compensated systems have been made to match at a temperature of 27°C. The two Zener diodes have been configured in reverse voltage bias, with two unity gain amplifiers added to, firstly, isolate both the reference voltage (ADC_REF) from the cathode of the upper Zener, and secondly to act as a current buffer for the Zener voltage drop to bias one or multiple SiPMs. The TL071 op-amp was used for the buffer op-amps.

As a result of the LTspice simulations with the temperature compensated and non-temperature compensated systems, Figure 3.24 and Figure 3.25 have been obtained. These show the resulting pulses from the output of the transimpedance amplifier and their peak-to-peak measurements over the temperature range of -20°C to 50°C with a step of 5°C . Without compensation, the slope of best fit has a gradient of -0.475 ± 0.020 and an intercept of 117.41 ± 0.51 , compared to the compensated system with a fit gradient of 0.0035 ± 0.019 and an intercept of 104.47 ± 0.49 (a 95% confidence interval). Therefore, it has been shown that the simulated drift in pulse magnitude has been reduced by more than a factor using the Zener compensation method over the tested temperature range.

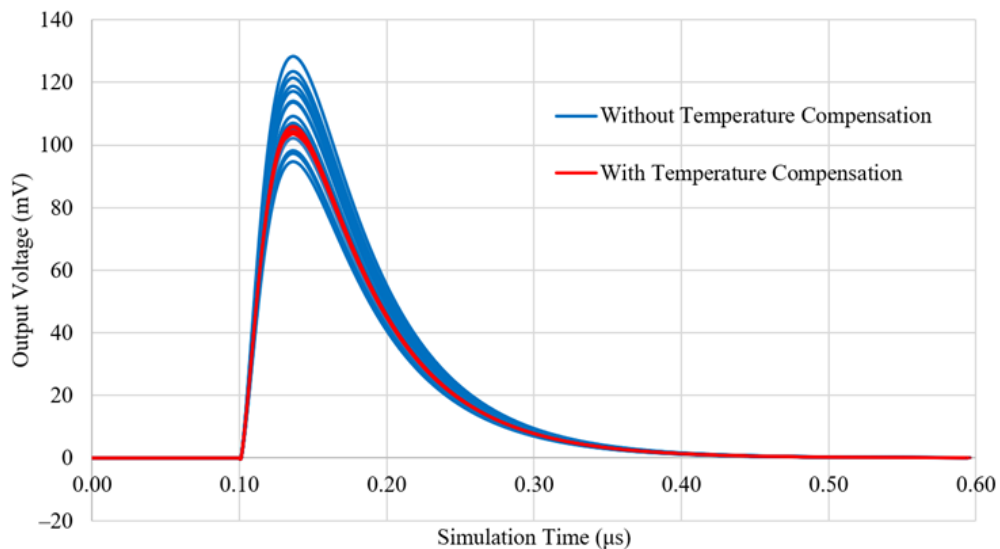


Figure 3.24: LTspice simulation of an amplified pulse from the two systems over the temperature range of -20°C to 50°C with a step of 5°C . Traces of blue correspond to the non-compensated system and red traces correspond to the Zener compensated system.

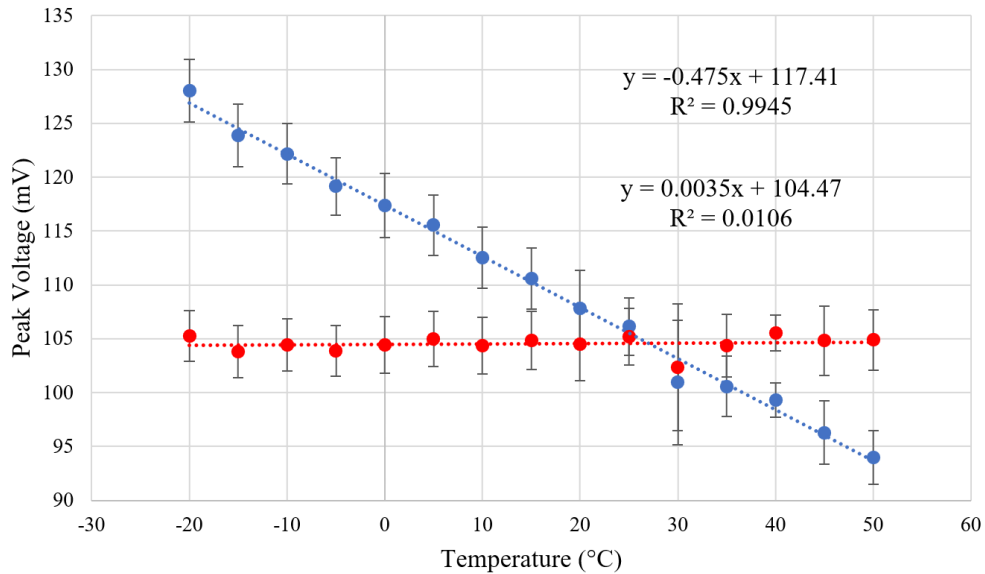


Figure 3.25: LTspice simulation plotting the peak to peak magnitude of each simulated pulse against temperature °C. Blue points correspond to the non-compensated system and red points correspond to the Zener compensated system, both fitted with a linear dotted line. Three sigma error bars have been added based on the results of 10 simulations.

3.9.2 Zener Diode Selection

While the simulations performed in the previous section deal with Zener diodes with set temperature coefficients, in practice, the diodes have a range of values in which the coefficients can lie between as defined by the manufacturer. Therefore, an experiment was conducted to find two suitable Zener diodes that match the SiPM. The experiment involved using a temperature controllable hotplate (Voltera V-One [119]) to which the Zener diodes were attached. An oscilloscope was used to measure the voltage drop over the two Zener diodes, and an infrared thermometer was used to measure the surface temperature of the Zener diodes. The relationship between temperature and voltage drop for the selected diodes is shown in Figure 3.26.

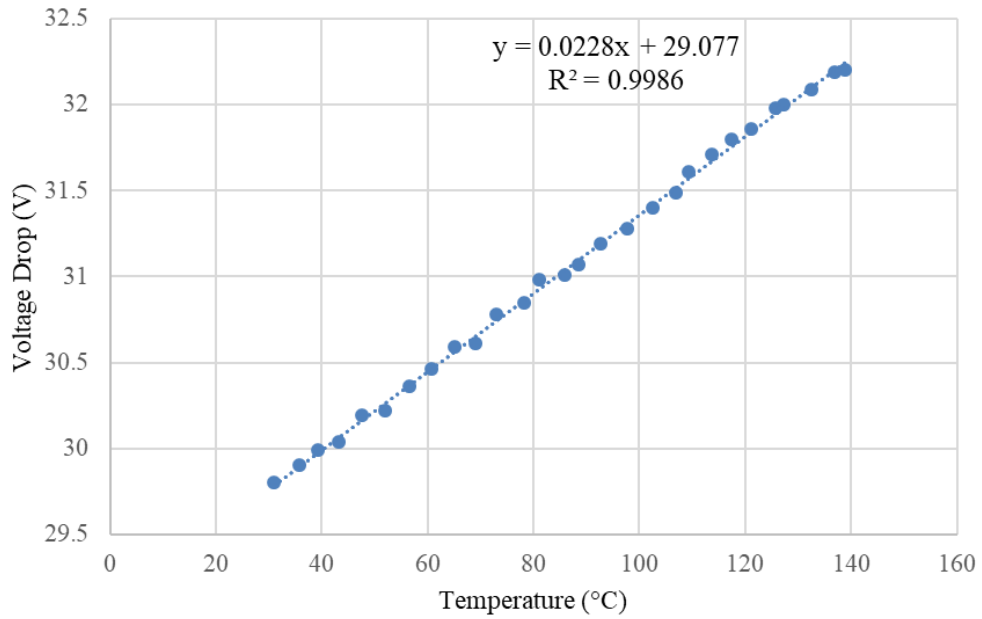


Figure 3.26: Measured voltage drop of the combined Zener diodes over the temperature range of 30°C to 140°C. A negative supply voltage of 32.61 V and a 10 kΩ biasing resistor were used. A linear line of best fit (dotted blue line) has been added to estimate the temperature dependence and voltage drop of the combined Zener diodes at 0°C. Voltages were measured to ± 0.01 V accuracy, and temperature was measured to $\pm 1^\circ\text{C}$ accuracy.

By fitting a linear trend line, the temperature coefficient can be shown to be 22.8 mV/°C with a voltage drop of 29.56 V at 2°C. This linear trend line can be extrapolated for a more suitable temperature range (selected to be -20°C to 30°C) as the temperature coefficient of each Zener diode has been defined as linear across their operating temperatures (-65 to 150°C [120], [121]). This extrapolated plot can be seen in Figure 3.27.

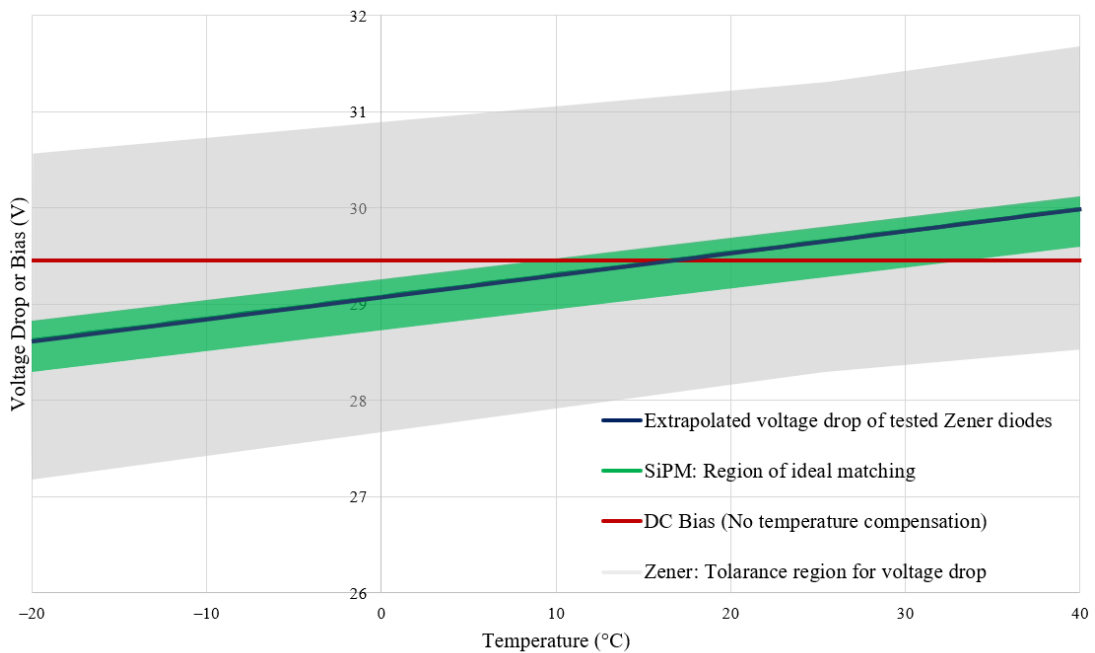


Figure 3.27: Combined plot of the extrapolated voltage drop caused by the measured Zener diodes compared with a set DC bias, ideal voltage drop region for biasing the SiPM, and the region of tolerance given to the Zener diode's voltage drop by the manufacturer.

In Figure 3.27, additional data has been plotted alongside the extrapolation of the measured Zener diode temperature drop (represented as a dark blue line). A red line represents a comparison to a set bias voltage (29.45 V) which is constant, unaffected by temperature. The green shaded region encapsulates the ideal bias voltage of the C-series SiPM for an overvoltage of 5 V above the breakdown voltage, and the exact breakdown voltage varies from part to part due to manufacturing tolerances [90]. Finally, a grey shaded region represents the tolerances in which the combined Zener pair's voltage drop could lie, these tolerances (shown in Table 2) have been taken from the respective datasheets of the diodes.

Table 2: Tolerances for voltage drop and temperature coefficients [90], [120], [121].

Specification	SiPM (with 5 V Overvoltage)	Zener Diode 5.6 V	Zener Diode 24.2 V	Zener Diodes Combined
Min Voltage Drop (V)	29.2	5.49	22.8	28.29
Max Voltage Drop (V)	29.7	5.73	25.6	31.33
Min Temperature coefficient (mV/°C)	21.5	-2	18.4	16.4
Max Temperature coefficient (mV/°C)	21.5	2.5	22	24.5

Interpreting Figure 3.27, using the set DC bias at 29.45 V would not be suitable below a temperature of approximately 10°C, as the voltage drop leaves the SiPM's region of ideal matching resulting in an overvoltage greater than 5 V, which could cause permanent damage to the SiPM, while the Zener voltage drop stays within the ideal region for the full temperature range.

As the measured Zener diodes have a 22.8 mV/°C temperature coefficient and the SiPM has a defined 21.5 mV/°C temperature coefficient, the resulting bias error, equation (3.16), for the tested Zener diodes with a C-series SiPM can be defined using the measured Zener diode behaviour and equation (3.11).

$$V_{\text{Overvoltage error}} = 0.11 + 0.0013T^{\circ\text{C}} \pm 0.25 \quad (3.16)$$

where the difference in bias voltage is caused by the imperfect matching when the SiPM(s) and Zener diodes are both held at a temperature T°C. The ± 0.25 represents the SiPMs breakdown voltage tolerance. Therefore, the implementation of this tested system would reduce the temperature dependence of the SiPM overvoltage from 21.5 mV/°C to 1.3 mV/°C.

3.9.3 Temperature Compensation Experiment Results

This experiment has been used to validate a Zener temperature compensation system; the SiPM and Zener diodes were placed onto a high-power resistor, and the power resistor was used to gradually heat the SiPM from a starting temperature of 30°C to 65°C, while the detector was collecting the spectra of a constant brightness and constant blinking LED. A slightly lower Zener voltage was used (3.9 V replacing 5.6 V) to ensure that the overvoltage stayed below 5 V. The setup for the experiment is shown in Figure 3.28 and the resulting data has been plotted in Figure 3.29.

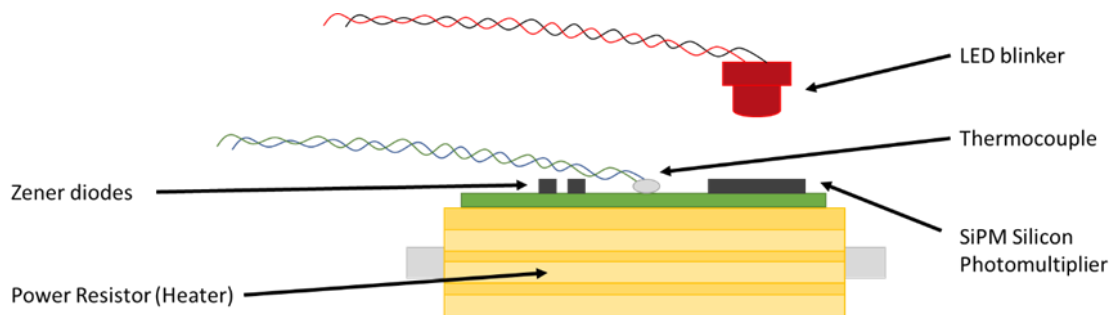


Figure 3.28: Detector setup used for testing the Zener diodes temperature compensation system.

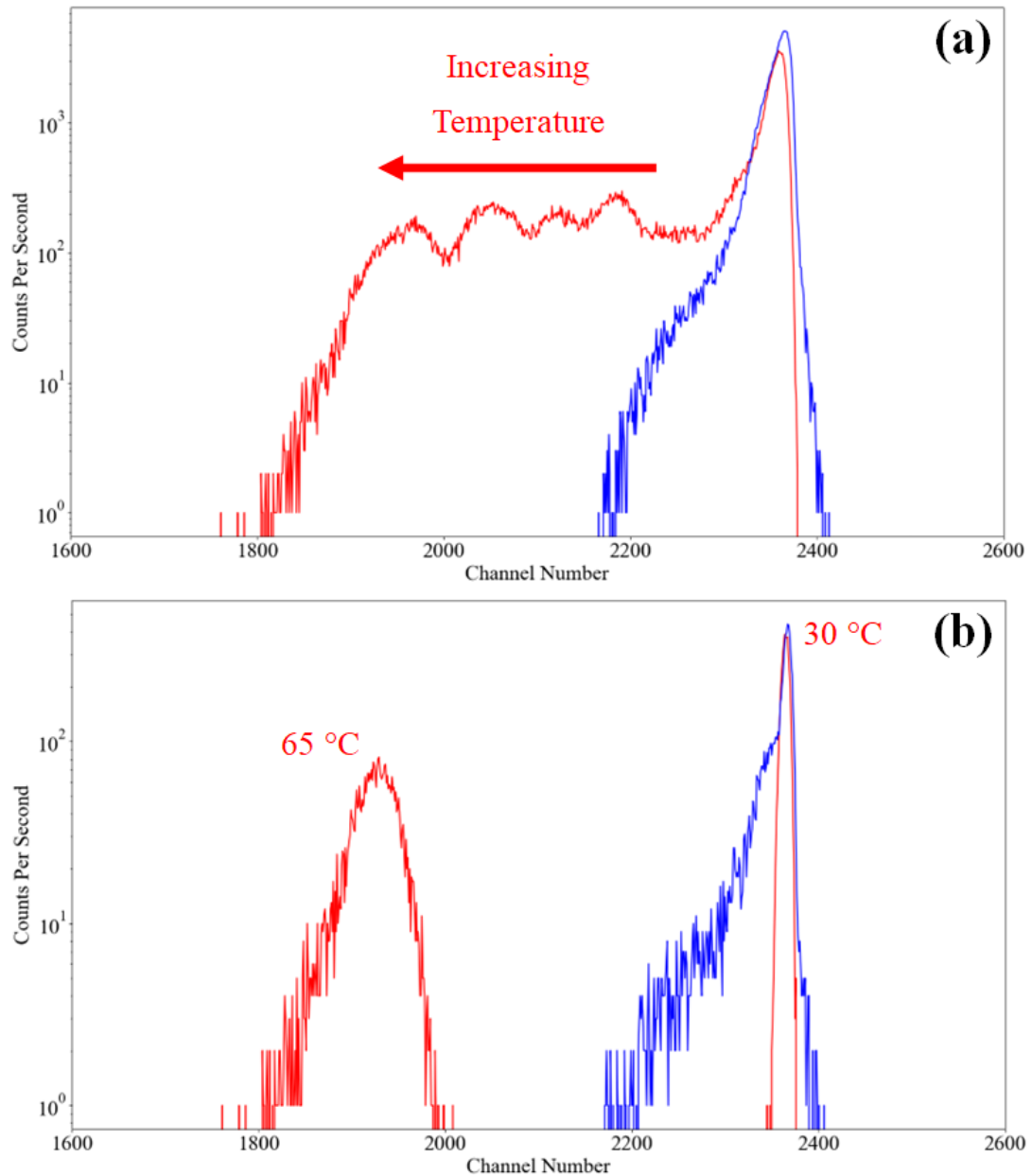


Figure 3.29: A log graph (a) plotting cumulative spectra taken over the full heating experiment. A log graph (b) of individual spectra taken at 30°C and 65°C, for both compensated (blue trace) and non-compensated (red trace) systems. Only channels 1600 to 2600 have been displayed for purposes of clarity.

As expected, in Figure 3.29 a clear shift can be seen in the non-compensated system when comparing its spectra taken at 30°C to its spectra taken at 65°C; this is explained as when the SiPM's temperature increases the breakdown voltage also increases, this increase in breakdown voltage lowers the SiPM overvoltage, therefore lowering the gain of the system at higher temperatures. The temperature-controlled system has undergone a small shift resulting in a side tail; this could be due to noise added by the increase in dark counts or the non-ideal

Zener diode matching but has remained as a single peak over the test duration. This reduction in gain variance caused by temperature changes will be useful for the measurements of photopeaks within spectra as they will shift less with ambient temperature changes.

3.10 Coincidence Counting Implementation

As previously discussed in section 2.7. Coincidence counting has been regularly implemented for the detection of tritium in existing systems. This section will explain the workings of coincidence counting as well as its integration into the newly developed detector.

As the manufactured ADC board has two channels, each channel was given its own set of SiPMs. Then within the FPGA two trapezoidal shapers can work simultaneously reading two voltage readings per clock cycle (20 ns) from each ADC. The output of the shapers forms the pulses into a trapezoidal signal with a rising edge, falling edge and flat top, in this implementation, the point at which this trapezoid reaches a set threshold is when the system deems that a pulse has been detected.

When in coincidence mode, this threshold must be met by both channels on the same clock cycle. Otherwise, pulses from either channel will be ignored as they are likely to be dark pulses (electrical noise). The diagram depicted Figure 3.30 shows two examples; where two pulses arrive simultaneously on both channel A and B and are accepted, and another where two dark pulses arrive randomly and are rejected.

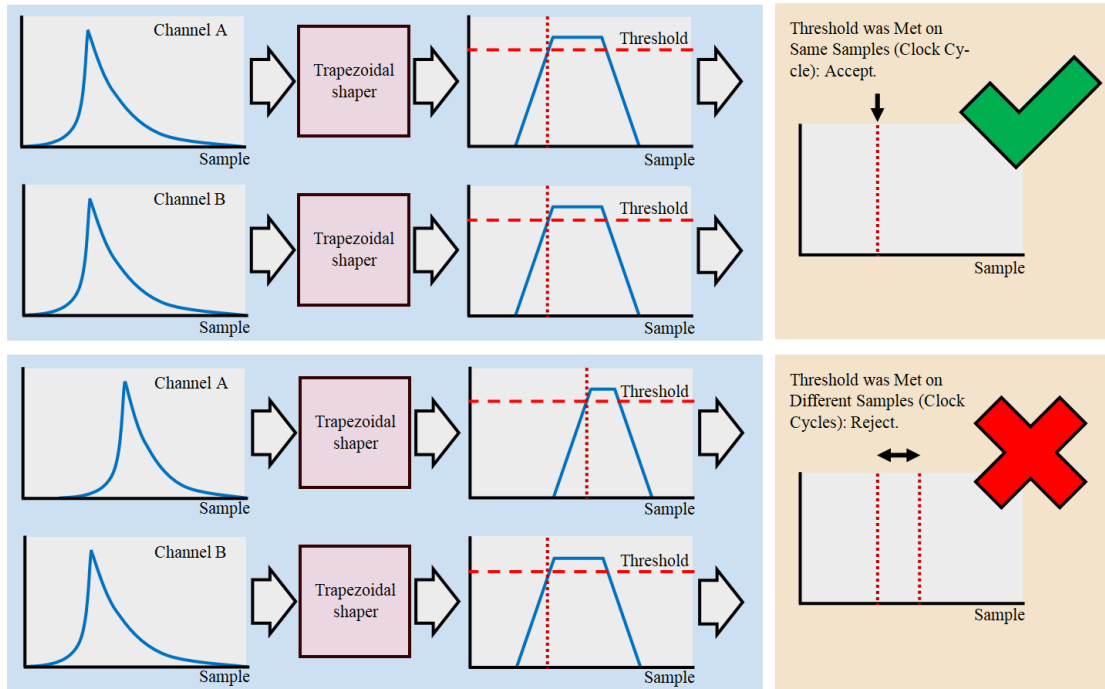


Figure 3.30: Diagram depicting data pipeline and coincidence checking: Upper example is of pulses being accepted, lower an example of random pulses being rejected.

3.11 System Validation with Sealed Sources

The purpose of these experiments is to calibrate and validate the backend system to show that it is capable of radiation detection. The experimental setup is as follows: the window of a cylindrical (40 mm dia. by 52 mm long) NaI(Tl) scintillator manufactured by Advatech [122] was placed onto the SiPM board containing three C-series SiPMs, using optical grade silicone grease to improve the light transfer between them. Along with the SiPMs, the amplifier and temperature compensation boards were placed together inside a light tight enclosure. This plastic enclosure had an O-ring seal placed around the hinge to eliminate light from entering through the lid once closed and locked. Sealed point sources ^{60}Co , ^{137}Cs , ^{22}Na , and ^{241}Am (with the respective activities of 4.46 kBq, 27.27 kBq, 0.60 kBq, and 33.51 kBq) were individually placed directly upon the cylindrical scintillator before the enclosure was closed. Figure 3.31 shows when ^{60}Co was placed on the detector.

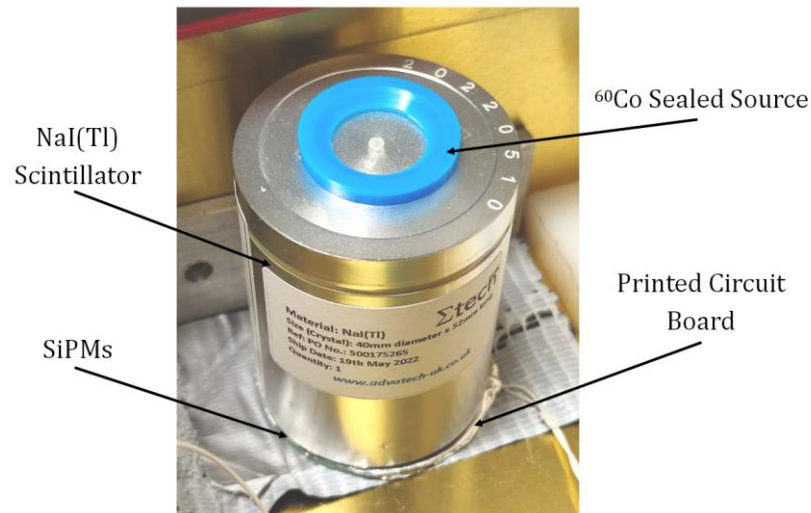


Figure 3.31: Image of ^{60}Co source placed upon the NaI(Tl) crystal. The SiPM sensor head has been placed below the circular window of the encapsulated crystal. After placement of the source, the lid was closed and locked to ensure that no ambient light could enter.

Figure 3.32, Figure 3.33, Figure 3.34 and Figure 3.35 show the spectra recorded by the developed detector for sealed sources of ^{60}Co , ^{22}Na , ^{241}Am and ^{137}Cs respectively. Additionally, Figure 3.36 shows the spectra recorded when both ^{137}Cs and ^{60}Co sources are measured simultaneously. Two background spectra at zoom levels 1 and 0.5 were recorded before testing and have been subtracted from the captured spectra of each source. Finally, a Gaussian fit was added around each detected peak using 50 channels below and above the peak channel and can be seen displayed on each plot as a dashed red line. The point at which the ADC saturates can be seen in Figure 3.32 as a peak close to channel $2,353 \pm 4$. Any pulses that saturate the ADC congregate together into this peak distribution, and as such will be excluded from the peak analysis.

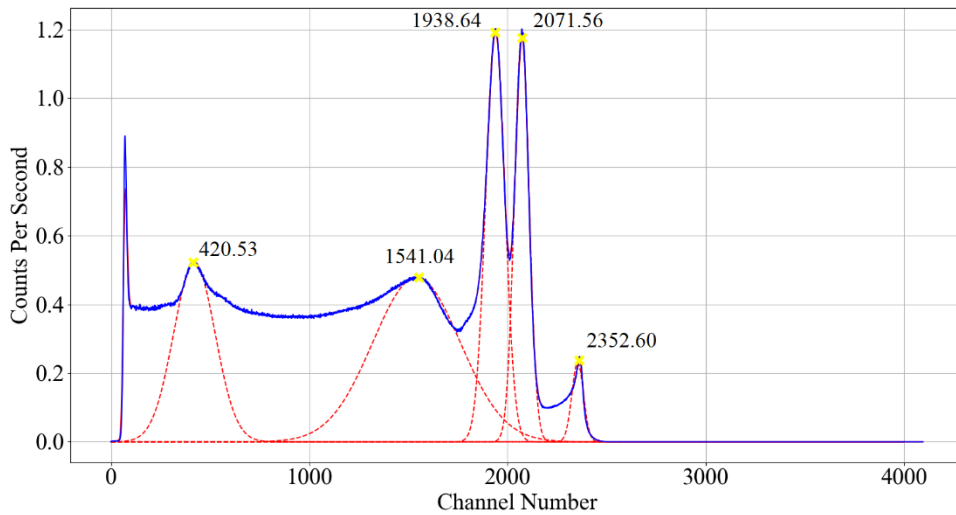


Figure 3.32: The spectrum of the ^{60}Co sealed source with background counts removed, taken at zoom level 1. Blue trace is raw channel data, solid red trace is 20 sample moving average, dashed red trace is Gaussian fit around peaks.

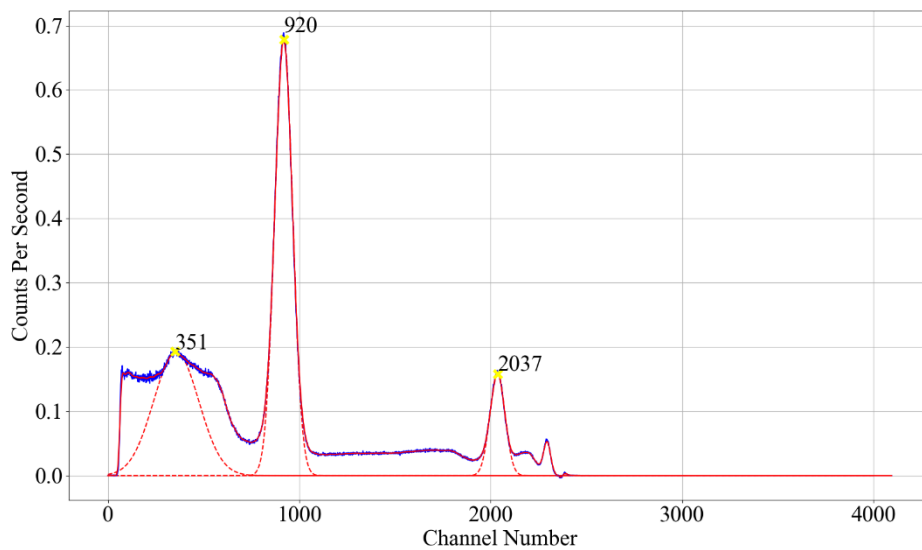


Figure 3.33: Spectrum of ^{22}Na sealed source with background counts removed, taken at zoom level 1. Blue trace is raw channel data, red trace is 20 sample moving average, dashed red trace is Gaussian fit around peaks.

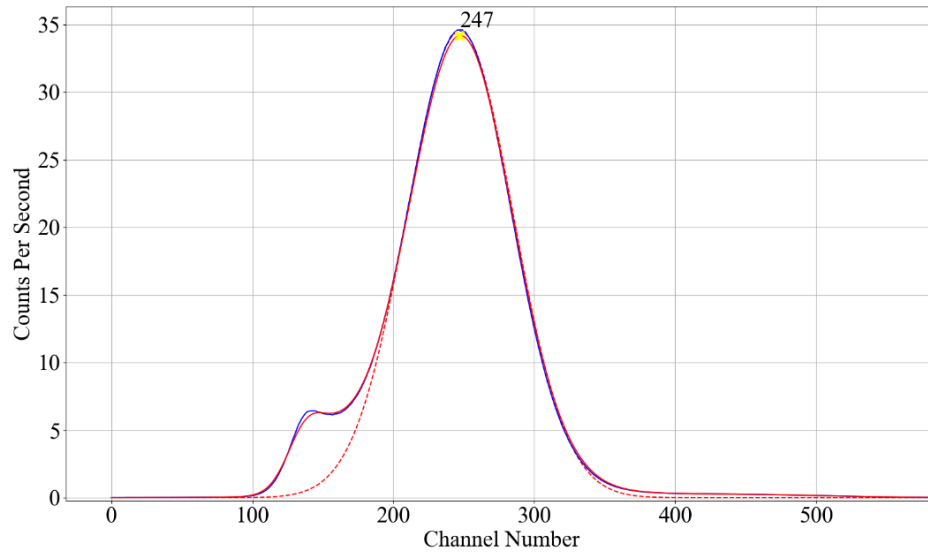


Figure 3.34: Spectrum of ^{241}Am sealed source with background counts removed, at zoom level 0.5. Blue trace is raw channel data, solid red trace is 20 sample moving average, dashed red trace is Gaussian fit around peaks.

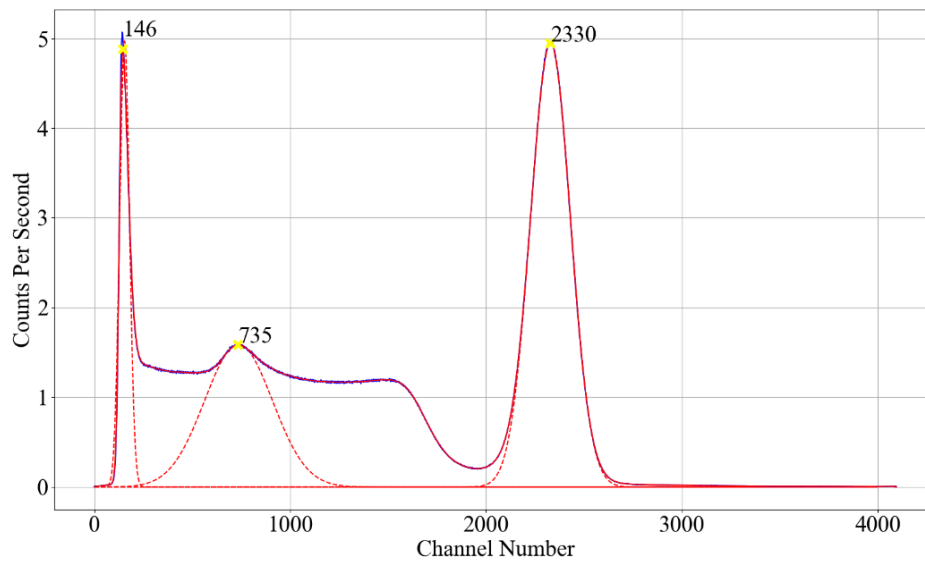


Figure 3.35: Spectrum of ^{137}Cs sealed source with background counts removed, taken at zoom level 0.5. Blue trace is raw channel data, solid red trace is 20 sample moving average, dashed red trace is Gaussian fit around peaks.

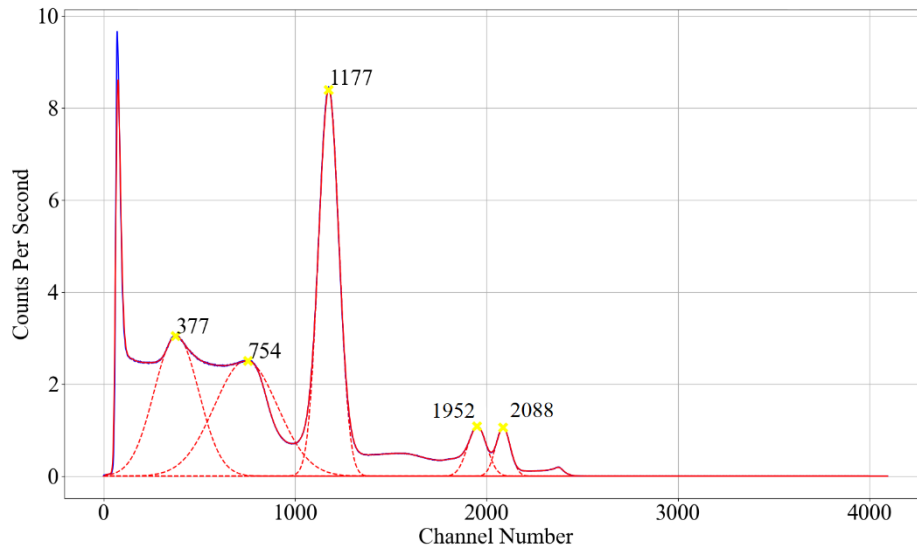


Figure 3.36: Spectra of ^{137}Cs and ^{60}Co sealed sources with background counts removed, at zoom level 1. Blue trace is raw channel data, solid red trace is 20 sample moving average, dashed red trace is Gaussian fit around peaks.

Table 3 displays the combination of detected peaks in each recorded spectrum with a known energy expected for the tested radioisotope. This was then used to plot a calibration fit for the detector (Figure 3.37). The lowest peak from ^{241}Am was not used due to the uncertainty in the recorded counts caused by the overlap with X-rays from its daughter nuclide ^{237}Np . The resolution for each photopeak has been calculated and plotted in Figure 3.38 by dividing the FWHM by the assigned photopeak energy.

Table 3: Calibration table of peak channels detected for the photopeaks of the tested sealed sources, ^{60}Co [171], ^{137}Cs [172], ^{22}Na [123], [173] and ^{241}Am [125].

Isotope	CPS	Collection Time (Hour)	Peak Channel ($\pm 3\sigma$)	Energy (keV)	Resolution ($\% \pm 3\sigma$)	FWHM (keV $\pm 3\sigma$)
^{60}Co	1,002.9	19.8	1,939 \pm 3	1,173.24	6.30 \pm 1.82	73.89 \pm 21.30
			2,072 \pm 2	1,332.50	4.27 \pm 1.16	56.86 \pm 15.47
^{137}Cs	3,614.4	9.5	1,164 \pm 1	661.66	11.82 \pm 3.07	78.18 \pm 20.29
^{22}Na	237.5	9.9	918 \pm 2	511.00	14.52 \pm 3.82	74.19 \pm 19.53
			2,036 \pm 5	1,274.53	5.57 \pm 1.55	71.01 \pm 19.78
^{241}Am	3,572.2	12.8	124 \pm 0	59.54	48.54 \pm 12.58	28.90 \pm 7.49
			72 \pm 3	26.34	-	-

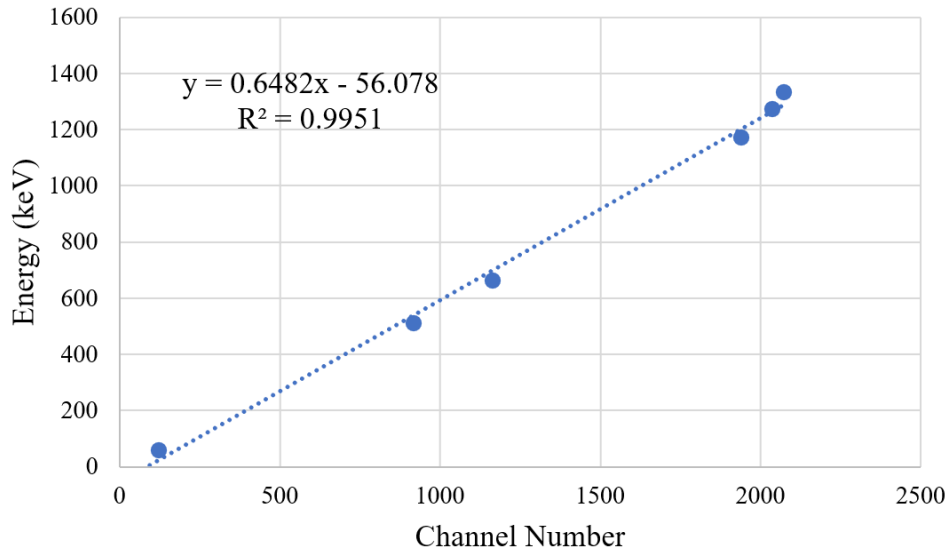


Figure 3.37: Calibration fit for the detector with three-sigma error bars based upon the collected peak channel data in Table 3. A line of best fit (dotted blue line) has been fitted on the data to relate each channel to a detection energy. The fit has a gradient and intercept standard error of 0.65 ± 0.02 and -56.08 ± 35.39 , respectively (a 95% confidence interval).

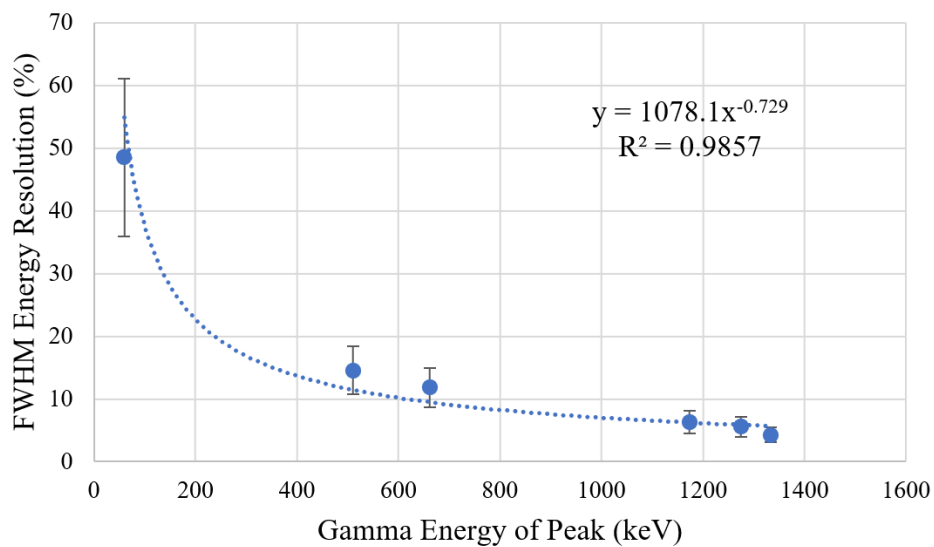


Figure 3.38: Energy resolution of the detector with three-sigma error bars. A power trend line has been added to the data alongside a value for the fit.

From Figure 3.37, a clear correlation between channel number and energy can be identified with a linear fit and an R^2 value of 0.9951. From this, the detector calibration equation (3.17) is obtained.

$$\text{Channel Energy (keV)} = 0.6482 \times \text{Channel Number} - 56.078 \quad (3.17)$$

Therefore, each channel represents 0.6482 keV at zoom level 1 and 0.3241 keV at zoom level 0.5. The saturation peak in Figure 3.32 can be used with equation (3.17), indicating that the detector begins to saturate approaching an energy of $1,469 \text{ keV} \pm 3 \text{ keV}$. The SiPMs were biased with two Zener diodes with Zener voltages of 5.6 V and 24.2 V.

The calculated FWHM energy for each Gaussian fit peak is displayed in Table 3 and plotted in Figure 3.38, followed by the detection efficiencies of each Gaussian fit peak displayed in Table 4 and plotted in Figure 3.39. The results show that the FWHM energy resolution and efficiency increase as the energy of the detected gamma peak decreases. This relationship can also be seen in other publications working with similar systems [102], [123], [124]. The detector achieves a peak efficiency of 27% for a gamma peak at 59.54 keV produced by ^{241}Am .

Table 4: Detection efficiency of each gamma peak, with all peak channels adjusted to a zoom of 1.

Source	Fitted Gamma Energy (keV)	Decay Branching Ratio	Detected Count Rate (CPS $\pm 3\sigma$)	Detection Efficiency (% $\pm 3\sigma$)
^{60}Co	1,173.24	1.00	144.8 ± 20.0	3.3 ± 0.5
	1,332.50	1.00	110.2 ± 11.2	2.5 ± 0.3
^{137}Cs	661.66	0.85	$1,269.5 \pm 30.9$	5.5 ± 0.1
^{22}Na	511.00	1.81	81.5 ± 6.1	7.5 ± 1.0
	1,274.53	1.00	17.1 ± 2.8	1.8 ± 0.5
^{241}Am	59.54	0.36 [125]	$3,268.3 \pm 45.2$	27.1 ± 0.1

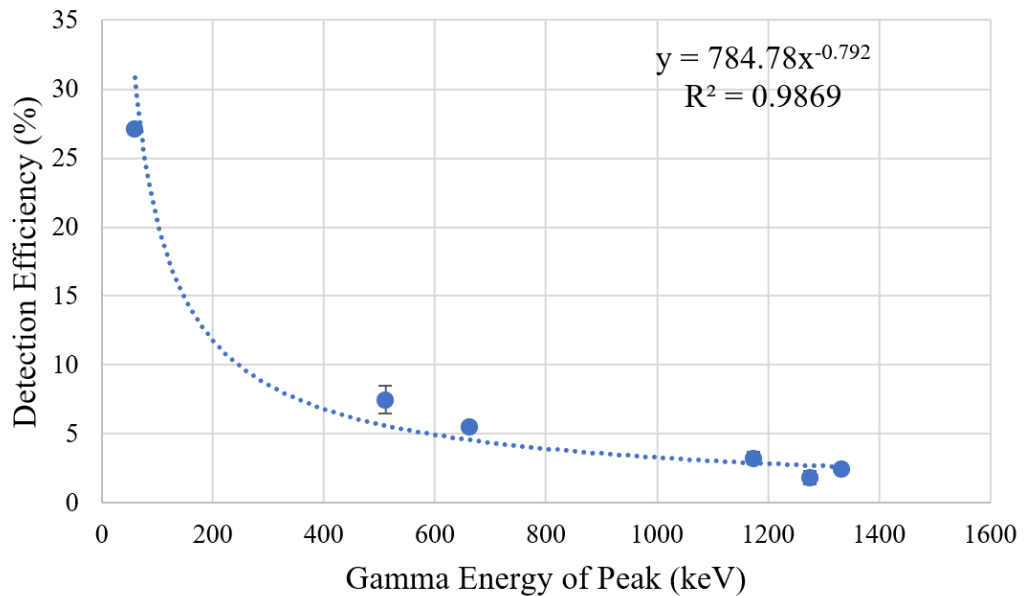


Figure 3.39: Plot of the calculated detection efficiency for each peak in the recorded spectra with three-sigma error bars. A power trend line has been added to the data alongside the value for the fit.

3.12 Conclusions

Circuits have been produced, including a SiPM amplifier and a dual ADC board capable of digitising SiPM pulses for trapezoid shaping. These boards, along with a single-board computer, can fit within a cylindrical diameter of 46 mm. The fully produced detector system is also low cost, with the majority cost being that of the scintillator. For figures showing further PCB and schematic designs for the detector see Appendix C.

A VHDL implementation of a trapezoidal shaper for the processing of SiPM pulses into a spectrum has also been produced and validated experimentally for different numbers of SiPMs (see appendix E for figures of VHDL code). This showed that using multiple SiPMs in parallel improved the resolution of the peaks in the detected spectra, while the shaper window did not have a large effect on the resolution. On the other hand, the shaping window affected the gain of the system,

finding that a triangular window resulted in peaks at higher channel numbers compared to trapezoidal windows for a set total delay length.

The sealed source radiation testing of the backend electrical system with a NaI(Tl) scintillator has produced a range of spectra used in obtaining the resolution and detection efficiency of the detector over the range of detected energies. A minimum energy resolution ($\Delta E/E$) of $4\% \pm 1\%$ was obtained for the 1,332.5 keV gamma peak from ^{60}Co and a maximum detection efficiency of 27% from a 59.54 keV ^{241}Am gamma peak. A fit has been produced to relate the channel number to energy, finding that the detector has a detectable energy range from 56 keV to $1,469 \text{ keV} \pm 3 \text{ keV}$ and a resolution of 648 eV at zoom level 1.

A new temperature compensation system has been designed and simulated using two serially connected Zener diodes. Temperature experiments have also found two suitable components, that being a SZMM5Z24VT1G and a SZMM3Z5V6ST1G Zener diode in combination, which would reduce the temperature dependence of the SiPM's overvoltage from $21.5 \text{ mV}/^\circ\text{C}$ to $1.3 \text{ mV}/^\circ\text{C}$. The Zener temperature compensation system was also validated experimentally using a heating experiment, showing a smaller shift in detected peaks within the recorded spectra when compared to a set bias system, over a temperature range of 30°C to 65°C .

This electrical progress is a large step towards the detection of low energy betas as well as the ability for the detector to be fitted within the small confines of the borehole. The inclusion of a database will allow the system to be left for long periods unattended and 'cut off' from exterior interaction. While visualisation using Bokeh was useful for the detection of noise in the early system development, FastSpec has been utilised far more due to it working with the trapezoidal shapers, from this point onwards only FastSpec will be used for collecting and displaying detector data.

4 Flow Cell Development

4.1 Introduction

Previous publications [71], [126], [127] have shown that granulated forms of calcium fluoride doped with europium ($\text{CaF}_2(\text{Eu})$) have a reasonable efficacy in detecting tritium. The work presented here builds on these works and demonstrates how a finely powdered scintillator maximises the active surface area and allows for good detection efficiency for a flow cell detector of limited size.

A granulated scintillator enhances some of the benefits of homogeneous solid scintillators by having a far higher surface area and allowing the liquid sample to pass and envelope the particulates instead of remaining at the face of a single solid crystal. Due to the relatively small geometric path length of betas emitted by tritium within solid scintillators (less than $1\ \mu\text{m}$ in $\text{CaF}_2(\text{Eu})$ [33]), using a solid scintillator thicker than $1\ \mu\text{m}$ would not be advantageous for increasing detection efficiency, as almost no interactions would occur at or over this depth. A needlessly thick scintillator would also increase the optical attenuation of the scintillation photons to the photomultiplier tube (PMT) or silicon photomultiplier (SiPM), further reducing overall efficiency. A diagram of a granulated scintillator is shown in Figure 4.1.

A previous study by Tarancón et al. [128] looking at radiation detection using plastic scintillating beads found an increase in detection efficiency from $0.24\% \pm 0.01\%$ to $0.53\% \pm 0.04\%$ when detecting tritium using $500\ \mu\text{m}$ to $1,000\ \mu\text{m}$ and $100\ \mu\text{m}$ to $250\ \mu\text{m}$ beads respectively. Additionally, a change in detection efficiency for carbon-14 was seen, $17.5\% \pm 1.5\%$ for $500\ \mu\text{m}$ to $1,000\ \mu\text{m}$ beads, and $41.8\% \pm 1.0\%$ for $100\ \mu\text{m}$ to $250\ \mu\text{m}$ beads [128]. A paper by T. L. Alton et al [126] found optimal radii for a granulated scintillator for tritium detection as

10 μm and 350 μm for carbon-14 detection. A larger radius is needed for carbon-14 compared to tritium as its maximum beta energy is greater and hence betas particles can travel further into the scintillator before interacting.

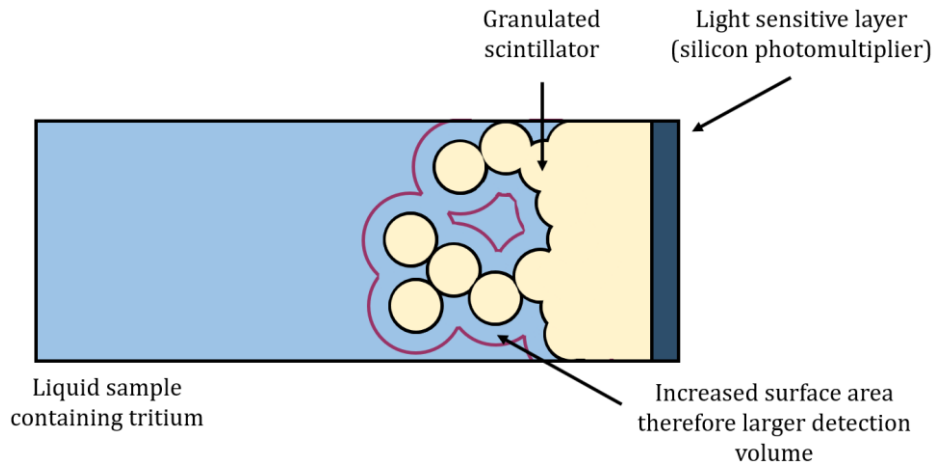


Figure 4.1: Diagram of a granulated scintillator in contact with a tritiated liquid sample.

The main benefit of granulated scintillators, compared to a liquid scintillator, is that the particles can be secured while allowing a sample to flow through the detection cavity. This allows the scintillator to be reused until it is soiled, as excess surface contamination of the scintillator will increase beta attenuation, resulting in reduced detection efficiency. If using a liquid scintillator, a cocktail would have to be expelled with the sample and then replaced. For in situ environments, a large volume of scintillation cocktail would have to be stored to feed such a flow cell, whereas a granulated flow cell could be periodically replaced with another. It should also be noted that scintillation cocktails are often a hazard to the environment due to their toxic nature and high solubility in water. For example, GoldStar LT2, commonly used for low energy beta and alpha detection, is very toxic to aquatic life with long-lasting effects [129]. Due to this hazard, any used sample mixture leaving the cavity would have to be stored for future removal and waste processing, while only the original sample would leave the granulated flow cell with sufficient filtering.

Granulated scintillators also have their downsides, principally that a granulated scintillator will have poorer optical properties compared to a conventional solid scintillator due to the number of boundaries each photon would have to pass in

reaching the photomultiplier detector. Second, the poorer mixing with sample compared with a liquid cocktail due to the finite particle size. Therefore, for these reasons, the validity of these granulated forms has been investigated within this chapter.

Following the study of granulated scintillators, a flow cell cavity must be designed and built to contain the granulated scintillator while allowing the liquid sample to flow continuously through. It must allow photons created by the scintillator to pass into one or more SiPMs for detection while keeping the SiPMs separated from the liquid using a window or other watertight barrier.

The flow cell along with supporting electronics and light tight enclosure will have to fit within a fume cabinet with internal dimensions of 164 cm width by 60 cm depth by 112 cm height, for experiments with open sources (discussed in Chapter 5).

4.2 Methods for Creating a Granulated Scintillator

To find the best method of converting the rough offcuts of BC408, and $\text{CaF}_2(\text{Eu})$ from Advatech, multiple powdering methods were investigated and are outlined in the chapter sections below.

4.2.1 Grinding Stone Method

The first method to be attempted was using a diamond sharpening stone, the scintillator (BC408) and stone were placed into a container of deionised water so that as powder was produced it would disperse into the water as to not escape into the atmosphere. By hand the block of scintillator was scraped across the stones face towards the surface of the pool. Periodically the stone was fully submerged into the water to allow powdered scintillator to make its way into the water. Once enough powder was collected the container was left over multiple days for the water to evaporate leaving the powdered BC408 behind.

It was quickly apparent that this method would be unsuitable, an hour of grinding produced a small thin layer of powder on the pool which would stick to the sides

of the tub making its removal difficult once the water had evaporated. Due to these difficulties, the method was not investigated further.

4.2.2 Ball Mill Method

A ball mill uses metal balls and flakes placed in a rotating tumbler to slowly break down a material introduced, the resulting powder mixes directly with the metal granules and therefore must be separated afterwards, this also greatly increases contamination from metal into the resulting scintillator powder.

Figure 4.2 shows a block of BC408 which has been left in the ball mill overnight, before milling the BC408 had a clear plastic-like appearance but afterwards was completely clouded with minimal difference in shape. In conclusion, this method is completely unsuitable as it was unable to break down the scintillator block and resulted in great amounts of contamination attaching to the surface of the scintillator that cannot be easily removed.



Figure 4.2: Two sections of BC408 scintillator both before (left) and after (right) being placed in the ball mill overnight.

4.2.3 Blade Grinder Method

The next method to be investigated involved an industrial blade grinder. A block of scintillator (BC408) is added into the grinding container and then left over a 4 min to 14 min period to process, every minute a sample was taken for testing with a Mastersizer 2000. From testing, this method can quickly produce finely powdered scintillator of both BC408 and $\text{CaF}_2(\text{Eu})$, an example of which can be seen in Figure 4.3.



Figure 4.3: Result of granulating BC408 within the blade grinder.

The Mastersizer 2000 can measure the size distribution of the granules using laser diffraction. The resulting data is displayed in Table 5 and plotted in Figure 4.4, the data consists of three percentiles: D_x (10), D_x (50) and D_x (90). Where each percentile measures the particle diameter size (μm) contained within 10%, 50% and 90% of the granulated scintillators total volume. For example a D_x (90) value of $0.64 \mu\text{m}$ means that 90% of the sample has a size of $0.64 \mu\text{m}$ diameter or smaller.

Table 5: Size distribution of ground BC408 obtained using Mastersizer 2000 (values have been averaged from multiple measurements of identical sample).

Grinding Time (Minute)	D_x (10) ($\mu\text{m dia} \pm 3\sigma$)	D_x (50) ($\mu\text{m dia} \pm 3\sigma$)	D_x (90) ($\mu\text{m dia} \pm 3\sigma$)
4	23.98 ± 0.33	47.08 ± 1.13	142.40 ± 1.64
6	13.48 ± 4.24	22.06 ± 5.36	62.54 ± 12.42
8	9.04 ± 4.16	15.98 ± 4.69	41.51 ± 10.34
10	6.32 ± 1.27	11.3 ± 1.46	32.03 ± 3.25
12	0.42 ± 0.00	0.50 ± 0.01	0.64 ± 0.02
14	0.42 ± 0.00	0.49 ± 0.01	0.65 ± 0.06

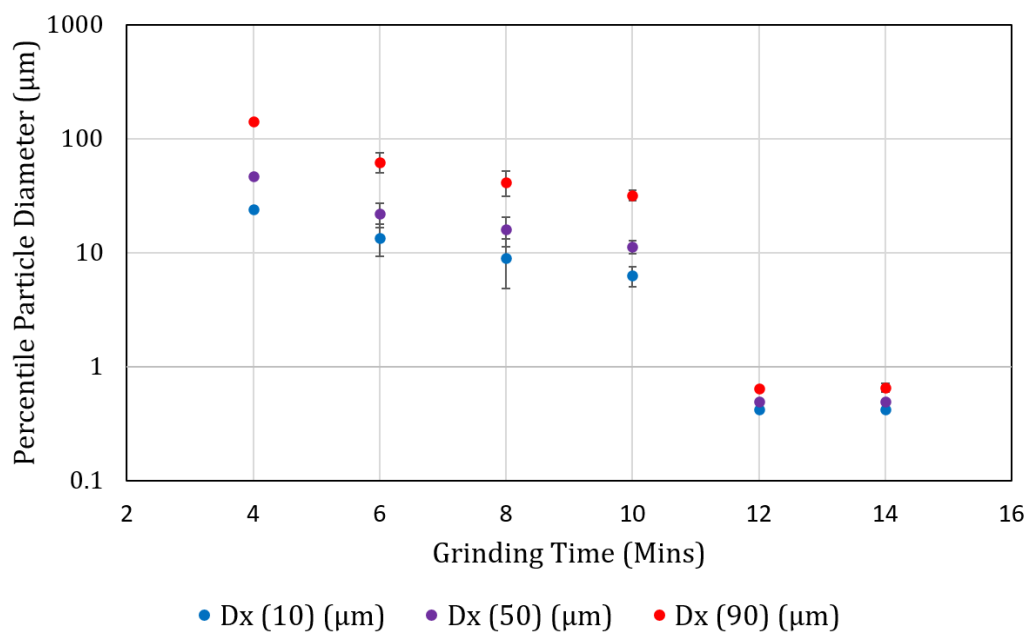


Figure 4.4: Plot of granulated BC408 size distribution against grinding time, data taken from Table 5.

The longer the scintillator was left to grind, the smaller the average size of the resulting powder, with the majority of the powder reaching an ideal radius for tritium detection ($10\ \mu\text{m}$) between 10 minutes and 12 minutes into grinding.

After using the blade ground BC408 and $\text{CaF}_2(\text{Eu})$ in experiments with the liquid scintillator counter (LSC) as discussed in section 4.6. It was noticed that the powder had yellowed over the following months as can be seen in Figure 4.5. The yellowing of the scintillator would increase the optical attenuation of scintillation photons therefore resulting in lower detection rates.



Figure 4.5: Ageing effect of vial containing dilute tritiated water with blade ground $\text{CaF}_2(\text{Eu})$ scintillator (left vial) alongside a vial containing granulated $\text{CaF}_2(\text{Eu})$ produced using a mortar and pestle (right vial, discussed in section 4.2.4).

It is believed that this yellowing is caused by contamination added to the powder while being crushed within the blade grinder. Inspection of the blades showed wear and tear, implying metal flakes had made their way into the sample. Over time due to the moisture, these flakes would rust hence causing the yellowing seen. While the grinder is stainless steel, holding a magnet to the blades showed they were not magnetic and therefore a magnet could not be used to remove the contaminate. A suggested alternative separation method could be to add chemicals capable of dissolving the contamination without affecting the scintillator, then washing the scintillator within a sieve.

4.2.4 Mortar and Pestle Method

As discussed within in the Literature Review (section 2.7.15) a method previously used for creating a granulated scintillator involves simply crushing the scintillator in a mortar and pestle, this quickly produced a large volume of product (approximately 20 g per 5 minutes). It was found in practice to be only suitable for $\text{CaF}_2(\text{Eu})$ which would easily shatter. On the other hand, BC408 could not be easily ground with any flakes of material getting stuck in the pores of the mortar which quickly lowered its grinding ability.



Figure 4.6: Image of $\text{CaF}_2(\text{Eu})$ crushed using the mortar and pestle method.

Another downside of this method was that grinding had to be performed by hand and regular breaks needed to be taken. Also grinding too vigorously would result in scintillator powder being spilt lowering the overall yield. Even with these downsides, the mortar and pestle method proved to be ideal for producing $\text{CaF}_2(\text{Eu})$ powder. For any BC408 testing, powder from the blade grinder will be used.

Also, as the resulting powder does not have a uniform particle size, separation using an auto sieve was used to filter the powder into multiple size distributions for further testing (discussed in section 4.4).

4.3 Potassium Chloride Liquid Packs

In the initial design of the back-end electrical system, access to open sources was limited and therefore laminated packs containing potassium chloride (KCl), granulated scintillator and deionised water were created, these packs could then be added on top of the SiPMs for counting, scintillation photons from interactions between the sample and scintillator could pass through the transparent sheets to the detector. KCl contains trace amounts of radioactive potassium (^{40}K) and can be dissolved in water. ^{40}K decays by three methods: Beta decay, electron capture and gamma decay, the maximum energy of these decay methods is 1.311 MeV, 1.505 MeV and 1.46 MeV respectively [130].

To test the electrical system with this waterborne source, two packs were created (shown in Figure 4.7) using laminated plastic sheets which would protect the moisture sensitive SiPMs from the samples. The edges of the packs were sealed using a strip heat sealer to contain the samples, this sealer was also used for producing the laminated flow cells discussed in section 4.11. A granulated BC408 scintillator created using the blade grinder method was added into both packs along with the samples of KCl and deionised water, the masses of which are displayed in Table 6.

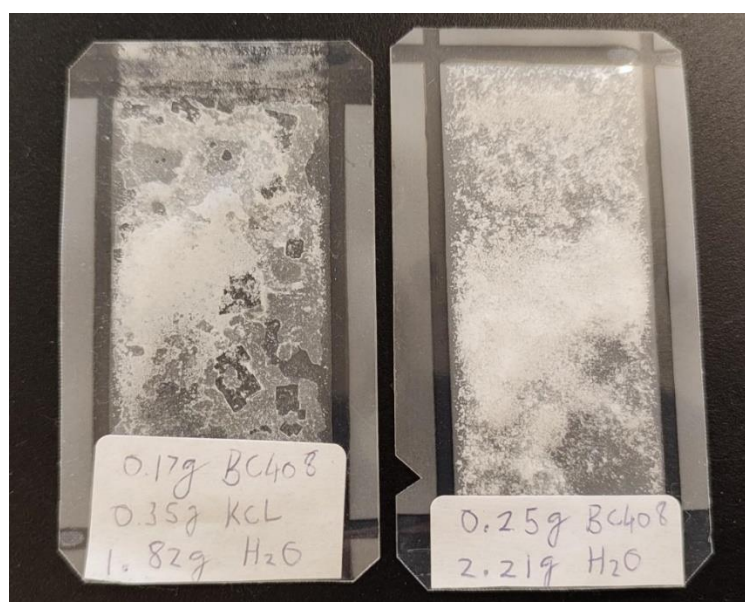


Figure 4.7: Image of both KCl packs. After the addition of granulated scintillator, KCl, and deionised water, all four sides were sealed using a manual hand sealer. The packs allowed the detector to be tested with a liquid source without risking damage to the detector electronics.

Table 6: Contents of both laminated sample packs.

Pack Name	KCl Added (g)	Deionised Water Added (g)	Granulated BC408 Added (g)
Background	0.00	2.21 ± 0.01	0.25 ± 0.01
KCl	0.35 ± 0.01	1.82 ± 0.01	0.17 ± 0.01

Ideally, the mass of the scintillator within each pack would be identical. A weighing scale was used to measure the mass of the scintillator within each pack, matching these masses was difficult as the pack was sealed before measurement in order to stop the contents from spilling onto the scale.

To find the activity contributed from the addition of KCl into the pack, firstly, the mass of potassium (K_g) added must be calculated using equation (4.1). Equation (4.2) can then be used to calculate mass of radioactive potassium-40 ($^{40}K_g$).

$$K_g = KCl_g \frac{K_{g/mole}}{KCl_{g/mole}} = 183.56 \pm 5.24 \text{ mg} \quad (4.1)$$

$$^{40}K_g = K_g \times 0.0117\% = 21.48 \pm 0.61 \mu\text{g} \quad (4.2)$$

Where KCl_g is the mass of KCl added, $K_{g/mole}$ and $KCl_{g/mole}$ are the grams per mole of potassium and potassium chloride respectively. 0.0117% is the percentage abundance of naturally occurring ^{40}K within potassium. Finally, the decay rate of this ^{40}K can be calculated with equation (4.3) and (4.4) [131].

$$N = \frac{m \times N_A}{M} = 3.24 \times 10^{17} \pm 9.19 \times 10^{15} \text{ Atoms} \quad (4.3)$$

$$\text{Sample Activity} = \frac{N \ln 2}{\tau} = 5.57 \pm 0.16 \text{ Bq} \quad (4.4)$$

Where N is the number of radioactive nuclei, m is the mass of ^{40}K in grams, N_A is Avogadro's constant, τ is the half-life of ^{40}K (4.027×10^{16} seconds [131]) and M is the molar mass of ^{40}K (39.9640 g/mol [132]). Therefore, the activity within the KCl pack is approximately 5.57 Bq.

These packs were then in turn placed upon the SiPM sensor head and counted. The background spectrum was taken over 1.2 hours followed by a measurement of the KCl Pack for 0.8 hours. Note the detector was configured with a single channel and settings identical to that used for the gamma calibration (discussed in section 3.11). The recorded spectra are plotted in Figure 4.8.

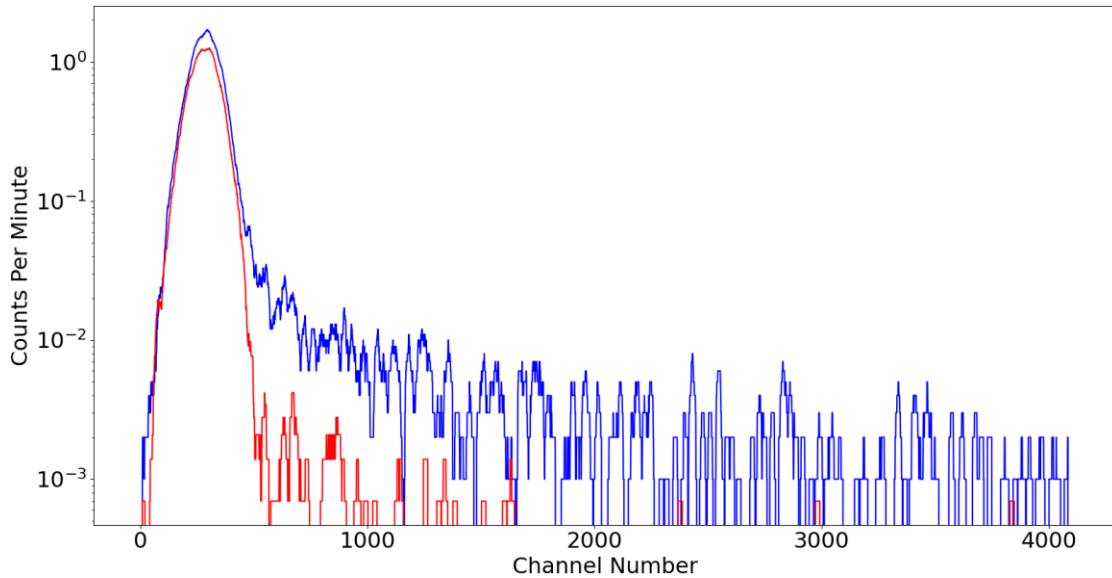


Figure 4.8: Captured raw spectrum data of background pack (red) and KCl pack (blue). Note spectrum counts have been plotted with log scale.

Measurements of the background obtained 201.6 CPM increasing to 279.1 CPM with the KCl pack, a difference of 77.4 CPM. From this, an estimated detection efficiency can be calculated using equation (4.5).

$$\eta_{K-40} = \frac{\text{Increase in CPS}}{\text{Activity added}} \times 100\% = 23.2\% \pm 2.9\% \quad (4.5)$$

As a result of this experiment, it has been shown that the developed backend system can detect a water dissolved radioactive source (potassium-40) using a granulated BC408 scintillator. It has also shown that clear laminated sheets allow photons created by the scintillator to pass and reach the SiPM while protecting the SiPM.

4.4 Auto Sieve Separation

With a method established to produce a scintillating powder, the next step requires particulates to be separated based on their size, so that each group size can be compared to find an ideal size for low energy beta detection.

An auto sieve is a vibrating platter in which a stack of sieves can be added and fixed. Auto sieves can be used for a wide range of applications from soil separation to check-screening food ingredients. For our application, this apparatus can be

used to separate hand-ground $\text{CaF}_2(\text{Eu})$ into a range of sizes as shown in Figure 4.9.

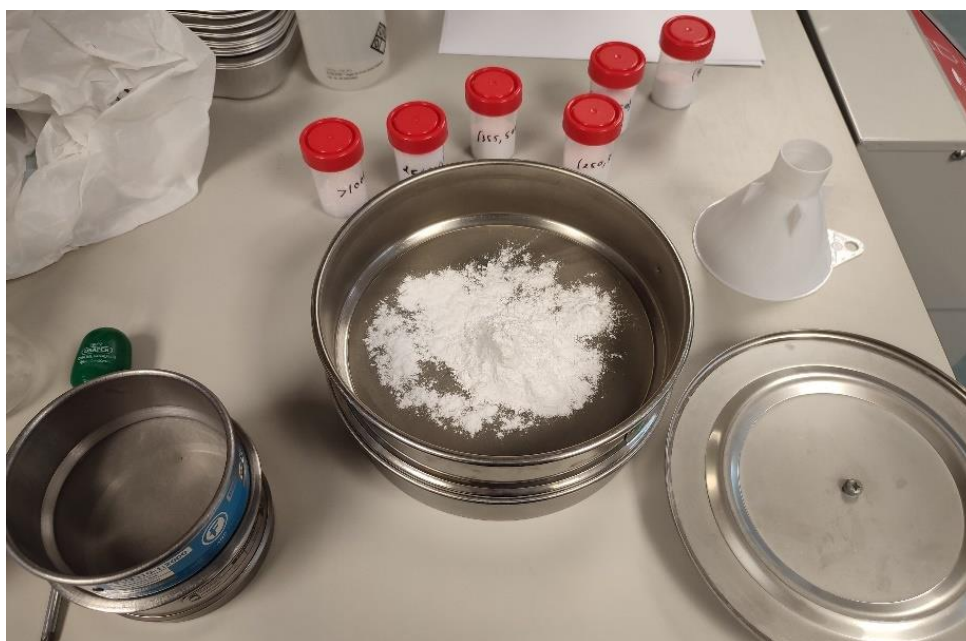


Figure 4.9: Final step of sieve separation, powder at and below $90\ \mu\text{m}$ is added to a $50\ \mu\text{m}$ sieve.

The usage of the sieve is as follows:

1. Each sieve was washed in an ultrasonic bath for 30 minutes with a small amount of added detergent to remove any surface grime.
2. Sieves were rinsed to remove all detergent and inspected for any debris stuck in the mesh. A thin brush was used to remove any debris remaining.
3. A drying cabinet was used overnight to remove all moisture.
4. Sieves were then stacked with larger mesh sizes towards the top of the tack, scintillator was then poured over the top sieve.
5. The stack was then fixed into the vibrating platter and left for 10 minutes on power level 8. A further 5 minutes was given to ensure that the powder had settled.
6. In turn, the contents of each sieve were then poured onto a clean sheet of paper, the handle of a heavy screwdriver was used to lightly tap around the outer edge to help detach any powder stuck to the sieve.

7. Using a funnel, the scintillator was poured from the paper into a storage container. After completion all sieves were washed and inspected.

4.5 Liquid Scintillation Counting Granulated $\text{CaF}_2(\text{Eu})$

Finer powders are more difficult to contain in flow cells as they can clog pores in filters and require higher back pressures to allow a consistent flow rate compared to their coarser counterparts [126], and so there is a trade-off between the size of powders that can be reliably contained using filters etc. and their ability to detect low energy betas. To ascertain the optimal size, the detection efficiency of different particle sizes has been determined. $5.00 \text{ g} \pm 0.01 \text{ g}$ of sieved $\text{CaF}_2(\text{Eu})$ powder of a specific size range was added to a glass vial along with $1.80 \text{ g} \pm 0.01 \text{ g}$ of diluted tritium producing a solution with an activity of $2,109.9 \text{ Bq g}^{-1}$. A set of control vials was also produced with $1.80 \text{ g} \pm 0.01 \text{ g}$ of deionised water mixed with the powdered scintillator instead of the diluted tritium to determine background count rates. All vials were then placed in a Tri-Carb 3170TR/SL liquid scintillation counter [133] for 240 minutes each and the activity was monitored between a lower limit of 2.0 keV and an upper limit of 18.6 keV. The resulting data collected by the LSC are shown in Table 7 for active sample vials and Table 8 for background vials. The difference in count rate between background and active vials is plotted in Figure 4.10.

Table 7: Masses within sample vials containing tritiated water, for powder testing with the LSC. Weights of scintillator added to each vial are to within ± 0.0001 g. All measurements were repeated three times for four hours each and statistics calculated. Background counts have been removed from listed counts.

Vial Number	Size Range (μm)	Detected Count (CPM $\pm 3\sigma$)	Powder Detection Efficiency %
1	500 to 1,000	31.3 \pm 0.6	0.01
2	355 to 500	45.5 \pm 4.6	0.02
3	250 to 355	61.8 \pm 5.2	0.03
4	125 to 250	100.8 \pm 2.5	0.04
5	90 to 250	306.9 \pm 12.6	0.14
6	50 to 90	383.4 \pm 12.4	0.17
7	≤ 50	440.7 \pm 29.9	0.20

Table 8: Activity of non-active control samples denoting background activity. All measurements were repeated three times for four hours each and statistics calculated.

Vial Number	Size Range (μm)	Detected Count (CPM $\pm 3\sigma$)
8	500 to 1,000	3.8 \pm 0.4
9	355 to 500	3.8 \pm 0.2
10	250 to 355	3.9 \pm 0.5
11	125 to 250	3.9 \pm 0.7
12	90 to 250	3.9 \pm 0.1
13	50 to 90	3.8 \pm 0.5
14	≤ 50	3.6 \pm 0.2

A clear trend can be seen in Figure 4.10, showing that as scintillator particle size decreases, the count rate detected by the LSC increases, resulting in a higher detection efficiency when using a finer particle size. This can be attributed to the smaller particulates having a greater surface area between the sample and scintillator and therefore a greater probability of a beta particle entering and interacting with the scintillator. The peak detection efficiency for tritium detection was measured at $0.20\% \pm 0.01\%$, for the size range up to $50 \mu\text{m}$, and so this sieve grid size was used to produce the powder for the laminated flow cells tested with dilute tritiated water (see section 5.2).

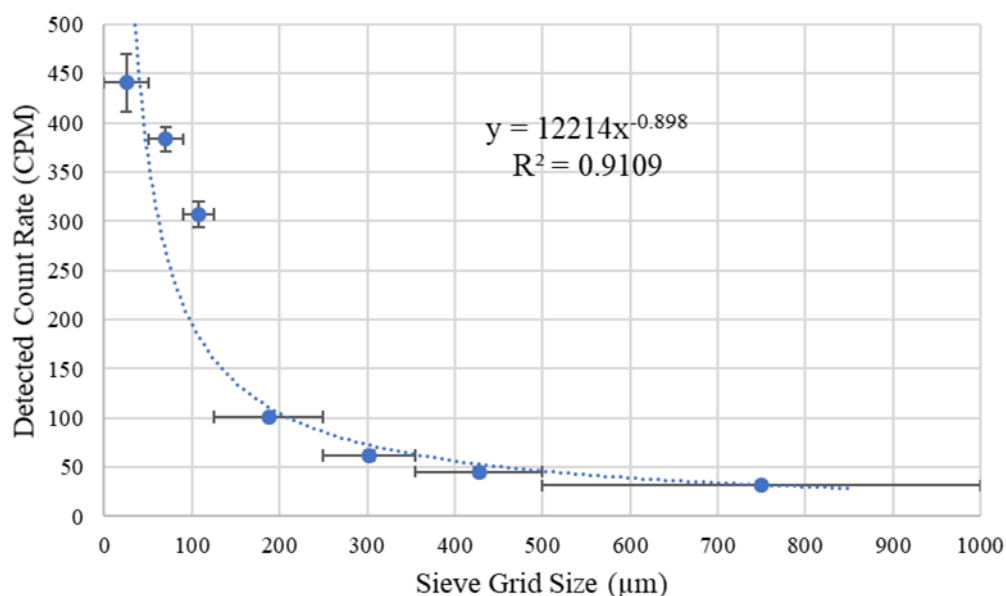


Figure 4.10: Graph of the resulting data from the counted vials containing mixtures of dilute tritium and $\text{CaF}_2(\text{Eu})$ scintillator. A power trendline (dotted blue line) has been added to the plot along with its R^2 value and trendline equation.

The count rates obtained for the finest powder group show an improvement over previously published results [127] which found for their $50 \mu\text{m}$ granulated $\text{CaF}_2(\text{Eu})$ scintillator a relationship of:

$$\text{CPM} = 0.1367 \times \text{Activity Concentration} \left(\frac{\text{Bq}}{\text{g}} \right) + 0.191 \quad (4.6)$$

Here, the concentration of tritium used in the vials was 2109.9 Bq g^{-1} resulting in a count rate of $440.7 \text{ CPM} \pm 29.9 \text{ CPM}$, while the relationship described in the previous publication formulates a count of approximately 288.6 CPM when

calculated for the same concentration. Notably, the size range of the scintillator had no clear effect on the background count rate, keeping to an average of 3.8 ± 0.6 CPM.

4.6 Liquid Scintillation Counting Granulated BC408

A granulated BC408 and $\text{CaF}_2(\text{Eu})$ scintillator was created using the blade grinder technique only. To compare this blade ground powder against $\text{CaF}_2(\text{Eu})$ produced using the mortar and pestle, blade ground BC408 and $\text{CaF}_2(\text{Eu})$ were each added to two vials and mixed with rather deionised water or dilute tritiated water, ethanol was also added with the BC408 scintillator to help the hydrophobic powder mix. Grinding and testing were conducted on the same day and therefore the BC408 did not start to yellow over the testing period. The activity of tritium added to the vial and resulting count rate detected by the LSC can be seen in Table 9 below.

Table 9: Weights and LSC count results from vials containing tritium and granulated BC408 or $\text{CaF}_2(\text{Eu})$ scintillator created using blade grinder.

Scintillator Type	Total Vial ^3H Activity (Bq)	Detected Count (CPM)	Powder Detection Efficiency (%)
$\text{CaF}_2(\text{Eu})$ (Blade Grind)	0	3.6	N/A
$\text{CaF}_2(\text{Eu})$ (Blade Grind)	3,744.70	24.7	0.01
BC408 (Blade Grind)	0	5.0	N/A
BC408 (Blade Grind)	3,743.66	357.9	0.16

The collected data shows that granulated BC408 can also be used for low beta detection, achieving a maximum detection efficiency of 0.16%, but its working life would be short due to the added impurities. Blade ground $\text{CaF}_2(\text{Eu})$ on the other hand performed poorly to its mortar and pestle counterpart which could be also related to the added impurities from the blades.

4.7 Scintillator Moulding

Prior literature has investigated the moulding of scintillators for additive manufacturing, where a plastic scintillator cube was printed using a 3D printer fed with a plastic scintillator filament [134]. Injection moulding of polystyrene pellets combined with dopants has also been developed using a screw extruder [135].

As previously mentioned, one downside of granulated scintillators is that filtering is required to hold the scintillator in place within the flow cell, otherwise the flow of the sample could carry particles from the flow cell. One method to diminish the movement and escape of granulated scintillators is the use of a heat treatment. If a powder is heated to its softening point, particles can begin to mould and glue to their neighbours, once cooled the particles will no longer move independently forming a sponge-like material which still contains pores for a sample to flow through.

$\text{CaF}_2(\text{Eu})$ has a high softening point of $1,087^\circ\text{C}$ making it difficult to mould with common lab equipment. But BC408 has a much lower softening point of 70°C [136], and therefore a bench top hotplate would be capable of raising the scintillator to a suitable melting temperature.

To stop the scintillator sticking to the hotplate as it was heated, a backing sheet was added, this sheet took the form of a clear lamination sheet (used previously in section 4.3). This layer would create a waterproof barrier protecting a PMT or SiPM placed beneath, while allowing scintillation photons to pass from the moulded scintillator.

Lamination sheets are made from two plastics a polyethylene terephthalate (PET) outer layer and an ethylene-vinyl acetate (EVA) inner layer, the latter possessing a low melting point around 100°C [137] allowing it to adhere to the scintillator as they are heated in contact. Figure 4.11 shows the first moulding experiment performed, approximately 1 g of granulated BC408 was poured onto a 4 cm by 4 cm patch of a lamination sheet. This sheet was then placed onto a hotplate for

5 minutes at 200°C before being removed and left to cool. A second patch also was created with BC408 but was not heated, this was to be used as a comparison.

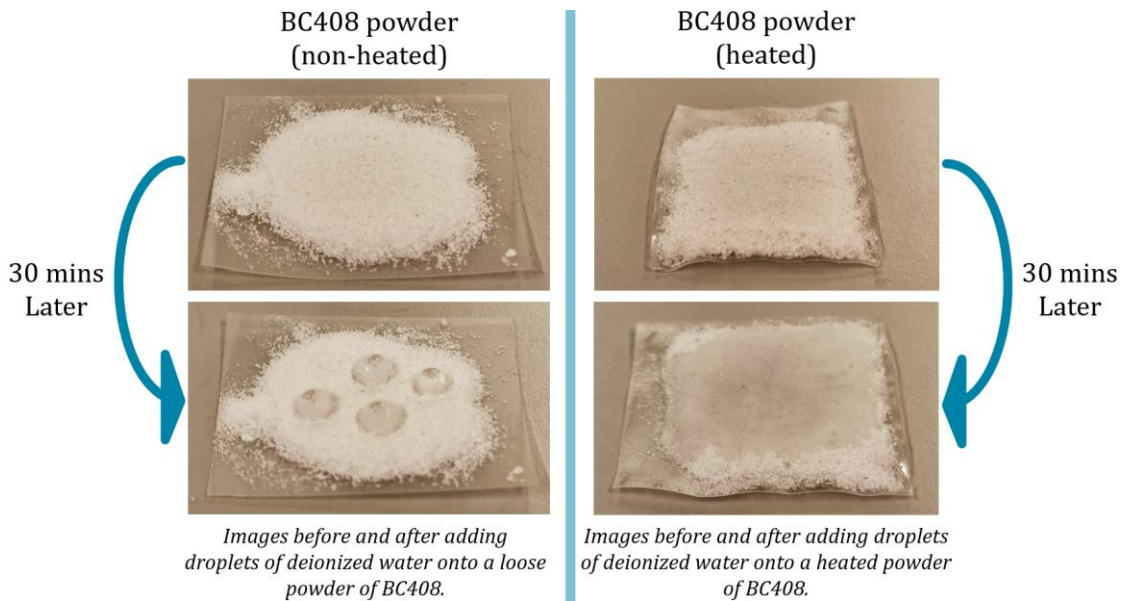


Figure 4.11: Result of droplets placed onto BC408 moulding patches.

The first thing of note is that the heated patch is solid and can be held at any angle without the scintillator detaching. Next, the absorption of water into the powders was tested by placing four drops of deionised water on the surface of both patches. Viewing Figure 4.11 clearly shows that before heat treatment the scintillator is hydrophobic causing droplets to bunch above the powder. But for the heated patch, the water quickly incorporates into the pores of the plastic scintillator.

This improvement of water absorption is of great advantage to low energy beta detection as the surface area will be far superior if the sample incorporates and mixes with the scintillator. Another improvement is in transparency, as the particles are partially melted into their neighbours there is a wider boundary for photons to pass directly from particle to particle, increasing the chance a photon reaches a photomultiplier.

A second experiment was undertaken with the aim of creating a waterproof packet for a SiPM with an exterior covered in BC408 scintillator. The steps of this manufacturing process are shown in Figure 4.12. Two sheets are laminated together leaving one end open, a forming rig was created to suspend the package

in the air while using a copper bar placed into the package to heat it from the inside out. Then powdered BC408 was poured onto the surface, flattened, and heated for 2 minutes at 240°C.

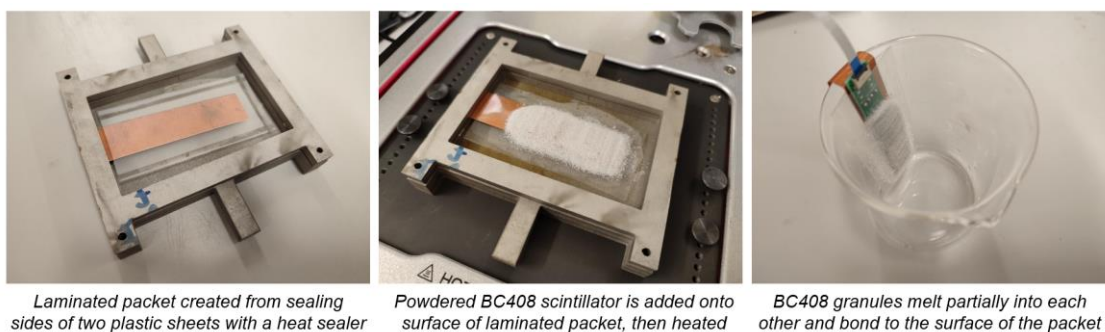


Figure 4.12: Images of the BC408 covered packet being manufactured.

After the heating process, a printed circuit board (PCB) was inserted into the package with a SiPM facing towards the moulded scintillator layer. In its current form the pack could be 'dipped' into a liquid sample while protecting the moisture sensitive SiPM within. Due to the discovery that the BC408 granulated scintillator contained impurities, further experiments with the moulded forms were not performed as focus shifted to the use of granulated $\text{CaF}_2(\text{Eu})$.

4.8 Conclusions

The study of granulated scintillators within an LSC has shown that the method presented in this work is capable of powdering a solid block of $\text{CaF}_2(\text{Eu})$ while allowing it to keep its scintillating properties. It has also demonstrated a relationship between size distribution and detected counts for tritiated water, obtaining a maximum detection efficiency of $0.20\% \pm 0.01\%$ and count of $440.7 \text{ CPM} \pm 29.9 \text{ CPM}$ for $\text{CaF}_2(\text{Eu})$ with particle sizes up to $50 \mu\text{m}$.

Multiple powdering methods have been investigated finding that a mortar and pestle produces significant amounts of granulated powder compared to the ball mill and grinding stone and with little introduced contamination, unlike the blade grinder method. The use of the auto sieve for the separation has been fruitful allowing multiple size groups to be tested and compared. As expected, sizes

approaching the ideal size for the detection of tritium show an increasingly better detection efficiency.

The moulding of BC408 has shown that the hydrophobic nature of loose BC408 powder can be greatly altered through heating, allowing liquid samples to mix and take advantage of the greatly increased surface area afforded by a powder as opposed to a solid block.

4.9 3D Printed Flow Cell

This first attempt at a flow cell used a 3D printed body. Included in the flow cell design were inlet and outlet hoses for the addition of tubing, and slots on either side of the flow cell for the addition of two 25 mm diameter sand core filters. These filters consist of fused granulated borosilicate glass, resulting in a pore-filled material permeable to liquids. These filters would keep the granulated scintillator held within the flow cell (see Figure 4.13 and Figure 4.14).

The base of the flow cell allowed the addition of a concave mirror to help re-direct and focus stray photons towards the SiPMs located at the top of the flow cell. A circular window cutout was added to allow photons to leave the flow cell cavity and reach the SiPMs that were placed in contact with the window, a top lid enveloped the SiPM to provide a light-proof enclosure. To keep a watertight seal, rubber sheets cut using a scalpel were placed between each 3D printed layer with four threaded rods passing through all layers. Four nuts could then be used to fasten and compress the rubber sheets with the layers to form a watertight flow cell. A CAD model of the flow cell and its layers is shown in Figure 4.15.

Chapter 4: Flow Cell Development

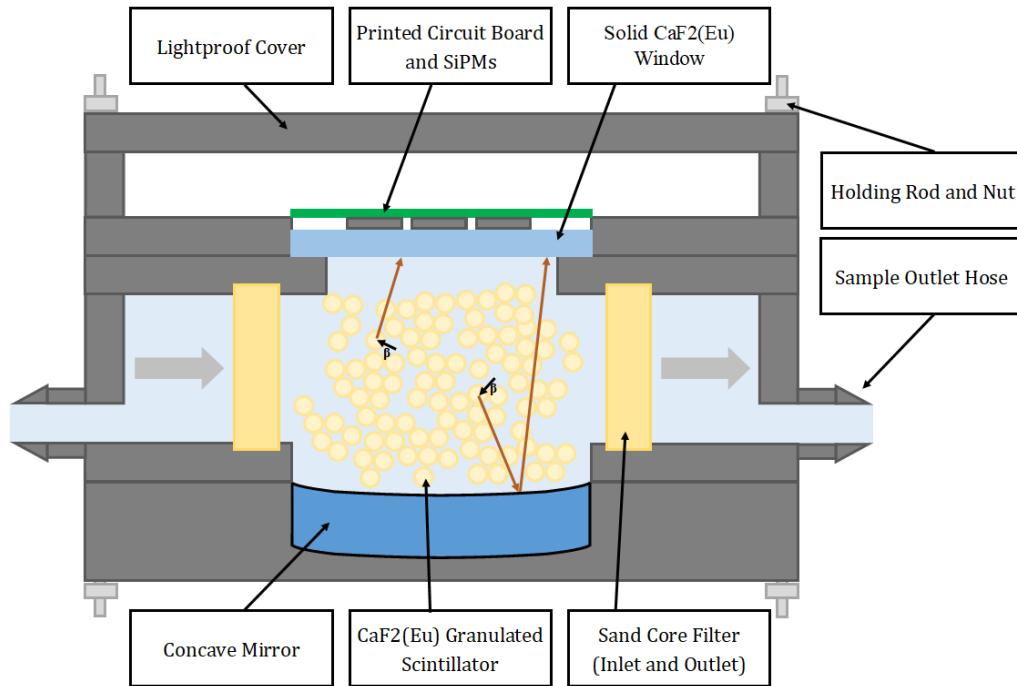


Figure 4.13: Diagram of first flow cell design labelled with key parts.

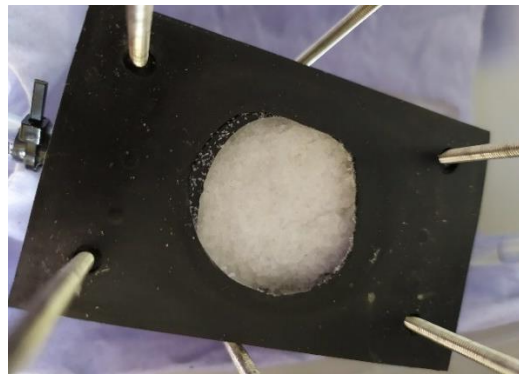


Figure 4.14: Top of 3D printed flow cell filled with granulated BC408 scintillator, before the addition of the window.

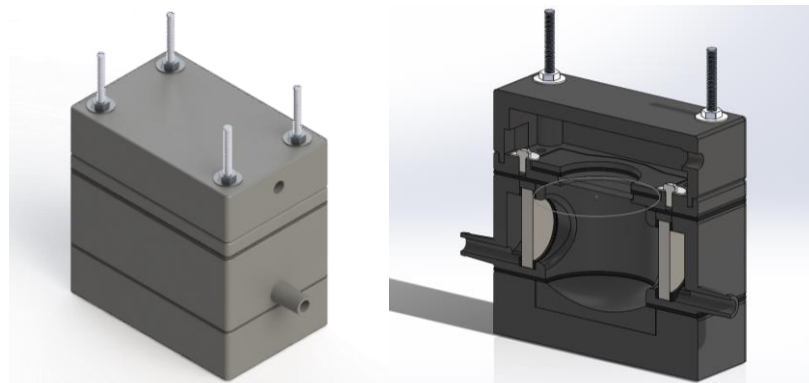


Figure 4.15: CAD rendering of 3D printed flow cell showing internal cavity, window and filters.

In this design the window itself could be a scintillator, being designed to hold a 27 mm diameter solid $\text{CaF}_2(\text{Eu})$ crystal, which would allow the testing of both powdered and solid scintillators.

In reflection the design had many issues, it was difficult to ensure the flow cell was fully filled with the liquid sample as the input and output hoses are located near the bottom of the flow cell. Thus, an air gap was likely to form under the solid $\text{CaF}_2(\text{Eu})$ window, this gap would impede beta radiation from reaching the scintillating window and also vary the sample volume within the flow cell between emptying and filling. As a result, this design led to great uncertainties in detection efficiency and minimum detectable activity (MDA).

Some other issues included that the flow cell casing was designed too large to fit within the 50 mm diameter design constriction and the removal of the light tight cover to access the SiPM required that all layers be loosened resulting in leaks. Finally, the design did not suit itself to coincidence counting as only one window was added. These downsides were addressed in the final design iteration.

4.9.1 Testing 3D Printed Flow Cell with Potassium Chloride

In the early development of the flow cell, potassium chloride (KCl) was used to validate that the 3D printed flow cell could indeed detect radiation. Unlike strontium-90 and tritium which are highly regulated and require strict working practices, KCl is easy to source and safe to handle. It is commonly used as a mineral supplement, a salt alternative, and has many other food related uses. Importantly for waterborne beta detection, it contains approximately 0.0117% of radioactive potassium-40 [131] and is soluble in water. KCl has also been used previously in this work (see section 4.3).

For the testing of the flow cell, a solution was created with 300 g of deionised water with 60 g of dissolved KCl. Using equation (4.1) and (4.2), the mass of radioactive ^{40}K added into the solution can be calculated as 3.68 mg. The activity of the sample was then calculated using equations (4.6) and (4.4) [131], finding an activity of 954.90 Bq.

To find how much of this activity is within the flow cell (which has a cavity volume of 34.925 cm^3), the volume of sample can be divided by the cavity volume. The volume of the sample can be found by taking the sum of the added masses and their respective densities (equation 4.7), then allowing the percentage of sample within the cavity volume to be obtained (equation 4.8).

$$\text{Volume of sample} = \frac{\text{Water}_g}{\text{Water}_\rho} + \frac{\text{KCl}_g}{\text{KCl}_\rho} = 330.3 \text{ cm}^3 \quad (4.7)$$

$$\text{Percentage of sample in cavity} = \frac{34.925}{330.3} \times 100\% = 10.6\% \quad (4.8)$$

The total sample activity within the flow cell cavity was then calculated by multiplying the total sample activity by the percentage within the cavity (equation 4.8), resulting in a decay rate of 100.97 Bq. Finally, the beta and gamma activity can be discerned by multiplying total activity by the percentage probability of the nuclei undergoing beta or gamma decay: 89.25% and 10.67% respectively. A beta decay rate of 90.12 Bq, and a gamma decay rate of 10.77 Bq were determined.

The first experiment using KCl was with the 3D printed flow cell with a solid $\text{CaF}_2(\text{Eu})$ window, no granulated scintillator was used at this point. 300 g of deionised water was passed through the cavity using a pump. A background spectrum was then recorded for 24.3 hours, then 60 g of KCl was added to the water loop and left to mix and pump around the cavity until it had visually dissolved, a second spectrum was then recorded for 26.6 hours. The resulting spectrum has been plotted in Figure 4.16. The electronics used to amplify and detect these pulses are discussed in section 3.3.

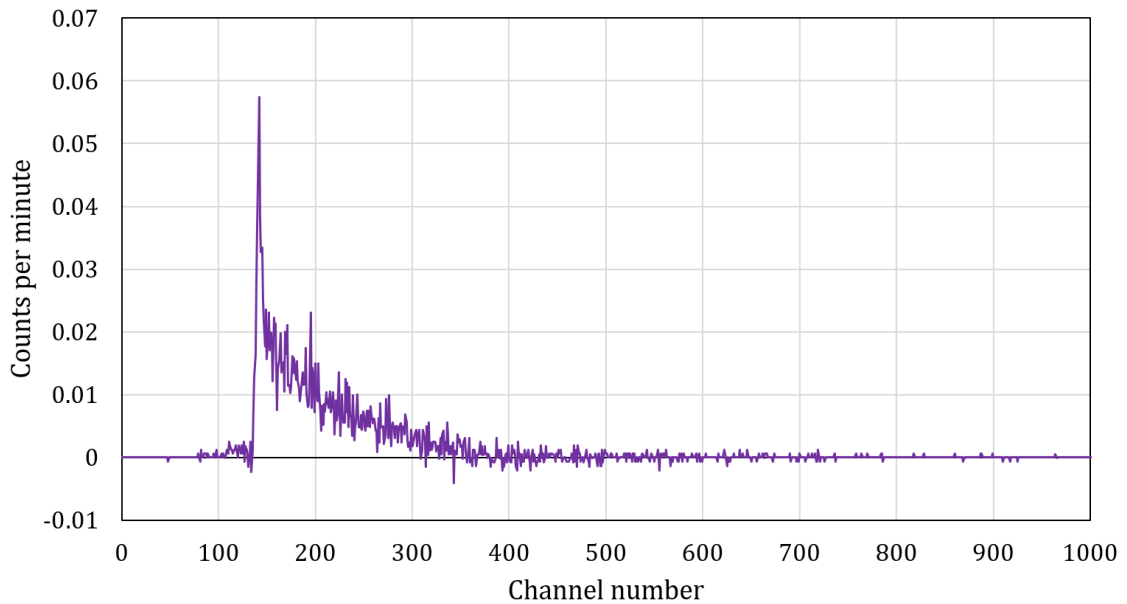


Figure 4.16: Recorded Spectrum containing raw count rate data (CPM) from KCl experiment with 3D Printed flow cell. Background counts have been removed.

In total, the background measurement had an average count rate of 0.7 CPM which increased to 2.7 CPM after the KCl was added to the loop. Assuming that the $\text{CaF}_2(\text{Eu})$ scintillator window can only interact with beta decay, as the activity of ^{40}K has been calculated, the detection efficiency (solid scintillator with KCl sample) can be estimated using equation (4.9).

$$\text{Detector efficiency} = \frac{1.935}{60 \times 90.12} \times 100\% = 0.04\% \quad (4.9)$$

4.10 Layered Flow Cell

Design of a layered flow cell followed the 3D printed flow cell which was too large to fit within a 50 mm borehole and allowed air pockets to build up within the flow cell cavity due to the placement of the inlet and outlet tubing. This layered flow cell was built from circular layers of laser cut clear acrylic, a diagram of the built flow cell is shown in Figure 4.17. The clear acrylic allowed visual inspection of the internal cavity and would act as a window for the SiPM while keeping them isolated from the liquid sample, as can be seen in Figure 4.18. Acrylic contact adhesive was used to adhere each section together, while rubber sheets were

added between key components to allow the flow cell to be taken apart for future maintenance.

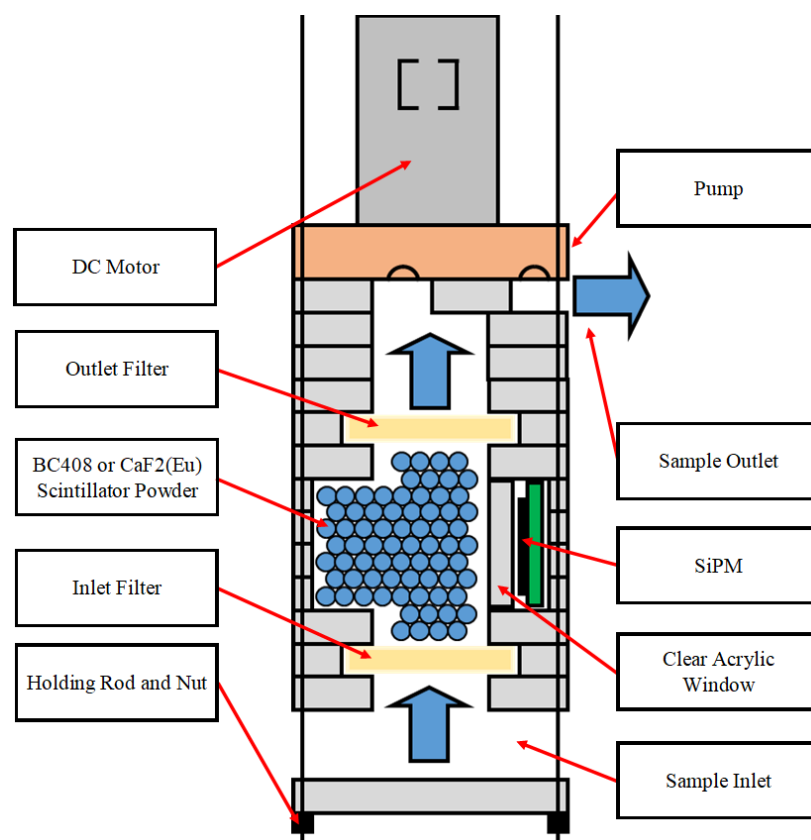


Figure 4.17: Cross-sectional diagram of layered acrylic flow cell design.

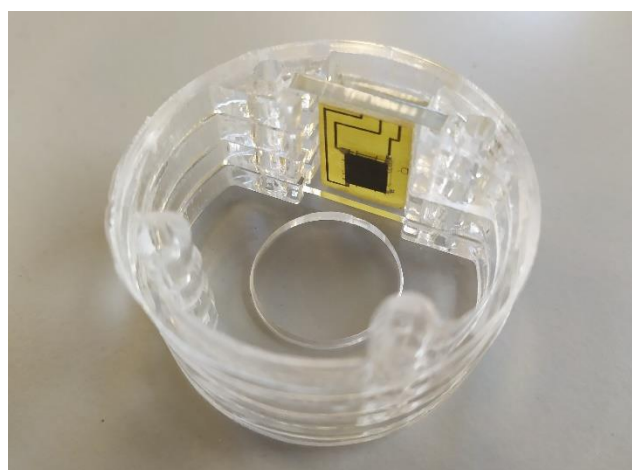


Figure 4.18: Image of inside of layered acrylic flow cell cavity.

The use of threaded rods for holding the layers together was inspired by the previous 3D printed design, the removal of four nuts would allow the flow cell and pump to be disassembled allowing their replacement. Filter paper stretched over

laser cut spacers would hold back the granulated scintillator placed within the flow cell as the sample was pumped through. Figure 4.19 shows a breakdown of the manufactured layered flow cell design with the flow cell's parts shown in order from left to right.



Figure 4.19: Layout of all parts of the laser cut flow cell, from left to right: Pump assembly, sample outlet, outlet filter (filter paper folded over acrylic spacer), cavity top rubber seal, cavity with SiPM holder, cavity bottom rubber seal, inlet filter (filter paper folded over acrylic spacer), inlet seal and faceplate.

Again, there were many downsides to this design, mainly:

- Glueing of the many layers was time consuming and difficult to ensure a watertight bond.
- The use of clear acrylic meant the flow cell would have to be placed in a light tight container or opaque outer casing for experiments.
- Filter paper stretched over laser cut spacers were not very robust as filters, as they could easily be ruptured when the pump was working at its rated voltage (12 V).
- Access to the SiPM for replacement required all layers to be disassembled.
- Design only had room for a single 10 mm by 10 mm SiPM not allowing for coincidence counting or testing of SiPM arrays.

4.11 Laminated Flow Cell

Following on from the previous two design iterations, a new form of flow cell utilising heat-based lamination has been implemented. In this process, two sheets of plastic are adhered along their edges to one another using heat, forming a

watertight seal. The benefit of this over a more conventional block or rectangular flow cell is that many laminated flow cells can be made rapidly with minimal equipment, with a single flow cell requiring 30 minutes of active work followed by two days for the adhesive to cure. The shape created by lamination is suited to coincidence counting as there are two flat transparent sides through which scintillation photons can pass, these sides can then be placed in contact with SiPMs or PMTs, to detect said photons.

Compressed polyester stuffing was used at each end to hold the scintillator within the flow cell. This stuffing had benefits over the previously used circular sand core filters and filter paper stretched over a rigid spacer, as the stuffing could easily fit into the contours of the inner surfaces of the laminated flow cell and would not easily rupture like the filter papers.

A cross-sectional diagram of the flow cell can be seen in Figure 4.20 labelled with its key components, three example beta decays are also included, showing how after entering the scintillator, resulting photons can travel outwards towards the two arrays of SiPMs, which are isolated from the liquid solution via the laminated sheets.

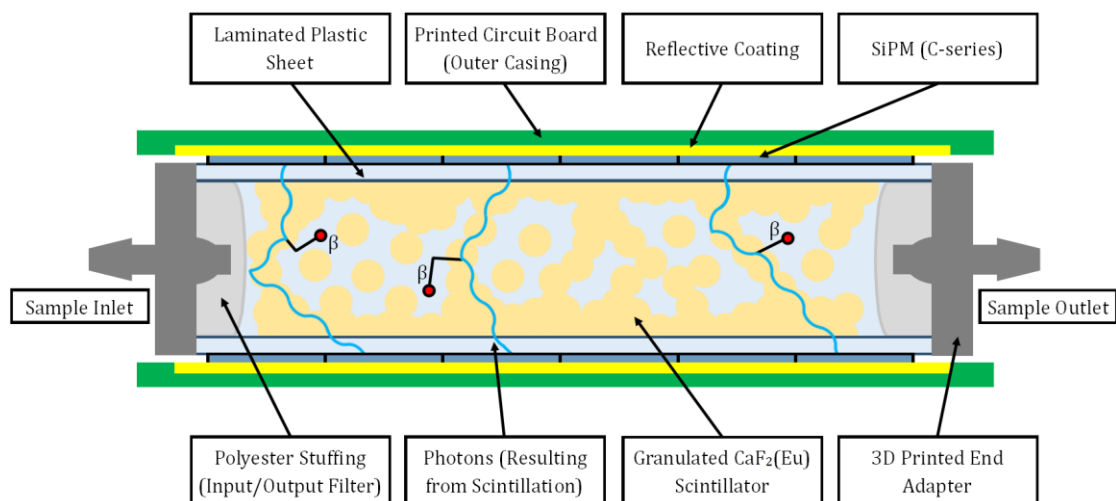


Figure 4.20: Cross-sectional diagram of laminated flow cell with outer casing, within the cavity three beta decays have been added showing paths photons take to reach both SiPMs.

The laminated cavities created for testing in Chapter 5 were filled with powdered scintillator produced in the prior experiment discussed in section 4.5. To start,

particulates with sizes up to 50 μm diameter were selected due to having the highest detection efficiency for tritium compared to the other size groups tested. Polyester filter wool is added into both ends to ensure retention of the scintillator powder during operation. The outer casing compacts the filter material improving its ability to retain the powder. Two stereo-lithographic (SLA, black resin [138]) printed end adapters allow standard clear silicone tubing to be connected to both sides of the flow cell cavity. The adapters have been designed with a ridge for the ends of the laminated envelope to slip into (see Figure 4.21), adding low viscosity glue allows a watertight connection with the flow cell (see Figure 4.22).

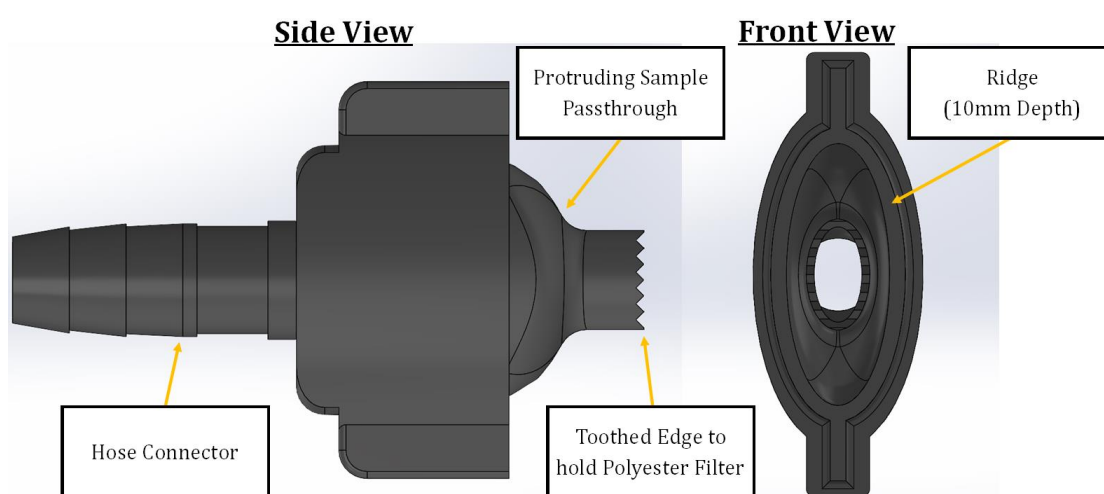


Figure 4.21: Side and front view of 3D printed end adapter labelled with key design features.

Scintillated photons produced in the flow cell are detected by SiPMs. SiPMs have been selected for this design as they can be configured in compact arrays. In this case, a column of SiPMs has been placed along the length of the flow cell. This configuration is easily extendable. The greater the length of the flow cell, the more SiPMs can be integrated resulting in an increase in the total surface area between the sample and scintillator, and an increased light detection area.

Another reason for the use of SiPMs over PMTs is their small thickness of 0.65 mm [90], around 29 times thinner than a comparably sized square PMT (R11265U series [139]) and around five times thinner than the smallest PMT brought to market (R12900U series [140]). The thickness of the sensor greatly affects the overall diameter and thickness of the flow cell assembly, and therefore SiPMs will

allow use of the detector in much more constrained applications like within thin pipes and boreholes. Finally, SiPMs are safer to operate when placed within proximity to water as they function using lower bias supplies, operating off tens of volts as opposed to thousands of volts, lowering the risk of electric shock.

Here, the length of the flow cell was approximately 18 cm end to end. The process of producing the flow cell is as follows, Figure 4.22 also shows the laminates being prepared and packed with scintillator and polyester filters before the end adapters were attached.

- Two rectangular laminate sheets are cut measuring 18 cm by 3.5 cm.
- The sides of the sheets are heat sealed together leaving an opening at each end. Excess sheet material is trimmed.
- One end of the laminated envelope is pinched shut and approximately 5 g of granulated scintillator is added, followed by polyester filter wool into both ends.
- Plastic adapters are bonded onto each end of the filled flow cell creating an enclosed cavity.

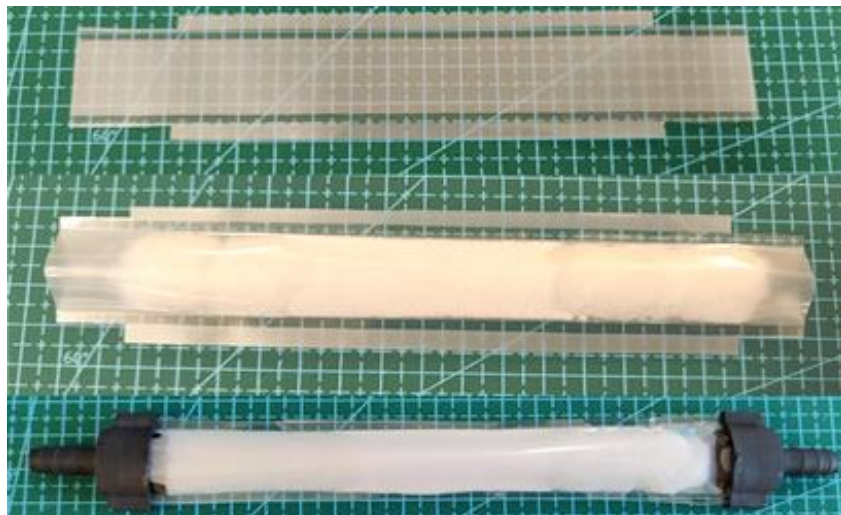


Figure 4.22: Images showing a flow cell being manufactured, (from top to bottom) sheets are cut and laminated, filled and end adapters attached.

To pair with the flow cell, an outer casing was devised to improve the overall rigidity of the cavity as well as to provide an anchor point for multiple SiPMs to run alongside the laminated faces. A custom printed circuit board (PCB) manufactured by JLCPCB [141] allowed the selective placement of a strip of solder pads compatible with the Onsemi C-series line of SiPMs as well as un-masked 'copper pours' which improves the inner reflectivity of the casing, acting as mirrors reflecting stray photons back into the cavity.

Multiple M2 screw holes were also included to allow even pressure across the whole length of the flow cell. Spacers made from small strips of PCB limited the thickness of the flow cell to approximately 4.8 mm while also helping to reduce light leakage entering from the edges. It was noted while testing the system that the pressure applied by the casing had a large effect on the flow rate through the flow cell and that making the casing too loose would allow scintillator powder to migrate into the polyester stuffing, reducing detection efficiency (discussed further in section 5.2.1). The addition of foam around the polyester filters helped to pinch the ends around the scintillator keeping it within the centre of the flow cell cavity once the casing was in place.

For the final design iteration of the casing design, thermal vias and external copper pours were added around the SiPMs to improve the temperature regulation from the cooling system (discussed in section 4.11.4) by reducing the thermal resistance across the casing walls. Discussion and modelling of thermal vias show a clear relationship between the number of vias and the thermal resistance across a simulated square PCB board [142]. PCBs utilising thermal vias have also been tested with liquid cooling systems [143] similar to the cooling system that will be discussed in this work. Figure 4.23 shows labelled images of the designed and tested flow cell both before and after assembly of the outer casing.

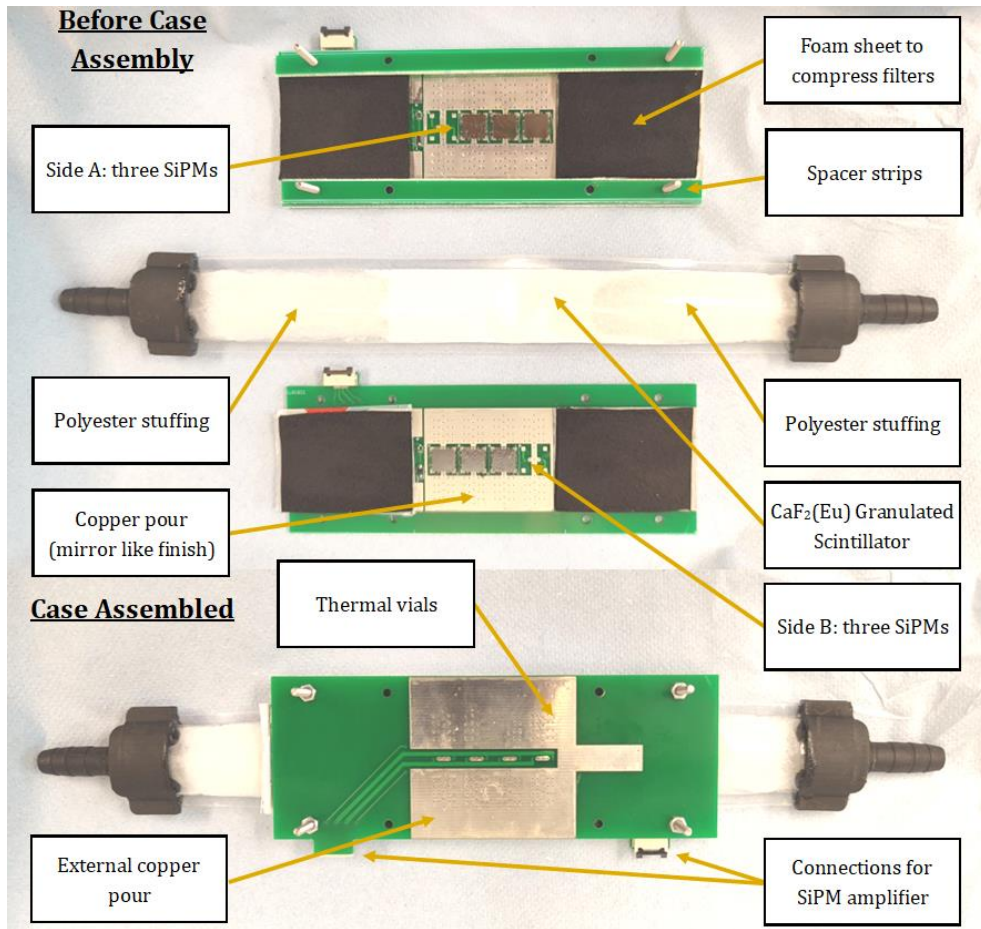


Figure 4.23: Image of flow cell and casing parts both before and after assembly of the outer casing around the laminated flow cell. Two flat flex cable (FFC) connectors allow rapid connection and disconnection of each SiPM array from the electrical system.

4.11.1 Flow Cell Filter Alternative

While manufacturing the flow cell, another type of filter was created using porous aquatic foam with 45 pores per inch (PPI). A heated line cutter was used to create extruded oval shapes so that the foam would fit the contour of the inner laminated sheet. The process allowed the rapid production of foam filters. Figure 4.24 shows the foam cutout and a flow cell containing said foam filter.

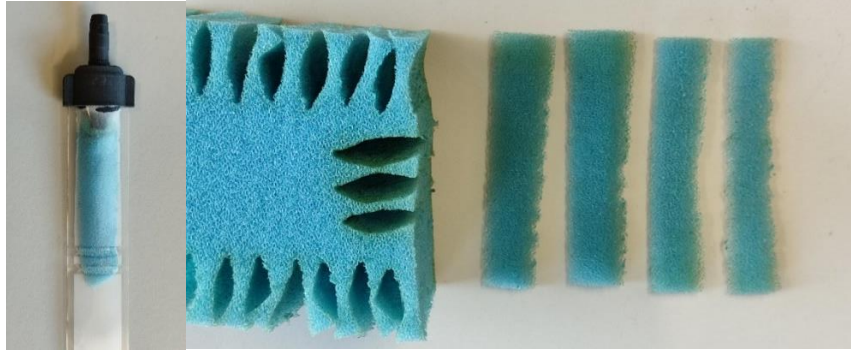


Figure 4.24: Image of manufactured flow cell with cut foam filter (left) and image of multiple foam filters being cut from solid block of 45 PPI aquatic foam.

The filters could also be bonded to the inner side of the laminated sheets by laminating horizontally across the flow cell. These filters were cut by hand leading to variations in shape and size, a cutting guide could be added to opposing sides of the foam to guide the line cutter around a predefined shape to improve repeatability.

4.11.2 Sensor Head Design and Development

The electrical system discussed in Chapter 3 was used for the laminated flow cell with some improvements to configurability. The improved system (shown in Figure 4.25) is made up of three key parts; a two-channel data acquisition board (DAQ), two independent SiPM amplifiers and two sensor heads. In addition, spectra data processed by the DAQ is sent to a single board computer (Raspberry Pi Zero W) so that they can be stored within a database for future access. The system can create energy spectra based on pulses emitted by SiPMs when scintillated photons reach both SiPM arrays, each SiPM array has its own SiPM amplifier board and analogue to digital converter (ADC) which from now on will be referred to as a 'channel'.

Additional rotary switches added to the amplifier boards allow the gain and time constants to be configured easily in testing with 4,096 possible settings. These settings were varied to maximise the spectral range for tritium decay while keeping noise to a minimum. Ribbon cables have been used with matching FFC connectors to allow parts to be easily swapped, reconfigured, and replaced. A total of six SiPMs have been used, three connected in parallel for each channel.

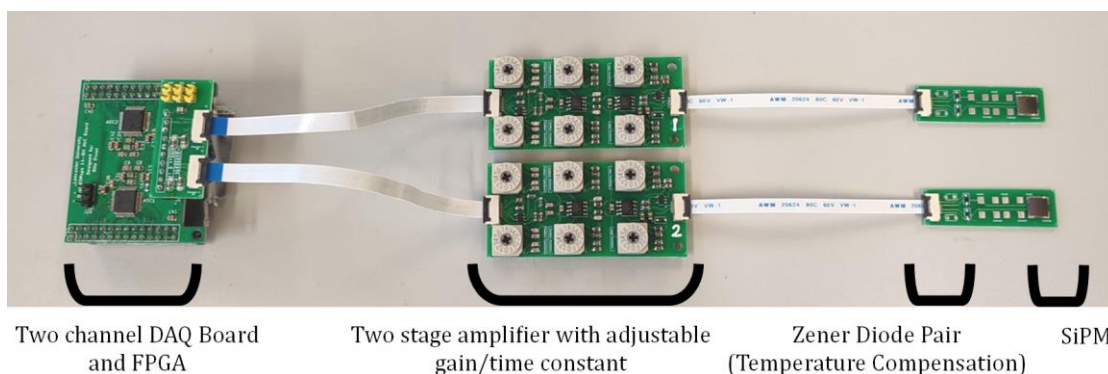


Figure 4.25: Image of electrical system used in the flow cell detector. Two channels perform coincidence counting with the SiPM sensor heads placed across the centre of the flow cell. Temperature stabilising Zener diodes have been placed in close proximity to the SiPMs to ensure good temperature matching.

As both sides of the flow cell are transparent, SiPMs can be added to both sides for coincidence counting. As previously discussed in Chapter 2, other detectors for tritium have also previously implemented coincidence counting, most commonly using photomultiplier tubes [66], [70], [71], [72], [73]. Coincidence counting reduces false counts caused by noise in the electronics and dark pulses from the SiPMs or PMT, which would otherwise overshadow counts from tritium decay. Prior literature on coincidence counting using two SiPMs integrated into the same chip package (3 mm by 3mm total size) has also been successfully implemented, demonstrating the suppression of dark count rate to 1.69% of that compared to non-coincidence counting [144], an oscilloscope was used to perform the pulse detection while a negative bias of 27 V was applied to the SiPMs. Coincidence counting using SiPMs has also been implemented for 3 mm by 3 mm C-series SiPMs using an oscilloscope with a 5 GHz sampling rate for pulse detection [145].

4.11.3 Bench Top Detector System

As the SiPMs can easily be saturated by external light sources, the flow cell, sample beaker, pump, amplifiers and DAQ board were placed within a light tight container [146] with sealed panel mount pass-throughs for coolant, serial communication, and power.

The flow cell forms a closed loop using silicone tubing and a reservoir containing the sample to be analysed, with a peristaltic pump [147] added to the outflow side

of the flow cell to pump the sample around the loop. The reservoir allows the concentration of tritiated water to be changed between measurements, as well as facilitating the flushing out of the flow cell after the experiment. As the pump inflow is connected to the outflow of the flow cell, the flow cell is operated under negative pressure to prevent leaks and to help force the sample through the scintillator powder. If the flow cell was operated under positive pressure, the laminated flow cell could balloon causing the contained powder to shift as the sample flows through. A diagram of the experimental detector setup can be seen in Figure 4.26, and a photograph of the detector system tested can be seen in Figure 4.27.

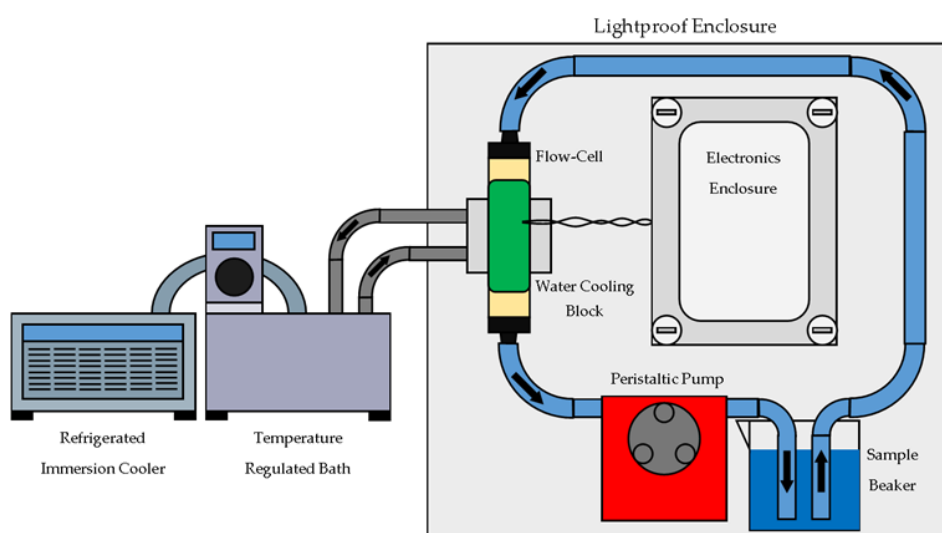


Figure 4.26: Diagram of detector setup, key parts include the light tight enclosure, silicon tubing, electronics enclosure, flow cell, flow cell casing, peristaltic pump and sample beaker. The cooling bath and cooling pump were placed directly next to the enclosure.

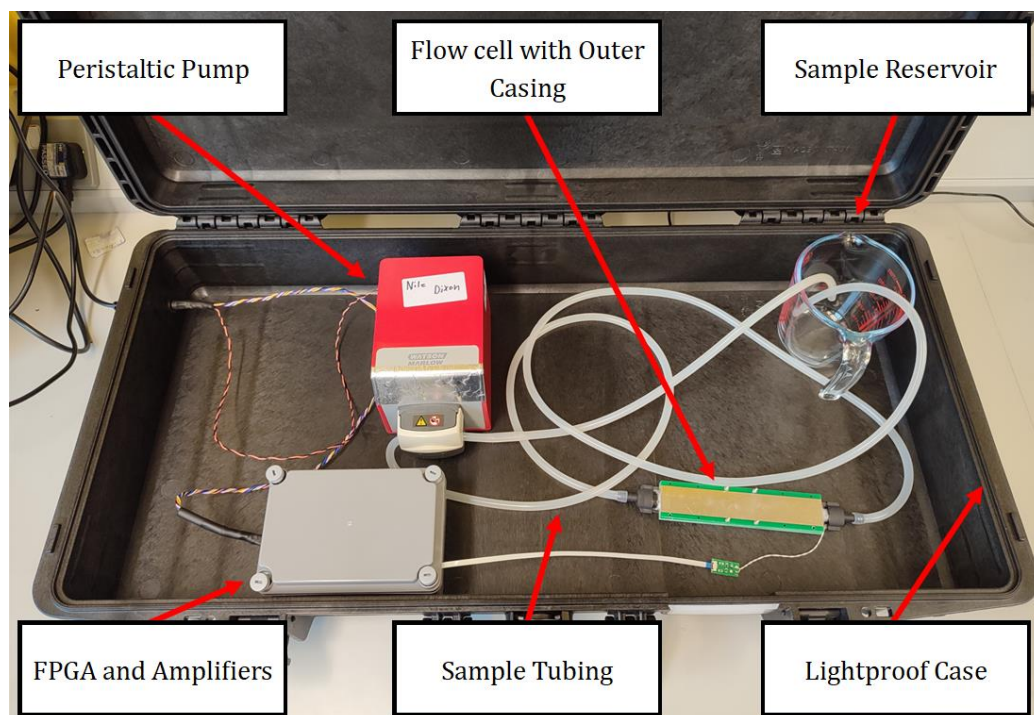


Figure 4.27: Image of detector system before the addition of the cooling and power supply unit, labelled with key parts.

The power supply for the DAQ board, single board computer, SiPM bias and amplifiers has been placed externally to reduce heat buildup within the enclosure, a single cable runs from the power supply unit to the detector providing all electrical connections. Four separate supplies were required for 3.3 V, 5 V, 12 V and -30.2 V.

4.11.4 Bench Top Cooling System

As counts from the detection of tritium will be received in conjunction with thermal noise from both SiPMs, it is important that the temperature of the detector system is kept constant or else the level of noise will vary across measurements leading to inconsistent results. A previous study [148] looked at the signal-to-noise ratio (SNR) of a PMT versus a SiPM cooled using a Peltier cell. They found that the SNR of the SiPMs would rise to that of the tested PMT at a temperature of 3°C [148], implying that to achieve comparable noise levels to existing PMT-based tritium flow cells, a cooling system for the SiPMs would be required. Another publication [149] notes the rate of this noise (dark rate) is

approximately 2 MHz at room temperature, decreasing to a few kHz at liquid nitrogen temperatures.

The solution implemented uses two hollow aluminium water blocks (40 mm height, 40 mm width and 12 mm thickness) which are placed and fixed around the outside of the flow cell casing. Coolant comprised of a mixture of 20% glycol ethylene to 80% deionised water was constantly passed through both heatsinks as the detector was running using the inbuilt pump of a 12 L Grant TX150 [150] at a flow rate of 66 mL s^{-1} (pump speed set at 1).

The coolant was kept at a constant temperature of 4°C using a regulated Grant liquid bath combined with an immersion cooler [151]. The immersion cooler consists of a heat exchanger with a cooling coil appendage that can be placed into a bath, the hot side of the exchanger is connected to a radiator to radiate heat into the atmosphere. The liquid bath contains a small heater to work against the cooling coil, by switching on and off the heater the temperature of the coolant can be regulated to a set temperature.

After a preliminary round of testing with this system it was found that the SiPMs were becoming damaged, this led to the realisation that condensation building up within the inside of the flow cell casing would pool around the SiPMs leading to moisture corrosion. While this damage could not be often identified visually, placing an oscilloscope on the output of the SiPM amplifiers would show greatly reduced electrical background noise (from 100 mVpp to below 20 mVpp) when damaged and a greatly reduced sensitivity to light. As the SiPM is formed from silicon bonded between two plastic sheets, a ridge is present around the edges of the device, through inspection it is believed this ridge is the point of entry of moisture into the device. As a result, an acrylic anti-corrosion coating was selectively added to the inner sides of the casing and edges of the SiPMs to resist moisture, with a total of three coats used. Before its addition the top faces of the SiPMs were covered with glossy plastic tape (see Figure 4.28) to stop the coating from adhering to the light sensitive faces directly, so as not to affect the window's transparency, this cover was then removed partway into drying.

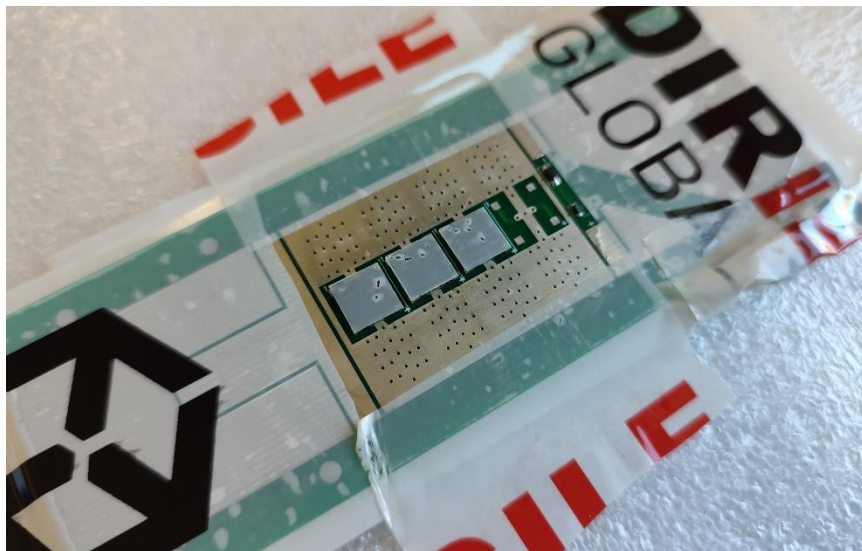


Figure 4.28: Image of SiPM sensors with masked front faces while adding the waterproofing anti corrosion coating.

In addition, 3 mm thick foam has also adhered to the open faces of the cooling blocks to help reduce condensation from moisture in the air. Finally, the set temperature of the cooling system was increased from originally 3°C to 4°C to help limit condensation. Since these changes, the detector has been successfully tested for multiple days continuously.

4.11.5 Temperature Effects on Background Count Rate

In the interest of investigating the influence of temperature on the SiPM output measurements, a continuous background reading of the flow cell filled with deionised water was measured as it was cooled down from room temperature (22.1°C to 4°C). The time taken to reach its set temperature was approximately 30 minutes.

The results are shown in Figure 4.29, where a clear exponential trend from 10 CPM of background counts at room temperature to 0.1 CPM at 4°C can be seen, signifying that as the SiPMs are cooled false counts introduced as the result of thermal noise is greatly reduced. The following plot in Figure 4.30 shows the variation of background count rate over approximately a day and a half. Without cooling and temperature stabilisation, variation is seen as temperatures rise in the day and fall in the night.

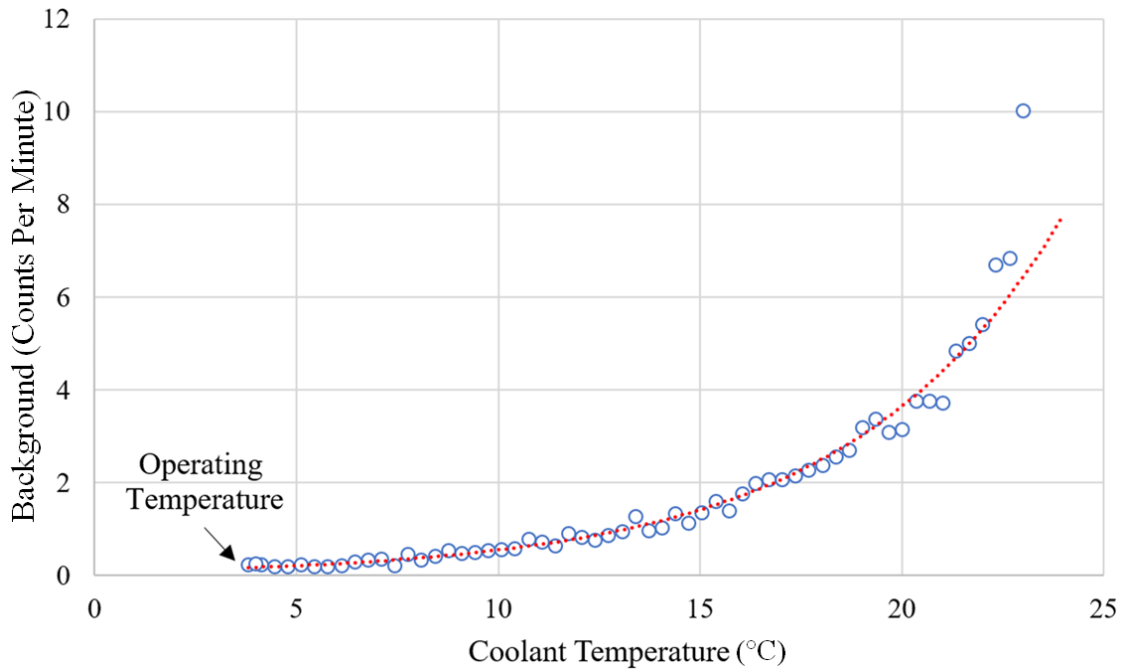


Figure 4.29: Graph plotting the total background CPM recorded (using gamma settings, see section 3.5) over the cooling period. An exponential fit (dotted red line) has been added to the data points.

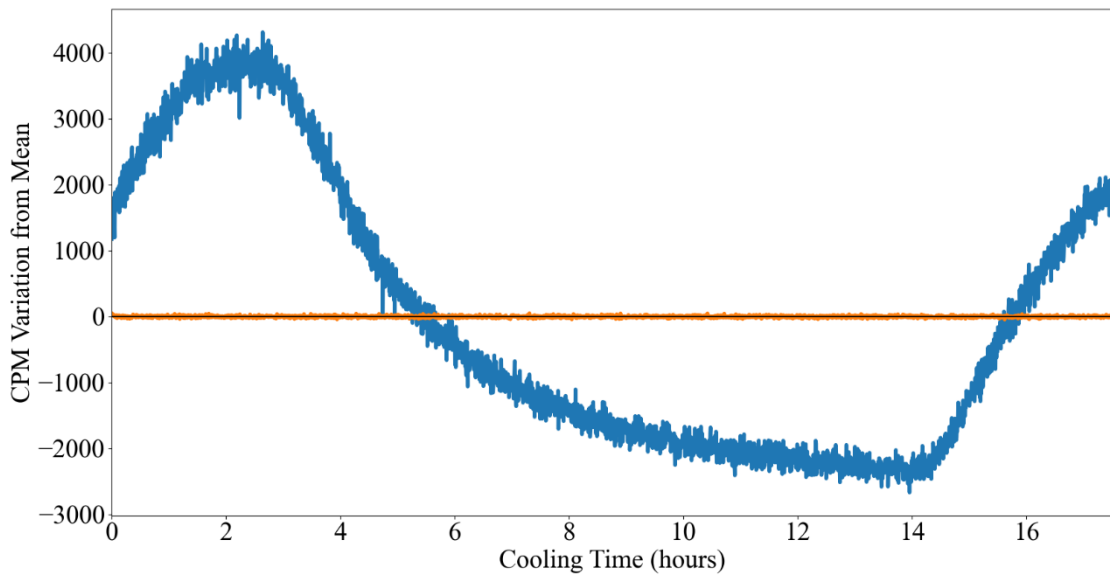
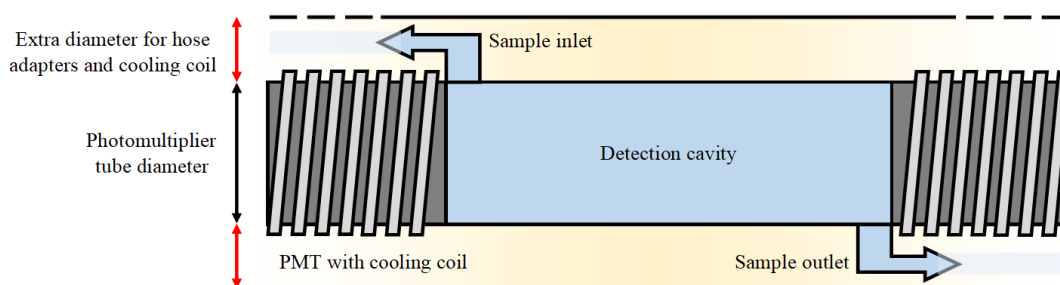


Figure 4.30: Graph plotting raw background total counts recorded (using tritium settings, see appendix D) with no temperature stabilisation (Blue trace), and with temperature stabilisation (Orange trace).

4.12 Improvements to Existing Detectors

An alternative flow cell design was originated to combine the backend electronics developed within this work with a more standard layered flow cell as seen in existing fibre and sheet flow cell designs [57], [66], [72]. One downside of these previous designs was the placement of inlet and outlet hoses, which would significantly increase the total diameter of the detector. The implementation of SiPMs over PMTs allows much greater flexibility of the inlet and outlet placement as while a hole cannot be drilled into a PMT window, a hole can be designed into a SiPM array. Figure 4.31 shows the suggested improvement of replacing actively cooled PMTs with SiPM arrays.

Standard Setup



Proposed

Alternative

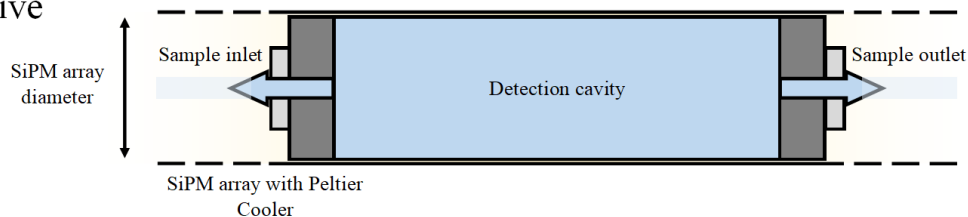


Figure 4.31: Cross sectional diagram of two coincidence counting systems, one using PMTs with cooling coils and a second with SiPM arrays and Peltier coolers.

Such an implementation would greatly compact the total required detector diameter, increasing its feasibility for installation within a borehole where space is limited. A prototype sensor head based on this ‘through hose SiPM array’ concept can be seen in Figure 4.32.

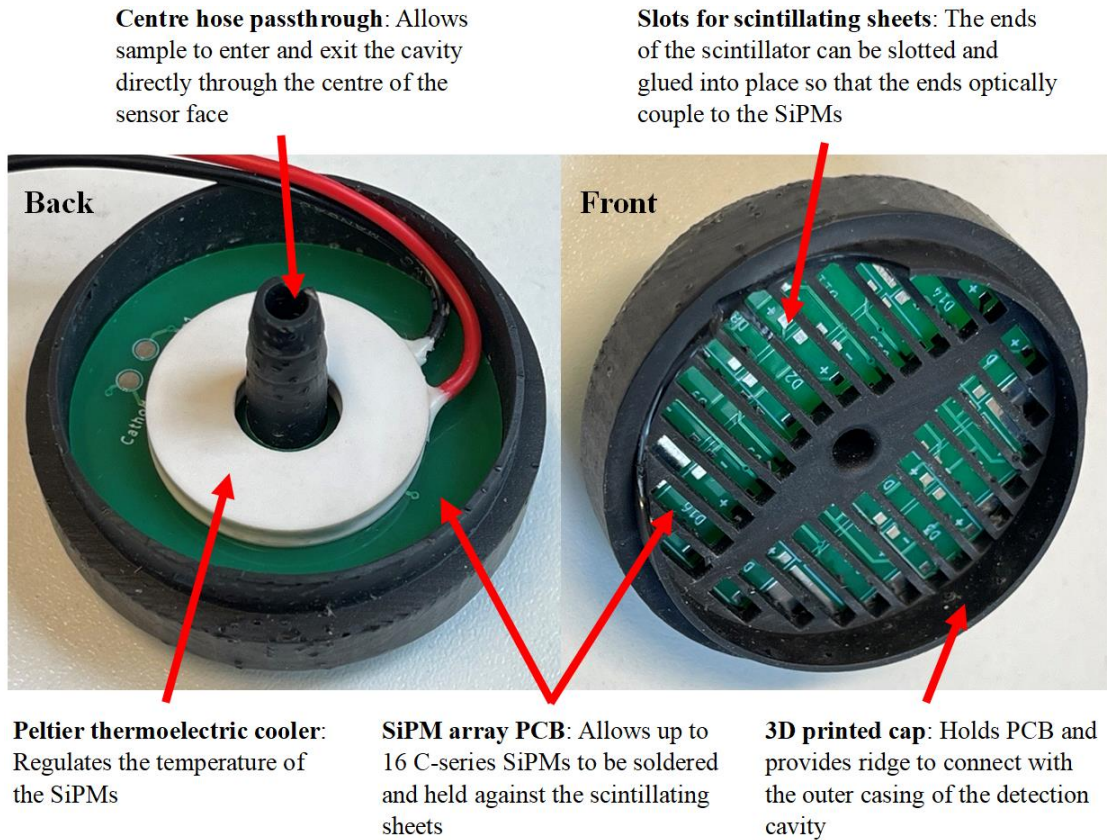


Figure 4.32: Concept SiPM array replacement for coincidence counting PMTs. The new design allows the placement of the inlet or outlet hose to pass directly through the centre of the detector face.

The 3D-printed body of the sensor heads has slots to insert and space the ends of multiple scintillator sheets. The SiPMs soldered in an array on a PCB will then optically couple to the inserted edges to detect scintillation photons. A Peltier thermoelectric cooler with a centre opening allows the hose to travel through the centre unimpeded while also allowing the SiPMs to be actively cooled. Peltier cooling is discussed further in section 6.5.

4.13 Conclusions

Three types of flow cell cavities: 3D printed, layered and laminated, have been manufactured and tested to identify design issues which were then rectified in the final iteration (laminated flow cell). KCl testing of the 3D printed flow cell with a solid $\text{CaF}_2(\text{Eu})$ scintillator showed that the flow cell could detect radiation from

the decay of naturally occurring ^{40}K , with a calculated detection efficiency of 0.04%.

The early electrical system has been replaced with a more suitable coincidence counting backend system. This backend system now allows quick configuration of both channel gain and filtering. It also allows each sensor head to be quickly connected and disconnected reducing the time and complexity of maintaining the flow cell cavity.

A bench top detector system has been created containing a laminated flow cell with SiPM arrays placed in direct contact with the transparent sides of the lamination sheets, silicon tubing to feed samples into and out of the flow cell, a peristaltic pump, coincidence counting backend electrical system, and a cooling system placed around the flow cell. This cooling keeps the temperature of the SiPMs and granulated scintillator constant to reduce the effect of temperature induced noise. All parts have been placed into a light tight case and installed within a fume cabinet for open-source experiments.

Suggested improvements to existing low energy beta detection systems have also been provided to reduce the overall detector diameter. By implementing an array of SiPMs as an alternative to PMTs, the inlet and outlet tubes can be passed through the photodetector instead of around them, streamlining the cavity design.

5 Detector Validation

5.1 Introduction

Over the previous chapters, an electrical system has been created, a granulated scintillator has been produced and characterised, and a laminated flow cell has been designed and manufactured to hold the granulated scintillator in contact with multiple silicon photomultipliers (SiPMs). To validate this system, multiple experiments have been completed to show that the detector can indeed detect low energy betas. Additional experiments have looked at the detectors behaviour with higher energy beta emitters (strontium-90) which could also be present within the borehole's groundwater. An example of a failed experiment has also been included to show how data from the detector can be used to identify problems that were then rectified.

Count rate data will also be studied to examine how quickly the flow cell fills, and to show that increased counts correlate with the addition of radioactivity. Finally, two radioactive borehole samples (9782 and 10202) obtained from the Sellafield site will be passed into the detector and analysed to see if this system is capable of identifying the presence of both low and high energy beta emitters within the solutions.

5.2 Tritium Experiments

To validate that the flow cell system is capable of low energy beta detection, the system was evaluated by passing multiple concentrations of dilute tritiated water through the cavity in turn while recording the spectrum and count rate. By passing multiple concentrations through the detector, the resulting recorded spectra and count rates should fluctuate accordantly to the change in activity within the cavity.

The sample of tritiated water used had an activity concentration of $2,058.08 \text{ Bq g}^{-1}$, and the total volume of the flow cell, filters, and piping was approximately 11 mL.

5.2.1 Issues with Filters

The first experiment with tritium resulted in the appearance of a new issue; a loss of scintillator from the flow cell cavity due to insufficient filtering. As the scintillator is required to detect beta particles, its partial or complete loss would result in far lower detection rates.

The experiment saw a sudden decrease in detected counts between the first and second round of testing, as a result, the flow cell system was dismantled finding that the scintillator normally held within the centre of the laminated cavity had migrated into the surrounding polyester stuffing away from the view of the SiPMs, we attribute this shift in scintillator to the lower readings. The measured count data is printed in Table 10, the recorded spectrums of rounds 1 and 2 are plotted in Figure 5.1, and the flow cell in question is shown in Figure 5.2.

Table 10: Count data recorded from experiment with tritiated water resulting in the loss of scintillator from the flow cell cavity. Measurement time recorded to within one sample (± 0.006 hours). Scales calibrated to ± 0.003 g.

Round No.	Post-Mixing Tritium Activity (Bq g^{-1})	Detected Counts (CPM $\pm 3\sigma$)	Measurement Time (Hour)
0 (background)	0	9.2 ± 0.3	22.3
1	102.05	12.5 ± 0.3	22.3
2	194.72	5.2 ± 0.2	21.5

Comparing round one to two, a decrease in counts of approximately 7.3 CPM can be seen, even though the mass of tritiated water and therefore the activity within the flow cell increased. Between each round the pump is used to mix and pass sample into the flow cell, this could have also led to the scintillator being flushed from the flow cell cavity.

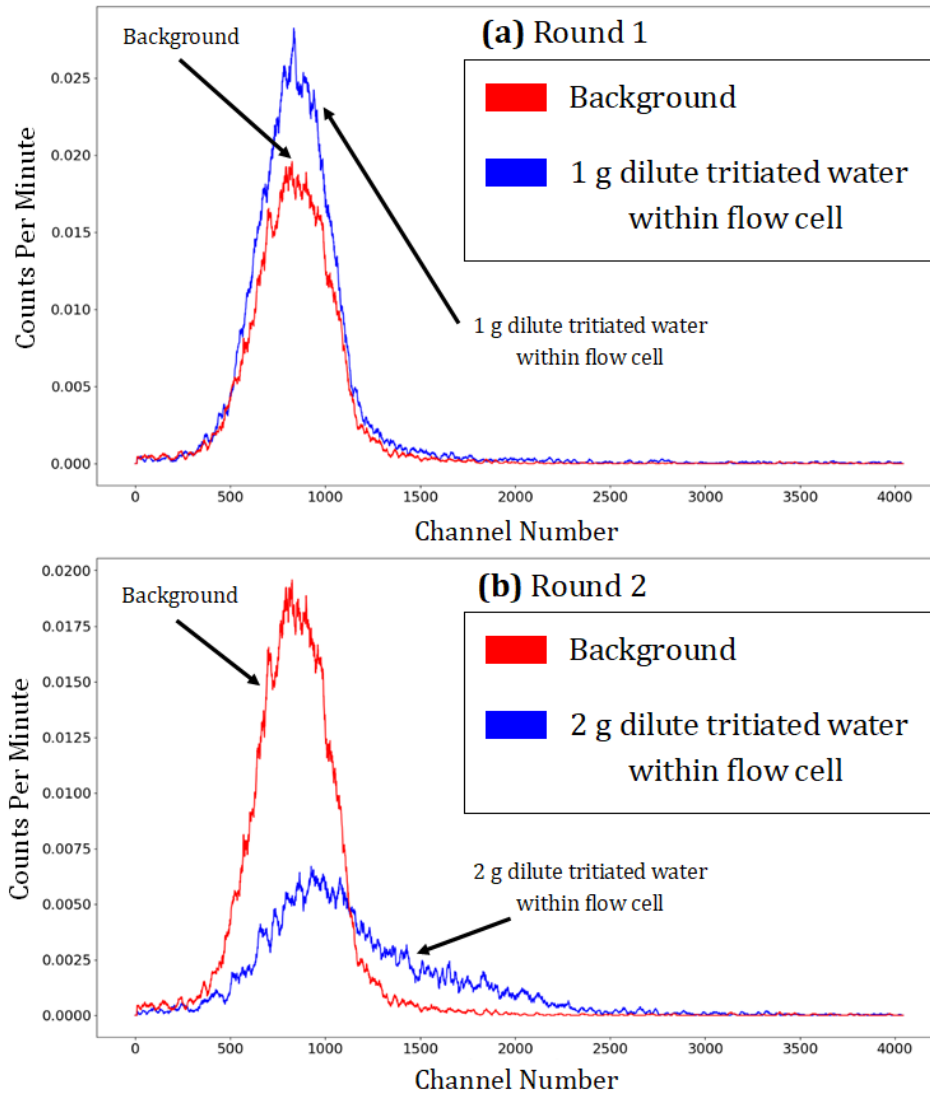


Figure 5.1: Raw spectra data from failed tritium experiment, red trace in both graphs plots the background measurements and blue traces plot the spectrums measured after the first (a) and second (b) addition of tritiated water.

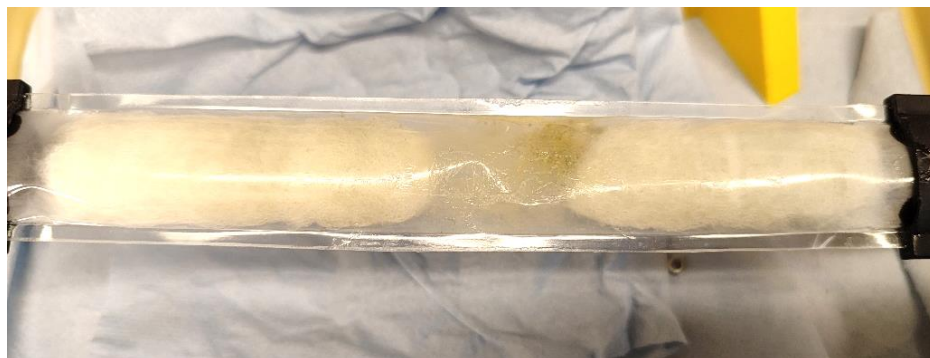


Figure 5.2: Image of flow cell after round 2 testing, due to insufficient filtering the scintillator has migrated away from the cavity centre.

To counteract this loss of scintillator, for the following experiments foam sheets were added to the inner sides of the flow cell casing to press down upon the flow cell filters (added foam sheets can be seen in Figure 4.23). This step helped to compact the fibres of the polyester stuffing and to ‘pinch’ each end of the flow cell cavity. Future inspections after the addition of the foam showed little to no powder migration or loss.

5.2.2 Tritium Detection Results

Following the addition of foam a new experiment was started. The flow cell system was cooled and kept at a constant temperature of 4°C to reduce background counts and therefore maximise the minimal detectable activity (MDA). A spectrum of background activity was measured with the detector filled with 20.003 g of deionised water. Then, a measured mass (see Table 11) of tritiated water was added to the sample reservoir and left to mix with the deionised water and circulate through the flow cell for four to six hours prior to measurement.

Table 11: Measurement time, mass of water, and mass of dilute tritiated water present in each round of the experiment. Scales calibrated to ± 0.003 g. Measurement time recorded to within one sample (± 0.006 hours).

Round No.	Total Water Mass (g)	Total Tritiated Water Mass Added (g)	Measurement Time (Hour)
0 (Background)	20.003	0	23.2
1	21.004	1.001	23.2
2	22.023	2.020	60.6
3	23.018	3.015	41.2
4	24.061	4.058	22.3
5	25.073	5.070	85.1

The detector was then left over multiple days (the exact measurement time is listed in Table 11) to record counts from the flow cell. Over this period, the pump was turned off to avoid the possibility of electrical noise affecting the recorded count rate. This process was repeated a further four times, cumulatively adding diluted tritiated water for a total of five measurements at five different tritium concentrations. By the last measurement, a total liquid sample of 25.07 ± 0.02 g was passing through the detector system with an activity of 416.18 Bq g^{-1} . Table 12 shows the count data collected by the detector per round.

Table 12: Detected CPM recorded by the flow cell detector for each round, along with the calculated full loop tritium activity concentration based upon the added mass of tritiated water. Detection efficiency has been calculated using equation (5.1) and (5.2).

Round No.	Post-Mixing Tritium Activity (Bq g^{-1})	Detected Counts (CPM $\pm 3\sigma$) (Background Removed)	Detection Efficiency of Activity in Cavity (%)
0	0	0 ± 0.3	-
1	98.08	3.7 ± 0.7	0.10
2	189.75	11.2 ± 0.5	0.16
3	269.57	14.6 ± 0.5	0.15
4	347.12	16.9 ± 0.7	0.13
5	416.18	22.8 ± 0.4	0.15

Included in Table 12 is the detection efficiency for the estimated amount of activity contained purely within the detection cavity itself i.e. excluding activity in the beaker, piping, and filters. This was obtained by assuming that the powder within the flow cell is packed randomly and loosely, therefore its primary porosity is approximately 41% [152]. When the flow cell was manufactured, $4.73 \text{ g} \pm 0.02 \text{ g}$ of scintillator was added. Given the density of the scintillator (3.18 g cm^{-3} [153]), the amount of sample within the powder can be estimated with equation (5.1).

$$V_{Liquid\ Sample} = \frac{0.41 \times Mass_{Scintillator}}{\rho_{CaF_2(Eu)}} = 0.61\ mL \quad (5.1)$$

Therefore, the detection efficiency of activity surrounding the scintillator (ϵ) can be calculated using the following equation (5.2) [154].

$$\epsilon\ (\text{Estimated activity in cavity})\ \% = 100 \times \frac{S - B}{60 \times A \times V} \quad (5.2)$$

Where S is the detected count rate of the sample (CPM), B is the detected count rate of background (CPM), A is the activity concentration ($Bq\ mL^{-1}$) and V is the volume of sample surrounding the scintillator (mL).

The measurements made by the detector show an increased count rate of 3.7 CPM, after the tritium activity concentration in the flow cell increased from $0\ Bq\ mL^{-1}$ to $98.08\ Bq\ mL^{-1}$. Figure 5.3 plots the background spectra taken by the detector before any tritium had been added, followed by Figure 5.4 which plots the spectra taken by the detector after each addition of tritiated water, the background counts have been removed.

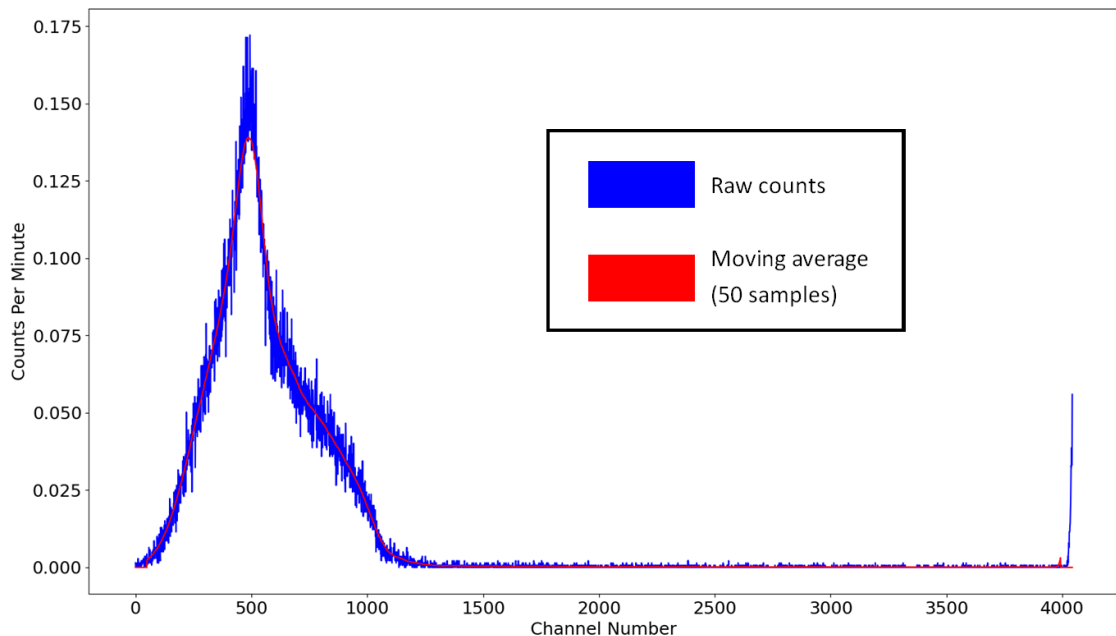


Figure 5.3: Spectrum of background taken by the flow cell detector while filled with deionised water. The blue trace plots the raw channel data, and red trace plots a 20-sample moving average.

The saturation of the analogue to digital converter (ADC) can be seen in Figure 5.3 as a peak at the far-right end of the spectrum. This is due to the high gain of the SiPMs amplifiers which results in pulses with energies above that which can be recorded by the top register of the ADC. This peak is therefore not a photopeak, but merely the sum of all the pulses caused by interactions that are more energetic than this scale.

Figure 5.4 shows the resulting spectra recorded by the detector for each tritium concentration. As expected, most counts occur at lower channel numbers, overlapping with the detector noise seen in the background measurement results (Figure 5.3). Due to the implemented detection algorithm discussed in section 3.7, in which shaped pulses must meet a threshold, channel counts start to decrease rapidly below approximately channel 500, as pulses start to be rejected as they can no longer be differentiated from background noise.

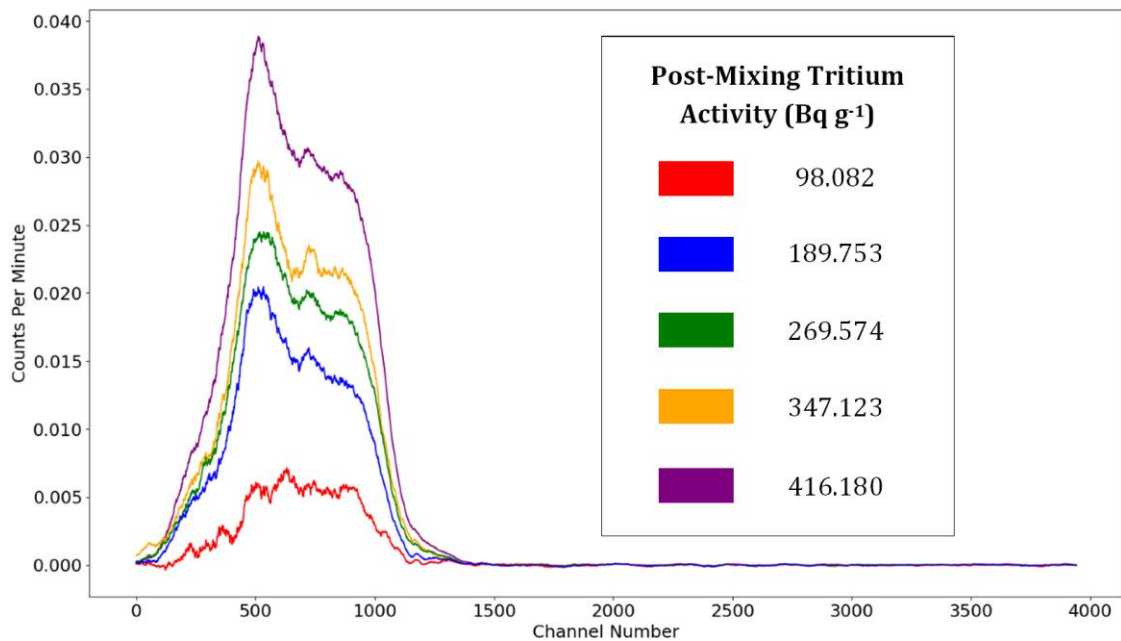


Figure 5.4: Spectrum taken by detector after each addition of tritium, background removed. A 50-sample moving average has been applied to each trace. Trace colours red, blue, green, orange and purple represent the spectra taken in rounds 1, 2, 3, 4 and 5 respectively.

Captured count data has then been plotted against the concentration of tritium activity in Figure 5.5. A set error of $\pm 20 \text{ Bq g}^{-1}$ has been included in the plot, this has been added to represent the uncertainty in the activity within the flow cell due to factors such as the incomplete mixing of the added tritiated water, the movement of powder within the cavity and air gaps being removed or introduced to the cavity as the sample is being passed. Interpreting Figure 5.5, a positive trend between tritium activity and counts per minute has been obtained. The added line of best fit provides a predicted behaviour shown by equation (5.3) of the form $y = mx + c$.

$$\text{Tritium Activity (Bq mL}^{-1}\text{)} = 18.24 \times \text{Detected CPM} + 9.89 \quad (5.3)$$

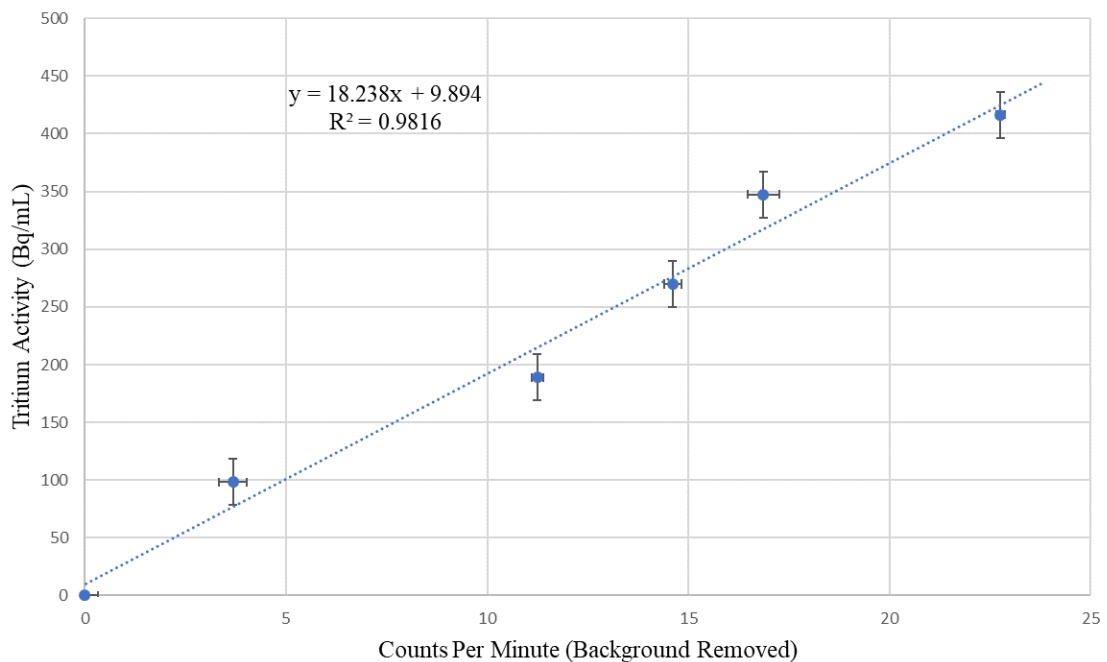


Figure 5.5: Tritium activity concentration within flow cell plotted against measured CPM, where concentrations ranged from 0 Bq g^{-1} to 416.18 Bq g^{-1} . A linear line of best fit (dotted blue line) has been added to predict the detectors overall response to the activity of tritium.

For calculating the minimum detectable activity (MDA) the following characteristic equation (5.4) [154] has been used, and the background count rate has been set as the recorded CPM from the first round (round 0) of the flow cell testing (58.9 CPM).

$$MDA(Bq mL^{-1}) = \frac{\frac{2.71}{t_s} + 3.29 \sqrt{\frac{B}{t_s} + \frac{B}{t_b}}}{60 \times \varepsilon \times V} \quad (5.4)$$

Where B is the background count rate (CPM), t_b is the background measurement time (minute), t_s is the sample measurement time (minute), ε is the detection efficiency and V is the volume of sample surrounding the scintillator (mL). If one day was allowed for measurement, the minimum detectable activity concentration of tritium can be calculated (see equation 5.5).

$$\begin{aligned} MDA(Bq mL^{-1}) &= \frac{\frac{2.71}{24 \times 60} + 3.29 \sqrt{\frac{58.861}{24 \times 60} + \frac{58.861}{23.236 \times 60}}}{60 \times 0.00139 \times 0.610} \quad (5.5) \\ &= 18.67 Bq mL^{-1} \end{aligned}$$

Minimum detecting time (MDT), equation (A.1) derived in Appendix B, will be used to see how long the detector would have to operate to achieve a given MDA. For the system to be able to detect activity at the WHO limit of $10,000 Bq L^{-1}$, the MDA for the detector would have to be $10 Bq mL^{-1}$. Therefore, the time the detector would have to take a measurement of background and of the sample can be calculated (see equation 5.6).

$$\begin{aligned} MDT(\text{minute}) &= \frac{15k^2 M \varepsilon V + k^2 B + \sqrt{30k^4 M B \varepsilon V + k^4 B^2}}{900M^2 \varepsilon^2 V^2} \quad (5.6) \\ &= 3.43 \text{ days} \end{aligned}$$

Where k is the one-sided confidence factor of 1.646 at 95% confidence. ε is the detection efficiency, V is the sample volume (mL), B is the background count rate (CPM), and M is the required MDA for the detector.

Before disposal of the flow cell used in the previous experiment. Another experiment was devised to take further measurements after the addition and mixing of a flush sample (consisting of 100% deionised water) for four to six hours before its removal. Flushing the flow cell reduces the activity that will be disposed of as solid waste with the flow cell.

The justification for this exercise is to demonstrate that the detected count rate reduces as the flush cycles remove activity. This removes the possibility of coincidences such as cumulative moisture damage to the SiPMs contributing higher and higher noise which is then being counted by the detector.

Note that prior to the flush measurements as much of the original diluted tritiated water sample was purged and disposed of before the addition of the two flush samples. The masses of deionised water added and removed per flush cycle are shown in Table 13, and the readings by the detector while the flow cell is filled with the flush sample is shown in Table 14.

Table 13: Deionised water added and removed over two flush cycles measured by the detector. Measurement time recorded to within one sample (± 0.006 hours). Scales calibrated to ± 0.003 g.

Round No.	Flush Water Added (g)	Flush Water Removed (g)	Measurement Time (Hour)
6 (Flush 1)	12.000	11.690	13.1
7 (Flush 2)	12.003	11.001	21.4

Table 14: Detected CPM recorded by the flow cell detector for flush cycles. Detection efficiency has been calculated using equation (5.1) and (5.2).

Round No.	Loop Tritium Activity (Bq mL^{-1})	Detected Counts (CPM $\pm 3\sigma$) (Background Removed)	Detection Efficiency of Activity in Cavity ($\% \pm 3\sigma$)
6 (Flush 1)	265.33	14.6 ± 1.0	0.15 ± 0.01
7 (Flush 2)	149.34	6.4 ± 0.7	0.08 ± 0.01

Interpreting Table 13 and Table 14 after the addition of the first flush sample, the detected count rate reduced by 8.2 CPM indicating that the flush did indeed reduce the activity within the cavity. The second flush reduced the count rate yet again by 8.2 CPM.

To conclude, while the flush does reduce activity within the flow cell it cannot fully eliminate residue tritium. One explanation for this could be from absorption of the original tritiated water sample into pores within the irregularly shaped scintillator particles, or the compaction of the scintillator powder over time reducing the flowrate through the scintillator making displacement of the sample harder. Fortunately, as more flow cells can be rapidly manufactured, a fresh flow cell can be used for the next rounds of testing.

5.3 Strontium-90 Experiments

Now that the detector has been validated with a low energy beta emitter (tritium), the next step is to characterise the detector with the presence of a higher energy beta emitter. Strontium-90 has been selected as it has a maximum beta energy of 546 keV [155], approximately 29 times greater than tritium with an additional maximum beta energy of 2,280 keV [156] from Yttrium, a daughter nuclide of strontium-90. It is also a common co-contaminant of tritium in Sellafield groundwater.

For testing within section 5.3 and section 5.4 flow cells with coarser grind sizes (150 μm to 250 μm) have been used for the experiments, this allows for faster flow rates and will increase the likelihood higher energy beta particles will interact with the scintillator. Finally, for this section the gain of the detector was lowered to reduce pulses which would saturate the ADC allowing the captured spectra to display higher energies. The gain settings used for the tritium and strontium-90 testing can be seen in Appendix D.

5.3.1 Count Rate Analysis

The methodology of the experiment is as follows: The detector was cooled to 4°C. Deionised water is added into a reservoir beaker and pumped around the flow cell and back to the reservoir, a background measurement is then taken. Next a measured mass of strontium-90 tracer is added into the reservoir, and the pump and measurements are simultaneously started. This allows the rise in count rate

as the tracer enters the flow cell to be analysed. Figure 5.6 shows the resulting data captured by this method.

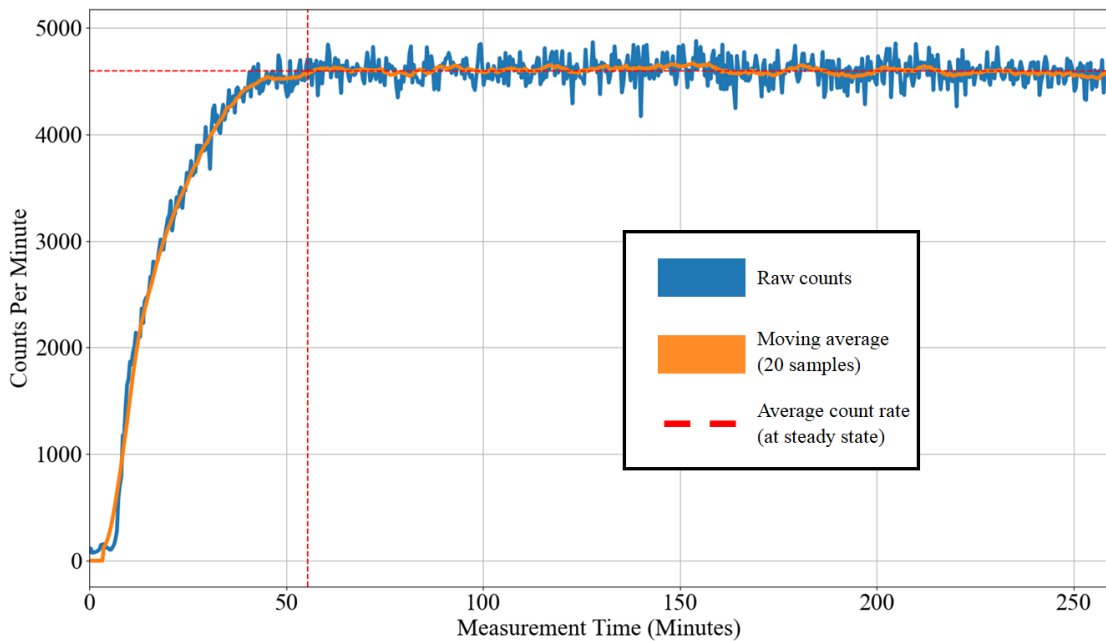


Figure 5.6: Plot of raw count rate data recorded by detector after the addition of 534.96 Bq of strontium-90 tracer. Blue, orange, vertical red and horizontal red line represent the raw count rate, 20 sample moving average, start of count rate average, and average count rate respectively.

As expected, when the strontium-90 tracer is introduced, the count rate measured by the detector increases to a maximum after a delay. This delay can be attributed to the time taken to pump the tracer through the inlet piping and the filling of the flow cell. A total of 534.96 Bq of strontium-90 tracer was added resulting in the count rate increasing from a background of $92.7 \text{ CPM} \pm 0.8 \text{ CPM}$ (taken prior to the tracer addition) to $4,599.7 \text{ CPM} \pm 14.5 \text{ CPM}$, an average taken of measurements after 53.7 minutes (shown as a dotted red vertical line on Figure 5.6).

The rise time (t_R) can be obtained to understand how quickly the flow cell fills. This can be calculated by measuring the time taken for the activity to rise from 10% to 90% of the maximum count rate. These are estimated to be 6.2 minutes for 10% and 32.0 minutes for 90% (measured from the orange trace in Figure 5.6), therefore rise time is 25.8 minutes.

After this experiment, the loop was purged, and a sample was taken to be tested using a LSC (calibration of the LSC is discussed in Appendix A). As a result, the

activity concentration after the experiment has been obtained as 41.26 Bq. Interestingly given uniform mixing the expected activity concentration is 61.98 Bq and hence activity has been removed or accumulated elsewhere in the detector.

Strontium is known to adsorb onto powders such as HDPE microspheres [157] and activated carbon [158]. It is therefore likely activity has been absorbed into the scintillator powder and retained in the flow cell, and so has been removed from the aqueous sample resulting in a measured disparity in activity concentration.

After flushing and replacing the flow cell, a second strontium-90 experiment was conducted, this time 31.93 Bq of strontium-90 tracer was added resulting in an increase from background to 333 CPM. Again, the rise in activity as the tracer entered the detection activity was recorded and is shown in Figure 5.7. As expected, as the activity added is lower compared to the previous strontium-90 test, the resulting increase in counts is similarly less. Again, an increase in the count rate can be seen as the flow cell cavity fills with the tracer sample.

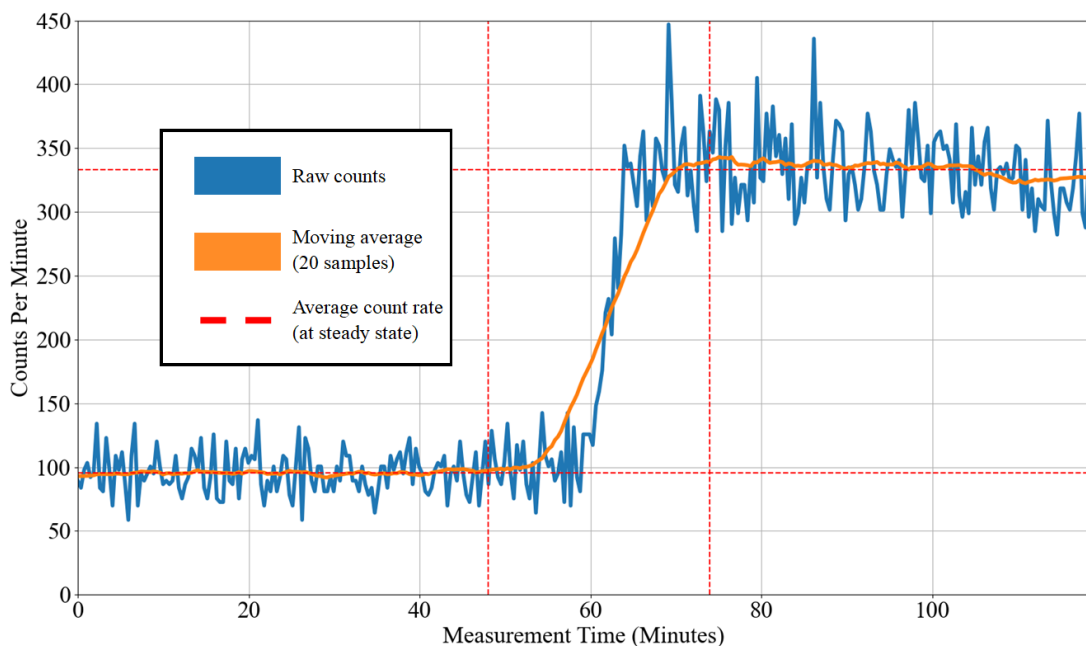


Figure 5.7: Plot of raw count rate data recorded by detector after the addition of 31.93 Bq of strontium-90 tracer. Blue, orange, vertical red and horizontal red lines represent the raw count rate, 20 sample moving average, start/end of count rate average and average count rate respectively.

5.3.2 Spectrum Analysis

This experiment involved measuring a spectrum of a sample containing tritiated water and comparing its recorded spectra with that of a sample containing strontium-90 tracer. Two separate flow cells were used to remove the possibility of cross contamination. Table 15 and Table 16 display the measurement times and quantities of tritiated water and strontium 90 tracer added. Figure 5.8 displays the two spectra captured by the detector, the red trace of the strontium-90 spectrum is smoother as the count rate detected was greater compared to the measured count rate of dilute tritiated water. Therefore, to provide a better comparison both spectra have been normalised to 1,000 total counts.

Table 15: Results from spectra measurement of diluted tritiated water. Measurement time recorded to within one sample (± 0.006 hours). Scales calibrated to ± 0.003 g.

Action	Deionised Water Within Flow Cell (g)	Tritiated Water Within Flow Cell (g)	Counts Per Minute (CPM $\pm 3\sigma$)	Measurement Time (Hour)
Background Measurement	21.999	0	87.8 ± 0.5	64.4
Measurement with tritiated water	21.999	2.059	96.8 ± 0.4	113.3

Table 16: Results from spectra measurement of diluted strontium-90 tracer. Measurement time recorded to within one sample (± 0.006 hours). Scales calibrated to ± 0.003 g.

Action	Deionised Water Within Flow Cell (g)	Strontium-90 Tracer Within Flow Cell (g)	Counts Per Minute (CPM $\pm 3\sigma$)	Measurement Time (Hour)
Background Measurement	24.988	0	92.7 ± 0.8	20.0
Measurement with strontium-90 tracer	24.988	5.684	4599.7 ± 14.5	3.3

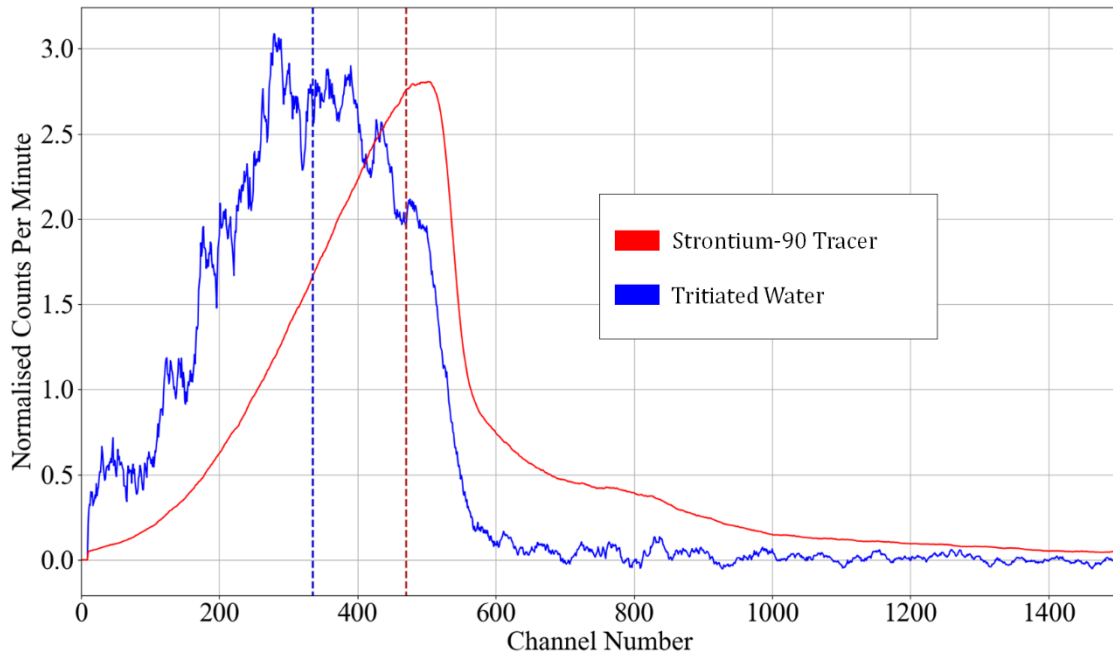


Figure 5.8: Spectrum taken of ^3H overlaid with spectrum taken of ^{90}Sr . Spectrums have been filtered using a 50 sample moving average and normalised each to 1,000 CPM to compare spectrum shape. Only channels from 0 to 1,500 have been shown for clarity.

As shown in Figure 5.8 a shift can be seen in the spectra between the detector being filled with dilute tritiated water and being filled with strontium-90 tracer, with a greater number of counts in higher channel numbers for strontium-90, implying the presence of a higher energy beta emitter.

While the results align with existing work on strontium-90 and tritium beta determination [159], the shift between sources is smaller than expected as the maximum energy emitted by yttrium-90 (the decay product of strontium-90) is 2.3 MeV [160], far greater than the maximum energy emitted by tritium. But upon reflection, there are two reasons believed to be causing this disparity:

- Due to the small size of the flow cell, high energy betas will escape out of the cavity before interacting with the granulated scintillator and hence will not be counted. The 2.3 MeV betas emitted ^{90}Y can penetrate up to 11 mm in water [160], which is larger than the thickness of the cavity (<4.8 mm).
- Calcium fluoride doped with europium ($\text{CaF}_2(\text{Eu})$) is a scintillator selected for its ability to detect low energy beta emitters, it has a comparatively low density and therefore is less capable of stopping high energy betas.

5.4 Sellafield Groundwater Experiments

So far ideal sources have been used to test the detector consisting of mostly deionised water. But to validate that the detector can indeed work with environmental samples, experiments must be conducted with samples from an actual borehole. While an installed 'filter pack' in each borehole should help minimise particulate matter, such material is still typically found in borehole samples due to filter packs design or a lack of effective well development.

Two groundwater samples from boreholes 9782 and 10202 were obtained from Sellafield for testing with the flow cell detector, these samples were selected due to the large contrast in strontium-90 activity (80,314 times more strontium-90 activity from the sample from borehole 10202 compared to 9782). The breakdown of the main radionuclides contained in each sample is displayed in Table 17 and Table 18. This data was obtained directly from Sellafield [161].

Each activity has been adjusted to the date of testing to consider the half-life of each radioisotope. Total beta represents the sum of all beta emitters excluding tritium. As strontium-90 makes up the majority of non-tritium beta activity, its half-life has been used to adjust these values. Therefore, the beta activity (sum of total beta and tritium) within 1 mL of samples from boreholes 9782 and 10202 is 2.06 Bq mL^{-1} and 40.92 Bq mL^{-1} respectively on the date they were tested within the detector.

Table 17: Measured activity of radioisotopes contained in sample from borehole number 9782 [161]. Total beta activity for day of testing has been adjusted using strontium-90 half-life.

Analyte Name	Data Sampled	Laboratory Result (Bq m⁻³)	Uncertainty Value	Activity on Day of Testing (Bq m⁻³) (17/05/24)
Carbon-14	15/11/2021	462	302	462
Strontium-90	22/06/2022	307	49	293
Tritium	22/06/2022	2,296,857	198,593	2,063,364
Total beta	22/06/2022	606	174	579

Table 18: Measured activity of radioisotopes contained in sample from borehole number 10202 [161]. Total beta activity for day of testing has been adjusted using strontium-90 half-life.

Analyte Name	Data Sampled	Laboratory Result (Bq m⁻³)	Uncertainty Value	Activity on Day of Testing (Bq m⁻³) (05/06/24)
Carbon-14	24/11/2021	6,580	512	6,580
Technetium-99	23/08/2022	1,260	58	1,260
Strontium-90	14/09/2022	24,656,309	1,904,349	23,670,057
Tritium	14/09/2022	3,093,543	234,268	2,805,844
Total beta	14/09/2022	39,700,000	298,000	38,112,000

For the experiments with these site groundwaters, the methodology is as follows. A background measurement was taken over multiple days with the flow cell filled with deionised water and cooled to a constant temperature of 4°C. After this, the flow cell was purged to remove as much water as possible, the reservoir was emptied and then filled with a measured mass of groundwater (enough to fully fill the detector cavity, reservoir, and tubing). The detector was then left overnight to

pump the sample into and around the flow cell. The day after the sample measurement is started and left-over multiple days to run.

5.4.1 9782 Experiment

Figure 5.9 displays the resulting spectrum recorded by the detector after the addition of 32.95 g of groundwater from borehole 9782. A fresh unused laminated flow cell has been used to eliminate contamination from the previous experiment and so a new background spectrum was taken prior to the addition of the sample has been removed from the plot. Count rate values have been provided in Table 19.

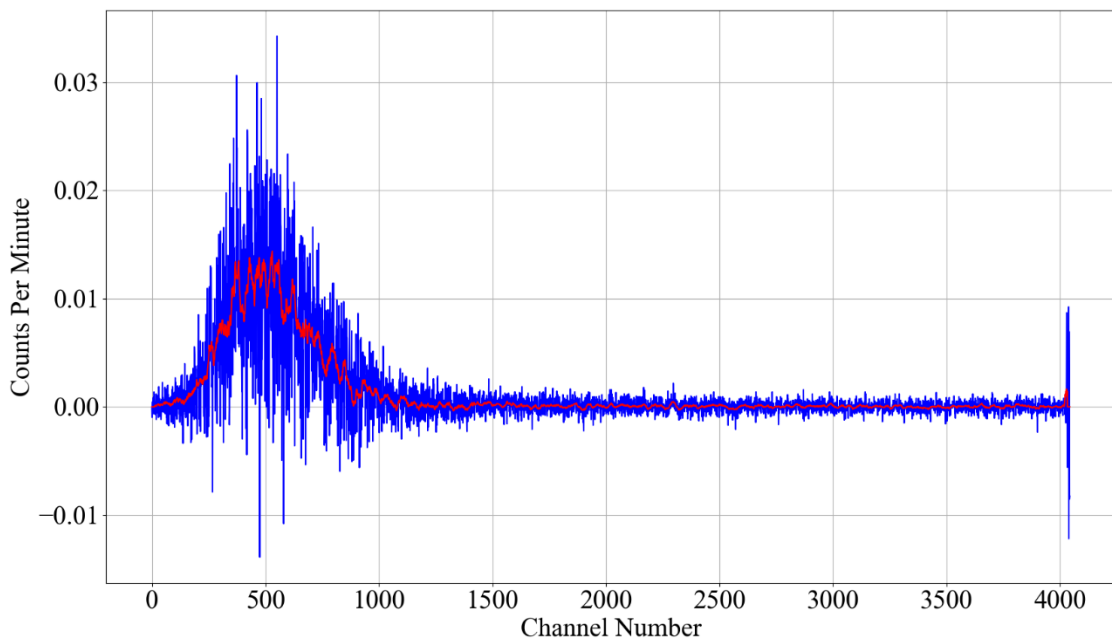


Figure 5.9: Spectrum taken by detector while flow cell is filled with groundwater from borehole 9782, background removed. Blue trace: Raw count data. Red trace: 10 point moving average.

Table 19: Count data and measurement times for borehole 9782 groundwater experiment. Measurement time recorded to within one sample (± 0.006 hours). Scales calibrated to ± 0.003 g. Measurement ended on 17/05/2024.

Action	Deionised water within Flow Cell (g)	9782 Sample Within Flow Cell (g)	Counts Per Minute (CPM $\pm 3\sigma$)	Measurement Time (Hour)
Background (Deionised water)	22.016	0	54.1 \pm 0.4	63.8
Flow cell purged	4.333	0	-	-
Flow cell filled with 9782	4.333	32.948	59.8 \pm 0.3	84.2

From the addition of 9782 into the flow cell, the measured count rate increased by 5.7 CPM \pm 0.7 CPM. Using equation (5.1) the volume of sample within the flow cell cavity can be calculated as 0.64 mL (flow cell contained 4.99 g of scintillator).

Also to note, not all the deionised water used for the background count was removed. Therefore, when the 9782 sample was introduced and mixed it was partially diluted. The reduction in activity concentration can be calculated by using equation (5.7), as the Sellafield samples consist of mainly water it will be assumed that 1 g of sample is equal to 1 mL volume.

$$\frac{\text{Activity concentration}_{\text{flow cell}} (\text{Bq mL}^{-1})}{\text{Activity concentration}_{9782} (\text{Bq mL}^{-1})} = \frac{\text{Volume}_{9782 \text{ sample}} (\text{mL})}{\text{Volume}_{\text{deionised water}} (\text{mL}) + \text{Volume}_{9782 \text{ sample}} (\text{mL})} \quad (5.7)$$

Therefore, the activity concentration is reduced by 88% due to the remaining deionised water within the flow cell added for the background count. This reduction will be accounted for when calculating the total detection efficiency. With Table 17, activity reduction, and the total volume within the scintillator powder, the detection efficiency can be calculated using equation (5.2) as 8.1% \pm 1.0% for the sum of total beta and tritium (2.06 Bq mL⁻¹).

5.4.2 10202 Experiment

Figure 5.10 displays the resulting spectrum recorded by the detector after the addition of approximately 22 g of groundwater from borehole 10202. A fresh flow cell has again been used, and therefore another background spectrum was taken prior to the addition of the sample has been removed from the plot. Table 20 displays the measured count rates for the deionised water (background) and 10202 filled flow cell.

Compared to the previous sample (9782), counts are present at greater channel numbers which indicates the added sample contains higher energy beta emitters. Also, the saturation peak (starting at approximately channel 4,026) is of a far greater magnitude than for the 9782 sample, implying that many detections are of too high of an energy, outside the ADC range of the detector. These results support that the built system can indeed detect the presence of higher energy beta emitters within the 10202 sample. Additionally, a much greater count rate has been measured, which can be attributed to the greater overall activity of the 10202 sample.

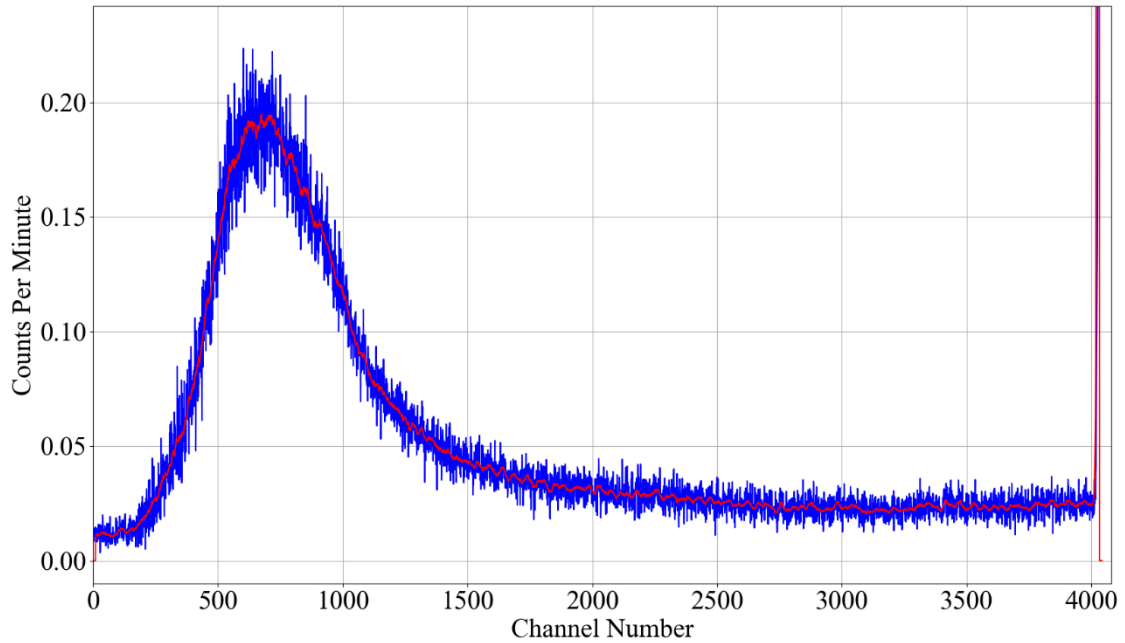


Figure 5.10: Spectrum taken by detector while flow cell is filled with groundwater from borehole 10202, background removed. Blue trace is raw count data. Red trace is 10 point moving average.

Table 20: Count data and measurement times for borehole 10202 groundwater experiment. Measurement time recorded to within one sample (± 0.006 hours). Scales calibrated to ± 0.003 g. Measurement ended on 05/06/2024.

Action	Deionised Water Within Flow Cell (g)	9782 Sample Within Flow Cell (g)	Counts Per Minute (CPM $\pm 3\sigma$)	Measurement Time (Hour)
Background (Deionised water)	22.034	0	50.6 \pm 0.3	84.3
Flow cell purged	5.474	0	-	-
Flow cell filled with 10202	5.474	21.993	407.9 \pm 1.6	23.1

For the detection efficiency calculations, the same methodology seen in the previous section (section 5.4.1) has been used. After the addition of 10202, the measured count rate increased by $357.3 \text{ CPM} \pm 1.9 \text{ CPM}$. The reduction in activity concentration due to the remaining deionised water was calculated with equation (5.7) resulting in a value of 80%. The scintillator powder volume has been calculated using equation (5.1) as 0.64 mL (for 4.93 g of scintillator) and the activity within the flow cell has again been taken for the sum of total beta and tritium (40.92 Bq mL^{-1}). Now using equation (5.2) the detection efficiency can be calculated as $28.6\% \pm 0.2\%$.

5.5 Conclusions

As a result of these experiments, a flow cell detector capable of the detection of low energy beta radiation has been designed, built, and validated using multiple samples of dilute tritiated water. An example of a flow cell failure has shown that recordings taken by the detector can be used to monitor the health of the flow cell.

256 hours of collected data from experiments with multiple concentrations of dilute tritiated water has obtained an average detection efficiency of 0.14% obtained from seven rounds of measurements. An MDA value has also been obtained finding that over a 24 hour counting period, the minimum concentration of tritium that can be detected is 18.67 Bq mL^{-1} . Recorded spectra (Figure 5.4) have also been obtained showing counts introduced after the addition of tritiated water follows the expected energy distribution for tritium. Recording spectrums also allows the possibility for other beta-emitting isotopes to be discriminated between in the future.

Experiments with strontium-90 tracers have allowed the flow cell cavity filling rise time to be estimated as 25.8 minutes, based on the increase of the count rate readout from 10% to 90% of the maximum count rate. These count readouts (Figure 5.6 and Figure 5.7) show a clear response to the addition and passing of strontium-90 tracer into the flow cell. While low energy beta emitters are the focus of this work, gaining an understanding of the detector's behaviour with higher

energy beta emitters will also assist in differentiating between multiple radioisotopes that could be present in an environmental sample.

Two environmental groundwater samples from the Sellafield site, from boreholes 9782 and 10202, have been passed into the detector and measured. The resulting recorded spectra and count rates have shown a detection efficiency of $8.1\% \pm 1.0\%$ and $28.6\% \pm 0.2\%$ respectively for samples 9782 and 10202. Comparing measurements of 10202 to 9782, the recorded 10202 spectrum shows a clear right-hand tail which has been attributed to the presence of far greater quantities of strontium-90 within the 10202 sample, compared to the 9782 sample activity which is mainly comprised of tritium.

The ability to rapidly manufacture flow cells has eliminated the possibility of sample residue spreading between experiments, greatly improving reliability and eliminating invalid measurements caused by cross-contamination. This rapid replacement of the flow cell cannot be achieved by other existing low energy beta detection systems due to them using a scintillator physically bonded to the photodetectors or detector casing. This also allows for easier maintenance in-situ, as when the scintillator becomes soiled or permanently contaminated, the flow cell can be quickly swapped for another without the detector having to be moved from the site.

6 In-situ Detector Outer Casing Design and Development

6.1 Introduction

For this detector to be useful to Sellafield, it must fit within the small confines of the on-site groundwater boreholes and ideally have no above ground infrastructure. Additionally, it must be easy to repair and maintain and run for long periods independently. This chapter details the development from the benchtop system discussed in sections 4.11.2, 4.11.3 and 4.11.4, into the final compacted detector casing.

This compaction process will require systems like the cooling and printed circuit board (PCB) connectors to be re-designed, keeping the methodology validated in previous chapters, but with new custom parts to facilitate its size reduction. Furthermore, the aim of this chapter is to provide methods that can assist the compaction of other existing low energy beta detectors in addition to our laminated flow cell system.

6.2 Battery Pack Design

For the detector to function independently without a constant mains power connection an alternative inbuilt battery source is required. This battery must be low noise and be capable of creating the following voltages and currents.

- 12 V at ~1 A runs the sample flow pump and thermoelectric coolers
- 5 V at 260 mA powers the Raspberry Pi Zero W
- 5 V at 10 mA powers the silicon photomultiplier (SiPM) Amplifiers and analogue to digital converters (ADCs)
- 3.3 V at 210 mA powers the pulse processing field programmable gate array (FPGA)
- -31 V at 0.1 mA supplies the SiPM bias

As components including the pump and Raspberry Pi create a large amount of noise on their supplies, it is ideal to separate their supplies from the other noise sensitive devices, mainly the SiPM Amplifiers. As a result, the battery pack was segmented to assign each to one of the listed voltages. Lithium-ion batteries were used as they come in a wide variety of sizes, used for AMR (Autonomous Mobile Robot) applications which require long run times [162], and have been integrated into wireless ground contamination monitoring systems [163].

The SiPM bias supply with Zener temperature compensation uses the least amount of current ~0.1 mA and so a low-capacity battery can be used. A total of 9 cells each with a 3.7 V nominal voltage were placed in series to achieve a 33.3 V potential. With a 450 mAh capacity the bias supply would last approximately 26.79 weeks before requiring a recharge.

For all other supplies 18650 lithium-ion cells were used each with a 3,250 mAh capacity [164], battery holders hold three batteries in parallel having a diameter of 41.7 mm, smaller than the inner bore of the casing allowing the packs to be easily slid in and out of the casing. 3D printed clips have been designed to attach each battery holder to their neighbour while allowing quick connection and disconnection for easy maintenance. Figure 6.1 below shows how the clip attaches

with screws to the negative terminal of the battery, and clips onto the positive of the next battery.

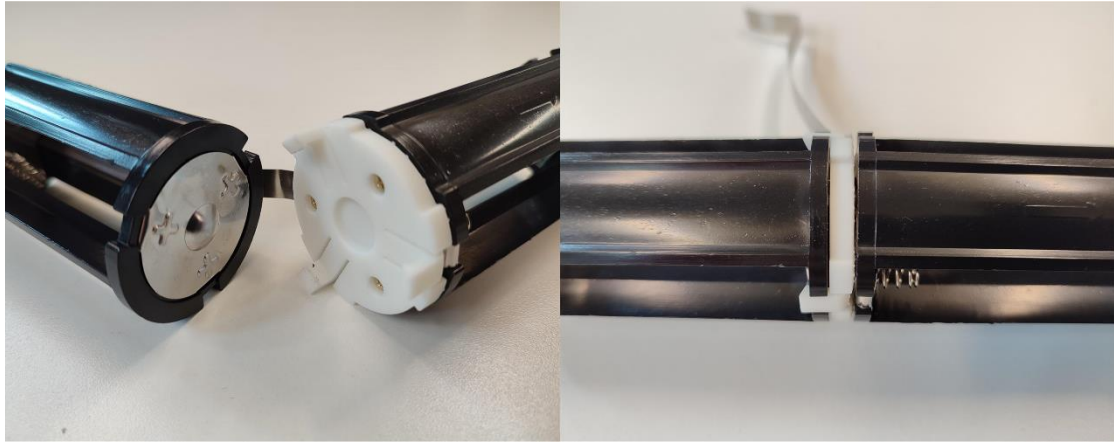


Figure 6.1: Images showing the attachment of two battery holders using a white 3D printed battery clip.

As the battery clips do not provide an electrical connection, nickel strips have been used to wire all holders in parallel maximising current capacity. One of the three screws located on each holder's negative terminal is used to hold one end of the strip while the other is held by the compressive force on the positive terminal by the neighbouring clip.

Care was taken before inserting cells into the holders by measuring the voltage of each cell to ensure they matched to within 0.05 V of each other, a greater voltage difference can cause excessively high current to or from the battery which could result in heating and permanent damage of the cell.

To keep the battery pack waterproof 3D printed adapters were created, an example of an adapter can be seen in Figure 6.2. Included are two redundant O-seals per end that are pressed between ridges in the adapter and the inner face of the casing. To keep the casing from sliding apart, four flush inset screws have been added on opposing sides of the casing, brass insets pressed into the adapter provide a firm thread to improve reliability. The adapter is hollow to allow power and signal cables to travel up and down the detector.

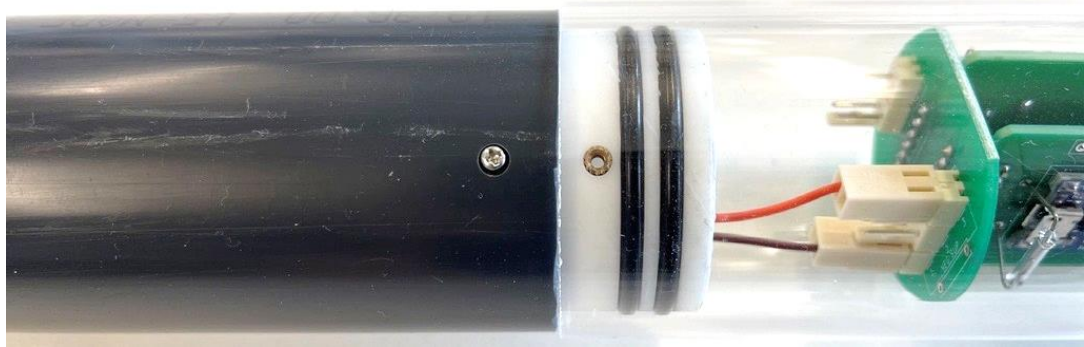


Figure 6.2: Image of waterproof casing adapter which holds together sections of the detectors outer casing. Brass inlet can be seen on right, inserted screw can be seen on left.

6.3 Supply Regulation and Protection

As lithium-ion batteries are being used, there is a requirement to include under-voltage and over-discharge protection to ensure the safety of the system and to ensure the battery will remain working reliably. For this multiple PCBs were designed and are shown disassembled in Figure 6.3, and assembled in Figure 6.4.

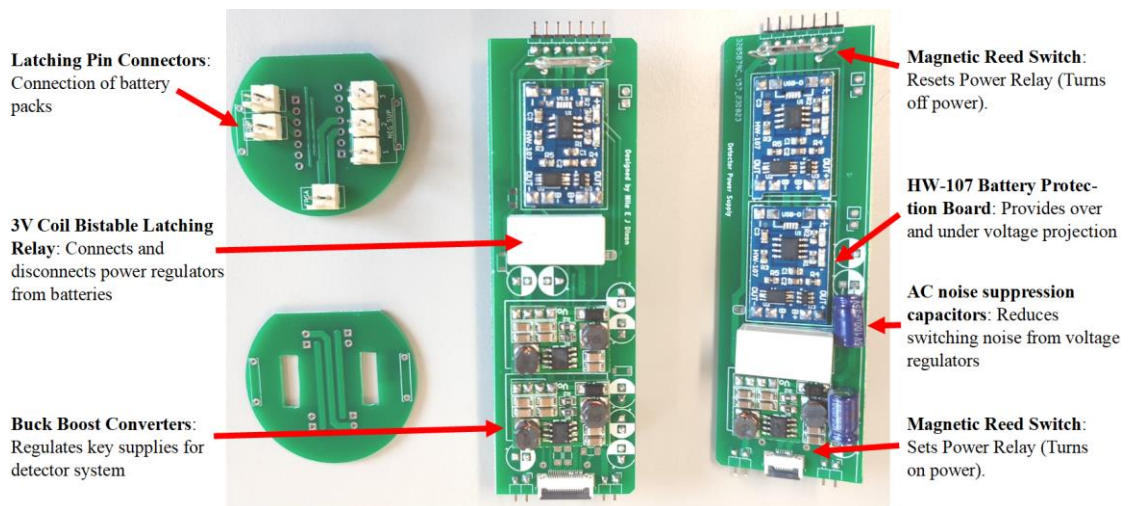


Figure 6.3: Image of supply regulation boards prior to assembly and fitting into the outer casing, labelled with key design features.

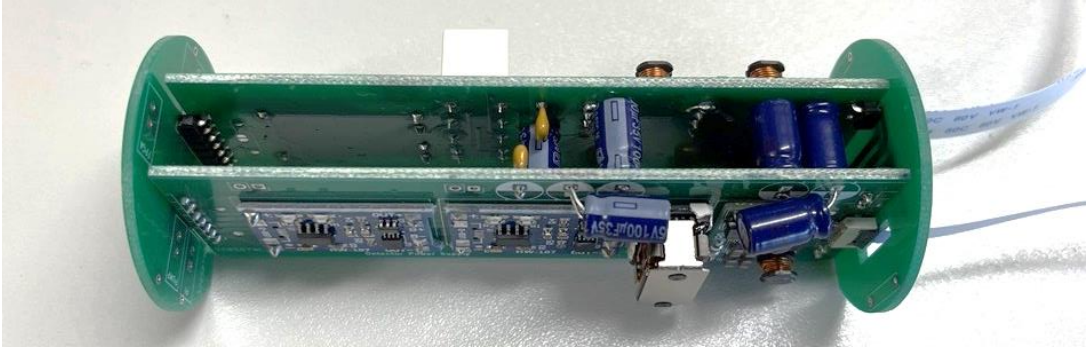


Figure 6.4: Image of supply boards fully assembled, cutouts in end (right) PCB allow ribbon cables to connect to Raspberry Pi shield.

Two safety features have been added, the first being a resettable fuse added to each output as a power supply energy limiter [165]. Unlike a standard wire fuse which once broken must be replaced, a resettable polymer fuse is made from layers of polymer and conductive particles which at room temperature provide a low-resistance path. In the case of a short, the increased current causes the polymer to warm and expand increasing its resistance greatly, the small amount of leakage current across the fuse keeps it in its tripped state until power is disconnected. Without power, the fuse is allowed to cool allowing for the low-resistance paths to reform. These devices are also referred to as having a positive temperature coefficient (PTC) [166].

Secondly, a HW-207 lithium-ion protection and charging board combines a TP4056 controller to ensure the safety of the battery pack by limiting charging current, and a DW01A battery protection IC which protects against over-charge, over-discharge and over-current. This board has been successfully integrated with other sensor and monitoring systems for weather [167] and fever screening [168].

To maximise the capacity of the batteries, buck-boost converter boards using the single ended primary inductor converter (SEPIC) topology have been incorporated to regulate the voltage supplies for the FPGA, SiPM Amplifiers and ADC supply. While literature is limited on the converter, testing by Lui [169] concluded that the converter could handle an input voltage range from 1.5 V to 6.5 V with a typical efficiency between 70% and 80%.

For ease of use, four magnetic reed switches have been integrated and combined with two latching relays. An operator can hold a small magnet up to the outer casing over the reed switches to connect and disconnect the detector's power supply without having to directly touch the PCBs or open the outer casing. This is important for in-situ maintenance where the detector needs disconnecting, but without disassembly.

6.4 Flat Flex Cable Interconnect Adapters

Figure 6.5 and Figure 6.6 show the adapter boards designed to convert the larger 2.54 mm pin headers into the much more compact flat flex cable (FFC) connectors. This will allow the boards tested in the benchtop system to be compacted for use in the final detector. An overall wiring schematic can be seen in Appendix C (Figure C.2) and shows how signal and power cables pass from board to board, duplicate cable connections to the same power terminals have been made to ensure minimal voltage drop over the ribbon cables.

By including FFC connectors each board could easily be disconnected and reconnected allowing for regular maintenance between periods of experimental testing. Each board can be removed individually and probed using pin breakout boards, and hardware alterations can also be made by swapping the amplifier or SiPM sensors heads as required.

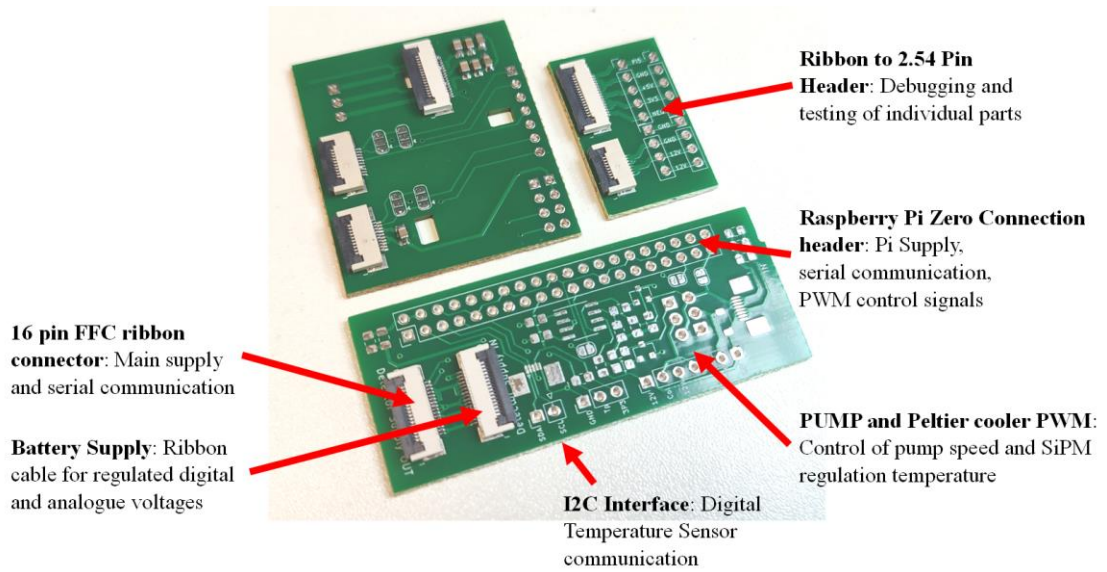


Figure 6.5: FFC interconnects for final detector electrical system. Includes an adapter for the ADC board, Raspberry Pi Zero shield and debugging breakout board.

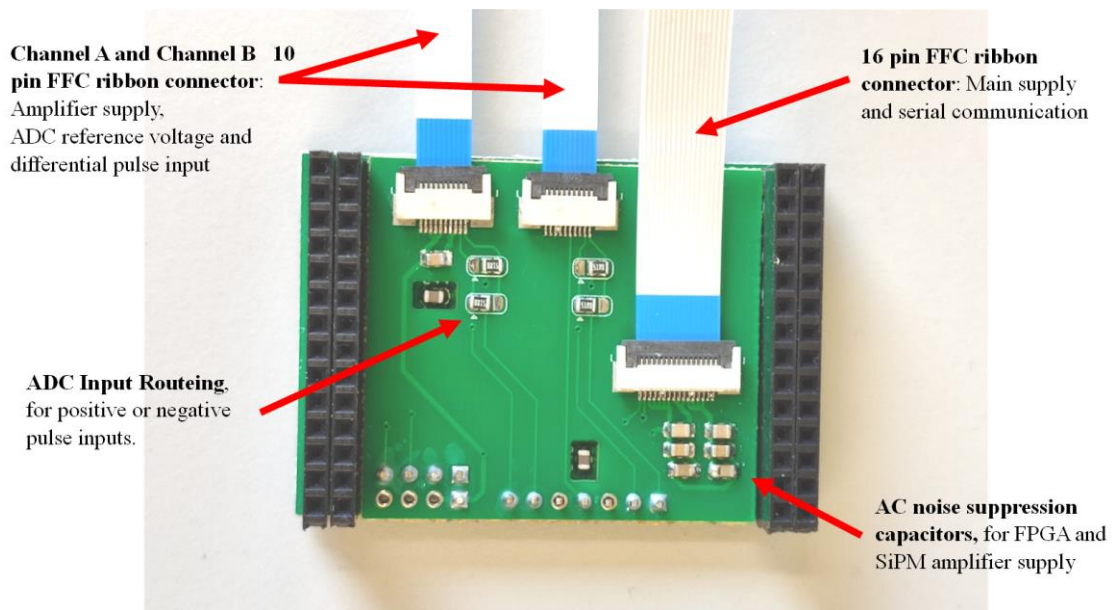


Figure 6.6: ADC Adapter board, this PCB was used to convert the original 2.54 mm pin header of the ADC board into FFC ribbon cables allowing for the system to fit within the cylindrical housing.

6.5 Compacted Cooling System

Due to the success of the implemented bench top cooling system which kept a consistent and reduced background count rate (discussed in section 4.11.5), a similar system has been created with two main differences: Custom 3D printed cooling blocks fit either side of the flow cell casing allowing coolant to remove heat, and Peltier coolers have been placed between the casing and cooling blocks to dissipate heat away from the internal SiPMs. The major factor for these changes is that the liquid cooling bath and aluminium cooling blocks cannot fit within the confines of the detector casing. Figure 6.7 shows the general principle of the updated system.

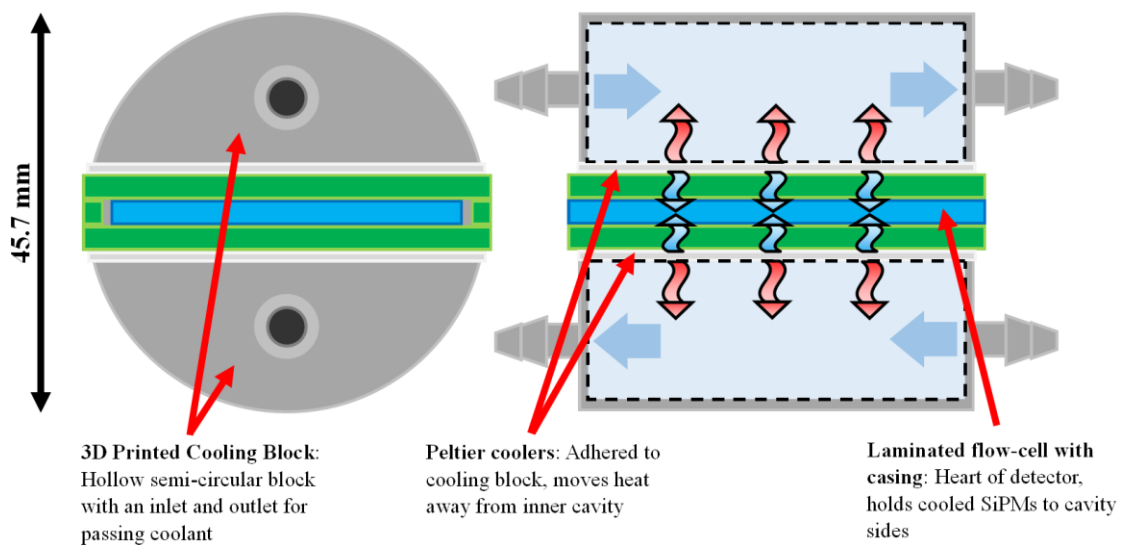


Figure 6.7: Diagram showing how the Peltier coolers move thermal energy away from the laminated flow cell and into the coolant.

The individual parts of the manufactured compacted cooling blocks can be seen in Figure 6.8, following this the fully assembled system can be seen annotated in Figure 6.9.

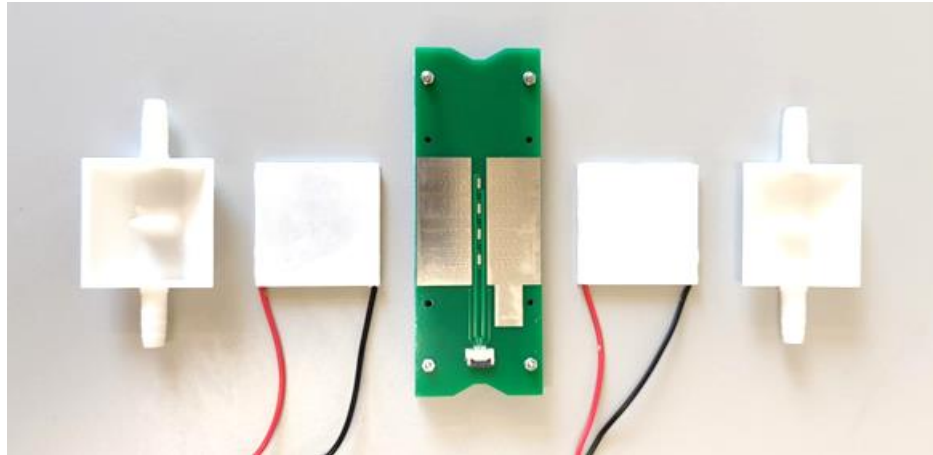


Figure 6.8: Image of separate cooling parts before being combined to create the cooling system.

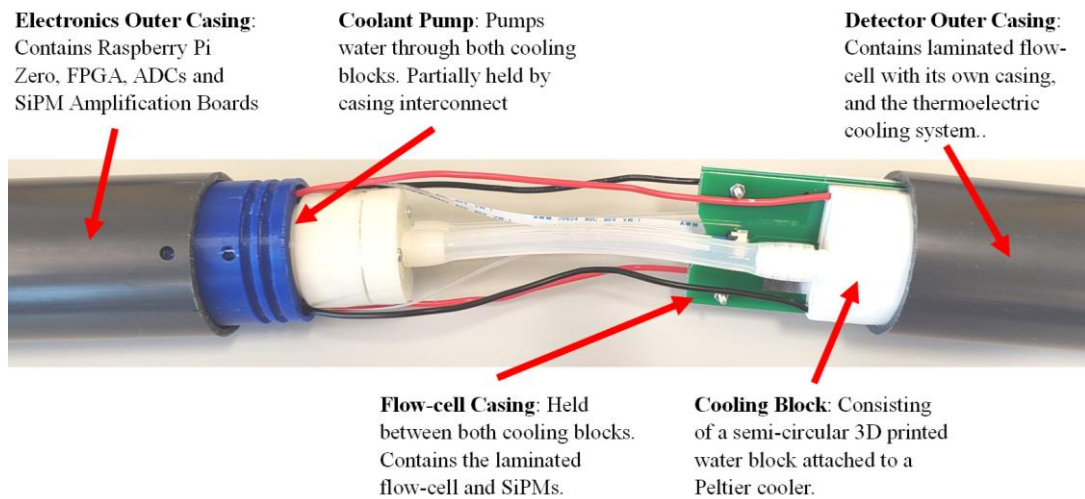


Figure 6.9: Image of compacted cooling system placed within the detector housing. The image is labelled with its key components.

Arctic MX-6 thermal paste [170] was added between the Peltier and flow cell casing surfaces to maximise thermal conduction.

A cooling experiment was performed with the compacted cooling system in the interest of studying its behaviour. In this setup three thermocouples were used, one was placed within the coolant reservoir (Pyrex beaker) and two were attached to the inner surface of each half of the flow cell casing where the SiPMs would normally be soldered. Every 10 seconds the temperature of each thermocouple was noted.

The pump was running at its maximum voltage of 6 V with a voltage of 24 V placed over both Peltier coolers connected in series. In the experiment, the minimum temperature of the internal casing reached -5.7°C and -5.4°C respectively. A plot of the measured temperatures over time can be seen in Figure 6.10.

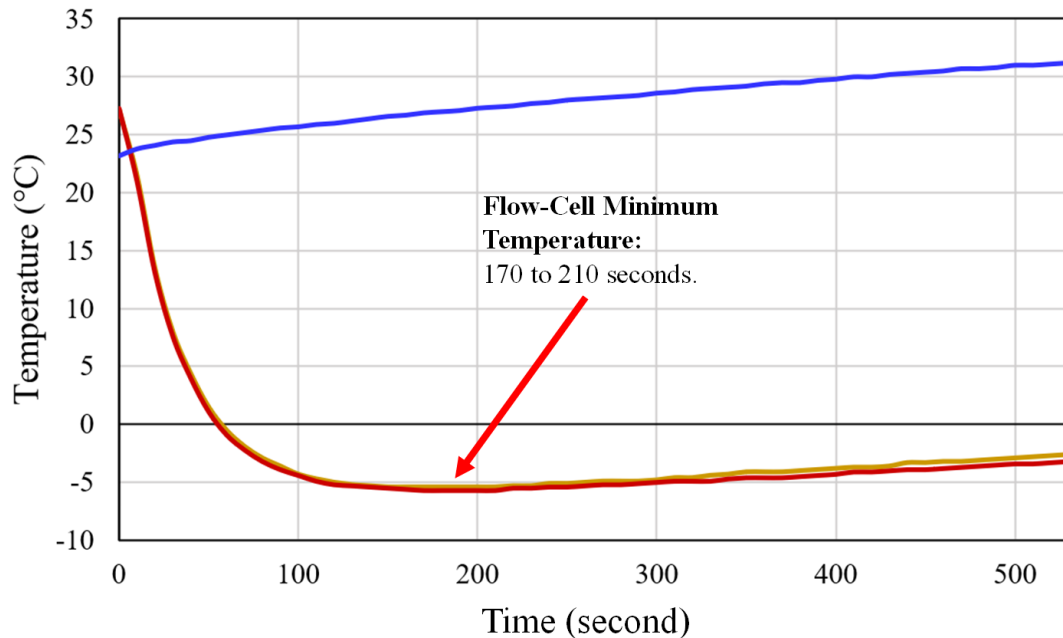


Figure 6.10: Graph of recorded temperatures from compacted cooler experiment. Blue trace is the reservoir, red plot is the inner casing attached to the first cooling block, and orange plot is the inner casing attached to the second cooling block.

As a result, it has been shown that this cooling system could reach a set temperature of 4°C , given the coolant reservoir can sink the heat continuously while the detector is running. For its in-situ environment, the borehole water will itself be used as a heat sink.

6.6 Activated Carbon Filtration

As the radioactive samples and tracers available for the validation testing had minimal to no sediment, filtration was not included in the benchtop system. However, the final detector will require some form of filtration when placed within an actual borehole. Figure 6.11 shows a suggested active carbon filter which can be placed in series before the detection cavity flow cell. The filter uses the same lamination process and hose adapters used to make the flow cell.



Figure 6.11: Image of concept active carbon filter made with the same method as the laminated flow cell but with active carbon instead of powdered scintillator.

The filter in Figure 6.11 measures approximately 34 cm long. The length was limited by the length of the strip laminator. With an automatic lamination machine, this filter could reach multiple meters in length if a significantly high pressure can allow a sample to pass through.

6.7 Conclusions

Figure 6.12 shows a photograph of the final detector system placed into a circular acrylic tube with an outer diameter of 50 mm, key areas of the detector are linked back to their corresponding sections discussing their design. A 30 cm ruler has been included for scale.

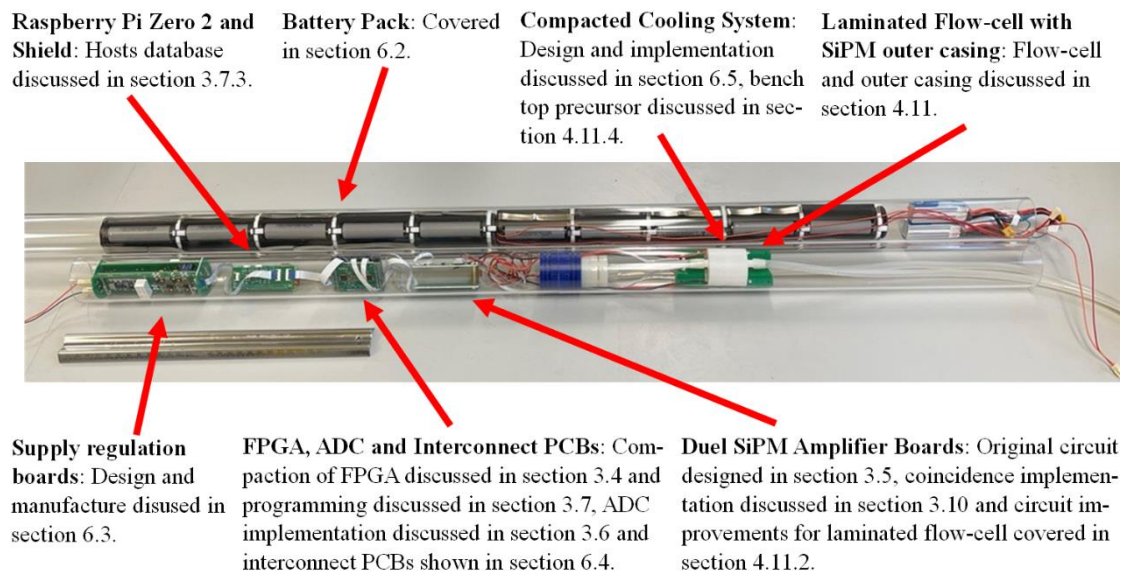


Figure 6.12: Image of final detector, compacted to fit within the confines of Sellafield's boreholes. A clear outer acrylic casing has been used to show the internal systems. Technology developed throughout this thesis have been integrated, labels have been added to link each part to their section within the thesis.

It has been demonstrated that the technology developed over the course of the project can indeed fit within the confines of the boreholes located on Sheffield and based on the literature review of previous flow cell detector systems, this is the first low energy beta detector to do so. In addition, not only is the flow cell able to fit but also the supporting electronics, communication systems and power supply (battery pack). Providing the detector is in the signal range of a wireless fidelity (Wi-Fi) network, the detector can fully fit within the ground with no above ground systems.

The compact cooling system has been shown to have a minimum cooling capacity of approximately -5°C based on the temperatures recorded of the inner flow cell casings. This is below the temperature of 4°C used to detect tritium as detailed in section 5.2.2 and therefore will allow the minimal detectable activity (MDA) of the detector to be further maximised.

7 Conclusions

As a result of this work, each objective informed by the needs of nuclear licensed sites like Sellafield, Dounreay, and Dungeness B, in contrast with currently existing low-beta detection systems has been met. To the best of our knowledge, the following novelties are a result of this work, and are stated in the following points:

- The first detection system to use Zener diodes for the compensation of a Silicon Photomultiplier's (SiPM) gain due to temperature drift.
- The first liquid flow cell beta detector capable of tritiated water detection within a 50 mm diameter. With a measured minimum detectable activity (MDA) of 18.67 Bq mL^{-1} for a 24 hour counting period.
- The first detection system to implement heat lamination for the rapid manufacture of scintillator-filled detector cavities.
- The largest number of granulated scintillator group sizes experimentally tested with dilute tritiated water.
- The first publication to discuss the use of an auto sieve for the separation of granulated scintillators.
- The first implementation of coincidence SiPMs for the detection of tritiated water.
- The first implementation of SiPMs arrays (3 SiPMs per channel) for the detection of tritiated water.

7.1 Effectiveness of Granulated Scintillators

The study of granulated scintillators (see Chapter 4) within an liquid scintillation counter (LSC) has shown that the method presented in this work can powder and separate a solid block of calcium fluoride doped with europium ($\text{CaF}_2(\text{Eu})$) into multiple particle size distributions while allowing it to keep its scintillating

properties. It has also demonstrated a relationship between size distribution and detected counts for tritiated water, obtaining a maximum detection efficiency of $0.20\% \pm 0.01\%$ and count rate of $440.7 \text{ CPM} \pm 29.9 \text{ CPM}$ for $\text{CaF}_2(\text{Eu})$, with particle sizes up to $50 \mu\text{m}$. Additional testing with blade ground BC408 has shown that a detection efficiency of 0.16% can be achieved for tritiated water, but the use of blade grinders has been shown to add impurities that visually cloud the scintillator over time.

7.2 Ease of Maintenance

Rapidly manufacturable laminated flow cells have allowed the internal cavity of the detector to be easily used and replaced, this was greatly beneficial to ensure no cross-contamination between experiments. Also, as the flow cell is not physically bonded to the SiPMs, the SiPMs can be reused multiple times. Suggestions have been provided on how the developed lamination technique can be used to create activated carbon filters (see section 6.6).

3D printed adapters for the outer detector casing have been designed to hold each key section in place with two inset screws (see section 6.2). This allows a single screwdriver to disassemble both the outer casing and the flow cell assembly. Splitting the battery pack from the backend electronics and flow cell allows it to be swapped for a fresh pack reducing overall downtime. The inclusion of battery pack protection and magnetic reed switches (see section 6.3) increases the reliability of the system which is of great importance to the nuclear industry.

7.3 Detection of Low Energy Betas

A flow cell capable of the detection of low energy betas has been designed, built, and validated using multiple samples of dilute tritiated water. This system has also implemented a coincidence counting system based on SiPMs as opposed to the more commonly used photomultiplier tubes (PMTs), which to our knowledge is the first of its kind experimentally verified with tritium, therefore making this system novel. The use of SiPMs will allow much greater flexibility compared to

PMTs, as the sensitive light detection area can be easily configured to the elongated shape of the flow cell, in the case of this detector a strip. Implementation of SiPMs has also made the detector safer to operate in wet environments due to the much lower required bias voltages.

Experiments with multiple dilutions of tritiated water have shown that the count rate measured by the detector increases with the addition of low energy betas into the flow cell cavity. For tritium detection, an average efficiency of 0.14% and MDA of 18.67 Bq mL^{-1} have been obtained. Comparing normalised spectrums taken of dilute tritiated water and strontium-90 tracer within the flow cell has shown the latter produces counts in higher channels, identifying the presence of the higher energy betas.

Compared with existing low energy beta detection systems, the system developed here shows an improved MDA over a continuous tritium monitor [73] (see section 2.7.9) which reports an MDA for liquid tritium at 133 Bq mL^{-1} for a 24 hour counting time. An MDA comparable to a real-time tritium-in-water monitor which reports $29.8 \text{ Bq mL}^{-1} \pm 3.6 \text{ Bq mL}^{-1}$ [70] (see section 2.7.6) has been achieved although requiring a longer measurement time (1 hour versus 24 hours). While a well-logging probe [64], [65] (see section 2.7.4) did see a lower MDA of 1.85 Bq mL^{-1} it did not take into account the capture and conversion of tritium before the cold trap, also this logging probe can only detect tritium and no other radioisotopes due to its method of separating gaseous tritium before measurement, unlike the detector proposed here which has been tested with both ^3H and ^{90}Sr . Finally, an underwater beta monitoring system [63] (see section 2.7.3) predicts a 2 year measurement time to reach a comparable MDA of 10 Bq g^{-1} , far longer than 24 hours to achieve a 18.67 Bq mL^{-1} MDA for the new laminated detector.

Two radioactive groundwater samples from Sellafield boreholes 9782 and 10202 were passed into the flow cell for detection. Results found a clear right-hand tail within the 10202 sample spectra, unlike the 9782 sample spectra, showing that the detector can recognise the far greater quantities of strontium-90 within the 10202 sample. The detector was also able to detect low energy betas emitted by

the 9782 sample, of which its activity is comprised mostly of tritium decay. A detection efficiency of $8.1\% \pm 1.0\%$ was calculated for sample 9782 and a detection efficiency of $28.6\% \pm 0.2\%$ was calculated for sample 10202, based on the total activity within the flow cell.

7.4 Backend System Compaction

Further compaction of the bench top system into the outer casing shows that this detector can indeed be powered from batteries, can be kept at a suitability low temperature using Peltier coolers, and that the developed circuit boards can fit within the size requirements. A connected database allows multiple spectrums to be stored and downloaded wirelessly over a private wireless fidelity (Wi-Fi) network removing the need for a constant wired connection to an operator's computer (see section 3.7.3). Storing multiple spectra over time has allowed the temperature stability and flow cell cavity fill time to be studied.

This built system is believed to be the only flow cell detector available which meets the size requirements for in-situ installation within current onsite 50 mm diameter boreholes, the only comparable system (see section 2.7.4) uses a completely different detection technique and can only fit within a borehole larger than 60 mm diameter. Suggestions have also been given on how the developed technology in this thesis can be integrated with existing sheet and fibre flow cells to reduce overall detector diameter (see section 4.12).

7.5 Temperature Stabilisation

A temperature compensation system has been included and validated using light emitting diode (LED) blink experiments (see section 3.9.3). It is believed that this is the first compensation system to take advantage of Zener diode combinations for the matching and active temperature sensing of the SiPMs. Multiple sensor head printed circuit boards (PCBs) were produced which include and hold the Zener diodes in close proximity to the SiPMs.

The inclusion of a cooling system has reduced the background count rate of the results due to the lower noise floor of the SiPMs when actively cooled, and therefore has lowered the minimal detectable activity (MDA) of the detector. The variation in background counts over time has also been reduced with the addition of the cooling system (see section 4.11.4), this allows an elevation in count rate to be attributed to the addition of low energy beta activity into the detector and not external temperature factors like time of day, season or heating from electronics. While the bench top system implemented a cooling bath, Peltier coolers with water blocks have also shown the ability to cool SiPMs down to below 4°C (see section 6.5).

7.6 Pulse to Spectrum Conversion

Multiple SiPM amplifier circuits have been designed and manufactured with the final iteration including rotary switches allowing the gain and filtering to be configured quickly. An analogue to digital converter (ADC) board has incorporated two ADCs that can run simultaneously to read from two independent input channels (see section 3.6).

The inclusion of an field programmable gate array (FPGA) has allowed a high-speed trapezoidal shaping algorithm to be implemented in coincidence counting mode, LED blink testing shows the effect of the shaping coefficients on spectrum resolution and full width half maximum (FWHM) (see section 3.8). Spectrum Accumulation has allowed pulses to be collected and stored within the FPGA random access memory (RAM) before their transmission to a MySQL database (see section 3.7) using python scripts to both insert spectra as a binary large object (BLOB) within each row, and to query each spectrum for it to be accessed remotely. Use of a MySQL database has allowed hundreds of spectra to be stored and allows for secure access using secure shell (SSH). This database is hosted within the detector itself for long-term storage without the need for a constant outside connection.

7.7 Future Work

While the design of the compacted detector is mostly complete, further practical work would be recommended to ensure each system; compacted FPGA, cooling and power supply system, has been adapted correctly from the tested benchtop system.

The diagram in Figure 7.1 shows a suggestion of how the compact detector could be tested within a fume cabinet by attaching the top end of the detector to a tripod and the other end submerged in a sample. Previous experiments with dilute tritiated water and strontium tracers can then be repeated and results compared with the previous benchtop system.

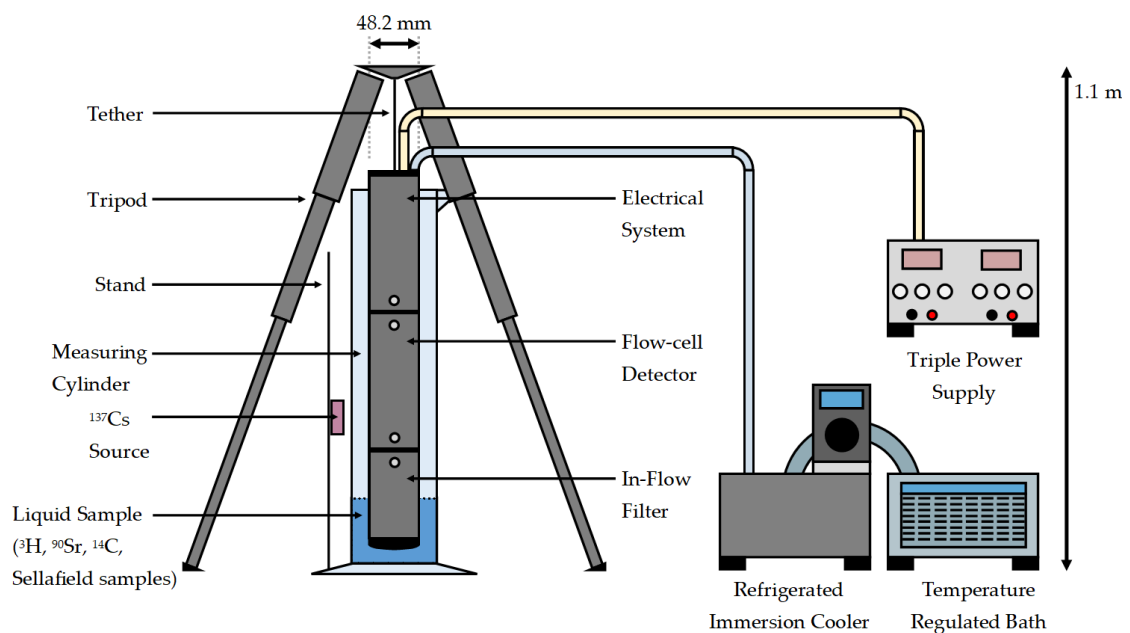


Figure 7.1: Suggested detector setup for testing in fume cupboard.

While scintillator moulding methods were formulated and tested in this work (see section 4.7), experiments comparing moulded scintillators to their unadulterated forms have yet to be investigated. Suggested experiments include adding an identical mass of BC408 powder to one vial and a block of loosely moulded BC408 powder to another for evaluation with an LSC.

Suggested improvements for a more conventional layered scintillating flow cell have been discussed in section 4.12 with sensor heads with Peltier cooling being

prototyped. Further work could be done to build a full system to compare the implementation of SiPMs in the laminated system to a more conventional layered flow cell.

Multiple flow cells with differing scintillator materials and particle sizes can be implemented within a single detector to differentiate between types of radiation helping to discriminate low energy betas in the presence of gamma and alpha emitters.

The effect of shielding the flow cell using lead blocks was not investigated but could be of interest to minimise the background count rate, which would increase MDA.

An issue yet to be rectified is the retention of activity within the flow cell. While laminated cavities can be rapidly manufactured and replaced to eliminate cross-contamination between test runs, this is not desirable for an in-situ detector which would aim to be deployed for long periods of time. Possible methods for reducing activity retention could include coating the scintillator particulates with a water proofing compound to decrease adsorption onto the scintillator surface; sourcing scintillator powder with spherical particulates free of cracks and crevasses which may trap or hold waterborne activity; or assessing alternative scintillators that were demonstrated experimentally to have low adsorption capacities for strontium-90. For the detection capabilities of tritium to be retained, any coatings applied to the particles would have to be extremely thin so that weak betas will not be fully attenuated before reaching the scintillator.

While the project has focussed on the measurement of tritium in the presence of strontium-90, the evidence suggests that detection of strontium-90 may be a simpler objective due to its stronger beta emission and the ability to use a coarser scintillator powder. If the issues of strontium-90 adsorption described above can be rectified, then this could enable the current system as is to be installed within a borehole for the monitoring of strontium-90, therefore providing a valuable contribution to in-situ groundwater monitoring.

8 References

- [1] J. Borg, *Dosimetry of low-energy beta radiation*, vol. 27. Riso National Laboratory, 1996. Accessed: Jul. 14, 2024. [Online]. Available:
<https://www.osti.gov/etdeweb/servlets/purl/385114>
- [2] J. S. Welsh, "Beta Radiation," *Radiation Oncology The Oncologist*, vol. 11, pp. 181–183, 2006, doi: 10.1634/theoncologist.11-2-181.
- [3] L. L. Lucas and M. P. Unterweger, "Comprehensive Review and Critical Evaluation of the Half-Life of Tritium," *J Res Natl Inst Stand Technol*, vol. 105, no. 4, 2000.
- [4] U.S. Department of Energy, "DOE Handbook - Design Considerations," 2014. Accessed: Jul. 14, 2024. [Online]. Available: <https://www.standards.doe.gov/standards-documents/1100/1132-BHdbk-1999/>
- [5] Oak Ridge National Laboratory, "Software: Rad Toolbox." Accessed: Jul. 14, 2024. [Online]. Available: <https://www.ornl.gov/crpk/software>
- [6] Health Protection Agency, "Review of Risks from Tritium: Report of the independent Advisory Group on Ionising Radiation," 2007, Accessed: Jul. 14, 2024. [Online]. Available: https://assets.publishing.service.gov.uk/media/5a7da092e5274a6b89a512ed/RCE-4_Advice_on_tritium.pdf

- [7] J. E. Phillips and C. E. Easterly, "Sources of Tritium," 1980. Accessed: Sep. 27, 2023. [Online]. Available: <https://www.osti.gov/servlets/purl/6867774>
- [8] P. W. Lisowski, "The Accelerator Production of Tritium Project," 1997, Accessed: Sep. 27, 2023. [Online]. Available: <https://ieeexplore.ieee.org/document/753415>
- [9] M. Kovari, M. Coleman, I. Cristescu, and R. Smith, "Tritium resources available for fusion reactors," *Nuclear Fusion*, vol. 58, no. 2, p. 026010, Dec. 2017, doi: 10.1088/1741-4326/AA9D25.
- [10] S. H. Son, S. K. Lee, and K. S. Kim, "Tritium production, recovery and application in Korea," *Applied Radiation and Isotopes*, vol. 67, no. 7–8, pp. 1336–1340, Jul. 2009, doi: 10.1016/J.APRADISO.2009.02.078.
- [11] R. J. Pearson, A. B. Antoniazzi, and W. J. Nuttall, "Tritium supply and use: a key issue for the development of nuclear fusion energy," 2018, doi: 10.1016/j.fusengdes.2018.04.090.
- [12] S. V. Ryzhkov and A. Y. Chirkov, *Alternative Fusion Fuels and Systems*. CRC Press, 2018. doi: 10.1201/9780429399398/ALTERNATIVE-FUSION-FUELS-SYSTEMS-SERGEI-RYZHKOV-ALEXEI-YU-CHIRKOV.
- [13] R. Andrade, S. Bhowmick, and A. K. Pund, "Application of tritium (^3H) as a tracer in seepage studies through hydraulic structures-NC-ND license (<http://creativecommons.org/licenses/by-nc-nd/4.0/>)," 2022, doi: 10.1016/j.hydres.2022.07.001.
- [14] I. K. Bronić and J. Barešić, "Application of Stable Isotopes and Tritium in Hydrology," 2021, doi: 10.3390/w13040430.

- [15] T. Yamanishi, H. Kakiuchi, H. Tauchi, T. Yamamoto, and I. Yamamoto, "Discussions on Tritiated Water Treatment for Fukushima Daiichi Nuclear Power Station Discussions on Tritiated Water Treatment for Fukushima Daiichi Nuclear Power Station," 2020, doi: 10.1080/15361055.2020.1716454.
- [16] Sellafield Ltd, "Monitoring our Environment Discharges and Environmental Monitoring Annual Report 2020," 2021. Accessed: Feb. 13, 2024. [Online]. Available: <https://www.gov.uk/government/organisations/>
- [17] Health Protection Agency, "Review of Risks from Tritium," 2007. Accessed: Nov. 07, 2023. [Online]. Available: https://assets.publishing.service.gov.uk/media/5a7da092e5274a6b89a512ed/RCE-4_Advice_on_tritium.pdf
- [18] A. M. Brues, A. N. Stroud, and L. Rietz, "Toxicity of Tritium Oxide to Mice," <https://doi.org/10.3181/00379727-79-19310>, vol. 79, no. 1, pp. 174–176, Jan. 1952, doi: 10.3181/00379727-79-19310.
- [19] A. L. Brooks, A. L. Carsten, D. K. Mead, J. C. Retherford, and C. R. Crain, "The Effect of Continuous Intake of Tritiated Water (HTO) on the Liver Chromosomes of Mice," *Radiat Res*, vol. 68, no. 3, pp. 480–489, Dec. 1976, doi: 10.2307/3574329.
- [20] World Health Organization, "Management of Radioactivity in Drinking-Water." Accessed: Sep. 27, 2023. [Online]. Available: <https://www.who.int/publications/i/item/9789241513746>
- [21] B. T. Wilkins, J. Brown, D. J. Hammond, and M. J. Youngman, "Requirements for the radiological monitoring of drinking water: Guidance provided to the Drinking Water Inspectorate," 2008. [Online]. Available: www.dwi.gov.uk

- [22] C. Smith, "How Sellafield is managing its decommissioning programme | New Civil Engineer." Accessed: Feb. 13, 2024. [Online]. Available: <https://www.newcivilengineer.com/innovative-thinking/how-sellafield-is-managing-its-decommissioning-programme-28-10-2022/>
- [23] Sellafield Ltd, "Groundwater monitoring at Sellafield: 2016 data review." Accessed: Dec. 15, 2022. [Online]. Available: <https://www.gov.uk/government/publications/groundwater-monitoring-at-sellafield-2014-data-review>
- [24] Sellafield Ltd, "Monitoring our Environment: Discharges and Environmental Monitoring," 2021, Accessed: Apr. 22, 2024. [Online]. Available: <https://www.gov.uk/government/organisations/sellafield-ltd>.
- [25] J. Graham, "Discussion of Sellafield Groundwater Monitoring System," National Nuclear Laboratory, 2024.
- [26] C. Sneddon, "Environmental Monitoring at Dounreay," Apr. 26, 2023. Accessed: May 16, 2024. [Online]. Available: https://www.dounreaystakeholdergroup.org/wp-content/uploads/2023/05/DSG2023C015_Environmental-Monitoring-Presentation.pdf
- [27] EDF Energy, "Dungeness B monthly report October 2015," 2015. Accessed: Jul. 14, 2024. [Online]. Available: https://www.edfenergy.com/sites/default/files/dnb_monthly_comms_report_oct.pdf
- [28] W. Parrish, ; T R Kohler, and T. R. Kohler, "Use of Counter Tubes in X-Ray Analysis," *Review of Scientific Instruments*, vol. 27, pp. 795–808, 1956, doi: 10.1063/1.1715380.

- [29] G. F. Knoll, *Radiation Detection and Measurement*, Fourth. John Wiley & Sons, Inc, 2010.
- [30] G. C. King, R. E. Imhof, and A. Adams, "A photomultiplier cooler for use over extended periods of operation," *J Phys E*, vol. 7, no. 11, p. 882, Nov. 1974, doi: 10.1088/0022-3735/7/11/007.
- [31] T. M. Tritt, "Thermoelectric Materials: Principles, Structure, Properties, and Applications," *Encyclopedia of Materials: Science and Technology*, pp. 1–11, 2002, doi: 10.1016/B0-08-043152-6/01822-2.
- [32] T. T. Alton, S. D. Monk, and D. Cheneler, "Beta particle energy spectra shift due to self-attenuation effects in environmental sources," *Nuclear Engineering and Technology*, vol. 49, no. 7, pp. 1483–1488, Oct. 2017, doi: 10.1016/J.NET.2017.05.001.
- [33] T. L. Alton and M. Physics, "In-Situ Monitoring of Groundwater Radionuclides with Emphasis on Tritium Detection", Accessed: Jul. 14, 2024. [Online]. Available: <https://eprints.lancs.ac.uk/id/eprint/130772/1/2019altonphd.pdf>
- [34] Institute for Nuclear Medical Education, "Nuclear Counting Statistics," in *INME - Principles of Radiation Physics*, Boulder, Colorado, ch. 14.
- [35] Sellafield Ltd, "Monitoring our Environment: Discharges and Environmental Monitoring Annual Report 2021," 2022. [Online]. Available: <https://www.gov.uk/government/organisations/sellafield-ltd>.
- [36] J. Graham, "10202 and 9782 Borehole Trend Data (Provided by Sellafield, not publicly available)," 2022.

- [37] H. Leon and F. Curtiss, *The Geiger-Muller Counter*. Washington, D.C.: United States Department of Commerce, 1950.
- [38] T. Seimiya, K. Sekine, and T. Sasaki, "Counting of tritium with a thin windowed Geiger-Müller counter tube," *J. SCI. INSTRUM*, vol. 42, pp. 906–907, 1965, doi: 10.1088/0950-7671/42/12/429.
- [39] P. R. Steinmeyer, *G-M Pancake Detectors: Everything You've Wanted to Know (But Were Afraid to Ask)*, vol. 10. RSO Magazine, 2005.
- [40] G. Michał and K. Rafał, "Studies of the applicability of CMOS and CCD sensors for detection, dosimetry and imaging of alpha, beta, gamma, X-ray and proton beam spots." Accessed: Jan. 12, 2024. [Online]. Available: https://www.researchgate.net/publication/274310254_Studies_of_the_applicability_of_CMOS_and_CCD_sensors_for_detection_dosimetry_and_imaging_of_alpha_beta_gamma_X-ray_and_proton_beam_spots
- [41] R. J. Ott, J. Macdonald, and K. Wells, "The performance of a CCD digital autoradiography imaging system," *Phys. Med. Biol*, vol. 45, pp. 2011–2027, 2000.
- [42] T. Muranaka and N. Shim, "Electrolytic Enrichment of Tritium in Water Using SPE Film," *Electrolysis*, Oct. 2012, doi: 10.5772/52705.
- [43] B. Kumar *et al.*, "A compact tritium enrichment unit for large sample volumes with automated re-filling and higher enrichment factor," *Applied Radiation and Isotopes*, vol. 118, pp. 80–86, Dec. 2016, doi: 10.1016/J.APRADISO.2016.07.018.

- [44] R. Bhave, R. T. Jubin, and B. Spencer, "Tritium Separation from High Volume Dilute Aqueous Streams," 2016. [Online]. Available: <http://www.osti.gov/scitech/>
- [45] G. Li, M. Liang, S. He, J. Liu, X. Pang, and Z. Zeng, "RO film-based pretreatment method for tritium determination by LSC," *Applied Radiation and Isotopes*, vol. 166, p. 109343, 2020, doi: 10.1016/j.apradiso.2020.109343.
- [46] American Water Works Association, "Reverse Osmosis and Nanofiltration: Manual of Water Supply Practices M46," p. 226, 2007.
- [47] Power+Energy, "Hydrogen Separators - Separating Hydrogen and its Isotopes," 2014. [Online]. Available: www.PowerandEnergy.com
- [48] P. Bossard and J. Mettes, "System and method for separating hydrogen gas from a mixed gas source using composite structure tubes," Sep. 2006.
- [49] C. Georgette Woods, "Tritium Removal by Membrane Separation," *Chancellor's Honors Program Projects*, 2001, Accessed: Nov. 07, 2023. [Online]. Available: https://trace.tennessee.edu/utk_chanhonoproj/506
- [50] J. B. Duncan and D. A. Nelson, "The separation of tritiated water using supported polyphosphazene membranes," *J Memb Sci*, vol. 157, no. 2, pp. 211–217, May 1999.
- [51] D. Stanga and P. Cassette, "Improved method of measurement for tritiated water standardization by internal gas proportional counting," *Applied Radiation and Isotopes*, vol. 64, pp. 160–162, 2006, doi: 10.1016/j.apradiso.2005.06.009.

- [52] R. A. Surette and R. G. C. McElroy, "A review of tritium-in-water monitors," 1986. Accessed: Feb. 21, 2024. [Online]. Available: http://inis.iaea.org/Search/search.aspx?orig_q=RN:20064358
- [53] S. A. Bruyere and L. C. Cadwallader, "Operating experience review of tritium-in-water monitors," *Fusion Engineering and Design*, vol. 87, no. 5–6, pp. 565–568, Aug. 2012, doi: 10.1016/J.FUSENGDES.2012.01.028.
- [54] H. Kang, S. Min, B. Seo, C. Roh, S. Hong, and J. H. Cheong, "Low energy beta emitter measurement: A review," Dec. 01, 2020, *MDPI AG*. doi: 10.3390/chemosensors8040106.
- [55] A. Bala, D. G. Jenkins, and S. Namadi, "Radiation detectors for nuclear well-logging application: A review," *Dutse Journal of Pure and Applied Sciences*, vol. 8, no. 2a, pp. 80–93, Jun. 2022, doi: 10.4314/DUJOPAS.V8I2A.9.
- [56] A. J. Parker, M. D. Aspinall, C. Boxall, F. D. Cave, and M. J. Joyce, "Radiometric techniques for the detection and assessment of tritium in aqueous media-a review," *Progress in Nuclear Energy*, vol. 162, p. 104733, 2023, doi: 10.1016/j.pnucene.2023.104733.
- [57] M. M. Chilest, "Evaluation of a Thin CaF₂(Eu) Scintillator for Detecting Tritium," *IEEE Trans Nucl Sci*, vol. 34, no. 1, 1987.
- [58] J. Woo Bae, K. J. Kang, and H. R. Kim, "Multi-channel plastic-scintillator-based detection system for monitoring tritium in air," *Rev. Sci. Instrum*, vol. 90, p. 93304, 2019, doi: 10.1063/1.5092543.
- [59] Epic Crystal, "Plastic Scintillator - Product Details." Accessed: Apr. 10, 2024. [Online]. Available: <https://www.epic-crystal.com/scintillation-crystals/plastic-scintillator.html>

- [60] P. Przewłocki and K. Frankiewicz, "CosmicWatch," <http://www.cosmicwatch.lns.mit.edu/>.
- [61] F. Paul, "Circuit Simulator Applet - Full screen version," <https://www.falstad.com/circuit/circuitjs.html>.
- [62] T. A. Laplace, B. L. Goldblum, J. A. Brown, and J. J. Manfredi, "Scintillator light yield measurements with waveform digitizers," *Nucl Instrum Methods Phys Res A*, vol. 959, Apr. 2020.
- [63] W. Nyun Choi, U. Lee, J. Woo Bae, and H. Reyoung Kim, "Minimum detectable activity of plastic scintillator for in-situ beta measurement system in ground water," *Nuclear Engineering and Technology*, vol. 51, no. 4, pp. 1169–1175, Jul. 2019, doi: 10.1016/j.net.2019.02.001.
- [64] C. Menninga and R. L. Brodzinski, "A Design Manual for a Well-Logging Probe Capable of Measuring Tritium," Columbus, 1981.
- [65] C. Menninga and R. L. Brodzinski, "A Well-Logging Probe for Measuring Tritium: Construction and Operating Manual," Columbus, 1983.
- [66] C. D. R. Azevedo *et al.*, "TRITIUM - A Real-Time Tritium Monitor System for Water Quality Surveillance; TRITIUM - A Real-Time Tritium Monitor System for Water Quality Surveillance," *2018 IEEE Nuclear Science Symposium and Medical Imaging Conference Proceedings (NSS/MIC)*, 2018.
- [67] Hamamatsu Photonics K.K., "Photomultiplier Tube R2154-02," Dec. 2010. Accessed: Jul. 14, 2024. [Online]. Available: https://www.hamamatsu.com/eu/en/product/optical-sensors/pmt/pmt_tube-alone/head-on-type/R2154-02.html

- [68] Kontron, "6U VME64x 6021 Full Size Chassis." Accessed: Feb. 06, 2024. [Online]. Available: <https://www.wiener-d.com/product/6u-vme64x-6021-full-size-chassis/>
- [69] CAEN, "724 Digitizer Family," 2019. Accessed: Jul. 14, 2024. [Online]. Available: <https://www.caen.it/subfamilies/724-digitizer-family/>
- [70] C. D. R. Azevedo *et al.*, "Development of a real-time tritium-in-water monitor," *physics.ins-det*, Dec. 2023, Accessed: Jul. 14, 2024. [Online]. Available: <https://doi.org/10.48550/arXiv.2202.11068>
- [71] T. Kawano, H. Ohashi, Y. Hamada, and E. Jamsranjav, "Comparative Testing of Various Flow-Cell Detectors Fabricated using CaF₂ Solid Scintillator," <http://dx.doi.org/10.13182/FST14-T39>, vol. 67, no. 2, pp. 404–407, Mar. 2017, doi: 10.13182/FST14-T39.
- [72] C. H. Dong, K. Y. Liao, R. Y. Xu, H. W. Liu, and Q. X. Zhang, "Design and preliminary test of tritiated water online detector system based on plastic scintillators," *Nuclear Science and Techniques*, vol. 33, 2022, doi: 10.1007/s41365-022-01115-w.
- [73] J. W. Bae, K. J. Kang, and H. R. Kim, "Efficiency enhanced electrolysis-based tritium continuous monitor," vol. 322, pp. 1323–1329, 2019, doi: 10.1007/s10967-019-06836-8.
- [74] S. Managanvi, "An advanced method for quick detection of heavy water leak in steam generators of pressurized heavy water reactors," 2019, doi: 10.1016/j.nucengdes.2019.110447.
- [75] G. Berhane, C. Boxall, F. Cave, M. Joyce, and J. Pates, "Tritium Detection by Electrochemical Assisted Radiometrics (TRIBECA)," Lancaster, 2019.

- [76] T. L. Rucker, H. H. Ross, and G. K. Schweitzer, "Scintillator-Fiber Flow-Cell Radioactivity Detector for Liquid Chromatography*," *Chromatographia*, vol. 25, pp. 31–36, Jan. 1988.
- [77] A. P. Clarke, T. Rajanayagam, and R. P. Pettitt, "European Patent Specification: EP2761287B1," 2012
- [78] N. P. Kherani, "An alternative approach to tritium-in-water monitoring," *Nuclear Instruments and Methods in Physics Research A*, vol. 484, pp. 650–659, 2002.
- [79] R. V. Osborne and A. S. Coveart, "A personal tritium monitor." Accessed: Jan. 24, 2024. [Online]. Available: http://inis.iaea.org/Search/search.aspx?orig_q=RN:12575883
- [80] Mirion Technologies, "B Ionix™ 3 | Portable Tritium Monitor," 2021. Accessed: Jul. 14, 2024. [Online]. Available: <https://www.mirion.com/products/technologies/radiation-monitoring-systems/tritium-measurement/portable-mobile-monitors/ionix-portable-tritium-monitor>
- [81] Mirion Technologies, "HT Ionix™ | Tritium Bubblers," 2021. Accessed: Jul. 14, 2024. [Online]. Available: <https://www.mirion.com/products/technologies/radiation-monitoring-systems/tritium-measurement/tritium-samplers/ht-ionix-tritium-bubblers>
- [82] Y. Sanada *et al.*, "Basic study on tritium monitor using plastic scintillator for treated water discharge at Fukushima Daiichi Nuclear Power plant," *J Nucl Sci Technol*, 2023, doi: 10.1080/00223131.2023.2258880.
- [83] S. Elísio, M. J. Joyce, J. Graham, and B. Greenhalgh, "An advanced blind-tube monitoring instrument to improve the characterization of subsurface radioactive plumes," *EPJ Web*

- Conf*, vol. 253, p. 08005, 2021, doi: 10.1051/EPJCONF/202125308005.
- [84] Advatech UK, “Scintillators crystals overview,” Radiation Detection Scintillator Crystals. Accessed: Jul. 14, 2024. [Online]. Available: <https://www.advatech-uk.co.uk/scintillators-crystals-overview.html>
- [85] Z. Koelloe, “Studies on a plastic scintillator detector for activity measurement of tritiated water,” Jul. 2015. Accessed: Dec. 12, 2022. [Online]. Available: http://inis.iaea.org/Search/search.aspx?orig_q=RN:48044138
- [86] G. Saatsakis *et al.*, “Luminescence efficiency of CaF₂:Eu single crystals: Temperature dependence,” *Procedia Structural Integrity*, vol. 26, pp. 3–10, 2020, doi: 10.1016/j.prostr.2020.06.002.
- [87] L. Peralta, “Temperature dependence of plastic scintillators,” *Nuclear Inst. and Methods in Physics Research*, vol. 883, pp. 20–23, 2018, doi: 10.1016/j.nima.2017.11.041.
- [88] A. N. Otte, D. Garcia, T. Nguyen, and D. Purushotham, “Characterization of three high efficiency and blue sensitive silicon photomultipliers,” *Nucl Instrum Methods Phys Res A*, vol. 846, pp. 106–125, Feb. 2017, doi: 10.1016/J.NIMA.2016.09.053.
- [89] Broadcom, “AFBR-S4N66C013: NUV-HD Single Silicon Photo Multiplier Data Sheet,” 2021. Accessed: Apr. 17, 2024. [Online]. Available: <https://docs.broadcom.com/doc/AFBR-S4N66C013-NUV-HD-Single-Silicon-Photo-Multiplier-DS>
- [90] Onsemi, “Silicon Photomultipliers (SiPM), Low-Noise, Blue-Sensitive, C-Series SiPM Sensors,” Feb. 2022. Accessed: Jul. 14,

2024. [Online]. Available: <https://www.onsemi.com/download/data-sheet/pdf/microc-series-d.pdf>
- [91] E. Kuznetsov, "Temperature-compensated silicon photomultiplier," *Nucl Instrum Methods Phys Res A*, vol. 912, pp. 226–230, Dec. 2018, doi: 10.1016/J.NIMA.2017.11.060.
- [92] V. Ivanovs *et al.*, "Temperature Stabilization of SiPM-Based Gamma-Radiation Scintillation Detectors," *RAD Association Journal*, vol. 3, no. 3, 2019, doi: 10.21175/radj.2018.03.028.
- [93] A. Bala, J. R. Brown, D. G. Jenkins, and P. Joshi, "Operation of scintillators and SiPMs at high temperatures and their application for borehole logging," *Nuclear Inst. and Methods in Physics Research*, vol. 997, p. 165161, 2021, doi: 10.1016/j.nima.2021.165161.
- [94] Arduino, "Arduino® UNO R3 - Product Reference Manual," Jun. 2024. Accessed: Jul. 14, 2024. [Online]. Available: <https://docs.arduino.cc/resources/datasheets/A000066-datasheet.pdf>
- [95] H. Al Hamrashdi, D. Cheneler, and S. D. Monk, "A fast and portable imager for neutron and gamma emitting radionuclides," *Nucl Instrum Methods Phys Res A*, vol. 953, 2020.
- [96] Renesas, "EL5171, EL5371 - 250MHz Differential Twisted-Pair Drivers," Aug. 2015. Accessed: Jul. 14, 2024. [Online]. Available: <https://www.renesas.com/us/en/document/dst/el5171-el5371-datasheet>
- [97] C. M. Lavelle *et al.*, "Approaches for single channel large area silicon photomultiplier array readout," *Cite as: AIP Advances*, vol. 9, p. 35123, 2019, doi: 10.1063/1.5088503.

- [98] Analog Devices, “AD9244 - 14-Bit, 40 MSPS/65 MSPS A/D Converter,” Norwood, 2005. Accessed: Dec. 12, 2022. [Online]. Available: <https://www.analog.com/media/en/technical-documentation/data-sheets/AD9244.pdf>
- [99] S. Wan *et al.*, “Design and characterization of multichannel front-end electronics for detectors at HIRFL and HIAF,” *Journal of Instrumentation*, vol. 18, no. 11, p. C11006, Nov. 2023, doi: 10.1088/1748-0221/18/11/C11006.
- [100] S. Mastroianni, “The Readout Controller for the Calibration System of the Muon g-2 Experiment,” *IEEE Trans Nucl Sci*, vol. 65, no. 4, pp. 1033–1039, 2018, doi: 10.1109/TNS.2018.2809699.
- [101] Brightspec, “Technical Specifications TOPAZ-SiPM - a miniature digital MCA,” 2020. Accessed: Jul. 14, 2024. [Online]. Available: https://www.brightspec.be/brightspec/downloads/Topaz-SiPM_Spec_V1.03.pdf
- [102] E. M. Becker and A. T. Farsoni, “Wireless, low-cost, FPGA-based miniature gamma ray spectrometer,” *Nucl Instrum Methods Phys Res A*, vol. 761, pp. 99–104, Oct. 2014, doi: 10.1016/J.NIMA.2014.05.096.
- [103] V. T. Jordanov and G. F. Knoll, “Digital synthesis of pulse shapes in real time for high resolution radiation spectroscopy,” *Nucl Instrum Methods Phys Res A*, vol. 345, no. 2, pp. 337–345, Jun. 1994, doi: 10.1016/0168-9002(94)91011-1.
- [104] J. Zhang, X. Qin, M. Y. Zhao, and X. Chen, “FPGA implementation of a real-time digital pulse processing analysis for radiation detectors,” *Applied Radiation and Isotopes*, vol. 176, p. 109900, Oct. 2021, doi: 10.1016/J.APRADISO.2021.109900.

- [105] P. S. Lee, C. S. Lee, and J. H. Lee, "Development of FPGA-based digital signal processing system for radiation spectroscopy," *Radiat Meas*, vol. 48, no. 1, pp. 12–17, Jan. 2013, doi: 10.1016/J.RADMEAS.2012.11.018.
- [106] A. Arriojas, H. Barros, and J. Walter, "FPGA based digital signal processing for high resolution low energy gamma spectrometry," vol. 1607, p. 65, 2014, doi: 10.1063/1.4890704.
- [107] L. Marques, A. Vale, and P. Vaz, "State-of-the-Art Mobile Radiation Detection Systems for Different Scenarios," *Sensors*, vol. 21, no. 4, 2021, doi: 10.3390/s21041051.
- [108] V. T. Jordanov, G. F. Knoll, A. C. Huber, and J. A. Pantazis, "Digital techniques for real-time pulse shaping in radiation measurements," *Nucl Instrum Methods Phys Res A*, vol. 353, no. 1–3, pp. 261–264, Dec. 1994, doi: 10.1016/0168-9002(94)91652-7.
- [109] Altera, "Overview: Using the ModelSim Software with the Quartus II Software." Accessed: Dec. 12, 2022. [Online]. Available:
https://www.slac.stanford.edu/grp/md/ecae/Overview_Using_ModelSim_with_Quartus_II.html
- [110] Bokeh, "Bokeh at a Glance," bokeh.org. Accessed: Jul. 14, 2024. [Online]. Available: <https://bokeh.org/>
- [111] Python Software Foundation, "Python 3.9.6," Jun. 28, 2021, *Python Software Foundation: 3.9.6*. Accessed: Jul. 14, 2024. [Online]. Available:
<https://www.python.org/downloads/release/python-396/>

- [112] “Matplotlib — Visualization with Python.” Accessed: Dec. 09, 2024. [Online]. Available: <https://matplotlib.org/>
- [113] MySQL, “MySQL Connector/Python Developer Guide.” Accessed: Apr. 08, 2024. [Online]. Available: <https://dev.mysql.com/doc/connector-python/en/>
- [114] D. J. Herbert, V. Saveliev, N. Belcari, N. D’Ascenzo, A. Del Guerra, and A. Golovin, “First results of scintillator readout with silicon photomultiplier,” *IEEE Trans Nucl Sci*, vol. 53, no. 1, pp. 389–394, Feb. 2006, doi: 10.1109/TNS.2006.869848.
- [115] A. Kleimenova *et al.*, “3x3 mm² SensL SiPM characterization for the New CHOD detector of the NA62 experiment at CERN,” in *International Conference on New Photo-detectors*, 2016. doi: 10.22323/1.252.0068.
- [116] Analog Devices, “LTspice XVII,” Oct. 31, 2023, *Analog Devices: Version 17.1.15*. Accessed: Jul. 14, 2024. [Online]. Available: <https://www.analog.com/en/resources/design-tools-and-calculators/ltspice-simulator.html>
- [117] K. D. Mcgee and M. C. Model, “Silicon Photomultiplier Modeling of CsI(Tl) with Front End Electronics using a Monte Carlo Model,” Aug. 14, 2019. Accessed: Dec. 12, 2022. [Online]. Available: https://ir.library.oregonstate.edu/concern/graduate_thesis_or_dissertations/gh93h539p?locale=zh
- [118] F. Villa, Y. Zou, A. Dalla Mora, A. Tosi, and F. Zappa, “SPICE Electrical Models and Simulations of Silicon Photomultipliers,” *IEEE Trans Nucl Sci*, vol. 62, no. 5, pp. 1950–1960, 2015, doi: 10.1109/TNS.2015.2477716.

- [119] Voltera, "V-One - PCB prototyping made easy," voltera.io. Accessed: Jul. 14, 2024. [Online]. Available: <https://www.voltera.io/v-one>
- [120] ON Semiconductor, "Zener Voltage Regulators: 500 mW SOD-523, Standard Tolerance Series," Nov. 2020. Accessed: Jul. 14, 2024. [Online]. Available: https://www.mouser.co.uk/datasheet/2/308/MM5Z2V4T1_D-1551523.pdf
- [121] ON Semiconductor, "Zener Voltage Regulators: 300 mW SOD-323 Surface Mount Tight Tolerance Portfolio," Dec. 2015. Accessed: Jul. 14, 2024. [Online]. Available: https://www.mouser.co.uk/datasheet/2/308/MM3Z2V4ST1_D-1101657.pdf
- [122] Advatech UK, "NaI(Tl) Scintillators - Encapsulated." Accessed: Dec. 12, 2022. [Online]. Available: https://www.advatech-uk.co.uk/nai_tl_scint_encap.html
- [123] I. Akkurt, K. Gunoglu, and S. S. Arda, "Detection Efficiency of NaI(Tl) Detector in 511-1332 keV Energy Range," *Science and Technology of Nuclear Installations*, Mar. 2014, doi: 10.1155/2014/186798.
- [124] H. El-Gamal, H. Negm, and M. Hasabelnaby, "Detection efficiency of NaI(Tl) detector based on the fabricated calibration of HPGe detector," *J Radiat Res Appl Sci*, vol. 12, no. 1, pp. 360-366, Jan. 2019, doi: 10.1080/16878507.2019.1672313.
- [125] Lunds Universitet, "WWW Table of Radioactive Isotopes, Gamma Energy Search A = 241," nucleardata.nuclear.lu.se. Accessed: Jul. 14, 2024. [Online]. Available:

<http://nucleardata.nuclear.lu.se/toi/Gamma.asp?sql=&A1=241&A2=241&Z=95>

- [126] T. Alton, S. Monk, and D. Cheneler, "Heterogeneous scintillator geometries to maximise energy deposition for waterborne beta particle detection," *Radiat Meas*, vol. 111, pp. 6–12, Apr. 2018, doi: 10.1016/J.RADMEAS.2018.02.004.
- [127] T. Kawano, T. Uda, T. Yamamoto, and H. Ohashi, "Tritium Water Monitoring System Based on CaF₂ Flow-Cell Detector," *Fusion Science and Technology*, vol. 60, no. 3, pp. 952–955, 2011, doi: 10.13182/FST11-A12573.
- [128] A. Tarancón, J. F. García, and G. Rauret, "First approach to radionuclide mixtures quantification by using plastic scintillators Influence of the diameter of the plastic beads," *Anal Chim Acta*, vol. 590, pp. 232–238, 2007, doi: 10.1016/j.aca.2007.03.033.
- [129] Hidex, "Safety Data Sheet: Gold Star LT2," 2022. Accessed: Jul. 14, 2024. [Online]. Available: <https://www.hidex.com/products/cocktails/scintillation-cocktails-for-vial-based-counters>
- [130] Canadian Nuclear Society, "Nu-Salt or NoSalt as a radioactive source fact sheet," Jan. 2008. Accessed: Sep. 21, 2023. [Online]. Available: https://www.nost.edu.au/icms_docs/133854_Radiation_-_Banana_potassium_40.pdf
- [131] P. Siegel, "Natural Radiation." Accessed: May 29, 2024. [Online]. Available: <http://www.siegelsoft.com/phy432/labman/natrad.pdf>

- [132] National Institutes of Health, "Potassium K-40 | K | CID 6328542 - PubChem." Accessed: Jun. 04, 2024. [Online]. Available:
<https://pubchem.ncbi.nlm.nih.gov/compound/Potassium-K-40>
- [133] PerkinElmer, "High Performance Liquid Scintillation Analyzers," Shelton, 2005. Accessed: Nov. 07, 2023. [Online]. Available:
https://resources.perkinelmer.com/corporate/content/relatedmaterials/brochures/bro_highperliquidscintanalyzers.pdf
- [134] S. Berns *et al.*, "A novel polystyrene-based scintillator production process involving additive manufacturing," *Journal of Instrumentation*, vol. 15, no. 10, p. P10019, Oct. 2020, doi: 10.1088/1748-0221/15/10/P10019.
- [135] M. Pancoko, H. L. Nuri, A. Manaf, A. Dimiyati, A. Jami, and H. Subhiyah, "Comparative Study between Fabricated Plastic Scintillator and Existing Product for Gamma Detection," *J Phys Conf Ser*, vol. 2377, no. 1, p. 012046, Nov. 2022, doi: 10.1088/1742-6596/2377/1/012046.
- [136] Luxium Solutions, "BC-400,BC-404,BC-408,BC-412,BC-416 Premium Plastic Scintillators," 2023. Accessed: Jul. 14, 2024. [Online]. Available:
<https://www.luxiumsolutions.com/radiation-detection-scintillators/plastic-scintillators/bc400-bc404-bc408-bc412-bc416>
- [137] N. Kumawat, S. S. Soman, S. Vijayavenkataraman, and S. Kumar, "Rapid and inexpensive process to fabricate paper based microfluidic devices using a cut and heat plastic lamination process," *Lab Chip*, vol. 22, no. 18, pp. 3377–3389, Jul. 2022, doi: 10.1039/d2lc00452f.

- [138] Formlabs, “formlabs - Black Resin 1 L,” formlabs.com. Accessed: Jul. 14, 2024. [Online]. Available: <https://formlabs.com/uk/store/materials/black-resin/>
- [139] Hamamatsu Photonics K.K., “Hamamatsu: R11265U and H11934 Series,” Sep. 2019. Accessed: Jul. 14, 2024. [Online]. Available: https://www.hamamatsu.com/content/dam/hamamatsu-photonics/sites/documents/99_SALES_LIBRARY/etd/R11265U_H11934_TPMH1336E.pdf
- [140] Hamamatsu Photonics K.K., “Hamamatsu: R12900U Series,” Aug. 2019. Accessed: Jul. 14, 2024. [Online]. Available: https://www.hamamatsu.com/content/dam/hamamatsu-photonics/sites/documents/01_HQ/01_news/01_news_2019/2019_08_29_en.pdf
- [141] JLCPCB, “JLCPCB - Easier One-Stop Solutions for PCB & PCBA Services,” jlcpcb.com. Accessed: Jul. 14, 2024. [Online]. Available: <https://jlcpcb.com/>
- [142] C. Negrea and P. Svasta, “Modeling of thermal via heat transfer performance for power electronics cooling,” in *2011 IEEE 17th International Symposium for Design and Technology of Electronics Packages, SIITME 2011 - Conference Proceedings*, 2011, pp. 107–110. doi: 10.1109/SIITME.2011.6102697.
- [143] D. Gautam, D. Wager, F. Musavi, M. Edington, W. Eberle, and W. G. Dunford, “A review of thermal management in power converters with thermal vias,” in *Conference Proceedings - IEEE Applied Power Electronics Conference and Exposition - APEC*, 2013, pp. 627–632. doi: 10.1109/APEC.2013.6520276.
- [144] Y. Peng *et al.*, “An interdigital SiPM with coincidence measurement for rejection of dark noise,” *Nuclear Inst. and*

Methods in Physics Research, vol. 912, pp. 217–220, 2018, doi: 10.1016/j.nima.2017.11.058.

- [145] T. Xu, S. Yao, S. Chen, Q. Wei, Y. Liu, and T. Ma, “Optimization of Dual Mode Readout of Sensl SiPM for TOF PET Detectors,” in *2015 IEEE Nuclear Science Symposium and Medical Imaging Conference (NSS/MIC)*, San Diego, CA, USA, 2015, pp. 1–4. doi: 10.1109/NSSMIC.2015.7581741.
- [146] Absolute Casing Ltd, “Maxcases - MAX800,” max-case.co.uk. Accessed: Jul. 14, 2024. [Online]. Available: <http://www.max-case.co.uk/store/p49/MAX800.html>
- [147] Watson-Marlow, “100 series cased pump,” wmfts.com. Accessed: Jul. 14, 2024. [Online]. Available: <https://www.wmfts.com/en/watson-marlow-pumps/cased-pumps/100-series-cased-pump/>
- [148] G. Adamo *et al.*, “Silicon Photomultipliers Signal-to-Noise Ratio in the Continuous Wave Regime,” *IEEE Journal of Selected Topics in Quantum Electronics*, vol. 20, no. 6, pp. 284–290, 2014, doi: 10.1109/JSTQE.2014.2346489.
- [149] P. Buzhan *et al.*, “Silicon photomultiplier and its possible applications,” *Nucl Instrum Methods Phys Res A*, vol. 504, no. 1–3, pp. 48–52, May 2003, doi: 10.1016/S0168-9002(03)00749-6.
- [150] Grant Instruments, “Optima TX150 Heated Circulating Bath,” grantinstruments.com. Accessed: Jul. 14, 2024. [Online]. Available: <https://www.grantinstruments.com/products/optima-tx150-heated-circulating-bath>

- [151] Grant Instruments, "CGR Refrigerated Immersion Coolers," grantinstruments.com. Accessed: Jul. 14, 2024. [Online]. Available: <https://www.grantinstruments.com/products/cgr-refrigerated-immersion-coolers>
- [152] F.A.L. Dullien, *Porous Media Fluid Transport and Pore Structure*, Second. 1991.
- [153] Advatech UK, "CaF₂(Eu) - Calcium Fluoride Scintillation Material," advatech-uk.co.uk. Accessed: Jul. 14, 2024. [Online]. Available: https://advatech-uk.co.uk/caf2_eu.html
- [154] S. Dizman and O. Mukhtarli, "Tritium concentrations and consequent doses in bottled natural and mineral waters sold in Turkey and Azerbaijan," *Chemosphere*, vol. 267, Mar. 2021, doi: 10.1016/J.CHEMOSPHERE.2020.128721.
- [155] E. Browne, "WWW Table of Radioactive Isotopes: Sr-90," nucleardata.nuclear.lu.se. Accessed: May 08, 2024. [Online]. Available: <http://nucleardata.nuclear.lu.se/toi/nuclide.asp?iZA=380090>
- [156] E. Browne, "WWW Table of Radioactive Isotopes: Y-90," nucleardata.nuclear.lu.se. Accessed: May 08, 2024. [Online]. Available: <http://nucleardata.nuclear.lu.se/toi/nuclide.asp?iZA=390090>
- [157] M. P. Johansen, E. Prentice, T. Cresswell, and N. Howell, "Initial data on adsorption of Cs and Sr to the surfaces of microplastics with biofilm," *J Environ Radioact*, vol. 190–191, pp. 130–133, Oct. 2018, doi: 10.1016/j.jenvrad.2018.05.001.
- [158] S. Chegrouche, A. Mellah, and M. Barkat, "Removal of strontium from aqueous solutions by adsorption onto activated carbon: kinetic and thermodynamic studies," *Desalination*, vol. 235, no.

1–3, pp. 306–318, Jan. 2009, doi:
10.1016/J.DESAL.2008.01.018.

- [159] A. Taranc, J. F. Garc, and G. Rauret, “Determination of beta emitters (Sr-90, C-14 and H-3) in routine measurements using plastic scintillation beads,” *Nuclear Instruments and Methods in Physics Research A*, vol. 516, pp. 602–609, 2004, doi: 10.1016/j.nima.2003.08.172.
- [160] Chemical Rubber Company, *CRC Handbook of Radioactive Nuclides*. Ohio: Chemical Rubber Company, 1969.
- [161] J. Graham, “Sellafield Ltd - Borehole Data Request,” National Nuclear Laboratory, 2023.
- [162] D. McNulty, A. Hennessy, M. Li, E. Armstrong, and K. M. Ryan, “A review of Li-ion batteries for autonomous mobile robots: Perspectives and outlook for the future,” *J Power Sources*, vol. 545, p. 231943, 2022, doi: 10.1016/j.jpowsour.2022.231943.
- [163] S. Min, K. H. Ko, B. Seo, J. Cheong, C. Roh, and S. Hong, “Wireless backpack system for detection of radioactive cesium on contaminated soil using portable plastic scintillator with efficient readout device,” *Electronics (Switzerland)*, vol. 10, no. 22, p. 2833, Nov. 2021, doi: 10.3390/ELECTRONICS10222833/S1.
- [164] Fogstar Ltd, “Samsung 35E 18650 Battery,” fogstar.co.uk. Accessed: Jul. 14, 2024. [Online]. Available: <https://www.fogstar.co.uk/products/samsung-35e-18650-battery>
- [165] F. A. Doljack, “PolySwitch PTC Devices—A New Low-Resistance Conductive Polymer-Based PTC Device for Overcurrent Protection,” *IEEE Transactions on Components, Hybrids, and*

Manufacturing Technology, vol. 4, no. 4, pp. 372–378, 1981, doi: 10.1109/TCHMT.1981.1135838.

- [166] P. G. Balakrishnan, R. Ramesh, and T. Prem Kumar, “Safety mechanisms in lithium-ion batteries,” *J Power Sources*, vol. 155, no. 2, pp. 401–414, Apr. 2006, doi: 10.1016/J.JPOWSOUR.2005.12.002.
- [167] A. Peddi and A. Peddi, “Designing a Low-Cost Weather Monitoring System using NodeMCU,” *International Research Journal of Engineering and Technology*, vol. 7, no. 5, pp. 830–833, 2020, Accessed: Jan. 22, 2024. [Online]. Available: <https://www.irjet.net/archives/V7/i5/IRJET-V7I5163.pdf>
- [168] T. Abuzairi, I. Sumantri, A. Irfan, and M. Mohamad, “Infrared thermometer on the wall (iThermowall): An open source and 3-D print infrared thermometer for fever screening,” *HardwareX*, vol. 9, Apr. 2020, doi: 10.1016/j.ohx.2020.e00168.
- [169] G. Lui, “Tested: Canton-Power DDO603SA 3.3V Buck-Boost Converter Module,” Dr. Gough’s Techzone. Accessed: Jul. 14, 2024. [Online]. Available: <https://goughlui.com/2018/07/03/tested-canton-power-ddo603sa-3-3v-buck-boost-converter-module/>
- [170] Arctic, “MX-6: Ultimate Performance Thermal Paste,” arctic.de. Accessed: Jul. 14, 2024. [Online]. Available: <https://www.arctic.de/en/MX-6/ACTCP00080A>
- [171] Lunds Universitet, “WWW Table of Radioactive Isotopes, Gamma Energy Search A = 60,” nucleardata.nuclear.lu.se. Accessed: Jul. 14, 2024. [Online]. Available: <http://nucleardata.nuclear.lu.se/toi/Gamma.asp?sql=&A1=60&A2=60&Z=27>

- [172] Lunds Universitet, "WWW Table of Radioactive Isotopes, Gamma Energy Search A = 137," nucleardata.nuclear.lu.se. Accessed: Jul. 14, 2024. [Online]. Available: <http://nucleardata.nuclear.lu.se/toi/Gamma.asp?sql=&A1=137&A2=137&Z=55>
- [173] Lunds Universitet, "WWW Table of Radioactive Isotopes, Gamma Energy Search A = 22," nucleardata.nuclear.lu.se. Accessed: Jul. 14, 2024. [Online]. Available: <http://nucleardata.nuclear.lu.se/toi/Gamma.asp?sql=&A1=22&A2=22&Z=11>

9 Appendix

Appendix A. Liquid Scintillation Counter Calibration

Liquid scintillation is the ideal method for the detection of tritium and low quantities of other beta-emitting tracers. It is commonly used in open-source laboratories to detect possible contamination of work surfaces and samples. As well as general safety, within this work liquid scintillation has been utilised to measure the quantity of tritium to strontium-90 within the flush samples used to clean the flow cell.

Overtime liquid scintillation counting (LSC) machines go out of calibration as their internal photomultiplier tubes (PMTs) degrade and therefore produce more noise and are less sensitive to incident photons. Because of this, a calibration procedure has been followed before the machine was used and the flow cells tested.

For calibration with tritium, a total of 21 vial standards were created consisting of three sets of seven concentrations of dilute tritiated water mixed with deionised water. The ratio of tritium to water was varied, but the combined mass of the sample and liquid scintillation cocktail was kept constant at 5 g sample to 10 g GoldStar [129], this ensured a constant quenching for all tested vials. The spectral index of external standard (tSIE) value, normally produced by the LSC to measure the quenching of the vials, could not be used as the machine's internal barium source had depleted resulting in invalid results being recorded.

The setup of the LSC is as follows, each of the vials were counted for 2 hours, and the energy band was set from 2 keV to 18.6 keV which is ideal for tritium while removing counts from pair production. Figure A.1 and Table A.1 show the resulting data recorded in the calibration.

Appendix A: Appendix

Table A.1 Measurement data recorded by LSC in the calibration routine. All values have been rounded to 2 d.p.

Tritiated Water	Tritium Activity	Measured Background	³H Detection
Added to Vial (mL)	Within Vial (Bq)	Removed (CPM)	Efficiency (%)
0.00	0.00	2.60	N/A
0.00	0.00	2.01	N/A
0.00	0.00	-0.08	N/A
0.10	21.26	152.96	11.99
0.10	21.46	154.93	12.03
0.11	22.73	160.76	11.79
0.20	42.78	307.21	11.97
0.20	43.12	308.94	11.94
0.20	43.15	311.18	12.02
0.40	85.74	621.21	12.07
0.40	85.45	612.01	11.94
0.41	86.25	618.88	11.96
0.60	127.69	919.85	12.01
0.61	128.59	919.21	11.91
0.60	126.52	906.92	11.95
0.80	169.33	1,221.41	12.02
0.81	171.72	1,230.91	11.95
0.80	170.19	1,216.27	11.91
1.01	212.97	1,528.42	11.96
1.00	211.67	1,525.10	12.01
1.01	214.41	1,535.49	11.94
0.00	0.00	-2.60	N/A
0.00	0.00	-2.01	N/A
0.00	0.00	0.08	N/A

Appendix A: Appendix

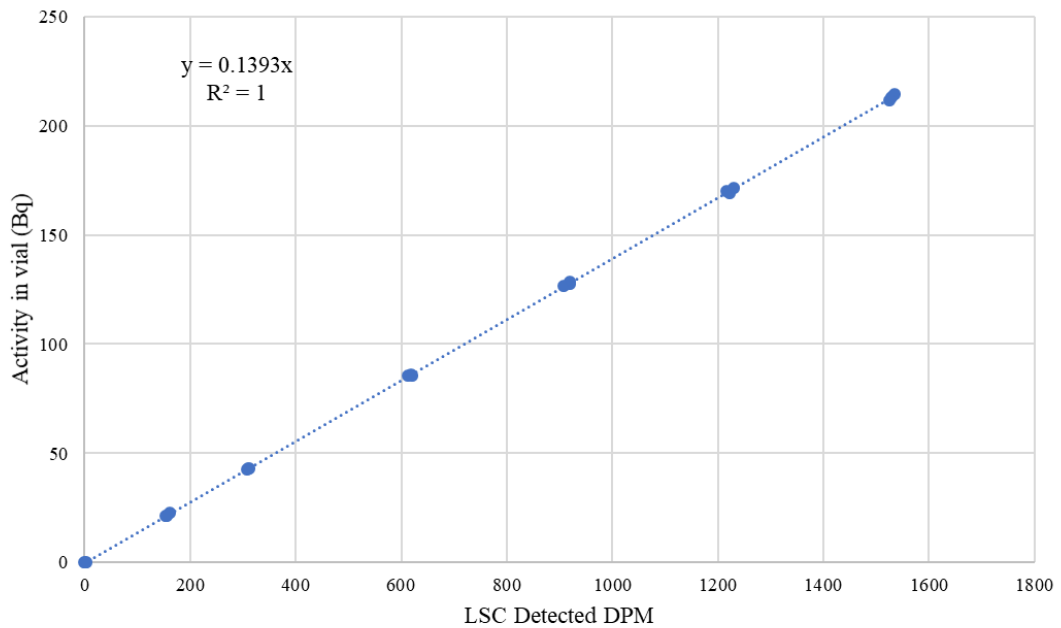


Figure A.1: Calibration graph relating detected disintegrations per minute (DPM) by the LSC to the actual tritium activity contained within the tested vial. A dotted blue line represents a linear line of best fit, forced through zero.

As expected, a linear relationship is seen between detected counts and activity. Using the formula for the line of best fit allows the LSC detected DPM to be converted into actual activity (given that the quenching within the vial is kept constant).

For calibration with strontium-90 a similar method was used, 16 vial standards were created consisting of four background vials and six pairs of strontium-90 containing vials with varying concentrations. The exact added quantities can be viewed in Table A.2 and results have been plotted in Figure A.2.

Appendix A: Appendix

Table A.2 Measurement data recorded by LSC in the calibration routine. All values have been rounded to 2 d.p.

⁹⁰ Sr Tracer Added to	⁹⁰ Sr Activity Within	Measured Background	⁹⁰ Sr Detection
Vial (mL)	Vial (Bq)	Removed (CPM)	Efficiency (%)
0.00	0.00	7.25	N/A
0.00	0.00	6.96	N/A
0.02	26.62	288.52	17.62
0.03	27.48	300.65	17.80
0.05	51.08	552.17	17.79
0.05	54.96	590.41	17.69
0.08	84.81	915.13	17.84
0.08	81.26	844.42	17.18
0.10	109.71	1,158.97	17.50
0.10	109.49	1,158.90	17.53
0.12	133.20	1,321.97	16.45
0.13	136.11	1,317.58	16.05
0.15	163.91	1,752.03	17.74
0.15	162.51	1,659.49	16.95
0.00	0.00	7.09	N/A
0.00	0.00	7.03	N/A

Appendix A: Appendix

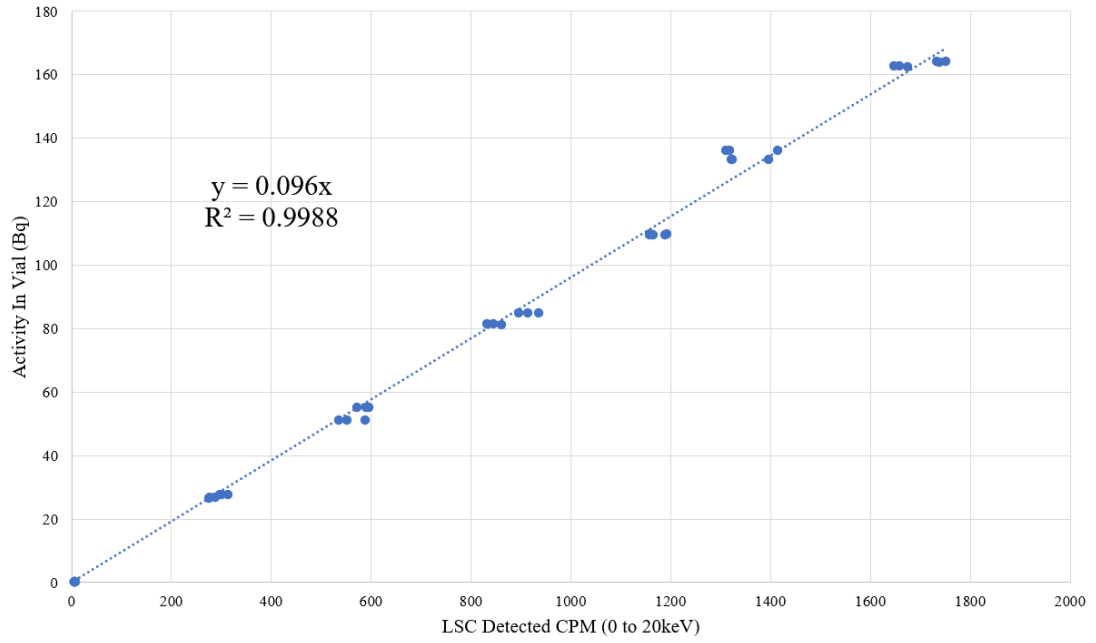


Figure A.2: Calibration graph relating detected DPM by the LSC to the actual strontium-90 activity contained within the tested vial. A dotted blue line represents a linear line of best fit, forced through zero.

Appendix B. Minimum Detecting Time

Minimal detectable activity (MDA) is a measure of how sensitive a detector is to a particular radioactive sample, given a pre-measured background count, and a set measurement time for both background and sample.

The aim of this Appendix is to define minimum detecting time (MDT) which here is defined as the time required to measure a background and a sample to a desired MDA. For this derivation, the measurement time of both the sample (t_s) and background (t_b) are the same ($t_s = t_b$).

MDT can be useful for finding how long a detector would have to stay in-situ before it can reach a particular MDA, given that the detector has been previously characterised with a known tritium source. If measuring tritium activity in water, it is useful to know how much time would be required to be capable of detecting activity below the WHO limit of 10,000 Bq L⁻¹.

Firstly, starting with the equation for efficiency ε :

$$\varepsilon = \frac{S - B}{60 \times A \times V}$$

Where B is the detected background in CPM, S is the detected CPM when measuring the sample, A is the activity of the sample (Bq mL⁻¹) and V is the volume of the sample within the detector (mL).

Now for the equation of minimum detectable activity (MDA):

$$MDA(\text{Bq mL}^{-1}) = \frac{2k \sqrt{\frac{B}{t_s} + \frac{B}{t_b} + \frac{k^2}{t_s}}}{60 \times \varepsilon \times V}$$

Where t_s and t_b are count times for the sample and background respectively in minutes. k is the one-sided confidence factor 1.646 at 95% confidence. Assuming the detector runs a background reading for the same amount of time as the sample reading i.e. $T = t_s = t_b$, the equation can be simplified to:

Appendix B: Appendix

$$MDA(Bq mL^{-1}) = \frac{k^2 + 2k\sqrt{2}\sqrt{BT}}{60 \times T \times \varepsilon \times V}$$

Given that the MDA, ε , V and B of the detector are known, the formular can be rearranged to be put in terms of T . From now MDA will be represented by M for clarity.

Simplify the form of the equation to,

$$M = \frac{l + n\sqrt{BT}}{pT}$$

Were,

$$l = k^2$$

$$n = 2k\sqrt{2}$$

$$p = 60 \times \varepsilon \times V$$

Rearrange to standard form polynomial,

$$MpT = l + n\sqrt{BT}$$

$$MpT - l = n\sqrt{BT}$$

$$(MpT - l)^2 = n^2BT$$

$$M^2p^2T^2 - 2lMpT + l^2 = n^2BT$$

$$M^2p^2T^2 - 2lMpT - n^2BT + l^2 = 0$$

$$(M^2p^2)T^2 - (2lMp + n^2B)T + l^2 = 0$$

Next solve for T using the quadratic equation,

$$T = \frac{-b \pm \sqrt{b^2 - 4ac}}{2a}$$

Appendix B: Appendix

$$T = \frac{2lMp + n^2B \pm \sqrt{(-2lMp - n^2B)^2 - 4M^2p^2l^2}}{2M^2p^2}$$

Multiplying out,

$$(-2lMp - n^2B)^2 = 4M^2p^2l^2 + 4lMpn^2B + n^4B^2$$

Adding back into equation,

$$T = \frac{2lMp + n^2B \pm \sqrt{4lMpn^2B + n^4B^2}}{2M^2p^2}$$

$$T = \frac{2lMp + n^2B \pm n\sqrt{4lMpB + n^2B^2}}{2M^2p^2}$$

Replacing l and n ,

$$T = \frac{2 \times k^2 \times Mp + (k2\sqrt{2})^2B \pm k2\sqrt{2} \sqrt{4 \times k^2 \times MpB + (k2\sqrt{2})^2B^2}}{2M^2p^2}$$

$$T = \frac{2k^2Mp + 8k^2B \pm k2\sqrt{2} \sqrt{4k^2MpB + 8k^2B^2}}{2M^2p^2}$$

Replacing p ,

$$T = \frac{2k^2M(60 \times \varepsilon \times V) + 8k^2B \pm k2\sqrt{2} \sqrt{4k^2MB(60 \times \varepsilon \times V) + 8k^2B^2}}{2M^2(60 \times \varepsilon \times V)^2}$$

$$= \frac{120k^2M\varepsilon V + 8k^2B \pm k2\sqrt{2} \sqrt{240k^2MB\varepsilon V + 8k^2B^2}}{2M^2(60\varepsilon V)^2}$$

$$= \frac{120k^2M\varepsilon V + 8k^2B \pm \sqrt{1920k^4MB\varepsilon V + 64k^4B^2}}{2M^2(60\varepsilon V)^2}$$

$$= \frac{60k^2M\varepsilon V + 4k^2B \pm \sqrt{480k^4MB\varepsilon V + 16k^4B^2}}{M^2(60\varepsilon V)^2}$$

Appendix B: Appendix

$$MDT(\text{minute}) = \frac{15k^2 M\epsilon V + k^2 B \pm \sqrt{30k^4 MB\epsilon V + k^4 B^2}}{900M^2 \epsilon^2 V^2}$$

As the time required to measure an activity above an infinite background would be infinite, the following statement must be true:

$$\lim_{B \rightarrow \infty} (MDT(\text{minute})) = \infty$$

If solution 1 (plus root),

$$\begin{aligned} \lim_{B \rightarrow \infty} \left(\frac{15k^2 M\epsilon V + k^2 B + \sqrt{30k^4 MB\epsilon V + k^4 B^2}}{900M^2 \epsilon^2 V^2} \right) \\ = \frac{k^2}{900M^2 \epsilon^2 V^2} \lim_{B \rightarrow \infty} \left(15M\epsilon V + B + \sqrt{30MB\epsilon V + B^2} \right) \end{aligned}$$

Substitute,

$$Q = 15M\epsilon V$$

$$J = \frac{k^2}{900M^2 \epsilon^2 V^2}$$

So,

$$\begin{aligned} J \lim_{B \rightarrow \infty} \left(Q + B + \sqrt{2QB + B^2} \right) &= J \lim_{B \rightarrow \infty} \left(Q + B + B\sqrt{2QB^{-1} + 1} \right) \\ &= J \lim_{B \rightarrow \infty} \left(Q + B \left(1 + \sqrt{2QB^{-1} + 1} \right) \right) \end{aligned}$$

Multiply by conjugate,

$$\left(1 + \sqrt{2QB^{-1} + 1} \right) \cdot \frac{\left(-1 + \sqrt{2QB^{-1} + 1} \right)}{\left(-1 + \sqrt{2QB^{-1} + 1} \right)} = \frac{2QB^{-1}}{\sqrt{2QB^{-1} + 1} - 1}$$

So,

Appendix B: Appendix

$$\begin{aligned}
 J \lim_{B \rightarrow \infty} \left(Q + B \left(\frac{2QB^{-1}}{\sqrt{2QB^{-1} + 1} - 1} \right) \right) &= J \lim_{B \rightarrow \infty} \left(Q + \frac{2Q}{\sqrt{2QB^{-1} + 1} - 1} \right) \\
 &= J \left(Q + \frac{2Q}{\sqrt{0 + 1} - 1} \right) = J \left(Q + \frac{2Q}{\sqrt{1} - 1} \right) = J(Q + \infty) = J \cdot \infty = \infty
 \end{aligned}$$

If solution 2 (minus root),

$$\begin{aligned}
 \lim_{B \rightarrow \infty} \left(\frac{15k^2 M \varepsilon V + k^2 B - \sqrt{30k^4 M B \varepsilon V + k^4 B^2}}{900M^2 \varepsilon^2 V^2} \right) \\
 = \frac{k^2}{900M^2 \varepsilon^2 V^2} \lim_{B \rightarrow \infty} \left(15M \varepsilon V + B - \sqrt{30MB \varepsilon V + B^2} \right)
 \end{aligned}$$

Substitute,

$$Q = 15M \varepsilon V$$

$$J = \frac{k^2}{900M^2 \varepsilon^2 V^2}$$

So,

$$\begin{aligned}
 J \lim_{B \rightarrow \infty} \left(Q + B - \sqrt{2QB + B^2} \right) &= J \lim_{B \rightarrow \infty} \left(Q + B - B \sqrt{2QB^{-1} + 1} \right) \\
 &= J \lim_{B \rightarrow \infty} \left(Q + B \left(1 - \sqrt{2QB^{-1} + 1} \right) \right)
 \end{aligned}$$

Multiply by conjugate,

$$\left(1 - \sqrt{2QB^{-1} + 1} \right) \cdot \frac{(-1 - \sqrt{2QB^{-1} + 1})}{(-1 - \sqrt{2QB^{-1} + 1})} = \frac{-2QB^{-1}}{1 + \sqrt{2QB^{-1} + 1}}$$

So,

$$\begin{aligned}
 J \lim_{B \rightarrow \infty} \left(Q + B \left(\frac{-2QB^{-1}}{1 + \sqrt{2QB^{-1} + 1}} \right) \right) &= J \lim_{B \rightarrow \infty} \left(Q - \frac{2Q}{1 + \sqrt{2QB^{-1} + 1}} \right) \\
 &= J \left(Q - \frac{2Q}{1 + \sqrt{0 + 1}} \right) = J \left(Q - \frac{2Q}{1 + \sqrt{1}} \right) = J(Q - Q) = J \cdot 0 = 0
 \end{aligned}$$

Appendix A: Appendix

Therefore, only solution 1 (plus root) results in the correct limit.

$$MDT(\text{minute}) = \frac{15k^2M\varepsilon V + k^2B + \sqrt{30k^4MB\varepsilon V + k^4B^2}}{900M^2\varepsilon^2V^2} \quad (\text{A.1})$$

Appendix C. Printed Circuit Board

Design Drawings and Schematics

Within this appendix are figures depicting the printed circuit board designs and schematics used for the flow cell detector. Copper traces on top of the board are coloured red, and copper traces below the board are coloured green. For manufacturing, Gerber files were created from these designs and sent to the manufacturer.

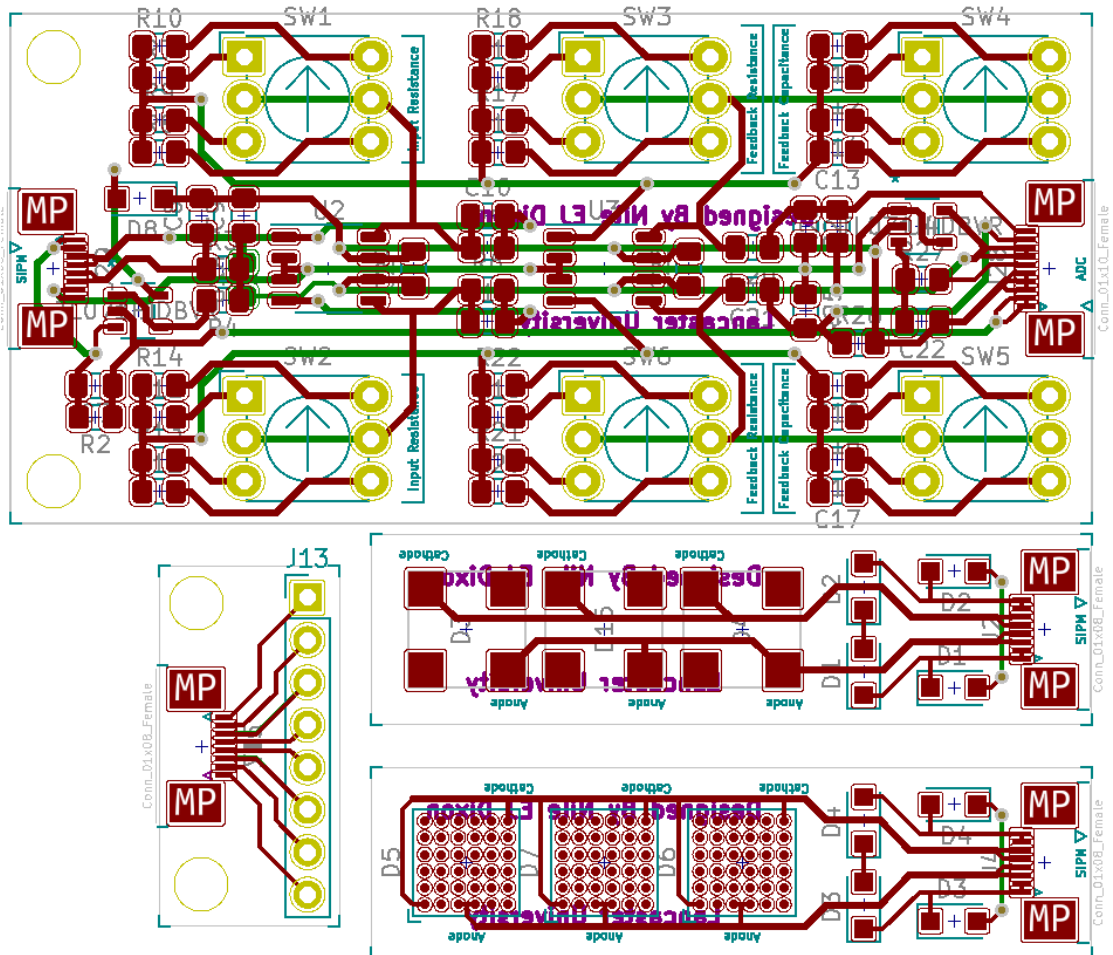


Figure C.1: Printed circuit board (PCB) design of silicon photomultiplier (SiPM) configurable amplifier, prototype SiPM sensor heads and flat flex cable (FFC) breakout board. Top copper shown in red, bottom copper shown in green.

Appendix C: Appendix

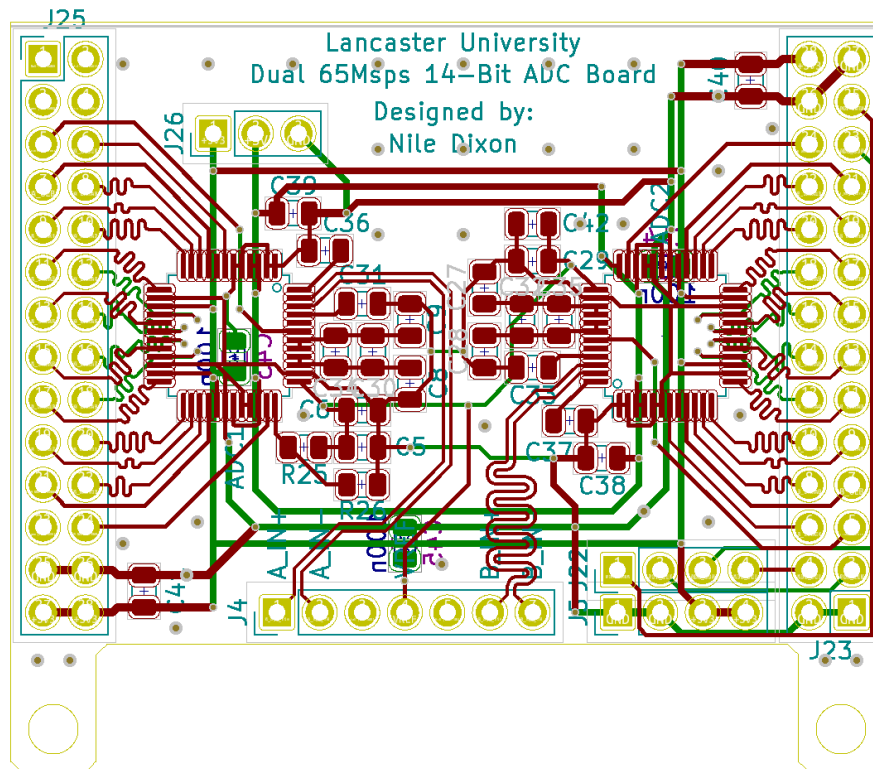


Figure C.4: PCB design for ADC board. Top copper shown in red, bottom copper shown in green.

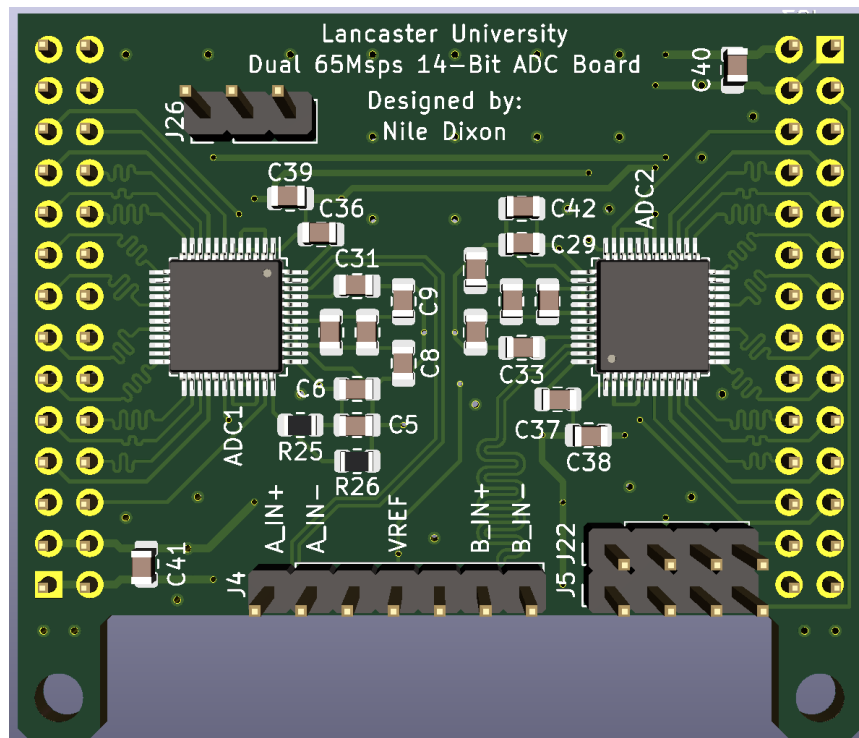


Figure C.5: 3D Visual rendering of ADC board.

Appendix C: Appendix

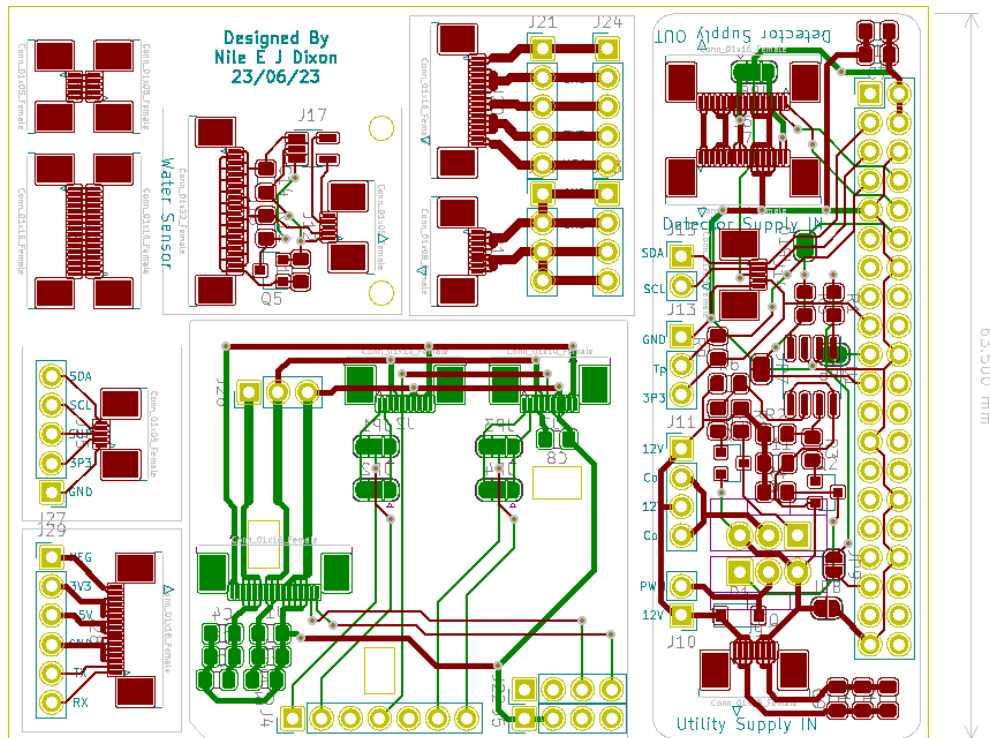


Figure C.6: PCB design for FFC adapter boards and raspberry pi zero hat. Boards were manufactured together and separated using a guillotine cutter. Top copper shown in red, bottom copper shown in green.

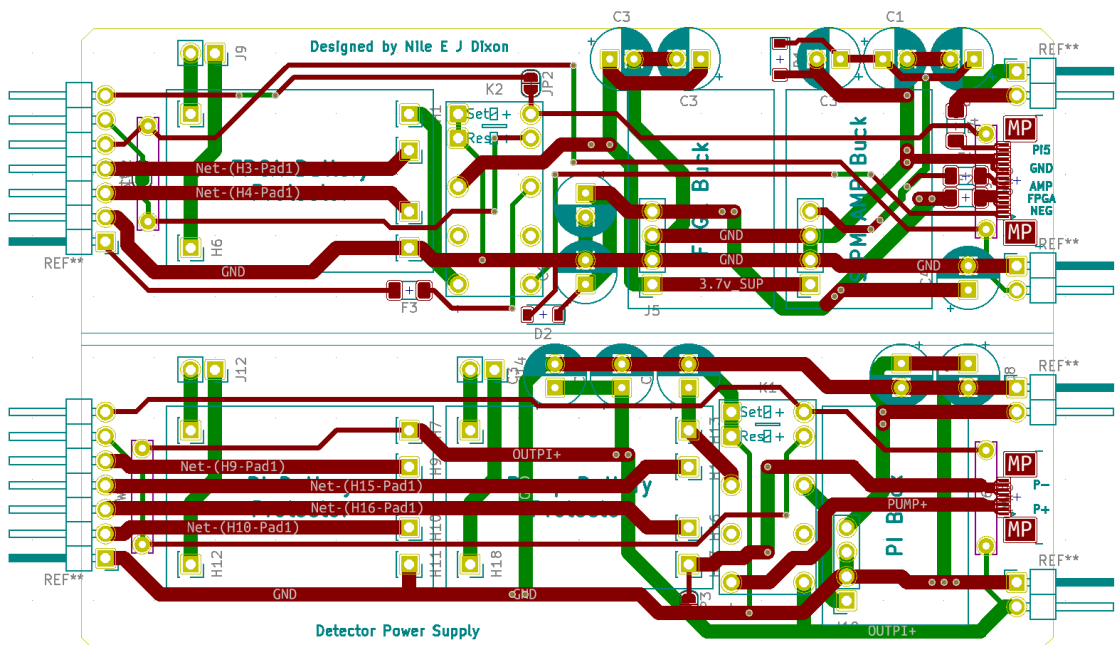


Figure C.7: PCB design of compacted power supply (main boards only). Top copper shown in red, bottom copper shown in green.

Appendix C: Appendix

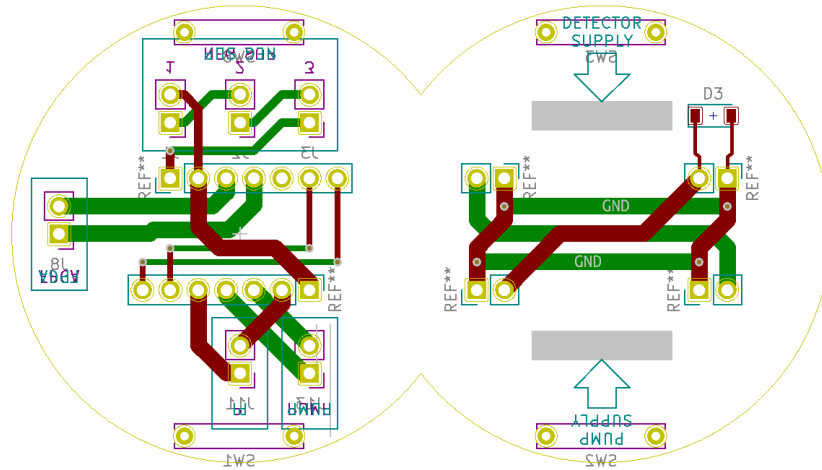


Figure C.8: PCB design of compacted power supply (side boards only). Top copper shown in red, bottom copper shown in green.

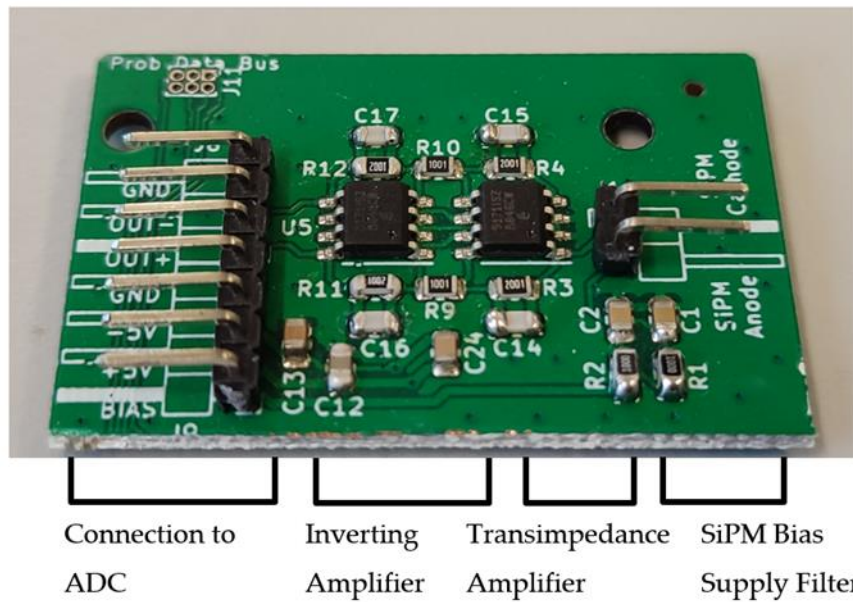


Figure C.9: Picture of manufactured SiPM amplifier board labelled with key sections, based on schematic shown in Figure 3.4. The board measures approximately 28 mm by 42 mm.

Appendix D. Detector Switch Settings

This appendix shows the amplifier settings (selected using six rotary switches) used in the experiments for the detection of tritium and strontium-90, discussed in Chapter 5.

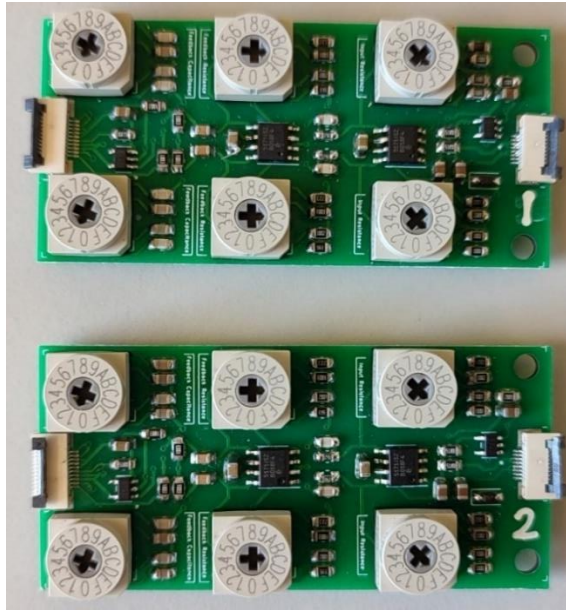


Figure D.1: Image of silicon photomultiplier (SiPM) amplifiers with settings used for the detection of ^3H and environmental borehole samples (switch settings are 1, C and E from left to right).

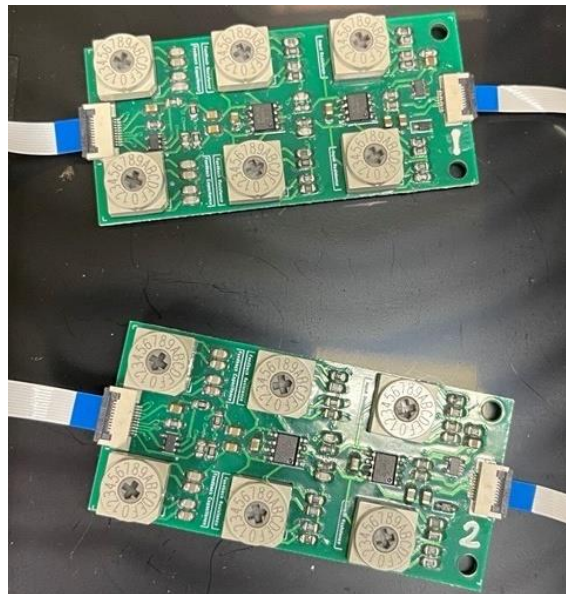


Figure D.2: Image of SiPM amplifiers with settings used for the detection of ^{90}Sr and ^3H mixtures (switch settings are 1, B and F from left to right).

Appendix E. Field Programmable Gate Array Pulse Shaper Code

This appendix consists of very high-speed integrated circuit (VHSIC) hardware description language (VHDL) code, used for detecting a shaping pulses from the SiPM amplifier boards digitised by the analogue to digital converter.

```
library IEEE;
use IEEE.STD_LOGIC_1164.ALL;
use IEEE.NUMERIC_STD.ALL;
use ieee.std_logic_signed.ALL;
```

Figure E.1: Code of included libraries.

```
entity ADC_Controller is
generic (
  Trapezoidal_Shaper : boolean := true;
  A_DELAY_1 : integer := 500;
  A_DELAY_2 : integer := 40;
  A_DELAY_3 : integer := 500;
  A_DELAY_4 : integer := 500;
  A_M : integer := 216;

  B_DELAY_1 : integer := 500;
  B_DELAY_2 : integer := 40;
  B_DELAY_3 : integer := 500;
  B_DELAY_4 : integer := 500;
  B_M : integer := 216;

  Threshold_Upper : integer := 380000
);
port(
  Clock_In : in std_logic;
  Reset : in std_logic;

  ADC_A_Data_Format : out std_logic;
  ADC_A_Clock : out std_logic;
  ADC_A_Stabilizer : out std_logic;
  ADC_A_OEB : out std_logic; --Active Low
  ADC_A_Data : in std_logic_vector(13 downto 0);
  ADC_A_Out_Of_Range : in std_logic;

  ADC_B_Data_Format : out std_logic;
  ADC_B_Clock : out std_logic;
  ADC_B_Stabilizer : out std_logic;
  ADC_B_OEB : out std_logic; --Active Low
  ADC_B_Data : in std_logic_vector(13 downto 0);
  ADC_B_Out_Of_Range : in std_logic;

  A_Trigger_Pin : out std_logic := '0';
  B_Trigger_Pin : out std_logic := '0';

  TX : out std_logic;
  Timer_TX : out std_logic
);
end ADC_Controller;
```

Figure E.2: Setup of delay lengths, shaped pulse threshold and the connections from the field programmable gate array (FPGA) to the analogue to digital converters (ADCs).

Appendix E: Appendix

```

Spectrum_Memory : component Spectrum_RAM
port map (
    clk_clk           => Clock_In,           --          clk.clk
    reset_reset_n    => Reset,              --          reset.reset_n
    pulse_data_in_address => sig_pulse_data_in_address, -- pulse_data_in.address
    pulse_data_in_clken => '1',            --          .clken
    pulse_data_in_chipselect => sig_pulse_data_in_chipselect, -- .chipselect
    pulse_data_in_write => sig_pulse_data_in_write, -- .write
    pulse_data_in_readdata => sig_pulse_data_in_readdata, -- .readdata
    pulse_data_in_writedata => sig_pulse_data_in_writedata, -- .writedata
    pulse_data_in_byteenable => "11", -- .byteenable
    pulse_data_out_address => sig_pulse_data_out_address, -- pulse_data_out.address
    pulse_data_out_chipselect => sig_pulse_data_out_chipselect, -- .chipselect
    pulse_data_out_clken => '1', -- .clken
    pulse_data_out_write => sig_pulse_data_out_write, -- .write
    pulse_data_out_readdata => sig_pulse_data_out_readdata, -- .readdata
    pulse_data_out_writedata => sig_pulse_data_out_writedata, -- .writedata
    pulse_data_out_byteenable => "11" -- .byteenable
);

```

Figure E.3: Setup of spectrum random access memory (RAM).

```

Trapezoidal_Shaper_Gen: if Trapezoidal_Shaper generate

    ADC_A_Clock <= Clock_In; -- Send clock to ADC A
    ADC_B_Clock <= Clock_In; -- Send clock to ADC B

    ADC_A_OEB <= '0'; -- turn on adc A's output
    ADC_B_OEB <= '0'; -- turn on adc B's output
    ADC_A_Data_Format <= '0'; -- Binary format
    ADC_B_Data_Format <= '0'; -- Binary format
    ADC_A_Stabilizer <= '1'; -- Use clock Stabilizer
    ADC_B_Stabilizer <= '1'; -- Use clock Stabilizer

    sig_pulse_data_out_chipselect <= '1'; -- Select Spectrum RAM

    sig_pulse_data_out_address <= Spectrum_Address_Count(11 downto 0);

    ADC_B_Data_16bit <= "00" & ADC_B_Data_Inv;
    ADC_A_Data_16bit <= "00" & ADC_A_Data_Inv;

```

Figure E.4: Start of shaper generation, both ADC outputs are turned on, FPGA clock sent to ADC clock input, binary format selected and 14-bit ADC values are padded to 16-bit for shaping algorithm.

```

process(Clock_In)
begin
  if (rising_edge(Clock_In)) then
    ADC_A_Data_Inv <= ADC_A_Data;
    A_Delay_Memory_1 <= A_Delay_Memory_1((16*(A_DELAY_1-1))-1 downto 0) & ADC_A_Data_16bit;
    A_Delay_Memory_2 <= A_Delay_Memory_2((16*(A_DELAY_2-1))-1 downto 0) & A_Delay_Memory_1((16*A_DELAY_1)-1 downto (16*(A_DELAY_1-1)));
    A_Delay_Memory_3 <= A_Delay_Memory_3((16*(A_DELAY_3-1))-1 downto 0) & A_Delay_Memory_2((16*A_DELAY_2)-1 downto (16*(A_DELAY_2-1)));
    A_SUM_1 <= signed(ADC_A_Data_16bit) - signed(A_Delay_Memory_1((16*A_DELAY_1)-1 downto (16*(A_DELAY_1-1))));
    A_SUM_2 <= signed(A_Delay_Memory_2((16*A_DELAY_2)-1 downto (16*(A_DELAY_2-1)))) - signed(A_Delay_Memory_3((16*A_DELAY_3)-1 downto (16*(A_DELAY_3-1))));
    A_SUM_4 <= A_ACC_1 + A_MUL_1;
    A_ACC_1 <= A_ACC_1 + A_SUM_3;
    A_MUL_1 <= A_SUM_3 * A_M;
    A_SUM_3 <= A_SUM_1 - A_SUM_2;
    A_Delay_Memory_4 <= A_Delay_Memory_4((32*(A_DELAY_4-1))-1 downto 0) & std_logic_vector(A_SUM_4);
    A_Delay_Out <= signed(A_Delay_Memory_4((32*A_DELAY_4)-1 downto (32*(A_DELAY_4-1))));
  end if;
end process;

```

Figure E.5: Shaping algorithm (duplicated for second ADC channel), each delay vector is used to shift ADC samples every clock cycle.

Appendix E: Appendix

```

process(Clock_In)
begin
  if (rising_edge(Clock_In)) then
    case ACC_Case is
      when Startup =>
        if (Int_Count = Int_Time) then
          ACC_Case <= Wait_ACC;
          Int_Count <= 0;
          ACC_Pause <= '0';
        else
          Int_Count <= Int_Count + 1;
        end if;
      when Wait_ACC =>
        if (signed(B_SUM_4) >= Threshold_Upper) and (signed(A_SUM_4) >= Threshold_Upper) and
          (signed(B_SUM_4_OLD) < Threshold_Upper) and (signed(A_SUM_4_OLD) < Threshold_Upper) then
          ACC_Case <= Run_ACC;
        end if;
        B_SUM_4_OLD <= B_SUM_4;
        A_SUM_4_OLD <= A_SUM_4;
      when Run_ACC =>
        A_ACC_2 <= A_ACC_2 + A_Delay_Out;
        B_ACC_2 <= B_ACC_2 + B_Delay_Out;
        if (Int_Count = Int_Time) then
          ACC_Case <= Update_RAM;
          sig_pulse_data_in_chipselect <= '1'; -- Select Spectrum RAM
          sig_pulse_data_in_write <= '0'; -- Read from Spectrum RAM
          Int_Count <= 0;
        else
          Int_Count <= Int_Count + 1;
          if (signed(A_PEAK) < A_ACC_2) then
            A_PEAK <= std_logic_vector(A_ACC_2);
          end if;
          if (signed(B_PEAK) < B_ACC_2) then
            B_PEAK <= std_logic_vector(B_ACC_2);
          end if;
        end if;
      when Update_RAM =>
        sig_pulse_data_in_write <= '1'; -- Write to Spectrum RAM
        sig_pulse_data_in_writedata <= sig_pulse_data_in_readdata + 1; -- Increment channel count
        ACC_Case <= Reset_PEAK;
      when Reset_PEAK =>
        A_PEAK <= (others => '0');
        A_ACC_2 <= (others => '0');
        B_PEAK <= (others => '0');
        B_ACC_2 <= (others => '0');
        sig_pulse_data_in_chipselect <= '0'; -- De-Select Spectrum RAM
        ACC_Case <= Wait_ACC;
      end case;
      A_OUTPUT_1 <= A_ACC_2;
      B_OUTPUT_1 <= B_ACC_2;
    end if;
  end process;

```

Figure E.6: Code of finite state machine (FSM) discussed in section 3.7.1.

```

process(Clock_In)
begin
  if(rising_edge(Clock_In)) then
    sig_pulse_data_in_address <= B_PEAK(29 downto 18);
  end if;
end process;

```

Figure E.7: Assigning peak of shaped pulse to address of spectrum RAM.

Appendix E: Appendix

```
process(Clock_In)
begin
  if (rising_edge(Clock_In)) then
    if (Finished_sending = '0') then --send data
      if (TX_Active = '1') then
        TX_DV <= '0';
        -- Wait
      elsif ((TX_Active = '0') AND (TX_DV = '1')) then
        -- Wait
      elsif(Spectrum_Address_Count = "1000000000000") then -- All sent
        Finished_sending <= '1';
      elsif(Spectrum_Address_Count = "10000000000001") then -- Start sending all
        TX_DV <= '1'; -- select serial
        TX_data_bus <= "10000000";
        Spectrum_Address_Count <= "0000000000000";
        flip <= '0';
      elsif (flip = '0') then
        TX_DV <= '1'; -- Select serial
        TX_data_bus <= '0' & sig_pulse_data_out_readdata(6 downto 0);
        TX_Upper <= sig_pulse_data_out_readdata(13 downto 7);
        sig_pulse_data_out_writedata <= (others => '0');
        sig_pulse_data_out_write <= '1';
        flip <= '1';
      elsif (flip = '1') then
        TX_DV <= '1'; -- Select serial
        TX_data_bus <= '0' & TX_Upper;
        Spectrum_Address_Count <= Spectrum_Address_Count + 1;
        sig_pulse_data_out_write <= '0';
        flip <= '0';
      end if;
    elsif (exposure < 1073741823) then
      exposure <= exposure + 1;
    else
      Finished_sending <= '0';
      exposure <= 0;
      Spectrum_Address_Count <= "10000000000001";
    end if;
  end if;
end process;
```

Figure E.8: Process that reads each detector channel from memory and transmits values by interfacing with a UART component.

Appendix F. Advatech Scintillator Comparison

To help identify scintillators suitable for low energy beta detection a comparison of the available scintillators offered by Advatech can be seen in Table F.1. Scintillators have been compared based on the key ideal features defined in section 2.8, colour coding has been used to show if it has a desired property (green) or an undesired property (red) with points 1 and -1 given respectively. Some properties are undefined and so have been excluded from the comparison.

Table F.1: Comparison of scintillators offered by Advatech.

Name	Intrinsically radioactive	Hygroscopic	Density	Light Yield	Peak λ	Points
BaF ₂ slow	No	Slightly	4.893	10	310	-2
BGO	Yes	No	7.13	8-10	480	-2
CaF ₂ (Eu)	No	No	3.18	30	435	3
CdWO ₄	Yes	No	7.9	28	490	-2
CeBr ₃	No	Yes	5.1	60	380	0
CeF ₃ slow	No	No	6.16	8	340	-1
CLYC(Ce)	No	Yes	3.31	20	370	-2
CsI	No	Slightly	4.51	2	315	-2
CsI(Na)	No	Yes	4.51	41	420	1
CsI(Tl)	No	Slightly	4.51	54	550	0
GAGG(Ce)	No	No	6.63	40-60	520	1
GFAG(Ce)	No	No	6.7	45	520	1
GSO(Ce)	No	No	6.7	8-10	430	1
LaBr ₃ (Ce)	No	Yes	5.2	63	380	0
LaCl ₃ (Ce)	No	Yes	3.86	49	350	0
LBC	No	Yes	4.9	70	380	0
LSO(Ce)	Yes	No	7.4	30	420	0
LuAG(Ce)	Yes	No	6.73	25	535	-3
LuAG(Pr)	Yes	No	6.73	20	310	-3
LuAP(Ce)	Yes	No	8.34	N/A	365	N/A
LYSO(Ce)	Yes	No	7.15	25	410	-1
Nal(Tl)	No	Yes	3.67	55	415	1
NB(WO)	No	No	7.57	N/A	540	N/A
PbF ₂	Yes	No	7.77	N/A	N/A	N/A
PWO	Yes	No	8.28	N/A	430,520	N/A
SrI ₂ (Eu)	No	Yes	4.55	115	435	1
YAG(Ce)	No	No	4.55	35	550	1
YAP(Ce)	No	No	5.37	25	370	0
YSO(Ce)	No	No	4.5	10	420	1
ZnSe(Te)	No	No	5.42	40	640	1
Plastic	No	No	1.06	N/A	430	4±1